DEVELOPMENT OF MULTI-WHEEL DRIVETRAIN CONTROL SYSTEM FOR FUTURE ELECTRIC COMBAT VEHICLE

by

Arnold Odrigo

A Thesis Presented in Partial Fulfillment
of the Requirements for the Degree of

Master of Applied Science
in
Automotive Engineering

Faculty of Engineering and Applied Science
University of Ontario Institute of Technology
Oshawa, Ontario, Canada

April 2017

ABSTRACT

In modern times, electric vehicle and autonomous driving control technology have been rapidly evolving for use in civilian passenger vehicles. They bring forth many benefits in improved mobility, cost savings and life-preserving benefits – all of which can be extended to military vehicles. In this thesis, a comprehensive drivetrain control system for a future fully-electric 8x8 multi-wheeled combat vehicle with autonomous navigation functionality is developed. The proposed combat vehicle is equipped with eight independently-actuated wheels using individual in-wheel driving motors and linear actuators for steering. The control system is intended to harness the flexibility of the electric drivetrain to enable different driving configurations over a range of conditions to maximize mobility, deployability and survivability. The system comprises of autonomous navigation via path preview sensors and a driver model, torque vectoring and skid steering through a single LQR-based active yaw controller, and feedforward zero side-slip rear-wheel steering control. Separate feedforward controllers were also developed for skid steering and rear-wheel steering to mimic existing mechanical implementations for comparison. Vehicle performance evaluation using the control system was divided into low-speed autonomous operation and high-speed manned operation. Under low-speed autonomous operation, the control system achieved stable skid steering up to 40 km/h with significantly reduced driver input effort compared to a conventional combat vehicle. In high-speed manned operation, the LQR torque vectoring controller performed well in stabilizing the vehicle motion over reduced friction conditions. Feedforward zero-side slip control steering the fourth axle improved cornering precision and yaw response below 50 km/h, and improved lateral motion stability steering all wheels up to a recommended operating speed of 80 km/h.

TABLE OF CONTENTS

LIST OF FIGURES

LIST OF TABLES

LIST OF SYMBOLS

Electric Powertrain Variables

I_{motor}	Rotational inertia of electric motor
I_{wheel}	Rotational inertia of wheel
$i_{subscript}$	Individual wheel motor current
n_{motor}	Motor gear reduction ratio
r_{eff}	Effective (loaded) tire rolling radius
T_{net}	Net torque on wheel
T_{motor}	Output motor torque
T_w	Output wheel torque
$\alpha_{subscript}$	Angular acceleration
$\omega_{subscript}$	Angular velocity

Vehicle Kinematic Model Variables

$C_{\alpha i}$	Total tire cornering stiffness per axle
F_X	Longitudinal tire force
F_Y	Lateral tire force
g	Acceleration due to gravity (metric)
k_{ij}	Wheel steer ratio between axles i and j
I_{ZZ}	Vehicle mass moment of inertia
M_Z	Yaw moment around centre of gravity
m	Vehicle mass
U	Longitudinal velocity
V	Lateral velocity
r	Yaw rate around centre of gravity
α_i	Tire slip angle
β	Vehicle side slip angle
$\delta_{subscript}$	Wheel steer angle
μ	Road friction coefficient

Control System Design Variables

[A]	State control matrix
[B]	Input control matrix
[C]	Output control matrix
[D]	Feedforward control matrix
[K]	Controller (LQR Control Gain) matrix
[Q]	State variable weighting matrix
[R]	Output variable weighting matrix
[u]	Input variable vector
[x]	State variable vector
[y]	Output variable vector

LIST OF GENERAL ABBREVIATIONS

4WS	Four-wheel steering
ABS	Anti-lock braking system
AVTP	Allied Vehicle Testing Publication
AWD	All-wheel drive
ESC	Electronic Stability Control
FMVSS	Federal Motor Vehicle Safety Standards
GPS	Global positioning system
IMU	Inertial measurement unit
ISO	International Organization for Standardization
LIDAR	Light Imaging, Detection and Ranging
LQG	Linear-quadratic-Gaussian
LQR	Linear-quadratic regulator
NATO	North Atlantic Treaty Organization
PID	Proportional-plus-Integral-plus-Derivative
RADAR	Radio Detection and Ranging
RPM	Revolutions per minute
RWD	Rear-wheel drive
SAE	Society of Automotive Engineers
SONAR	Sound Navigation and Ranging
TCS	Traction Control System
VDC	Vehicle Dynamics Control
RPM	Four-wheel steering

ACKNOWLEDGEMENTS

I express my sincerest gratitude to my parents and grandparents for the endless love and support they have given me throughout my life, especially in the arduous journey of completing this master's thesis.

I would also like to thank my supervisor, Dr. Moustafa El-Gindy, for having strong faith in my ability, witnessing my potential and allowing me to realize it through this work. I am grateful for this opportunity to have finally defined for myself a clear path in what I wish to pursue as an engineer.

I would like to express my appreciation to Volvo Group Trucks Technology and General Dynamics Land Systems – Canada for funding and providing technical assistance in this work.

Finally, I wish to thank all my friends – the new ones whom I've met on this journey and the ones who have been by my side through the years, unfaltering – for your support, encouragement and the wonderful times we've had together on this journey.

CHAPTER 1
INTRODUCTION

1.1 Motivation

Automotive technology for civilian vehicles has been evolving at an astounding pace, bringing rise to drastic improvements in mobility and safety. However, as this technology is applied relatively swiftly to civilian vehicles, military-use vehicles appear to somewhat lag. The most notable of these new automotive technologies are electric powertrains and autonomous driving control, both of which military applications can greatly benefit from. Electric vehicles boast significantly reduced mechanical complexity, thereby increasing robustness while reducing maintenance costs and operational downtime [1]. Using a fully electric design also allows for more flexibility in implementing various established vehicle control systems, such as traction control (TCS), electronic stability control (ESC) and active torque vectoring, with significantly faster response and overall greater performance [2]. Autonomous driving paired with such control systems can further increase the safety and stability of a vehicle. By eliminating human error, the risk of accidents is reduced as electronic systems and algorithms can process large amounts of data and react significantly faster than a human driver [3].

Autonomous control and electric drive can be potentially applied to multi-wheeled combat vehicles in military applications to further improve mobility and robustness across more volatile and unpredictable working environments. Multi-wheeled combat vehicles are used worldwide by armed forces for various applications. They provide high-speed mobility for both on- and off-road applications where battle tanks with tracks are insufficient. Multi-wheeled combat vehicles also provide a high degree of modularity in terms of weaponry, armour, and other mission-specific requirements. However, with this modularity comes the cost of increased payload as requirements for these combat vehicles evolve, thus impacting vehicle mobility.

When equipped with an electric powertrain, a multi-wheeled combat vehicle is granted the same benefits as civilian vehicles mentioned before, with the added degree of thermal and acoustic stealth from reduced heat and noise generation. Rapidly evolving

power systems will only improve the performance and range of an electric combat vehicle, as well as provide a unified power source for mobility, protection, and weaponry [4]. Autonomous driving capabilities in a multi-wheeled combat vehicle will further save lives in front-line operation with faster decision-making and reaction times, which combined with more powerful vehicle dynamics and stability control, can prevent fatal incidents. Common incidents in combat vehicles include rollover and spinout – both of which are induced by sudden, sharp driver input and overcorrection because of delayed response time combined with the large mass and typically high center of gravity. Additionally, in operating as a reconnaissance, support, or remote weaponry vehicle [5], more lives can be further saved by eliminating the need for human drivers in high-risk environments.

1.2 Scope

This thesis aims to explore and maximize the potential of a proposed fully-electric 8x8 combat vehicle in terms of mobility and control. The vehicle is equipped with autonomous driving capability and a proposed powertrain layout consisting of eight independently-actuated wheels. That is, each wheel consists of its own in-hub electric motor and linear actuator for driving and steering, respectively. This design reduces mechanical complexity and increases the flexibility of the vehicle as differentials are eliminated from the powertrain. The left and right wheels are also mechanically decoupled to allow for variable steering geometry in different configurations.

Given the flexibility of the powertrain, the applications and feasibility of skid steering, rear-wheel steering and torque vectoring will be investigated on this specific combat vehicle. Skid steering, in this work, will be exclusively reserved for autonomous driving. Powertrain and controller design are completed with the use of Simulink, and vehicle testing is performed in TruckSim. Autonomous driving will be simulated by path following, therefore this thesis does not cover localization algorithms or obstacle avoidance. In the aspect of vehicle drivetrain and control, modeling of the power system, suspension system and braking control are not considered in the scope of this work.

1.3 Objectives

The objective of this work is to develop a drivetrain and vehicle dynamics control system for the proposed future electric combat vehicle. The vehicle used in this work will consist of the same dimensions and specifications as that of [6] and uses the electric motors found in the version of the vehicle from [7]. The development process of the control system will consist of:

- Developing a linear-quadratic (LQR) controller capable of achieving stable skid steering at up 40 km/h and acting as a torque vectoring system above 40 km/h by coordinating the output of the independent electric motors,
- Investigating the effects and behaviour of fourth-axle and all-wheel steering using the proposed drivetrain configuration and feedforward control methods,
- Testing all proposed vehicle and control system configurations against a model of an existing combat vehicle via software-in-the-loop using TruckSim and Simulink; including all-wheel drive, rear-wheel drive, skid steering, torque vectoring and various rear steering control methods,
- Proposing final recommendations for the vehicle control system based on the best-performing configurations as a guideline for further development of the proposed vehicle.

1.4 Working Fundamentals

To establish a fundamental understanding of the concepts throughout this work, this section outlines basic principles of vehicle handling and feedback control theory.

1.4.1 Tire Mechanics

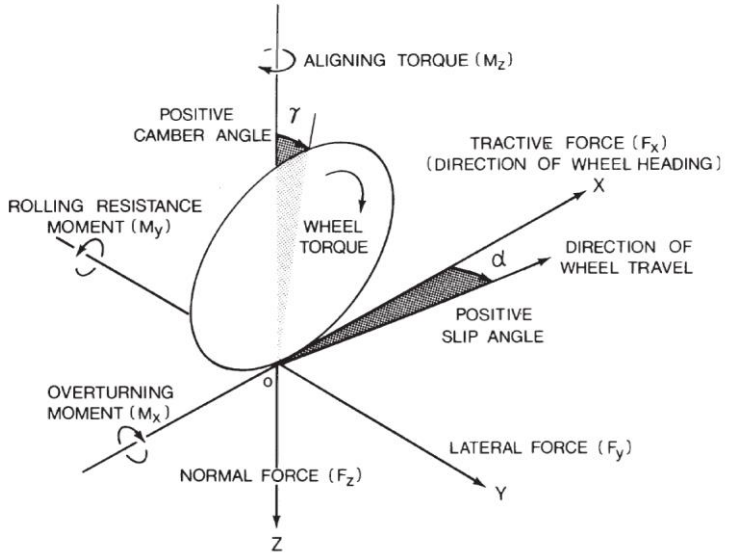

Figure 1-1 Forces and Moments on a Tire in the SAE Coordinate System [8]

The pneumatic tire plays a crucial role in defining the handling characteristics of a wheeled vehicle, as it is the vehicle's main point of contact with the road. Figure 1-1 presents the forces and moments acting on a tire, with respect to the SAE coordinate system. In this coordinate system, downward force and clockwise moment are considered positive, for reference. The forces in the horizontal plane play a key role in dictating the motion of the vehicle.

1.4.1.1 Longitudinal Tire Force

The longitudinal, or tractive force, F_X, is responsible for propelling the vehicle forward. With a normal load applied, the tire creates a contact patch with the ground. When a driving torque is applied to the wheel, tread elements are compressed as they enter the contact patch area. This tread compression effectively creates a difference in the linear speed of tire measured from the hub, V, and the linear speed of the tire as if it was free-rolling, $r\omega$, which is shown in the equation for longitudinal slip, below;

$$i = \left[1 - \left(\frac{V}{r\omega}\right)\right] \times 100\% = \left[1 - \left(\frac{r_{eff}}{r}\right)\right] \times 100\% \qquad \textbf{1-1}$$

The amount of tractive force generated by the tire is a function of the longitudinal slip (or % skid), as shown by the Pacejka tire model in Figure 1-2. Through the Pacejka tire model, it was determined that peak tractive force is achieved in the region of 15% to 20% longitudinal slip.

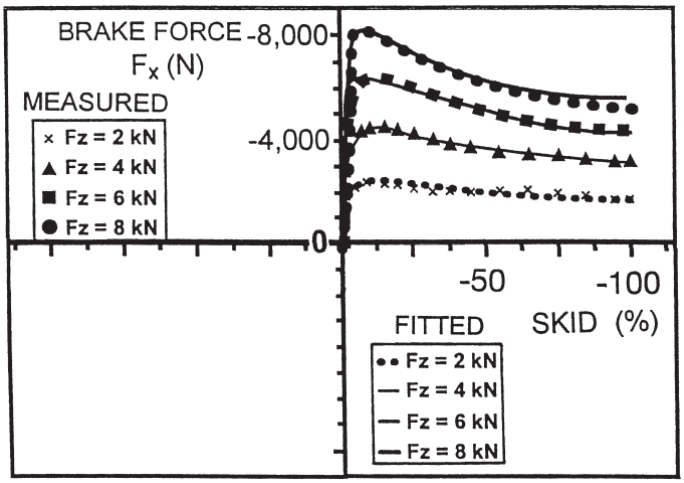

Figure 1-2 Pacejka Tire Model for Tractive Force vs. Longitudinal Slip [8] [9]

1.4.1.2 Lateral Tire Force

The lateral, or cornering force (F_Y) dictates the ability of the vehicle to corner by generating an aligning moment when a wheel is steered. When a wheel is steered, the contact patch will deform in such a manner that the centre of pressure shifts from the centre of the wheel, creating a displacement known as the pneumatic trail (t_p), as shown in Figure 1-3 . The force from this centre of pressure acts in the lateral direction of the tire, and the distance from centre of the tire in which this force acts creates the self-aligning moment which changes the direction of the vehicle. The deformation of the contact patch results in a slip angle (α), which is the resulting delay in reaction of the tire to the steering input, as shown in Figure 1-3;

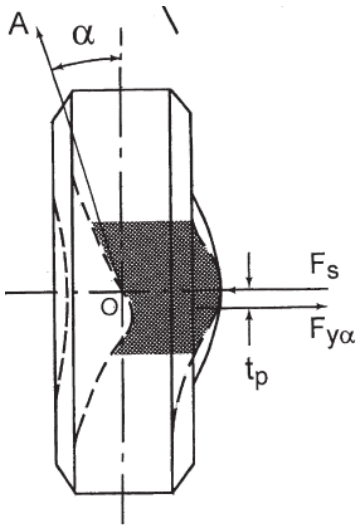

Figure 1-3 Deformation of Contact Patch in Cornering [8]

Cornering force is generated by the tire as a function of slip angle, as shown in the Pacejka tire model in Figure 1-4. Within the 3° to 5° range of slip angle, the generation of cornering force is linear as the deformation of the contact patch is elastic. It is within this range that stable cornering is maintained.

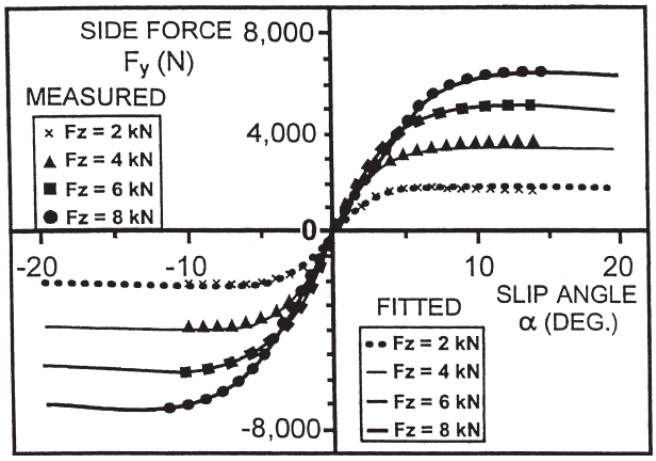

Figure 1-4 Pacejka Tire Model for Cornering Force vs. Slip Angle [8] [9]

The cornering stiffness of a tire, C_α, is the slope of the linear-elastic region of the relationship between cornering force and tire slip angle. This parameter is used to characterize a tire in a linear, two-degree-of-freedom vehicle representation, and plays a key role in determining the characteristic response of a vehicle configuration; this is discussed in the following subsection. From both models in Figure 1-2 and Figure 1-4,

increasing the normal load F_Z will increase both tractive and cornering forces. By determining the maximum tractive and cornering forces per given normal load, a working envelope can be constructed which define the operational limits of the tire, known as the friction ellipse as shown in Figure 1-5. The equation for the friction ellipse is given as;

$$\left(\frac{F_y}{F_{y,max}}\right)^2 + \left(\frac{F_x}{F_{x,max}}\right)^2 = 1 \qquad \textbf{1-2}$$

Using this relation, the available cornering force can be determined given the presence of a tractive force, and vice versa.

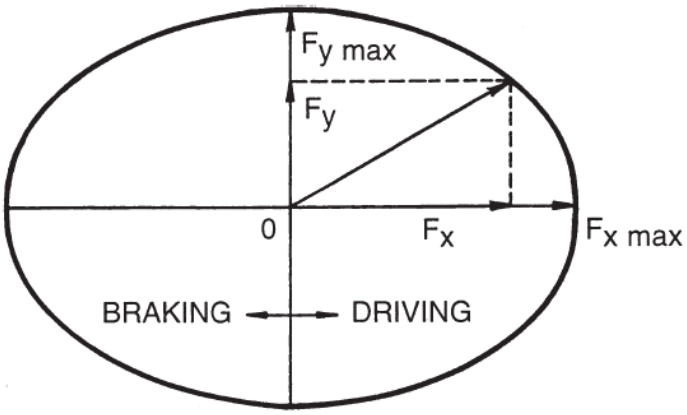

Figure 1-5 Friction Ellipse of a Tire [8]

It is upon these tire mechanics which modern vehicle dynamics control systems such as anti-lock braking (ABS), electronic stability control (ESC) and traction control (TCS) are built upon. By maximizing these tire forces during and braking and driving, these systems work together to stabilize the vehicle and improve its overall mobility regardless of operating conditions.

1.4.2 Kinematics of Conventional Steering

Factors such as tire cornering stiffness and vehicle dimensions greatly affect the steering characteristics of the vehicle. For a conventional front-steered vehicle, steady-state handling characteristics can be easily determined using a simplified, linear bicycle model. This model reduces the vehicle into a single-track representation where each tire has

effectively double the cornering stiffness, as shown in Figure 1-6. Key assumptions made for this model are:

- Lateral load transfer is negligible,
- Lateral acceleration is limited such that tire dynamics remain in the linear-elastic range,
- Effects of suspension on the steerable axle are neglected,
- Longitudinal speed is constant.

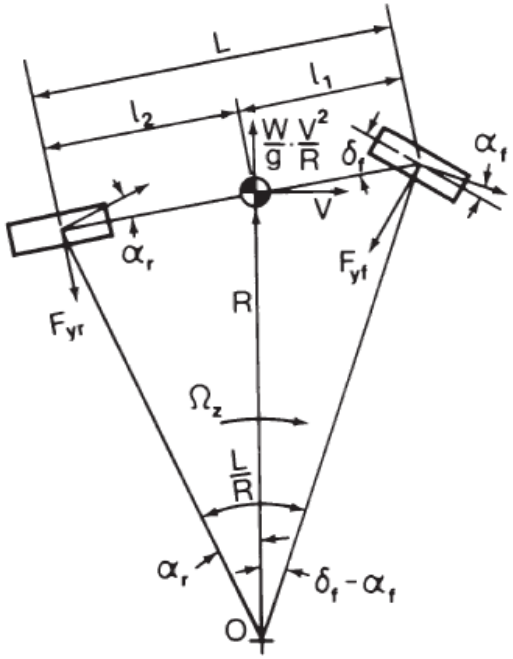

Figure 1-6 Two-Degree-of-Freedom Bicycle Model [8]

In Figure 1-6 above, L is the wheelbase, l_i is the distance of each axle to the centre of gravity, α is the tire slip angle, δ is the wheel steer angle and R is the turning radius, measured from the instantaneous centre of velocity to the vehicle center of gravity. Another parameter not shown on the bicycle mode is the vehicle side slip, β, which is the angle between the intended orientation and actual orientation of the vehicle. By deriving the kinematic equations of this bicycle model, one can obtain steady-state parameters such as yaw rate response, vehicle side slip response and understeer gradient. The understeer

gradient (K_{us}) is a measure of how the required steering input changes along a constant radius turn, as lateral acceleration increases.

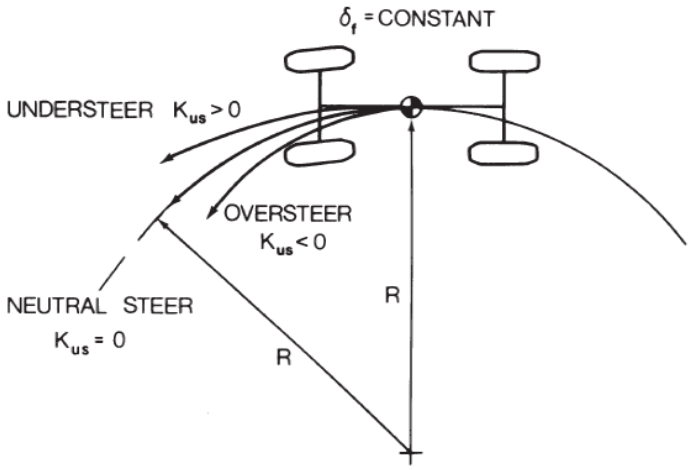

Figure 1-7 Curvature Response of Vehicle with Different Understeer Gradients [8]

As can be seen in Figure 1-7, neutral steering vehicles will maintain a constant turning circle without requiring any change in steering input meaning the understeer gradient is zero. An oversteering vehicle at its critical speed will continually reduce its turning radius given a constant steering input, and will eventually spin out. For this scenario, the understeer gradient is negative as less steering input is required to maintain a constant circle. An understeering vehicle at its characteristic speed will exceed the grip limits of its tires, becoming incapable of creating the lateral force required to maintain a constant circle, thus will require greater steering input to stay on course. In this scenario, the understeer gradient is positive.

Simplified linear bicycle models can be developed for several configurations apart from the conventional front-steered vehicle for the same purpose of determining steady-state vehicle response and curvature response via the understeer gradient. It is through development of a linear bicycle model for specific and unique vehicle configurations that feedback control algorithms can be created, as done by many of the works presented in this review.

1.4.3 Basic Control System Theory

A control system is an assembly of processes or subsystems – or in control terminology, "plants" – which, given an input will provide a corresponding output. With all realizable control systems, the output response will not completely match the desired input. Figure 1-8 illustrates an example of typical control system response to an input.

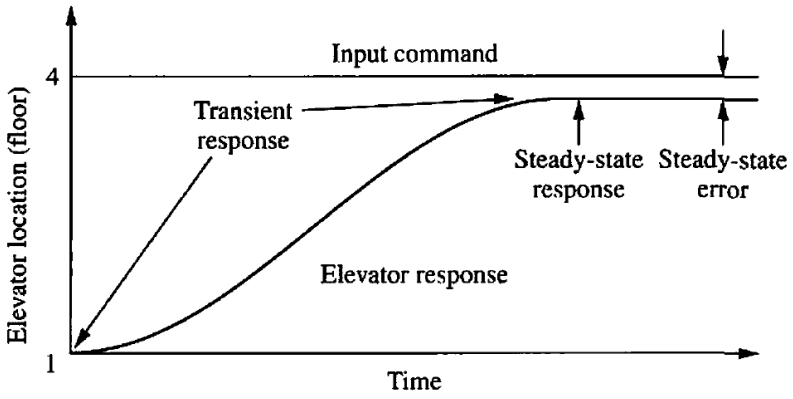

Figure 1-8 Response to Input of an Elevator Control System [10]

When an input is received and control system responds, there will always be a transient portion in which the output will take time to reach as close as possible to the input command. Once the steady-state is reached, there will be a difference between the desired input and the actual output response, which is known as the steady-state error. To change or improve the system responses, controllers are introduced. Two forms of control systems are discussed here – feedforward and feedback.

1.4.3.1 Feedforward Control

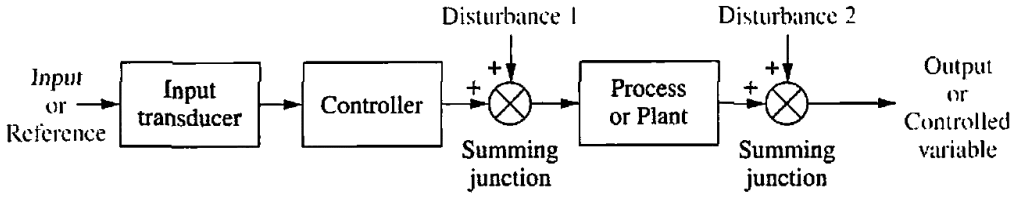

Figure 1-9 Feedforward Control System [10]

A feedforward, or open-loop control system processes an input signal through a controller which then delivers a control signal to the process, or plant, to produce an

actuation. Feedforward systems are cost-effective as they are simple to design and implement. However, the most major drawback to feedforward systems is that they are unable to resist external disturbances which greatly affect the output of the process.

1.4.3.2 Feedback Control

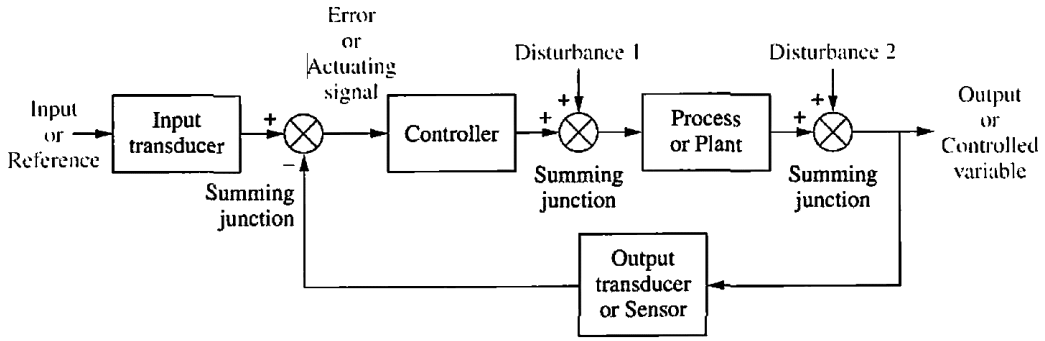

Figure 1-10 Feedback Control System [10]

A feedback, or closed-loop control system consists of the same key components as a feedforward system – a controller and a process – however, the process output is now monitored. An error signal, which is the difference between the output signal and the input signal, is then sent to the controller. Because the controller uses an error signal as opposed to a direct input, the control system can account for and resist external disturbances. This enables the process output to constantly remain stable, however the controller only acts if system error exists.

1.4.3.3 Types of Control Algorithms

Many types of control methods exist, each with unique traits and purposes. Controllers of each type were surveyed in this thesis as part of the development process of the multi-wheel drivetrain control system. The most commonly-used method in the industry is classical feedback control, or proportional-integral-derivative (PID) control. This control method uses error signal to thus apply a control signal to the process based on a summation of proportional, integral and derivative corrections. These individual components of the PID controller account for the present, past and future values of the error

signal, respectively. PID control is also available in P, PI and PD configurations, depending on application.

Optimal feedback control uses controllers which define a control law by minimizing a defined cost function [11]. Cost functions are typically defined based on both state variables – the process output – and control variables – the controller output. A typical application of optimal control in vehicle systems is a linear quadratic regulation (LQR) or linear-quadratic-Gaussian (LQG) controller. These controllers operate by using an optimization algorithm to minimize both input (i.e. steering wheel angle) and state (i.e. vehicle yaw rate) to generate a control signal.

Robust feedback control uses controllers which are design around system uncertainties to best resist external disturbances, changes in operating conditions or changes in process dynamics [12]. Typical applications of robust control in vehicle systems include H_∞ and sliding mode controllers. The use of H_∞ control is particularly popular for complex multi-input multi-output vehicle dynamics control systems which introduce greater degrees of system uncertainty.

Intelligent control methods rely on artificial intelligence based on human knowledge or learning ability to apply control to a process [13]. Control methods include fuzzy logic controllers, neural networks, and Bayesian controllers such as Kalman filters or extended Kalman filters. Such control methods in vehicle applications are increasingly popular in autonomous driving technology, particularly in obstacle avoidance algorithms or sensor data processing.

1.5 Outline

This work in this thesis is delivered in seven chapters, listed below:

- **Chapter 1** outlines the motivation and scope of the work completed, and provides a review of key fundamental concepts relevant to the scope of the work.
- **Chapter 2** provides a survey of implementations and control techniques for skid steering, torque vectoring, rear steering, and autonomous driving control, upon which a foundation for designing the multi-wheel drivetrain control system is built.
- **Chapter 3** outlines the tools and methodologies used to create the simulations involved in this work. This chapter also discusses the single-track vehicle models used to design each controller in the drivetrain control system.
- **Chapter 4** discusses the architectural design of the multi-wheel drivetrain control system and the roles and functions of each component. The control system is organized into the upper and lower control architectures. The upper level includes the driver model for autonomous skid steering mode, speed controller, active yaw controller and longitudinal slip controller. The lower level consists of the motor current distribution system, electric motor models and the feedforward rear steering controller.
- **Chapter 5** presents test results of the future electric combat vehicle operating in low-speed autonomous driving mode using skid steering. All tests occur on a sine wave path with three different road conditions – ideal friction, low friction and off-road.
- **Chapter 6** presents test results of the future electric combat vehicle operating in high-speed manned driving mode with torque vectoring and various rear steering configurations. High-speed tests include a modified J-turn procedure, 100-ft radius circle skid pad, FMVSS 126 ESC test and the NATO double lane change maneuver.
- **Chapter 7** concludes upon the completed work, presents further recommendations, and discusses future work to be embarked upon.

CHAPTER 2
LITERATURE REVIEW

2.1 Chapter Introduction

This chapter presents a review of past works conducted on three methods of improving heavy vehicle mobility: differential torque (or skid) steering, torque vectoring, and rear steering. The performance and limitations of each are surveyed within the scope of this review, as well as respective methods of control. Implementations and control methods used for autonomous driving are also reviewed in this chapter. The review of these works will serve as a guideline in the development of the drivetrain control system for the future electric combat vehicle.

2.2 Differential Torque or "Skid" Steering

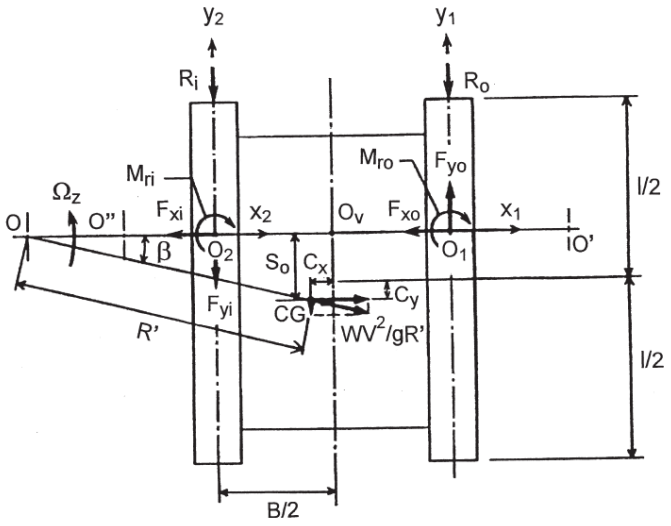

Figure 2-1 Kinematics of Skid Steering on a Tracked Vehicle [8]

Differential torque steering, or colloquially, "skid steering" is a method of inducing yaw motion by means of creating a difference in speed between the left and right tracks of the vehicle. This method is commonly employed by heavy tracked vehicles which typically use a double differential mechanism to distribute power to opposing tracks, as such vehicles have no wheels which can be turned [14]. The term "skid steering" arises from the consequential skidding of the tracks during a maneuver. The basic kinematics of skid

steering on a tracked vehicle are depicted in Figure 2-1, in which the net difference in longitudinal forces on opposing tracks dictate the yaw moment about the centre of gravity.

2.2.1 Skid Steering on Multi-Wheeled Vehicles with Pneumatic Tires

Skid steering on wheeled vehicles has been a prevalent research topic for many in the automotive field. The limiting factor in implementing skid steering on wheeled vehicles is the use of pneumatic tires, which undergo physical deformation in maneuvers, unlike solid metal tracks. Vehicle dimensions normal loading, weight distribution play a crucial role in determining the effectiveness of a pneumatic tire in skid steering.

In the scope of military vehicles, skid steering is less commonly implemented on wheeled vehicles as opposed to tracked vehicles. The AMX-10RC 6x6 combat vehicle used by the French military [14] and the GTK Boxer 8x8 combat vehicle used by both German and Dutch militaries [15] are notable examples of skid-steered multi-wheeled combat vehicles. Both vehicles are powered by internal combustion engines which rely on a differential mechanism like that used in tracked vehicles to control torque output. The GTK Boxer 8x8 vehicle is a unique implementation which allows for multiple steering methods. Conventional steering of the front two axles occurs at higher speeds and skid steering at lower speeds by means of differential braking to reduce turning circle.

When skid steering with pneumatic tires, simultaneously slowing the inner wheels and speeding up the outer wheels minimizes the transient response time in cornering due to tire deformation [16]. As the number of axles increases, the directional stability and handling capability of the vehicle decreases. Consequently, power consumption and tire wear increased. The relationship between axle numbers and individual vehicle performance metrics is not linear, and it was commonly observed that a three-axle (6x6) configuration was ideal for handling and stability, as well as to reduce tire wear and power consumption [17]. By focusing the mass distribution over the central axle and stiffening suspension to reduce roll, power consumption during a maneuver can be further reduced [18].

Given operating conditions that maintain linear-elastic tire behaviour – that is, no greater than 5° tire slip angle and 20% longitudinal slip – a similar turning circle can be achieved as that of a conventionally-steered vehicle at the same speed [19]. For most skid-

steered vehicle configurations on certain maneuvers, linear-elastic tire behaviour can be maintained up to 40 km/h [19]. However, as lateral acceleration increases, a skid-steered vehicle will tend to demonstrate neutral or oversteering characteristics, depending on the number of axles and mass distribution. At lower speeds, a skid-steered vehicle has a greater capability of further reducing turning circle compared to an equivalently-dimensioned vehicle with conventional steering axles. This requires that tires on the outer axles exceed their limits of adhesion and begin to slip in both lateral and longitudinal directions [19]. Conversely, it can be said that with lower overall surface friction, a skid-steered vehicle can perform much better than a conventionally-steered vehicle, which requires a greater amount of tire-road adhesion.

2.2.2 Survey of Skid Steering Control Algorithms

With the rising interest in unmanned ground vehicles, skid steering has become a popular method of maneuvering due to its simplicity in implementation and control. The use of independent electric motors on such vehicles allows for a wider range of control algorithms to be used more practically, as the number of actuators in the system is greatly reduced. Various control algorithms which have been used in regulating yaw motion through skid steering are surveyed.

Colyer and Economou [20] used a system of two fuzzy logic controllers to translate steering and throttle input into differential and mean driving current, respectively. A third fuzzy logic controller was used to prioritize the differential current when a steering command was introduced as a measure of preventing tire saturation. They later expanded the fuzzy logic system to include a controller that accounted for tire-ground interaction to regulate the output priority of differential and mean driving currents [21]. Economou et al. [22] take a different approach with fuzzy logic controllers by predicting differential and mean driving currents at various turning circles, as opposed to relating the operational limits of the individual electric motors as a proportion to an input command. During operation, a turning circle is then estimated from the input command and the fuzzy logic system outputs the required motor currents based on the established knowledge base for the specific vehicle.

Song et al. [23] introduced the use of a sliding mode observer to estimate tire slip on an unmanned ground vehicle with skid steering. This was intended to improve the maneuverability over soft and unpredictable surfaces to aid the autonomous control system respond with the appropriate control inputs to the electric drivetrain. This was found to reduce anomalies within the vehicle's trajectory tracking system. Lucet et al. [24] employ a sliding mode controller on a skid-steered 6x6 unmanned ground vehicle to improve trajectory tracking by minimizing yaw rate and longitudinal speed error. The system performed well in simulation and was thus extended to testing in a real 4x4 vehicle to observe robustness of performance in a different drivetrain configuration [25]. Jin et al. [26] use a sliding mode control law to track and minimize error in individual wheel speed to maintain a desired forward and yaw motion generated by a path-following controller. The desired motion determined by the path-following controller was made to account for the limits of tire-road adhesion.

Kang et al. [27] opted to use lateral and longitudinal tire force measured at each wheel as monitored state for feedback control. Lateral and longitudinal forces per tire are optimized by a control algorithm and translated into a torque output per individual motor. The effect of suspension on the normal load on each tire is considered for this control system to work. Unlike other works in which state feedback is used, the tire-road adhesion is directly observed at the individual tire with force estimators rather than observing vehicle body motion. Nazari and Naraghi [28] proposed a control architecture which combined fuzzy logic and sliding mode control methods to drive a skid-steered mobile robot. The sliding mode controller is used to generate distance error and error rate, which are used by a fuzzy logic controller to output required yaw motion to dictate different motor torque output. Aslam et al. [29] use the fuzzy logic and sliding mode combination to improve the skid steering capability of a similar robot. Like other works, a sliding mode control law is used to minimize error in forward velocity and yaw rate, however online gain tuning is achieved via a fuzzy controller. This improved the power consumption of the vehicle during skid steering maneuvers versus conventional sliding mode control algorithms.

2.3 Torque Vectoring

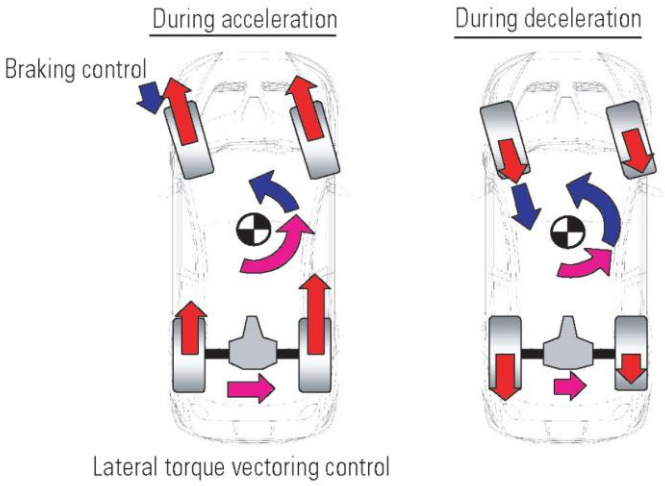

Figure 2-2 Improving Cornering Through Lateral Torque Distribution Control [30]

Torque vectoring is a means of actively controlling the left-right torque distribution in a manner that promotes improved cornering performance and stability when tires reach or exceed their maximum cornering potential. In high lateral acceleration cornering maneuvers, load transfer will reduce the grip of the inner wheels, thus bringing them closer to their limits of adhesion. Depending on several design factors, a vehicle may understeer or oversteer when the tires are saturated. Torque vectoring can be achieved through differential braking by harnessing the anti-lock braking system or through a torque vectoring differential, shown below in Figure 2-3.

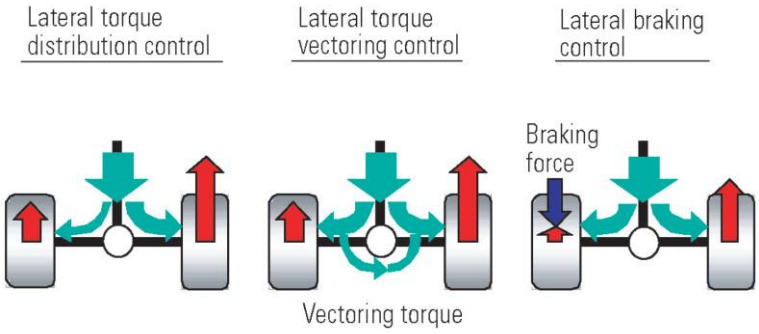

Figure 2-3 Traditional Differential, Torque Vectoring Differential, and Brake Torque Vectoring [30]

As of recent times, torque vectoring is popularly equipped on high-performance passenger vehicles to maximize traction, improve lateral stability and improve cornering performance. An exemplary implementation is the Mitsubishi Super All-Wheel Control (S-AWC) system [30]. This system combines an active centre differential (ACD) and active yaw control (AYC) differential to intelligently distribute power in the longitudinal and lateral directions, respectively. Differential braking through the anti-lock braking system is equipped on the front wheels while the ACD and AYC directly control the proportion of power distribution in the rear. This combined method of torque vectoring has shown to greatly improve the stability and performance of the Mitsubishi Lancer Evolution X during high lateral acceleration cornering. As found in the works of D'urso [7] and Ragheb [6], direct yaw control through torque vectoring yields great potential in improving the mobility of a conventionally-steered combat vehicle.

2.3.1 Torque Vectoring by Braking vs. by Differential

Torque vectoring through differential braking commonly uses the anti-lock braking system as a means of coordinating lateral torque distribution. During a maneuver, the inner wheels of the turn are slowed down to create the torque difference. This method of creating differential torque is inefficient due to energy loss and slow response [2] [30]. With brake torque vectoring the vehicle is forced to slow down during a corner, thus degrading its performance. When compared to a torque vectoring differential, brake torque vectoring can result in up to ten times greater energy loss during a corner [31]. Thus, on a given set of conditions a vehicle with brake torque vectoring will consume more power in maintaining a constant speed and heading when exiting a maneuver. It has been found that with higher actuation delay come higher yaw rates and vehicle side slip, which indicates poorer lateral stability [2]. While brake torque vectoring is easy and cost-effective to implement, its dissipative and intrusive nature can gradually degrade longitudinal and lateral performance as brakes wear down, adding a degree of uncertainty implementing control algorithms.

Torque vectoring by a mechanical differential offers the most flexible and efficient option in lateral torque distribution. By nature, this method is less dissipative compared to a brake-based solution and will respond significantly faster. Using electronically-controlled mechanisms yield improved overall performance through much faster response

time by directing tractive force as opposed to braking force [32]. Limited slip differentials (LSD) are available in both purely mechanical and electronically-controlled forms. Mechanical LSDs rely upon clutch packs, gear meshes and high-viscosity fluid to keep left-right torque distribution equal until one wheel loses traction [6] [33]. When traction is lost on a wheel, the mechanism will favour power delivery to the opposing wheel with greater grip. Electronically-controlled differentials extend upon that by activating lateral torque distribution under conditions met within the control algorithm [34]. The use of an electronic control algorithm increases the flexibility of implementation to a larger number of vehicle configurations. Recent developments in electric and hybrid-electric vehicles now present the opportunity to harness individual wheel motors to replace differentials, as they further simplify control algorithms and processes.

2.3.2 Survey of Torque Vectoring Control Methods

With the increasing use of electronic systems in vehicles, control algorithms to improve handling dynamics and stability continue to evolve. Hybrid electric and fully-electric vehicles further increase the simplicity in implementing torque vectoring, thus allowing for greater potential in more effective and robust algorithms. Different control algorithms and actuation methods are explored in this section.

Esmailzadeh et al. [35] proposed and compared an optimal and "semi-optimal" control law for regulating external yaw moment output for a fully-electric four-wheeled vehicle. The optimal control law used linear quadratic regulation to determine speed-dependent gains for yaw rate, lateral velocity and steer angle to output an external yaw moment. The "semi-optimal" control law foregoes the lateral velocity gain to simplify the control method. It was found that the simpler "semi-optimal" control law using the two-degree-of-freedom linear kinematics performed as effectively as the optimal control law which accounted for yaw velocity in three degrees of freedom. Cheli et al. [36] also employ linear quadratic regulation to control external yaw moment output for a fully-electric four-wheeled vehicle. The cost function in this work only incorporates vehicle side slip and yaw rate instead of steer angle, lateral velocity and yaw rate, thus using a simpler two-degree-of-freedom dynamic model. They also provide simpler tuning parameters through the state and output weighting matrices, as opposed to the previous work.

Mokhiamar and Abe [37] proposed to optimize lateral and longitudinal tire force distribution for a four-wheeled vehicle with direct yaw control and all-wheel steering to minimize tire wear and saturation. Using driver input commands, lateral and longitudinal forces are determined by inverse use of the Pacejka tire model to satisfy the limit conditions of the friction circle. These forces are then used to direct the desired motion of the vehicle based on yaw rate and side slip reference model response, which the vehicle is then made to follow. Cho et al. [38] apply this method of tire force control onto a conventional four-wheeled vehicle as a component of a unified chassis control architecture. The optimal tire force distribution method is used in a different manner to that of [37], in that driver input is first given to a reference side slip and yaw rate model. The response of the reference models is then used to determine optimal tire forces and overall yaw moment. The tire force distribution is actuated by coordination of electronic stability (direct yaw moment) control, active front steering and continuous suspension damping control. Kim et al. [39] later apply this unified chassis control architecture to a 6x6 all-wheel steered hybrid electric military vehicle, in which direct yaw control is achieved by independent wheel motor control.

Jalili-Kharaajoo and Besharati [40] proposed a sliding mode traction control law for a four-wheeled electric vehicle with independent motor control to improve cornering performance and traction on low-friction surfaces. The control law works by coordinating existing vehicle systems including anti-lock braking, anti-slip regulation and electronic stability control, in a hierarchical structure. Anti-slip regulation is given higher priority in the coordination of the multiple systems, with electronic stability control only activating to correct yaw motion when error and error rate exceed a given threshold. Kim et al. [32] utilize a sliding mode control law on a vehicle equipped with a transfer case and torque vectoring differential to coordinate actuation of the hardware depending on driver input. This system borrows the optimal tire force distribution methods of [37] and [38] to determine yaw moment output. The sliding mode controller determines whether to use the torque vectoring system to improve handling and vehicle response or to maintain stability in the absence of high driver input demand. Unlike the previous work, the driver has more direct control in activating the torque vectoring functionality.

Liu et al. [41] applied linear parameter varying (LPV) control with mixed sensitivity H_∞ loop-shaping for torque vectoring on a hybrid electric vehicle. The vehicle was equipped with electric motors in the rear which controlled torque distribution and rear tractive effort, while the front wheels were powered by an internal combustion engine. Vehicle side slip and yaw rate were used as the state feedback parameters for the controller to determine the require torque vectoring output. The control design which incorporated feedback and feedforward provided good reference tracking and robustness in extreme, non-ideal driving conditions. The overall control scheme prevented performance degradation when the electric motors were saturated. Poussot-Vassal et al. [42] employ a similar control scheme onto a conventional vehicle. While both [41] and [42] use vehicle side slip and yaw rate as state feedback parameters, this work used a coordination of active front steering and brake-based torque vectoring to control vehicle yaw motion. D'Urso [7] implemented a similar control scheme to [42] onto an 8x8 fully-electric combat vehicle in which the H_∞ controller coordinates both torque vectoring and active rear steering, as opposed to front. All control schemes worked particularly well on low-friction surfaces where maximum tractive force was severely limited.

2.4 Supplementary Rear-Wheel Steering

Rear-wheel steering is a method of controlling lateral tire force generation across all tires by means of steering the rear axle in relation to the front. The resulting lateral forces can thus be used either to reduce vehicle side slip at higher speeds or reduce turning circle at lower speeds. Rear-wheel steering provides the advantage of reducing the response time in lateral motion during a maneuver and it has been shown that the rear wheels are as effective as the front in generating yaw motion [43]. Where rear-wheel steering begins to fail is on vehicles that "contra-steer" – steering the rear wheels in the opposite orientation to the front – at high speeds. With this configuration, transient tire force generation between front and rear are opposite in direction, making control difficult for the driver. When the lateral tire force behaviour exceeds the linear-elastic range with rear wheel steering, it only gives the driver a false sense of control without tangible improvement in handling performance [44]. Thus, at high speeds, the rear wheels may be steered in the same

orientation as the front to reduce the phase difference between yaw rate and lateral acceleration

Rear wheel steering can be achieved either passively or actively. An example of passive rear wheel steering includes the Weissach axle which is implemented in earlier models of Porsche vehicles, which relies on the suspension arms to create toe-in and reduce oversteering behaviour [45]. Active rear wheel steering is a method in which the driver has direct control over the rear steering angles, as opposed to relying on suspension geometry. This can be achieved by a linked mechanism which duplicates the front steering system onto the rear, or through independent actuators, which respond accordingly to driver input. In the scope of combat vehicles, rear wheel steering is commonly implemented by contra-steering the rear wheels in response to the front. Some 8x8 vehicles have all axles steered such as the PARS combat vehicle [46], while others will only have the rear-most axle steered, such as the Piranha V [47]. The primary purpose of rear wheel steering on these vehicles is to improve maneuverability for tight urban spaces. Active rear wheel steering is the primary focus in this work, for which feedforward implementations are surveyed.

2.4.1 Rear Steering Control Methods

Control of rear-wheel steering can be achieved in both feedforward and feedback forms. Feedforward rear steering involves direct translation of the front steering angle into the rear by means of a fixed or variable relationship. Feedback rear steering requires state monitoring and feedback – commonly vehicle side slip and yaw rate – to achieve active control of the rear wheel steer angles.

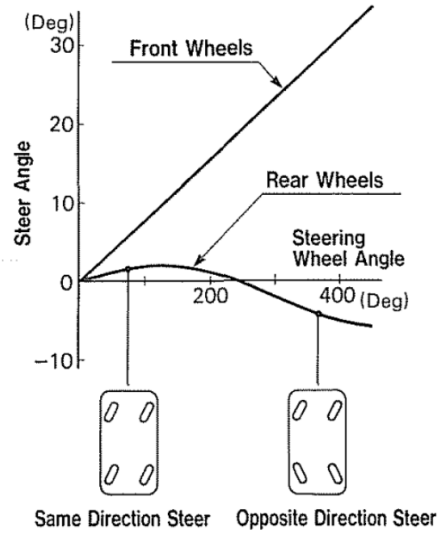

Figure 2-4 Steer Angle-Dependent 4WS used by Honda [48]

Feedforward rear-wheel steering may come in the form of either steer-angle dependent or zero side-slip control [49]. Steer-angle dependent rear-wheel steering is a method of turning the rear wheels in direct relation to the front wheel angles. When steering wheel angle input is small, the rear wheels are steered in the same orientation as the front. When greater steering wheel angle input exceeds a set threshold, the rear wheels will be steered in the opposite direction as the front wheels. This type of feedforward control method was implemented by Honda and was found to greatly reduce delay in vehicle yaw response with respect to driver input [48]. The relationship between front and rear wheel angles in the steer angle-dependent system is demonstrated in Figure 2-4 above.

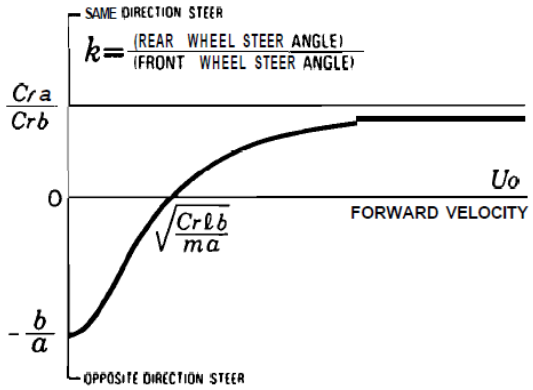

Figure 2-5 Zero Side-Slip Front-to-Rear Wheel Angle Relationship [49]

Another form of feedforward rear steering control is the zero side-slip method. To implement the zero side-slip control method, a two-degree-of-freedom bicycle model which incorporates a rear steer angle is developed for the target vehicle. Deriving the steady state kinematic equations from the bicycle model and setting vehicle side slip to zero will yield a speed-dependent transfer function which relates the rear steering angle to the front. An example of the range of front to rear ratios generated by the transfer function is shown in Figure 2-5 above. The zero side-slip control method is employed by Nissan in their Super HICAS (High Capacity Actively Controlled Steering) [50] system and Mazda in their Speed-Sensing Four-Wheel Steering (SS-4WS) [51] as a means of reducing turning circle at lower speeds and stabilizing the vehicle at higher speeds. At higher speed cornering, zero-side slip control will result in understeer due to the rear wheels being oriented in the same direction as the front. Conversely the steer angle-dependent method will promote oversteer as driver demands higher steering input, leading to the rear wheels being increasingly steered in the opposite orientation to the front.

To alleviate the issues of trade-offs with either implementation of feedforward rear steering, feedback control methods have been proposed which commonly rely on yaw rate response as a control variable. State-space representations are derived from two-degree-of-freedom bicycle models which incorporate steering on all axles, upon which controllers are synthesized. Robust control methods are typical used in feedback rear steering control for the disturbance rejection. Hiraoka et al. [52] use the feedforward zero side-slip control method and employ a sliding mode control law to minimize model uncertainty and introduce disturbance rejection. Yin et al. [53] use μ-synthesis and H_∞ for full feedback control in a four-wheel steered vehicle for robust rear steering over various low-friction surfaces. Kreutz et al. [54] propose and compare two forms of feedback control for rear-wheel steering – a traditional method which is developed from a bicycle model and a mass-spring-damper approach. The mass-spring-damper approach only activates rear steering during the transient portion of a maneuver and gradually straightens the rear wheels as the vehicle reaches steady state behaviour. Bayar and Unlusoy [55] compared the zero side-slip feedforward method to feedback methods using yaw rate feedback using multi-wheeled vehicles. They found that the feedback methods generally provided lower yaw rate and lateral acceleration response compared to the feedforward method when only the

front and rear wheels are steered, thus recommended that more axles be allowed to steer to improve the response.

2.5 Autonomous Driving

In recent times, there has been an increasing demand and interest in autonomous vehicle technology. Autonomous passenger vehicles aim to reduce the number of road accidents by eliminating human error in the driving environment. Using computing hardware and intelligent algorithms, autonomous vehicles have the ability to make critical decisions and respond much faster than a normal human driver. In a military application, autonomous vehicles can help reduce the risk of fatality by eliminating the need for human operators in highly-volatile environments such as reconnaissance or front-line combat operations.

2.5.1 Implementations of Autonomous Driving

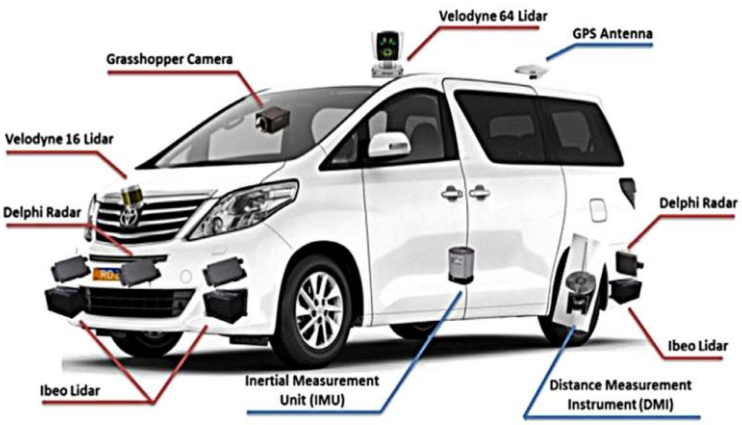

Figure 2-6 Example of Sensor Implementation on Autonomous Vehicle [56]

Autonomous vehicle control can be achieved through an array of sensors such as ultrasonic sensors, optical sensors and global positioning systems – all of which are used to follow paths and avoid obstacles in real, active environments. These sensors are intended to work together to replicate human driver functions of following the path, observing the environment, and utilizing data to take decisive actions on the premise of obstacle avoidance or undesired vehicle behaviour.

Global positioning (GPS) is a commonly implemented component in many autonomous vehicles with the primary purpose of navigation [56] [57]. GPS data can be used to determine where the vehicle is in current three-dimensional space, and where it is intended to go. Autonomous vehicles will also be equipped with inertial measurement units (IMU) which provide real-time data of vehicle motion such as acceleration and yaw at high-frequency intervals [57]. Where a GPS and IMU combination may fail is in the event of a covered or underground area, in which the positioning signal may be lost. This combination alone does not account for obstacle data, which in turn does not provide the vehicle with emergency avoidance procedures.

The use of cameras and various range sensors are used to compensate for the deficiencies of GPS and IMU alone. SONAR, LIDAR, RADAR and infrared sensors have all been used as range sensors for navigation algorithms to track vehicle trajectory or determine the presence of obstacles such as pedestrians and moving vehicles [56] [58] [59]. They may also be used in simultaneous localization and mapping (SLAM) algorithms to model the terrain surrounding the vehicle and determine ideal, navigable paths [60]. Cameras may be used in place of, or in conjunction with any combination of range sensors to mimic human depth perception as another approach to obstacle avoidance and trajectory tracking [56]. A notable camera implementation is in a mining vehicle which scans barcodes at pre-determined locations in a mine to navigate without GPS, while using LIDAR to map the surroundings [61].

2.5.2 Trajectory Tracking Algorithms

As the scope of this work is to assess the performance of a comprehensive vehicle control system operating in different modes, localization and obstacle avoidance algorithms are omitted from this review. Instead, mathematical path-following algorithms are surveyed for modeling basic human driving behaviour over controlled, ideal conditions. Many of the algorithms surveyed use vehicle motion or planar coordinate data – all of which can be derived from the many sensor implementations discussed in the previous subsection – to generate a steering command, much like a human driver.

The simplest and most popular method of driver modeling is by some form of proportional-integral-derivative (PID) controller. Chatzikomis and Spentzas [62] use two

PD controllers to generate steering wheel angle – one to minimize heading error and one to minimize position error. The inputs are combined using a speed-dependent gain scheduling system based on mathematically-derived vehicle yaw response. Menhour et al. [63] coordinate the output of two PID controllers using an optimization algorithm with the H_∞ constraint to introduce robust disturbance rejection. One PID controller uses path preview data to generate steering based on lateral deviation while the other uses yaw rate error generated with respect to a linear reference model. Ding et al. [64] also use PID control to minimize the heading and position error for a trailer intended to follow the motion of its tractor to reduce rearward amplification. A speed-dependent scheduling system is also used which contain experimentally-determined gains values, as opposed to using mathematical derivation. Tan et al. [65] implement a combination of fuzzy logic and PID to create a driver model for a fully-electric vehicle. Like other works, the PID controller in this work uses path preview information to generate steering based on lateral deviation. However, gain scheduling is handled by a fuzzy logic controller which depends on yaw motion error.

Adaptive and optimal control laws have also been used for driver modeling in various forms. Bulirsch et al. [66] use an optimal control law generate steering wheel angle by minimizing vehicle side slip, yaw rate, and horizontal plane position error in one cost function, thus being able to account for vehicle body motion. Ungoren and Peng [67] proposed an optimal control law to minimize lateral motion error collected from preview data and generate a steering wheel angle. The controller is tuned by weighting to closely match the average behaviour of 22 surveyed human drivers on a simulation test course. Edelmann et al. [68] proposed a two-layer adaptive control model which combines feedforward anticipatory control based on experimental human driver data and predictive feedback control to correct lateral deviation of the vehicle center of gravity.

2.6 Chapter Summary

In this chapter, a review of skid steering, torque vectoring, rear steering and autonomous driving control has been conducted. The performance, limitations and control techniques of each have been reviewed for designing and proposing a comprehensive drivetrain control system for a future electric combat vehicle with autonomous driving capabilities.

Skid steering and torque vectoring control methods share many core principles in control techniques from the perspective of torque distribution for yaw motion generation. The difference between skid steering and torque vectoring lies in their intended purpose. Skid steering is a directive method of torque distribution to generate yaw motion in the absence of mechanical steering, while torque vectoring is a corrective action to generate yaw when tires reach their limits. Both are classically implemented through some form of differential mechanism, with torque vectoring making use of braking more commonly than skid steering. Likewise, both benefit from the advancements in electric motor and control technologies in modern times.

Between skid steering and torque vectoring, the most popular control algorithms are sliding mode, linear quadratic regulation (LQR), and H_∞, with each algorithm employing different forms of state feedback to control various types of actuators. For this work, an LQR optimal controller will be selected to handle both skid steering and torque vectoring in one package. The controller will use vehicle side slip and yaw rate as control states to generate an external yaw moment, as inspired by [35] and [36]. This serves to be more practical and cost-effective to implement when considering industry-standard and readily-available sensor hardware. At this stage in development, the future electric combat vehicle control system will not require the disturbance rejection or multi-output control granted by an H_∞, as testing of the vehicle will occur over controlled conditions and only yaw moment is required from the controller to translate into individual motor signals for the electric powertrain, borrowed from the vehicle in [7].

For testing, a conventional internal combustion engine-equipped combat vehicle will be used as a baseline in simulation against the future electric combat vehicle. For up to 40 km/h on low friction and off-road surfaces, skid steering will be tested against the

conventional vehicle using two control techniques. One control technique uses the shared LQR controller for torque vectoring, and another is a feedforward controller developed from a modified bicycle model inspired by [8]. The feedforward controller will serve as a baseline for comparison to mimic the behaviour of a fixed double differential mechanism found in internal combustion engine-equipped skid steering vehicles. For greater than 40 km/h, conventional steering will be enabled and the LQR controller assumes the corrective role of torque vectoring.

Rear-wheel steering is commonly used on four-wheeled passenger vehicles to reduce yaw response delay or reduce turning circle by means of directly controlling lateral forces at the rear wheels. The focus of this work is on active rear steering, which grants direct control of both front and rear wheel steer angles through one input. In the scope of active rear steering, steer angle-dependent and zero side-slip control methods are available. Steer angle-dependent control steers the rear wheels in the same orientation as the front with small driver input, and with the opposite orientation for large input. Zero side-slip control aims to minimize vehicle side slip by introducing speed as a feedforward control variable. Contrary to steer angle-dependent control, the rear wheels are steered in the opposite orientation to the front to reduce turning circle at low speeds, and in the same orientation at the front for higher speeds. At the same high range of speeds, steer angle-dependent control will induce unsafe oversteer while zero-side slip will tend to understeer. Various feedback methods have also been surveyed, in which robust control techniques are popular.

To implement rear-wheel steering on the future electric combat vehicle, this work will take the approach of decoupling rear steering control from a central controller; thus, feedforward control is desired. By this decoupling, rear steering can be quickly disabled without the need to rebuild the controller. Control can be disabled on the third axle of the vehicle for fourth-axle rear steering, the third and fourth axles for conventional front steering, or enabled for both rear axles for all-wheel steering. Keeping rear steering as separate control actuations also allows the torque vectoring controller to maintain compatibility with skid steering mode. Testing will occur in controlled environments; thus, robust rear steering control is not required at this initial stage of the future electric combat vehicle control system development. For the proposed design, the zero side-slip

feedforward method will be used, as it has been found to be safer than steer-angle dependent control. To mimic the existing contra-steering configurations on existing combat vehicles for a baseline comparison, a basic feedforward controller using fixed negative ratios for steering the rear wheels in relation to the front will be used. All rear-wheel steering tests will be performed with fourth-axle steering and all-wheel steering, similar to [55].

With the rising demand for autonomous vehicle technology, this work seeks to propose a foundation for an autonomous control system for the future electric combat vehicle. Several sensor implementations and control techniques have been used for autonomous driving control. GPS units have been commonly used for navigation in conjunction with inertial measurement units (IMU) to monitor vehicle body motion. Various sensors such as SONAR, RADAR, and LIDAR have been used to determine range for localization purposes and obstacle avoidance algorithms. Due to the limitations of the simulation environment used in this work and the scope of this work, localization and obstacle avoidance will not be considered. For navigation, path-following controllers have been popularly built upon classical PID control, with some form of intelligent knowledge-based control method working in parallel for obstacle avoidance. With the availability of path preview sensors in the simulation environment to emulate the function of GPS, IMU and range sensor systems, a gain-scheduled PID path-following driver model will be used for the autonomous driving function of the future electric combat vehicle. Gains will be manually tuned based on vehicle operating speed as with [64], and the autonomous driving function will be reserved specifically for skid steering. The path-following controller in this work will emulate high-level driver function by using lateral path error to determine a required steering wheel input. This is to reduce the overall complexity of the actuator control network, especially with the use of skid steering in autonomous driving mode. The design of the path-following driver model will also allow for scaling up to high-speed driving as its output will be compatible with the input of the proposed torque vectoring controller.

CHAPTER 3
SIMULATION TOOLS AND CONTROL SYSTEM DEVELOPMENT

3.1 Introduction

In this chapter, the tools and methodologies used to design and evaluate the combat vehicle control system are discussed. First, the TruckSim simulation environment and the roles of its individual key components are outlined. The use of MATLAB and Simulink is also explained in this chapter.

The synthesis process of the active yaw controller using the linear quadratic regulator (LQR) is outlined, including the development of tuning parameters and the role of a pre-compensation scaling factor. To develop the active yaw controller, a set of linear, two-degree-of-freedom bicycle models are used to derive the kinematic equations. With these equations, methods of developing a state-space representation and steady-state gain values are outlined.

This chapter also discusses the development of feedforward control systems for both passive and active rear steering using different modeling representations for each respective method. Modified Ackermann geometries are presented for passive fourth-axle and all-wheel steering to determine fixed front to rear steering axle relationships. An all-wheel steered bicycle model is used to derive a speed-dependent relationship to relate the front and rear steering axles in a variable manner.

3.2 Vehicle Testing and Modeling Tools

3.2.1 TruckSim Simulation Environment

The TruckSim simulation environment provides the ability to evaluate control systems and external powertrain models designed in Simulink through software-in-the-loop (SIL) testing. When simulations are conducted with SIL, TruckSim provides any form of desired raw vehicle data output by the non-linear multi-degree of freedom vehicle model. Key components of the TruckSim program are discussed in the following subsections.

3.2.1.1 Non-Linear Multi-Degree-of-Freedom Vehicle Model

(a) **(b)**

Figure 3-1 Future Electric Combat Vehicle Model (a) and Real Combat Vehicle (b) [7]

Figure 3-1(a) shows the physical shape of the virtual vehicle model, equipped with the proposed electric powertrain and control systems, and Figure 3-1(b) shows the existing combat vehicle. The TruckSim vehicle model utilizes the physical specifications of the real vehicle, which cannot be disclosed in this work due to confidentiality. All possible degrees of freedom available to the real vehicle are included in the model. A vehicle model with the conventional internal combustion engine powertrain of the existing vehicle is used as the reference for evaluation. This reference vehicle was modeled and validated by [6] through a similar software-in-the-loop simulation process compared against experimentally-determined data from real world testing.

3.2.1.2 Tire Characteristics

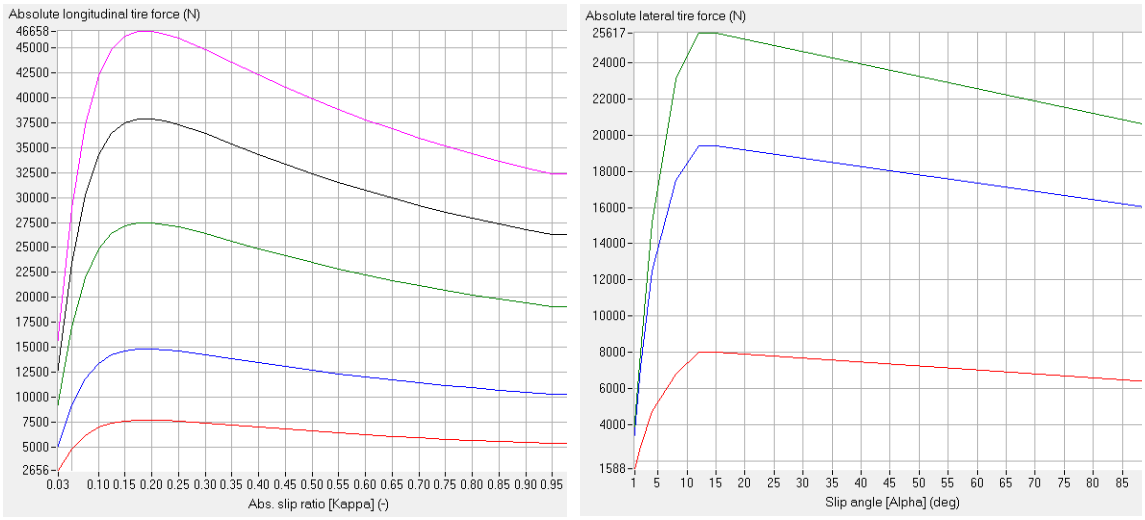

(a) **(b)**

Figure 3-2 Longitudinal (a) and Lateral (b) Tire Force Characteristics

Figure 3-2(a) shows the longitudinal force characteristics of the tire on the vehicle. Figure 3-2(b) shows the lateral force characteristics of the tire. The family of curves in each figure represent the characteristic behaviour of the tire at different normal loads (F_Z). The provided tire characteristics were obtained through modeling and validation of a Michelin 12.00R20 XML TL 149J off-road tire by [6], and implemented in TruckSim as a lookup table. From Figure 3-2(a), the longitudinal slip at which peak tractive force F_x occurs is obtained, to set a slip threshold for the longitudinal slip controller discussed in the following chapter.

3.2.1.3 Steering Mechanism Characteristics

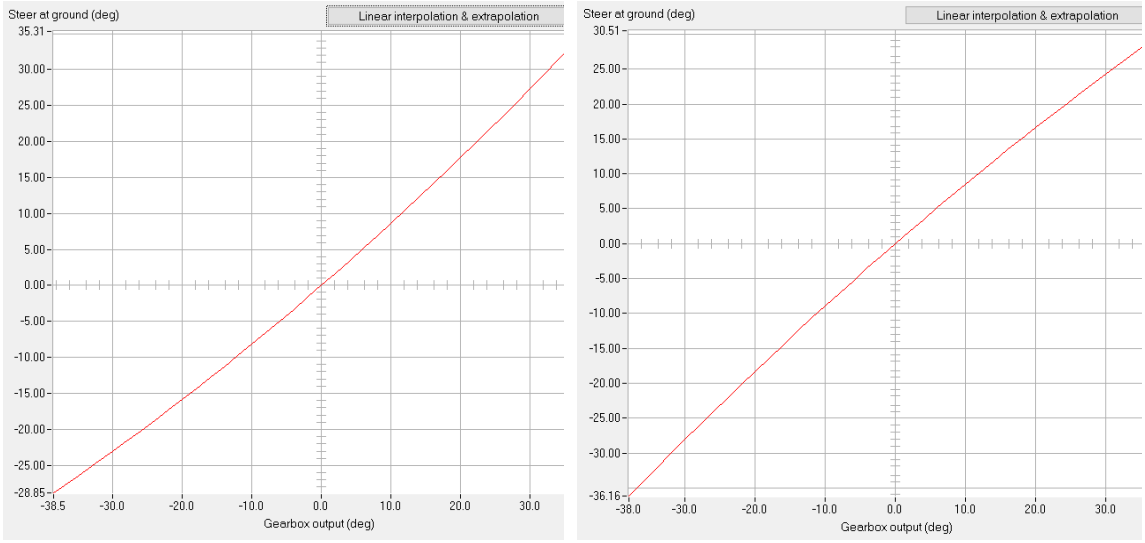

(a) **(b)**

Figure 3-3 Steering Wheel to Ground Wheel Angle for Left (a) and Right (b) Wheels

Steering axle characteristics relating the driver steering input to the ground wheel angle are shown above; Figure 3-3(a) for the left wheel and Figure 3-3(b) for the right wheel of the first axle. Lookup tables to mimic the steering mechanism behaviour of the existing combat vehicle were available for both first and second axles and used in all vehicle configurations throughout this work. While these lookup tables are used for the virtual mechanism within the non-linear vehicle model, they are also used within Simulink for the skid steering control system discussed in the following chapter.

3.2.1.4 Driver Models

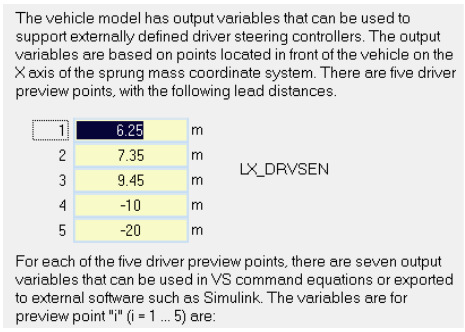

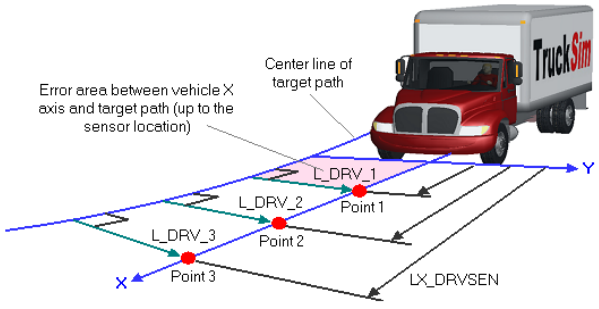

Figure 3-4 Driver Sensors and Preview Points in TruckSim

Three options for driver models are available in the TruckSim environment, all of which are used in this work and are compatible with the control system modeled in Simulink:

- Open-loop steering; in which the vehicle operates independent of a road using a steering wheel angle time history – either recorded from another vehicle or a standardized pattern required for a test procedure. This is used in the Modified J-Turn and FMVSS 126 ESC tests, discussed in the results chapter.
- Closed-loop path follower; in which an internally-programmed driver function within TruckSim follows a path provided by the user for a specific test procedure. This is used in the 100-ft Circle and NATO Double Lane Change tests, discussed in the results chapter.
- External driver model; in which the driver functionality is taken out of TruckSim and into a user-programmable PI controller. The controller uses lateral distance error and area error collected by sensors placed in front of the vehicle at specified distances, as shown in Figure 3-4 above. This is used for the skid steering control system, discussed in the following chapter.

3.2.2 MATLAB and Simulink

MATLAB provides the programming platform for storing parameters and mathematically modeling the linearized kinematics of the combat vehicle. It also contains proprietary algorithms required to synthesize the controllers used in this work. Simulink provides a graphical modeling interface and utilizes mathematical solver systems to create the control structure. An S-Function is used to import and export vehicle control data for software-in-the-loop (SIL) simulation with TruckSim. It is within Simulink that the external electric powertrain model and control systems are implemented, which rely on incoming vehicle data from the TruckSim S-function to return appropriate control actions to the full vehicle model.

3.2.2.1 Electric Powertrain Model

The proposed electric powertrain of the combat vehicle consists of eight permanent magnet AC motors with the following specifications;

Maximum Rotational Speed	6000 RPM
Maximum Operating Voltage	400 V
Maximum Operating Current	375 A
Maximum Power Output	150 kW

The electric powertrain model is modeled within Simulink and uses a three-dimensional characteristic lookup table of the proposed motors to calculate output motor torque. The electric motor lookup table used in this work is presented in Figure 3-5, which relies on motor rotational speed and motor current as inputs. Each curve corresponds to a magnitude of motor current input. Using the given wheel speed and motor current, Simulink will interpolate within the lookup table to generate an output motor torque. The lookup table also includes negative current curves to account for spinning in reverse, as rotational speed is read as a scalar from the TruckSim environment.

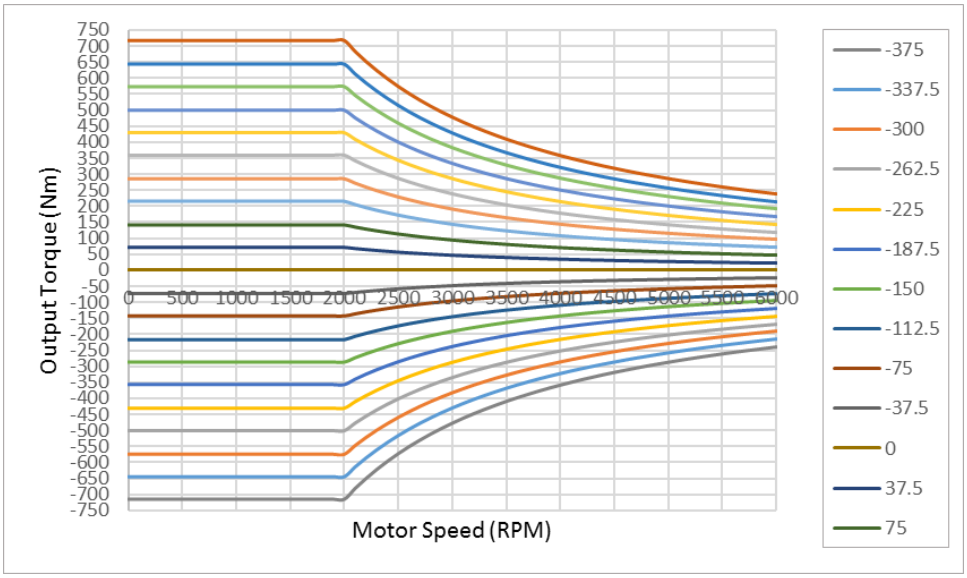

Figure 3-5 Electric Motor Lookup Table [7]

To model a single electric motor, the rotational inertias of the wheel, I_{wheel} and the motor hub, I_{motor} are taken into consideration to calculate the required motor rotational

speed for the lookup table, as shown by the equations below. The net motor torque, isolating the effect of the wheel on the ground is;

$$T_{net} = T_{motor} - I_{motor}\alpha_{motor} \quad \textbf{3-1}$$

Accounting for tractive force F_X and the motor reduction, the net torque at the wheel is;

$$T_{net}n_{motor} - F_X r_{eff} = I_{wheel}\alpha_{wheel} \quad \textbf{3-2}$$

Where r_{eff} is the effective rolling radius of the tire and n_{motor} is the motor gear reduction ratio of 10:1. Isolating for α_{wheel} and integrating obtains the rotational speed;

$$\omega_{wheel} = \int \alpha_{wheel} = \int \left(\frac{T_{net}n_{motor} - F_X r_{eff}}{I_{wheel}}\right) dt \quad \textbf{3-3}$$

To obtain the required motor rotational speed, the wheel rotational speed is multiplied by the motor gear reduction ratio;

$$\omega_{motor} = \omega_{wheel}n_{motor} \quad \textbf{3-4}$$

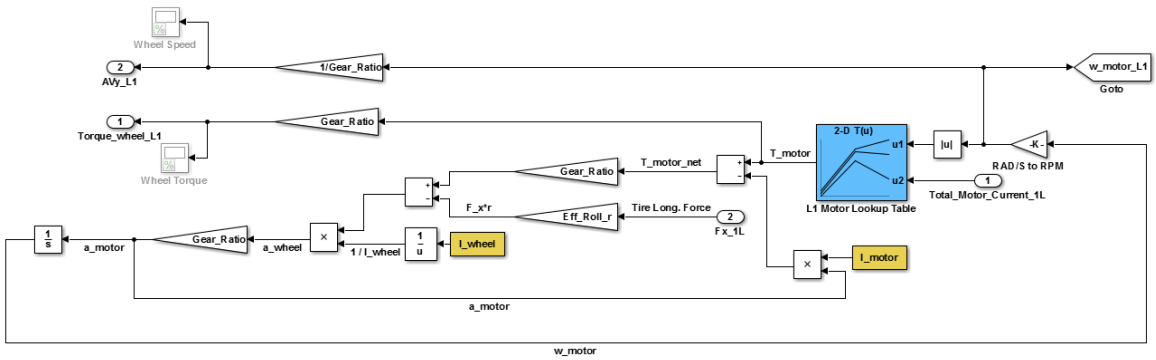

Figure 3-6 Electric Motor Model in Simulink

Figure 3-6 shows the above equations modeled in Simulink. Tractive force F_X is read from the TruckSim environment to perform continuous calculation of motor rotational speed. To send data to the TruckSim environment, motor torque is multiplied by the reduction to obtain wheel torque, while motor speed is divided by the reduction.

3.3 Vehicle Models for Active Yaw Control

3.3.1 Reference Two-Degree-of-Freedom Bicycle Model

3.3.1.1 State-Space Matrices for Control System Synthesis

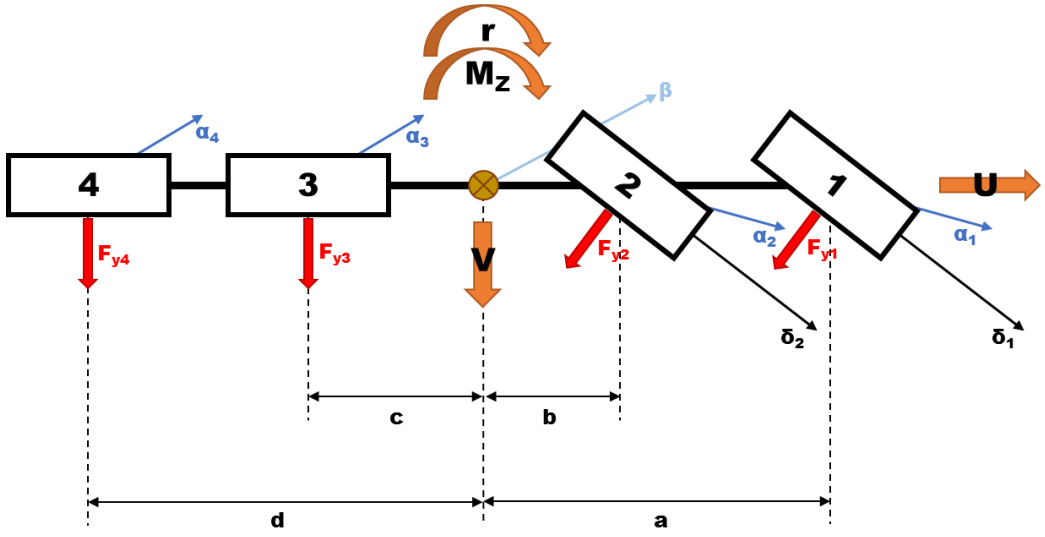

Figure 3-7 Bicycle Model for 8x8 Front-Steered Combat Vehicle

Figure 3-7 presents the two-degree-of-freedom bicycle model of the multi-wheeled combat vehicle layout. This model is used for both generating the gains for determining desired values, and the state-space model for synthesizing the active yaw controller. For this model, key assumptions are made to validate its use:

- Longitudinal speed is assumed constant (zero acceleration),
- Load transfer in the lateral and longitudinal directions are negligible,
- All resistive forces (aerodynamic, grade, rolling resistance) are neglected,
- Left and right wheel ground angles are assumed parallel, thus averaged for simplification,
- Left and right tire cornering stiffness are equal and are added for a single tire representation,
- All tires operate within linear (elastic) characteristics,
- Small angle approximation is in effect.

Development of the state-space model will be discussed first, followed by the gains for desired steady-state yaw rate and vehicle side slip. The equations of motions are first derived from the bicycle model free-body diagram in Equations 3-5 and 3-6.

$$m(\dot{V} + Ur) = F_{y1} + F_{y2} + F_{y3} + F_{y4} \quad \textbf{3-5}$$

$$I_{zz}\dot{r} = aF_{y1} + bF_{y2} - cF_{y3} - dF_{y4} + M_Z \quad \textbf{3-6}$$

With small angle approximation, the wheel slip angles for the front tires are defined in Equation 3-7 and in Equation 3-8 for the rear non-steered tires;

$$\alpha_1 = \delta_1 - \left(\frac{V + ar}{U}\right) \quad \alpha_2 = \delta_2 - \left(\frac{V + br}{U}\right) \quad \textbf{3-7}$$

$$\alpha_3 = -\left(\frac{V - cr}{U}\right) \quad \alpha_4 = -\left(\frac{V - dr}{U}\right) \quad \textbf{3-8}$$

Lateral tire force – assuming linear tire behaviour – is a multiplication of tire cornering stiffness by wheel slip angle, as given in general form in Equation 3-9 for the front tires and Equation 3-10 for the rear tires.

$$F_{yf} = C_{\alpha f}\left[\delta_f - \left(\frac{V + x_f r}{U}\right)\right] \quad \textbf{3-9}$$

$$F_{yr} = C_{\alpha r}\left[-\left(\frac{V - x_r r}{U}\right)\right] \quad \textbf{3-10}$$

Where x_f is the distance of the front tire to the centre of gravity (CG) and x_r is that of the rear. Note that for these equations, the value of tire cornering stiffness is for two tires. Substituting the above equations into Equations 3-5 and 3-6, we obtain;

$$m(\dot{V} + Ur) = C_{\alpha 1}\left[\delta_1 - \left(\frac{V + ar}{U}\right)\right] + C_{\alpha 2}\left[\delta_2 - \left(\frac{V + br}{U}\right)\right] + C_{\alpha 3}\left[-\left(\frac{V - cr}{U}\right)\right] + C_{\alpha 4}\left[-\left(\frac{V - dr}{U}\right)\right] \quad \textbf{3-11}$$

$$I_{zz}\dot{r} = aC_{\alpha 1}\left[\delta_1 - \left(\frac{V + ar}{U}\right)\right] + bC_{\alpha 2}\left[\delta_2 - \left(\frac{V + br}{U}\right)\right] - cC_{\alpha 3}\left[-\left(\frac{V - cr}{U}\right)\right] - dC_{\alpha 4}\left[-\left(\frac{V - dr}{U}\right)\right] + M_Z \quad \textbf{3-12}$$

Vehicle side slip is accounted for by Equation 3-13 below, to used in further simplification of the above equations.

$$\beta = \frac{V}{U} \quad \dot{\beta} = \frac{\dot{V}}{U} \tag{3-13}$$

Substituting the above into Equations 3-11 and 3-12, organizing terms and isolating for $\dot{\beta}$ and $\dot{r}$ will yield;

$$\dot{\beta} = \left[\frac{C_{\alpha1}\delta_1 + C_{\alpha2}\delta_2}{mU}\right] + \left[-\frac{C_{\alpha1} + C_{\alpha2} + C_{\alpha3} + C_{\alpha4}}{mU}\right]\beta + \left[\frac{-aC_{\alpha1} - bC_{\alpha2} + cC_{\alpha3} + dC_{\alpha4} - mU^2}{mU^2}\right]r \tag{3-14}$$

$$\dot{r} = \left[\frac{aC_{\alpha1}\delta_1 + bC_{\alpha2}\delta_2}{I_{zz}}\right] + \left[\frac{-aC_{\alpha1} - bC_{\alpha2} + cC_{\alpha3} + dC_{\alpha4}}{I\_zz}\right]\beta + \left[\frac{-a^2C_{\alpha1} - b^2C_{\alpha2} + c^2C_{\alpha3} + d^2C_{\alpha4}}{I_{zz}U}\right]r + \frac{M_Z}{Izz} \tag{3-15}$$

Equations 3-14 and 3-15 above can be combined into matrix form, shown in Equation 3-16 below, to obtain the state-space model of the vehicle;

$$\begin{bmatrix}\dot{\beta}\\ \dot{r}\end{bmatrix} = \begin{bmatrix}\left(-\frac{C_{\alpha1} + C_{\alpha2} + C_{\alpha3} + C_{\alpha4}}{mU}\right) & \left(\frac{-aC_{\alpha1} - bC_{\alpha2} + cC_{\alpha3} + dC_{\alpha4} - U^2}{mU^2}\right)\\ \left(\frac{-aC_{\alpha1} - bC_{\alpha2} + cC_{\alpha3} + dC_{\alpha4}}{I_{zz}}\right) & \left(\frac{-a^2C_{\alpha1} - b^2C_{\alpha2} + c^2C_{\alpha3} + d^2C_{\alpha4}}{I_{zz}U}\right)\end{bmatrix}\begin{bmatrix}\beta\\ r\end{bmatrix} + \begin{bmatrix}\frac{C_{\alpha1}}{mU} & \frac{C_{\alpha2}}{mU}\\ \frac{aC_{\alpha1}}{I_{zz}} & \frac{bC_{\alpha2}}{I_{zz}}\end{bmatrix}\begin{bmatrix}\delta_1\\ \delta_2\end{bmatrix} + \begin{bmatrix}0 & 0\\ 0 & \frac{1}{Izz}\end{bmatrix}\begin{bmatrix}0\\ M_Z\end{bmatrix} \tag{3-16}$$

From this equation, the various components of the state-space model are obtained. The state matrix, *A*, is:

$$A = \begin{bmatrix}\left(-\frac{C_{\alpha1} + C_{\alpha2} + C_{\alpha3} + C_{\alpha4}}{mU}\right) & \left(\frac{-aC_{\alpha1} - bC_{\alpha2} + cC_{\alpha3} + dC_{\alpha4} - U^2}{mU^2}\right)\\ \left(\frac{-aC_{\alpha1} - bC_{\alpha2} + cC_{\alpha3} + dC_{\alpha4}}{I_{zz}}\right) & \left(\frac{-a^2C_{\alpha1} - b^2C_{\alpha2} + c^2C_{\alpha3} + d^2C_{\alpha4}}{I_{zz}U}\right)\end{bmatrix} \tag{3-17}$$

The input matrix, *B* is:

$$B = \begin{bmatrix}\frac{C_{\alpha1}}{mU} & \frac{C_{\alpha2}}{mU}\\ \frac{aC_{\alpha1}}{I_{zz}} & \frac{bC_{\alpha2}}{I_{zz}}\end{bmatrix} \tag{3-18}$$

And the output matrix, *C*, is:

$$C = \begin{bmatrix} 0 & 0 \\ 0 & \frac{1}{I_{zz}} \end{bmatrix} \quad \textbf{3-19}$$

3.3.1.2 Steady-State Vehicle Side Slip and Yaw Rate Relations

To determine the desired yaw rates and vehicle side slip for a given ground wheel steering angle δ, all transient values ($\dot{\beta}, \dot{r}, M_z$) are assumed to be zero. The model is further simplified by the assumption that the ground wheel steer angle of the second axle is related to that of the first by a constant value, *k*, such that;

$$\delta_2 = k\delta_1 \quad \textbf{3-20}$$

With all transient values set to zero, Equation 3-20 above can be substituted into 3-16 derived in the previous subsection to give;

$$\begin{bmatrix} \left(-\frac{C_{\alpha1} + C_{\alpha2} + C_{\alpha3} + C_{\alpha4}}{mU}\right) & \left(\frac{-aC_{\alpha1} - bC_{\alpha2} + cC_{\alpha3} + dC_{\alpha4} - U^2}{mU^2}\right) \\ \left(\frac{-aC_{\alpha1} - bC_{\alpha2} + cC_{\alpha3} + dC_{\alpha4}}{I_{zz}}\right) & \left(\frac{-a^2C_{\alpha1} - b^2C_{\alpha2} + c^2C_{\alpha3} + d^2C_{\alpha4}}{I_{zz}U}\right) \end{bmatrix} \begin{bmatrix} \beta \\ r \end{bmatrix} = -\begin{bmatrix} \frac{C_{\alpha1}}{mU} & \frac{C_{\alpha2}}{mU} \\ \frac{aC_{\alpha1}}{I_{zz}} & \frac{bC_{\alpha2}}{I_{zz}} \end{bmatrix} \begin{bmatrix} \delta_1 \\ k\delta_1 \end{bmatrix}$$

3-21

To obtain steady-state gain values, $\frac{\beta}{\delta_1}$ and $\frac{r}{\delta_1}$, both sides of Equation 3-21 are divided by δ_1. The *B* state-space matrix on the right side of the equation is also further simplified to yield the result below.

$$\begin{bmatrix} \left(-\frac{C_{\alpha1} + C_{\alpha2} + C_{\alpha3} + C_{\alpha4}}{mU}\right) & \left(\frac{-aC_{\alpha1} - bC_{\alpha2} + cC_{\alpha3} + dC_{\alpha4} - U^2}{mU^2}\right) \\ \left(\frac{-aC_{\alpha1} - bC_{\alpha2} + cC_{\alpha3} + dC_{\alpha4}}{I_{zz}}\right) & \left(\frac{-a^2C_{\alpha1} - b^2C_{\alpha2} + c^2C_{\alpha3} + d^2C_{\alpha4}}{I_{zz}U}\right) \end{bmatrix} \begin{bmatrix} \frac{\beta}{\delta_1} \\ \frac{r}{\delta_1} \end{bmatrix} = \begin{bmatrix} \left(-\frac{C_{\alpha1}}{mU} - k\frac{C_{\alpha2}}{mU}\right) \\ \left(-\frac{aC_{\alpha1}}{I_{zz}} - k\frac{bC_{\alpha2}}{I_{zz}}\right) \end{bmatrix}$$

3-22

From the above system of equations, steady-state vehicle side slip is obtained by the following;

$$\frac{\beta}{\delta_1}=\frac{\begin{vmatrix}\left(-\frac{C_{\alpha1}}{mU}-k\frac{C_{\alpha2}}{mU}\right) & \left(\frac{-aC_{\alpha1}-bC_{\alpha2}+cC_{\alpha3}+dC_{\alpha4}-U^2}{mU^2}\right)\\ \left(-\frac{aC_{\alpha1}}{I_{zz}}-k\frac{bC_{\alpha2}}{I_{zz}}\right) & \left(\frac{-a^2C_{\alpha1}-b^2C_{\alpha2}+c^2C_{\alpha3}+d^2C_{\alpha4}}{I_{zz}U}\right)\end{vmatrix}}{\begin{vmatrix}\left(-\frac{C_{\alpha1}+C_{\alpha2}+C_{\alpha3}+C_{\alpha4}}{mU}\right) & \left(\frac{-aC_{\alpha1}-bC_{\alpha2}+cC_{\alpha3}+dC_{\alpha4}-U^2}{mU^2}\right)\\ \left(\frac{-aC_{\alpha1}-bC_{\alpha2}+cC_{\alpha3}+dC_{\alpha4}}{I_{zz}}\right) & \left(\frac{-a^2C_{\alpha1}-b^2C_{\alpha2}+c^2C_{\alpha3}+d^2C_{\alpha4}}{I_{zz}U}\right)\end{vmatrix}} \qquad \textbf{3-23}$$

Further algebraic simplification yields the final steady-state relationship between ground wheel steer angle and vehicle side slip, presented below;

$$\frac{\beta}{\delta_1}=\frac{\left(-\frac{C_{\alpha1}}{mU}-k\frac{C_{\alpha2}}{mU}\right)\left(\frac{-a^2C_{\alpha1}-b^2C_{\alpha2}+c^2C_{\alpha3}+d^2C_{\alpha4}}{I_{zz}U}\right)-\left(-\frac{aC_{\alpha1}}{I_{zz}}-k\frac{bC_{\alpha2}}{I_{zz}}\right)\left(\frac{-aC_{\alpha1}-bC_{\alpha2}+cC_{\alpha3}+dC_{\alpha4}-U^2}{mU^2}\right)}{\left(-\frac{C_{\alpha1}+C_{\alpha2}+C_{\alpha3}+C_{\alpha4}}{mU}\right)\left(\frac{-a^2C_{\alpha1}-b^2C_{\alpha2}+c^2C_{\alpha3}+d^2C_{\alpha4}}{I_{zz}U}\right)-\left(\frac{-aC_{\alpha1}-bC_{\alpha2}+cC_{\alpha3}+dC_{\alpha4}}{I_{zz}}\right)\left(\frac{-aC_{\alpha1}-bC_{\alpha2}+cC_{\alpha3}+dC_{\alpha4}-U^2}{mU^2}\right)} \qquad \textbf{3-24}$$

In a similar manner, steady-state yaw rate with respect to ground wheel steer angle can be obtained by;

$$\frac{r}{\delta_1}=\frac{\begin{vmatrix}\left(-\frac{C_{\alpha1}+C_{\alpha2}+C_{\alpha3}+C_{\alpha4}}{mU}\right) & \left(-\frac{C_{\alpha1}}{mU}-k\frac{C_{\alpha2}}{mU}\right)\\ \left(\frac{-aC_{\alpha1}-bC_{\alpha2}+cC_{\alpha3}+dC_{\alpha4}}{I_{zz}}\right) & \left(-\frac{aC_{\alpha1}}{I_{zz}}-k\frac{bC_{\alpha2}}{I_{zz}}\right)\end{vmatrix}}{\begin{vmatrix}\left(-\frac{C_{\alpha1}+C_{\alpha2}+C_{\alpha3}+C_{\alpha4}}{mU}\right) & \left(\frac{-aC_{\alpha1}-bC_{\alpha2}+cC_{\alpha3}+dC_{\alpha4}-U^2}{mU^2}\right)\\ \left(\frac{-aC_{\alpha1}-bC_{\alpha2}+cC_{\alpha3}+dC_{\alpha4}}{I_{zz}}\right) & \left(\frac{-a^2C_{\alpha1}-b^2C_{\alpha2}+c^2C_{\alpha3}+d^2C_{\alpha4}}{I_{zz}U}\right)\end{vmatrix}} \qquad \textbf{3-25}$$

Further algebraic simplification yields the final steady-state relationship between yaw rate with respect to ground wheel steer angle can be obtained by;

$$\frac{r}{\delta_1}=\frac{\left(-\frac{C_{\alpha1}+C_{\alpha2}+C_{\alpha3}+C_{\alpha4}}{mU}\right)\left(-\frac{aC_{\alpha1}}{I_{zz}}-k\frac{bC_{\alpha2}}{I_{zz}}\right)-\left(\frac{-aC_{\alpha1}-bC_{\alpha2}+cC_{\alpha3}+dC_{\alpha4}}{I_{zz}}\right)\left(-\frac{C_{\alpha1}}{mU}-k\frac{C_{\alpha2}}{mU}\right)}{\left(-\frac{C_{\alpha1}+C_{\alpha2}+C_{\alpha3}+C_{\alpha4}}{mU}\right)\left(\frac{-a^2C_{\alpha1}-b^2C_{\alpha2}+c^2C_{\alpha3}+d^2C_{\alpha4}}{I_{zz}U}\right)-\left(\frac{-aC_{\alpha1}-bC_{\alpha2}+cC_{\alpha3}+dC_{\alpha4}}{I_{zz}}\right)\left(\frac{-aC_{\alpha1}-bC_{\alpha2}+cC_{\alpha3}+dC_{\alpha4}-U^2}{mU^2}\right)} \qquad \textbf{3-26}$$

3.3.2 Differential Lateral Tire Force Model for Skid Steering

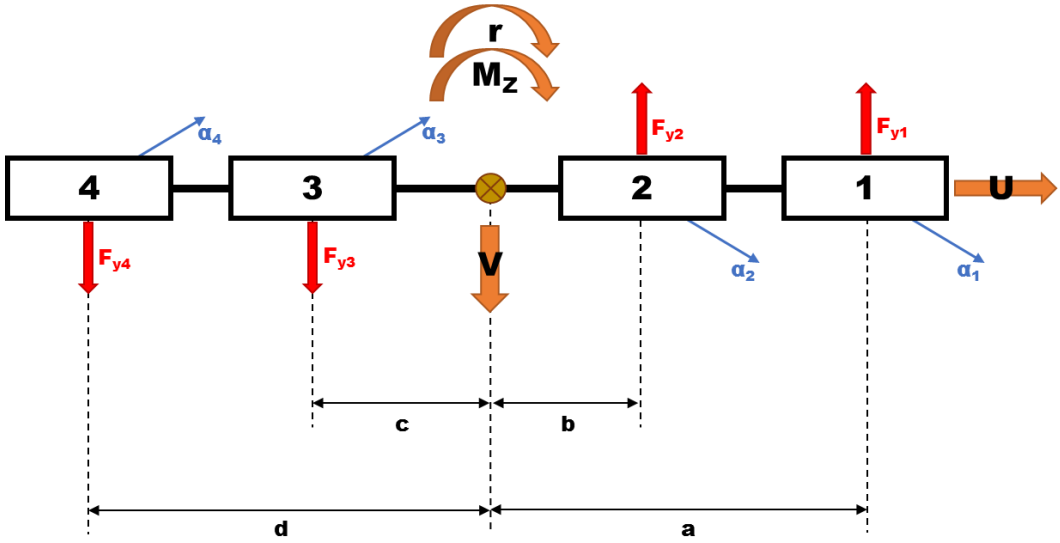

Figure 3-8 Bicycle Model for Skid Steered 8x8 Combat Vehicle

Figure 3-8 presents a two-degree-of-freedom bicycle model developed for skid steering. Like other skid steering models presented in literature, forces on opposing sides of the vehicle centre of gravity work together to generate a yaw moment. This model is intended to further simplify skid steering kinematics into a linear, steady-state system by using differential lateral tire forces generated by the yawing motion, as opposed to differential longitudinal forces. As such, the following assumptions are made for this model:

- The road is assumed to be rigid and smooth with ideal surface conditions,
- Longitudinal speed is assumed constant and low,
- All load transfer and suspension geometry effects are negligible,
- Vehicle centre of gravity is assumed to be very low,
- Effect of vehicle track width is neglected,
- All wheels are fixed straight (zero toe and camber, no mechanical backlash)
- All resistive forces (aerodynamic, grade, rolling resistance) are neglected,
- Left and right tire cornering stiffness are equal and are added for a single tire representation
- All tires operate within linear (elastic) characteristics,

- Small angle approximation is in effect.

With the steady-state nature of the model, the free body diagram of the skid steering bicycle model yield the following kinematic equations. Note that all transient parameters are zero, however an external moment still exists as the driver of yaw motion in this model.

$$m(Ur) = -F_{y1} - F_{y2} + F_{y3} + F_{y4} \quad \textbf{3-27}$$

$$0 = -aF_{y1} - bF_{y2} - cF_{y3} - dF_{y4} + M_Z \quad \textbf{3-28}$$

With the lack of a ground wheel steering angle, the equations for wheel slip angles on the front axles become the form presented in Equation 3-29 below. Wheel slip angles for the rear remain the same as presented in Equation 3-8 in the previous section, however opposite in sign.

$$\alpha_1 = -\left(\frac{V + ar}{U}\right) \quad \alpha_2 = -\left(\frac{V + br}{U}\right) \quad \textbf{3-29}$$

As stated in the previous section, lateral tire force F_y is a multiplication of combined tire cornering stiffness and wheel slip angle. Using this relationship, the kinematic equations thus become;

$$m(Ur) = C_{\alpha1}\left[\left(\frac{V + ar}{U}\right)\right] + C_{\alpha2}\left[\left(\frac{V + br}{U}\right)\right] + C_{\alpha3}\left[\left(\frac{V - cr}{U}\right)\right] + C_{\alpha4}\left[\left(\frac{V - dr}{U}\right)\right] \quad \textbf{3-30}$$

$$0 = -aC_{\alpha1}\left[\left(\frac{V + ar}{U}\right)\right] - C_{\alpha2}\left[\left(\frac{V + br}{U}\right)\right] + cC_{\alpha3}\left[\left(\frac{V - cr}{U}\right)\right] + dC_{\alpha4}\left[\left(\frac{V - dr}{U}\right)\right] + M_Z \quad \textbf{3-31}$$

Rearranging above equations to isolate all terms with speeds *U*, *V* and yaw rate *r* to one side, and external yaw moment M_Z on the other yields the following system of equations;

$$0 = C_{\alpha1}\left[\left(\frac{V + ar}{mU}\right)\right] + C_{\alpha2}\left[\left(\frac{V + br}{mU}\right)\right] + C_{\alpha3}\left[\left(\frac{V - cr}{mU}\right)\right] + C_{\alpha4}\left[\left(\frac{V - dr}{mU}\right)\right] - Ur \quad \textbf{3-32}$$

$$M_Z = aC_{\alpha1}\left[\left(\frac{V + ar}{U}\right)\right] + C_{\alpha2}\left[\left(\frac{V + br}{U}\right)\right] - cC_{\alpha3}\left[\left(\frac{V - cr}{U}\right)\right] - dC_{\alpha4}\left[\left(\frac{V - dr}{U}\right)\right] \quad \textbf{3-33}$$

Like with the state-space model in the previous section, the system of equations can be organized into matrix form to prepare for determining the steady-state yaw moment gain, as presented below;

$$0 = \left[\frac{C_{\alpha1} + C_{\alpha2} + C_{\alpha3} + C_{\alpha4}}{mU}\right]V + \left[\frac{aC_{\alpha1} + bC_{\alpha2} - cC_{\alpha3} - dC_{\alpha4} - U^2}{mU}\right]r \quad \textbf{3-34}$$

$$M_Z = \left[\frac{aC_{\alpha1} + bC_{\alpha2} - cC_{\alpha3} - dC_{\alpha4}}{U}\right]V + \left[\frac{a^2C_{\alpha1} + b^2C_{\alpha2} + c^2C_{\alpha3} + d^2C_{\alpha4}}{U}\right]r \quad \textbf{3-35}$$

$$\begin{bmatrix}0\\M_Z\end{bmatrix} = \begin{bmatrix}\left(\frac{C_{\alpha1} + C_{\alpha2} + C_{\alpha3} + C_{\alpha4}}{mU}\right) & \left(\frac{aC_{\alpha1} + bC_{\alpha2} - cC_{\alpha3} - dC_{\alpha4} - mU^2}{mU}\right)\\ \left(\frac{aC_{\alpha1} + bC_{\alpha2} - cC_{\alpha3} - dC_{\alpha4}}{U}\right) & \left(\frac{a^2C_{\alpha1} + b^2C_{\alpha2} + c^2C_{\alpha3} + d^2C_{\alpha4}}{U}\right)\end{bmatrix}\begin{bmatrix}V\\r\end{bmatrix} \quad \textbf{3-36}$$

To solve for external yaw moment M_Z, the system in Equation 3-36 above is manipulated into the following form;

$$r = \frac{\begin{vmatrix}\left(\frac{C_{\alpha1} + C_{\alpha2} + C_{\alpha3} + C_{\alpha4}}{mU}\right) & 0\\ \left(\frac{aC_{\alpha1} + bC_{\alpha2} - cC_{\alpha3} - dC_{\alpha4}}{U}\right) & M_Z\end{vmatrix}}{\begin{vmatrix}\left(\frac{C_{\alpha1} + C_{\alpha2} + C_{\alpha3} + C_{\alpha4}}{mU}\right) & \left(\frac{aC_{\alpha1} + bC_{\alpha2} - cC_{\alpha3} - dC_{\alpha4} - mU^2}{mU}\right)\\ \left(\frac{aC_{\alpha1} + bC_{\alpha2} - cC_{\alpha3} - dC_{\alpha4}}{U}\right) & \left(\frac{a^2C_{\alpha1} + b^2C_{\alpha2} + c^2C_{\alpha3} + d^2C_{\alpha4}}{U}\right)\end{vmatrix}} \quad \textbf{3-37}$$

Finally, in solving the relation presented above, the steady-state external yaw moment gain with respect to yaw rate is determined. The simplified general form is presented below;

$$\frac{M_Z}{r} = \frac{1}{\sum C_{\alpha i}}\left[\frac{\left(\sum C_{\alpha i}\right)\left(\sum x_f^2 C_{\alpha i} + \sum x_r^2 C_{\alpha i}\right) - \left(\sum x_f C_{\alpha i} - \sum x_r C_{\alpha i}\right)\left(\sum x_f C_{\alpha i} - \sum x_r C_{\alpha i} - mU^2\right)}{U}\right] \quad \textbf{3-38}$$

Where $C_{\alpha i}$ is the combined tire cornering stiffness of each axle i, x_f is the distance of the respective front axle from the centre of gravity, and x_r is the distance of the respective rear axle from the centre of gravity.

This steady-state gain value serves two purposes – to be used in conjunction with Equation 3-26 which generates a desired yaw rate from ground wheel steering input to create the feedforward skid steer control system, and to serve as a tuning parameter for the active yaw controller, to be discussed in the following section.

3.4 Synthesis of Active Yaw Controller

3.4.1 Linear Quadratic Regulator (LQR) Control Method

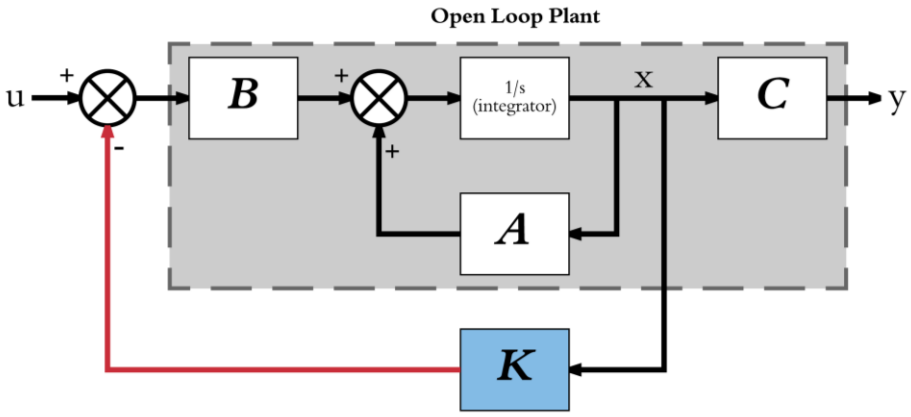

Figure 3-9 LQR Control Gain in Feedback with Open-Loop Plant

The optimal control law used to synthesize the LQR controller is inspired by those proposed in [35], [36], all of which used vehicle side slip β and yaw rate r as controlled state variables. The state-space model derived in the previous section can be expressed in the general form as:

$$\dot{x} = [A]x + [B]u$$
$$y = [C]x + [D]u \qquad \textbf{3-39}$$

Where *[A]* is the state matrix representing the system, *x* is the state variable vector consisting of vehicle side slip and yaw rate, [β, r]. The matrix *[B]* is the input, or control matrix. This multiplies input variable vector, *u*, which consists of the ground wheel steer angles of the first and second axles, [δ_1, δ_2]. The matrix *[C]* is the output matrix, which corresponds to a control output for the system. The output vector *y* which consists solely of external yaw moment as of the form [0, M_Z] is a multiplication of the of the output matrix and state variable vector. The matrix *[D]* is a feedthrough matrix for the input variable and is not required in this control system.

In Figure 3-9, the grey area which encloses the *[A]*, *[B]* and *[C]* matrices comprise the open loop plant built from the linearized ideal vehicle model. When implemented in Simulink, the open loop plant portion of the control model in Figure 3-9 consists of function

blocks which calculate the desired vehicle side slip and yaw rate, as defined by Equations 3-24 and 3-26, respectively. Vehicle side slip and yaw rate are actively monitored via the TruckSim environment, from which the respective desired values are subtracted to generate the state variable vector x¸ as used in Equation 3-40, below.

State feedback is implemented to add a control force to the system. The state variable vector *x* is multiplied by the control gain matrix *[K]*, which is placed in negative feedback with the open loop plant, as shown in Figure 3-9 above, and in matrix form below;

$$u = -Kx = -[K]\begin{bmatrix}\beta - \beta_{des} \\ r - r_{des}\end{bmatrix} \quad \textbf{3-40}$$

A cost function known as the performance index *J* must be minimized to obtain the control gain matrix *[K]*, and is defined as;

$$J = \int (x^T[Q]x + u^T[R]u)dt \quad \textbf{3-41}$$

Where *[Q]* is the state variable weighting matrix and *[R]* is the output variable weighting matrix. These weighting matrices serve as tuning parameters for the cost function, and will be discussed in the following subsection. To generate the control gain matrix *[K]*, the **lqr** black-box function within MATLAB uses the *[A]*, *[B]*, *[Q]*, and *[R]* matrices to generate the cost function and perform the optimization process required to minimize the value of the cost [11] [69] [70].

3.4.2 Weighting Matrices for Performance Index Tuning

Weighting matrices are used to adjust the performance index *J* in order to generate a control gain matrix *[K]* through the optimization process. The weighting matrix *[Q]* limits state variable deviation from the target values, while the weighting matrix *[R]* limits output control action deviation. Both are symmetric positive diagonal matrices of $m \times m$ dimensions, where m corresponds to the number of state variables in the system.

Past works which rely on the LQR control have used the identity matrix to define both *[Q]* and *[R]*. The identity matrix serves as a starting point for manual tuning using constant multipliers to adjust either weighting. The weighting matrices used in this control

system synthesis process are inspired by [11], [36], [71] which take the general form presented below for a system of two state variables;

$$Q = \begin{bmatrix} \frac{1}{x_{1,max}^2} & 0 \\ 0 & \frac{1}{x_{2,max}^2} \end{bmatrix} \quad R = \begin{bmatrix} \frac{1}{y_{1,max}^2} & 0 \\ 0 & \frac{1}{y_{2,max}^2} \end{bmatrix} \qquad \textbf{3-42}$$

Where x_i corresponds to each state variable and y_i corresponds to each output control variable. In the case of this work, given the state-space model derived in the previous section, the weighting matrices are defined as such;

$$Q = \begin{bmatrix} \frac{1}{\beta_{max}^2} & 0 \\ 0 & \frac{1}{r_{max}^2} \end{bmatrix} \quad R = \begin{bmatrix} 1 & 0 \\ 0 & \frac{1}{M_{Z}{}_{max}^2} \end{bmatrix} \qquad \textbf{3-43}$$

The maximum state values for the elements of the *[Q]* matrix are defined as;

$$\beta_{max} = 3° \quad r_{max} = \frac{\mu g}{U} \qquad \textbf{3-44}$$

To obtain maximum external yaw moment $M_{Z,max}$ for the *[R]* matrix, the maximum yaw rate r_{max} from the above definition is substituted into Equation 3-38 along with target vehicle speed to account for the vehicle mass, tire cornering stiffness and dimensions.

By introducing vehicle speed and road surface friction as variables for tuning the weighting matrices, an element of adaptivity is introduced should active state monitoring be available. Yaw rate and vehicle speed are easily monitored and widely implemented, while vehicle side slip and road surface friction prove to be more abstract. Methods of vehicle side slip estimation are further elaborated in [72] [73] [74] [75] [76], and methods of road friction estimation are further elaborated in [76] [77] [78] [79] [80], as they are not in the scope of this work. With active state monitoring capabilities in TruckSim, vehicle states can be constantly updated within the weighting matrices, allowing for continuous online optimization, and updating of the control gain matrix *[K]*.

3.4.3 Pre-Compensation Scaling Factor

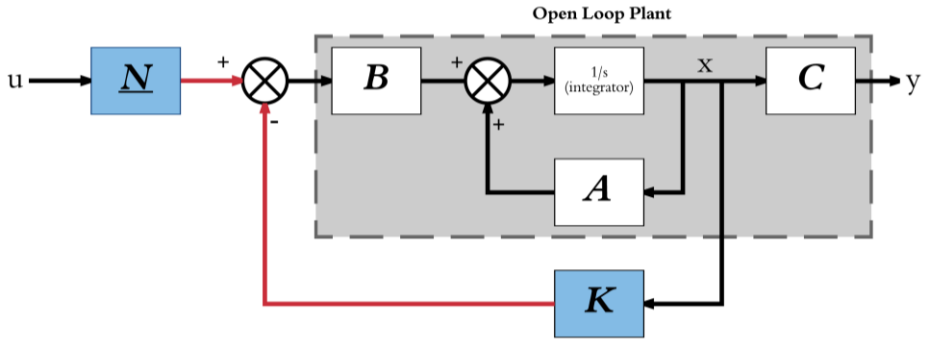

Figure 3-10 Placement of Pre-Compensation Scaling Factor

To harness the active yaw controller for skid steering operation, a pre-compensation scaling factor $\bar{N}$ is introduced into the system. Implementing a pre-compensation scaling factor is inspired by aircraft dynamics control using the linear quadratic regulation approach, such examples being [70] [81]. The basic purpose of the scaling factor is to amplify the input before the addition of the feedback control force to reduce steady-state error and to scale the input with respect to a desired output.

In this system, the ground wheel steer angle δ is required by the open loop plant because it forms the elements of the input vector u. The wheel steer angle is scaled so that it requires less uncompensated effort from the driver when generating the resulting output control vector y to achieve a given external yaw moment M_Z. This consequently increases the external yaw moment output per degree of input wheel steer angle. Some works have used a scaling algorithm to determine the scaling factor [81]. The algorithm relies on the steady-state error generated by the uncompensated system with the control gain *[K]* already generated. This work follows a different manual approach in which uncompensated input from the driver is monitored during an active simulation. Then, using the same simulation procedure, the scaling factor is manually adjusted until a maximum value is determined that induces oscillation in the driver input. The scaling factor is then adjusted down until the driver input is reduced as much as possible without oscillation.

3.5 Design of Rear Steering Control Methods

This section covers the vehicle models used for designing both active and passive rear steering control methods. Both active and passive methods are feedforward control systems that work in parallel with the active yaw controller of the respectively-equipped vehicles. The passive system depends on fixed ratios determined graphically through the development of low-speed modified Ackermann steering geometries. Thus, the rear wheels of the combat vehicle are steered in relation to the front by a fixed proportion, regardless of forward speed. The active system expands on this by introducing speed as a variable in an algebraically-derived function which determines both the orientation and proportion of steering for the rear wheels in relation to the front. Development for both fourth-axle steering and all-wheel steering are discussed here.

3.5.1 Modified Ackermann Geometries for Fixed "Passive" Rear Steering

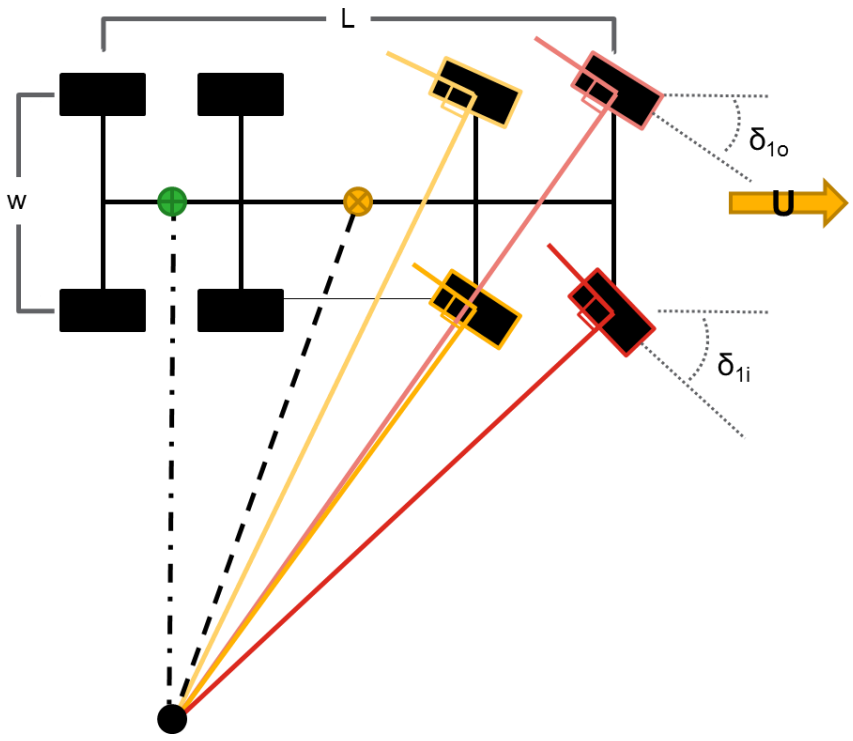

Figure 3-11 Ackermann Geometry for 8x8 Front-Steered Combat Vehicle

To understand the development of the modified geometries for rear steering, the basic model for conventional front steering is first established, as shown in Figure 3-11. The Ackermann steering geometry is established under the assumption of extremely low speed to determine the relationships between the angles of all steerable wheels to prevent tire scrubbing during a maneuver.

The inner wheel angle of the first axle δ_{1i} is used as the reference with which all other steerable wheels are defined. An instantaneous center is obtained by intersecting two lines: the line of the stationary rear axle and the line perpendicular to the front-most inner wheel. In the case of the multi-wheeled combat vehicle, a virtual stationary axle is positioned exactly between the two rear axles, marked by the green point on the vehicle model. The black point marks the instantaneous centre outside of the vehicle through which all lines from steerable wheels are determined in relation to the reference wheel. Using an appropriate graphical scaling factor, turning radius can be measured from the distance between the instantaneous centre and the vehicle centre of gravity. A constant ratio between first and second axle wheel angles, k_{12}, can be determined by Equation 3-45 below. All other wheel angles in the equation are measured graphically from the geometric layout in Figure 3-11 using an appropriate scaling factor. Subscript *i* denotes the inner wheel, and subscript *o* denotes the outer.

$$k_{12} = average\left[\left(\frac{\delta_{2i}}{\delta_{1i}}\right), \left(\frac{\delta_{2o}}{\delta_{1o}}\right)\right] \qquad \textbf{3-45}$$

3.5.1.1 Fourth-Axle Steering Model

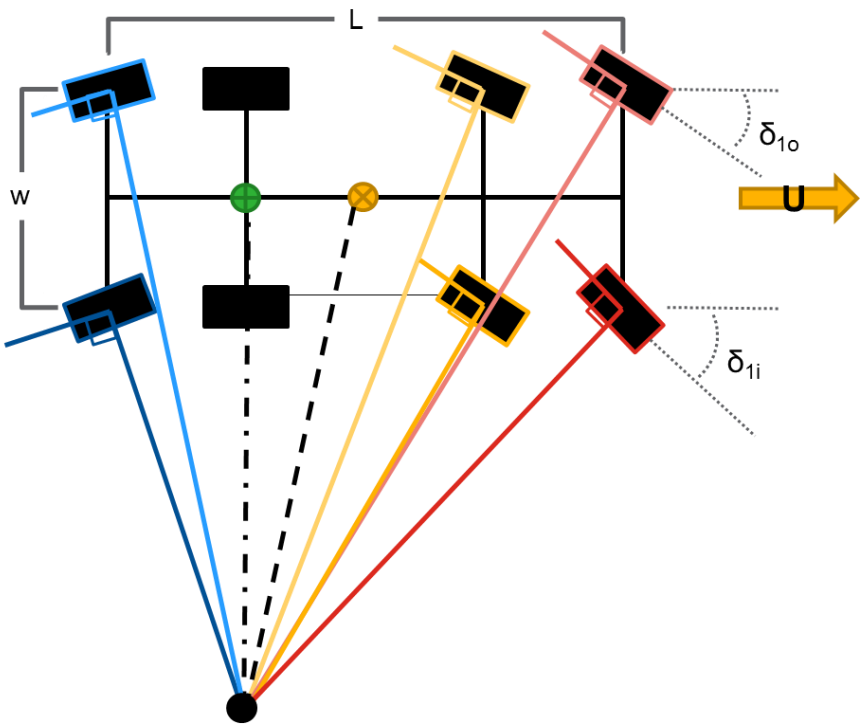

Figure 3-12 Ackermann Geometry for Fourth Axle Steered 8x8 Combat Vehicle

Figure 3-12 presents the modified Ackermann steering geometry for the fourth-axle steering configuration. The third axle is the stationary reference axle with which the instantaneous centre intersects. From this geometry, a ratio relating the fourth and first axle, k_{14}, is determined in a similar manner to k_{12}, using Equation 3-45.

3.5.1.2 All-Wheel Steering Model

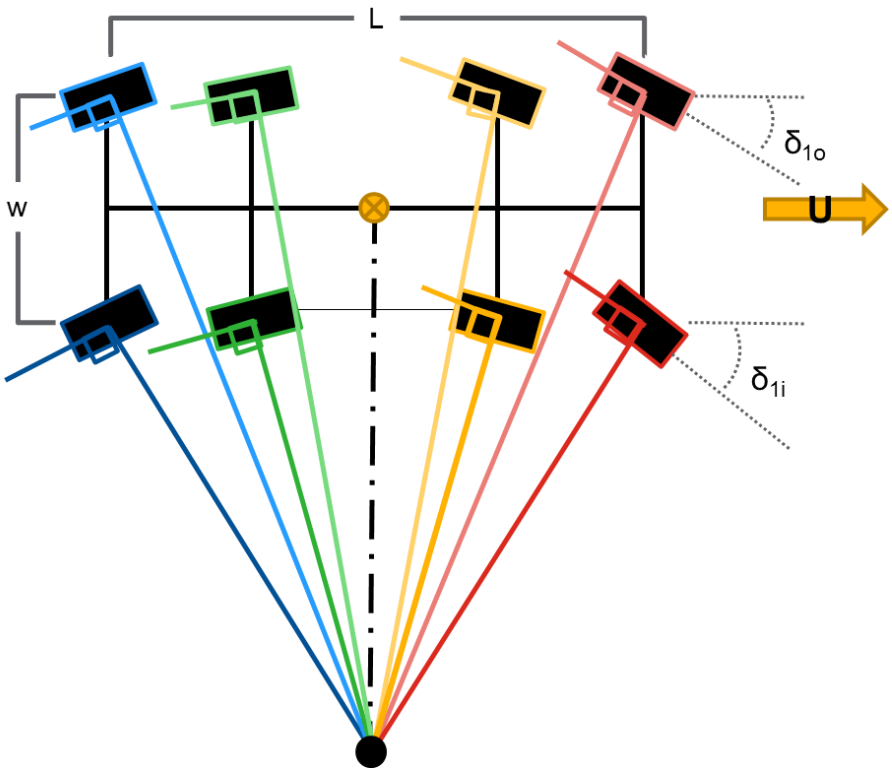

Figure 3-13 Ackermann Geometry for All-Wheel Steered 8x8 Combat Vehicle

Figure 3-13 presents the modified Ackermann steering geometry for the all-wheel steered configuration. As all wheels are steered, the centre of gravity serves as the intersection point for the instantaneous centre. From this, a ratio relating the second and third axles, k_{23} is determined in a similar manner described in the previous subsection, with Equation 3-45. A new ratio k'_{14} must also be determined to relate the first and fourth axle to account for the effect of the now active third axle. A ratio relating the third and fourth axle, k_{34} is also required from this geometry to be used in the process of deriving the function for active rear steering, outlined in the following section.

3.5.2 All-Wheel Steered Bicycle Model for Zero Side-Slip "Active" Rear Steering

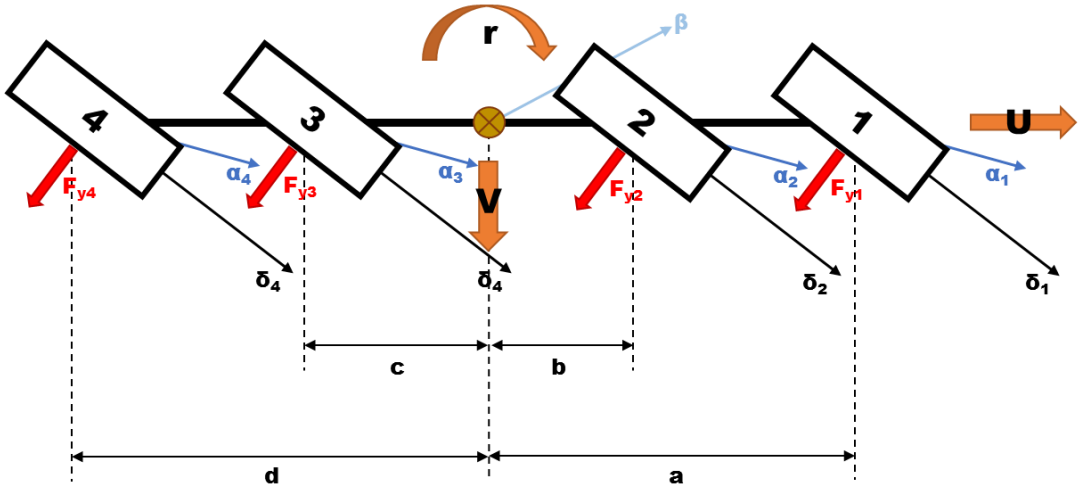

Figure 3-14 Bicycle Model for All-Wheel Steered 8x8 Combat Vehicle for Feedforward Zero-Side Slip Rear Steering Controller

To develop the active rear steering controller to minimize vehicle side slip β, a modified two-degree-of-freedom bicycle model is required in which all axles are steered. This model follows the same assumptions as outlined in 3.3.1.1 to maintain validity. The model is in steady state; thus, all transient terms are neglected and no external yaw moment is applied. With the introduction of a rear steering input, Equation 3-8 thus becomes;

$$\alpha_3 = \delta_3 - \left(\frac{V - cr}{U}\right) \quad \alpha_4 = \delta_4 - \left(\frac{V - dr}{U}\right) \tag{3-46}$$

To derive the active rear steering controller to relate the first axle to the fourth, the following relations must be introduced;

$$\delta_2 = k_{12}\delta_1 \quad \delta_3 = k_{43}\delta_4 \tag{3-47}$$

Where k_{12} is the fixed ratio relating the first and second axle, and k_{43} relates the third and fourth. These ratios are determined with the method outlined in Section 3.5.1, with the modified Ackermann geometry for all-wheel steering. With the substitution of Equation 3-46 and 3-47 into the original bicycle model in Section 3.3.1.1, the new equations of motion in steady state become;

$$m(Ur) = C_{\alpha1}\left[\delta_1 - \left(\frac{V+ar}{U}\right)\right] + C_{\alpha2}\left[k_{12}\delta_1 - \left(\frac{V+br}{U}\right)\right] + C_{\alpha3}\left[k_{43}\delta_4 - \left(\frac{V-cr}{U}\right)\right] + C_{\alpha4}\left[\delta_4 - \left(\frac{V-dr}{U}\right)\right] \quad \textbf{3-48}$$

$$0 = aC_{\alpha1}\left[\delta_1 - \left(\frac{V+ar}{U}\right)\right] + bC_{\alpha2}\left[k_{12}\delta_1 - \left(\frac{V+br}{U}\right)\right] - cC_{\alpha3}\left[k_{43}\delta_4 - \left(\frac{V-cr}{U}\right)\right] - dC_{\alpha4}\left[-\left(\frac{V-dr}{U}\right)\right] \quad \textbf{3-49}$$

Algebraic manipulation of the equations of motion in a similar fashion outlined in 3.3.1.2 yields the system in matrix form below;

$$\begin{bmatrix} \left(-\frac{C_{\alpha1}+C_{\alpha2}+C_{\alpha3}+C_{\alpha4}}{mU}\right) & \left(\frac{-aC_{\alpha1}-bC_{\alpha2}+cC_{\alpha3}+dC_{\alpha4}-U^2}{mU^2}\right) \\ \left(\frac{-aC_{\alpha1}-bC_{\alpha2}+cC_{\alpha3}+dC_{\alpha4}}{I_{zz}}\right) & \left(\frac{-a^2C_{\alpha1}-b^2C_{\alpha2}+c^2C_{\alpha3}+d^2C_{\alpha4}}{I_{zz}U}\right) \end{bmatrix} \begin{bmatrix} \beta \\ r \end{bmatrix} = \begin{bmatrix} \left\{-\left(\frac{C_{\alpha1}+k_{12}C_{\alpha2}}{mU}\right)\delta_1 - \left(\frac{C_{\alpha3}+k_{43}C_{\alpha4}}{mU}\right)\delta_4\right\} \\ \left\{-\left(\frac{aC_{\alpha1}+bk_{12}C_{\alpha2}}{I_{zz}}\right)\delta_1 - \left(\frac{cC_{\alpha3}+dk_{43}C_{\alpha4}}{I_{zz}}\right)\delta_4\right\} \end{bmatrix} \quad \textbf{3-50}$$

To obtain the ratio between first and fourth axles in which vehicle side slip is zero, the system of equations is solved to isolate for β, using the method below, in which

$$\beta = 0 = \frac{\begin{vmatrix} \left\{-\left(\frac{C_{\alpha1}+k_{12}C_{\alpha2}}{mU}\right)\delta_1 - \left(\frac{C_{\alpha3}+k_{43}C_{\alpha4}}{mU}\right)\delta_4\right\} & \left(\frac{-aC_{\alpha1}-bC_{\alpha2}+cC_{\alpha3}+dC_{\alpha4}-U^2}{mU^2}\right) \\ \left\{-\left(\frac{aC_{\alpha1}+bk_{12}C_{\alpha2}}{I_{zz}}\right)\delta_1 - \left(\frac{cC_{\alpha3}+dk_{43}C_{\alpha4}}{I_{zz}}\right)\delta_4\right\} & \left(\frac{-a^2C_{\alpha1}-b^2C_{\alpha2}+c^2C_{\alpha3}+d^2C_{\alpha4}}{I_{zz}U}\right) \end{vmatrix}}{\begin{vmatrix} \left(-\frac{C_{\alpha1}+C_{\alpha2}+C_{\alpha3}+C_{\alpha4}}{mU}\right) & \left(\frac{-aC_{\alpha1}-bC_{\alpha2}+cC_{\alpha3}+dC_{\alpha4}-U^2}{mU^2}\right) \\ \left(\frac{-aC_{\alpha1}-bC_{\alpha2}+cC_{\alpha3}+dC_{\alpha4}}{I_{zz}}\right) & \left(\frac{-a^2C_{\alpha1}-b^2C_{\alpha2}+c^2C_{\alpha3}+d^2C_{\alpha4}}{I_{zz}U}\right) \end{vmatrix}} \quad \textbf{3-51}$$

Since $\beta = 0$, further manipulation of Equation 3-51 above will yield;

$$\left\{-\left(\frac{C_{\alpha1}+k_{12}C_{\alpha2}}{mU}\right)\delta_1 - \left(\frac{C_{\alpha3}+k_{43}C_{\alpha4}}{mU}\right)\delta_4\right\}\left(\frac{-a^2C_{\alpha1}-b^2C_{\alpha2}+c^2C_{\alpha3}+d^2C_{\alpha4}}{I_{zz}U}\right) = \left\{-\left(\frac{aC_{\alpha1}+bk_{12}C_{\alpha2}}{I_{zz}}\right)\delta_1 - \left(\frac{cC_{\alpha3}+dk_{43}C_{\alpha4}}{I_{zz}}\right)\delta_4\right\}\left(\frac{-aC_{\alpha1}-bC_{\alpha2}+cC_{\alpha3}+dC_{\alpha4}-U^2}{mU^2}\right) \quad \textbf{3-52}$$

Finally, by rearranging all terms in Equation 3-52 above, the speed-dependent zero side slip ratio relating the first and fourth axles, $k_{14,\beta=0}$, is derived as shown below;

$$k_{14,\beta=0} = \frac{\delta_4}{\delta_1}$$

$$= \frac{\left[\left\{\left(\frac{aC_{\alpha1} + bk_{12}C_{\alpha2}}{I_{zz}}\right)\left(\frac{-aC_{\alpha1} - bC_{\alpha2} + cC_{\alpha3} + dC_{\alpha4} - U^2}{mU^2}\right)\right\} - \left\{\left(\frac{C_{\alpha1} + k_{12}C_{\alpha2}}{mU}\right)\left(\frac{-a^2C_{\alpha1} - b^2C_{\alpha2} + c^2C_{\alpha3} + d^2C_{\alpha4}}{I_{zz}U}\right)\right\}\right]}{\left[\left\{\left(\frac{C_{\alpha3} + k_{43}C_{\alpha4}}{mU}\right)\left(\frac{-a^2C_{\alpha1} - b^2C_{\alpha2} + c^2C_{\alpha3} + d^2C_{\alpha4}}{I_{zz}U}\right)\right\} - \left\{\left(\frac{cC_{\alpha3} + dk_{43}C_{\alpha4}}{I_{zz}}\right)\left(\frac{-aC_{\alpha1} - bC_{\alpha2} + cC_{\alpha3} + dC_{\alpha4} - U^2}{mU^2}\right)\right\}\right]}$$

3-53

Equation 3-53 is programmed into a feedforward function block within Simulink to generate an angle for the fourth axle. The same function is used to translate the ground wheel steer angle of the second axle into the third axle. Figure 3-15 shows output of Equation 3-53 within the total operating range of the combat vehicle from 0 to 80 km/h. Below 50 km/h, the system will steer the rear wheels in the opposite direction to the front. As speed gradually increases, the rear wheels will steer increasingly in the same orientation as the front.

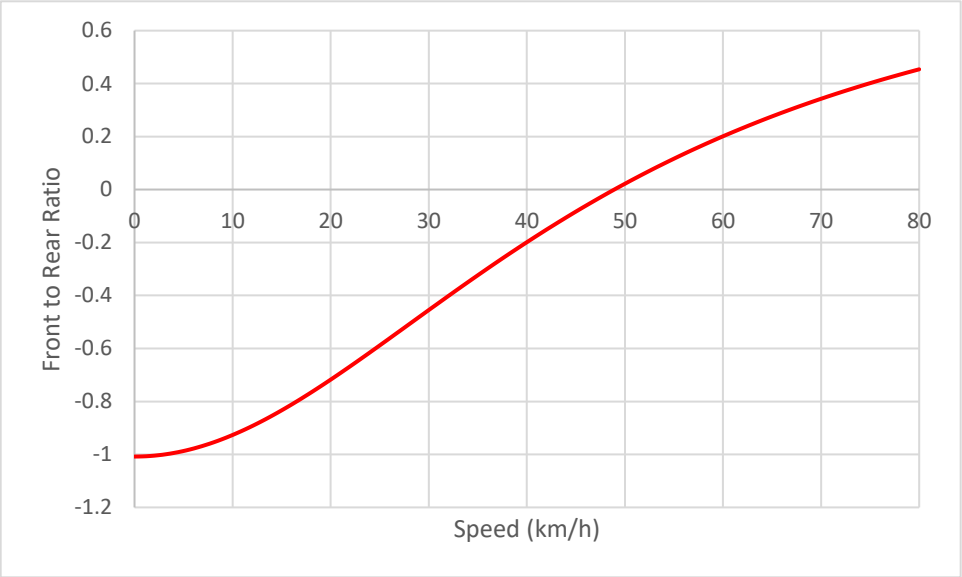

Figure 3-15 Speed-Dependent Variable Ratio of Front to Rear Wheel Steer Angle from 0 to 80 km/h

3.6 Chapter Summary

This chapter has outlined the simulation tools and control methodologies used in this work to model and evaluate the proposed vehicle drivetrain and its respective control systems. First, the TruckSim simulation environment and its key components used were outlined. Next, the roles of MATLAB and Simulink were outlined as a means of interaction with TruckSim for software-in-the-loop simulation.

The synthesis process for the active yaw controller – using the linear quadratic regulator method – is outlined in this chapter. However, two key vehicle models were first presented, which are used for the controller synthesis process;

- The reference two-degree-of-freedom bicycle model in which the front two axles are steered. From this model, equations of motion are derived to develop the state-space representation of the linear vehicle kinematics. This state-space representation is used for controller synthesis and for determining the desired steady-state gains for vehicle side slip and yaw rate.
- The differential lateral force tire model, which is a two-degree-of-freedom bicycle model with no steerable axles, used to determine the desired steady-state relationship between yaw rate and yaw moment about the center of gravity. This relationship is required for generating the feedforward skid steering controller and used as a tuning parameter for the active yaw controller.

Finally, both passive and active methods of rear steering control are discussed. A feedforward control method is developed for both passive fourth-axle and passive all-wheel steering using a modified Ackermann geometry. Using the geometry for each respective rear steering method, fixed ratios relating front wheel steer angles to the rear are determined. A feedforward control method for active rear steering is developed, which relies upon vehicle speed to determine the ratio and orientation in which the rear axles are steered with respect to the front. Development of the active rear steering controller required a steady-state bicycle model in which all axles are steered and vehicle side slip is assumed to be zero.

CHAPTER 4
COMPREHENSIVE VEHICLE CONTROL ARCHITECTURE

4.1 Introduction

This chapter serves to outline the final design and function of the vehicle control system as well as its individual components for the proposed electric powertrain. Figure 4-1 presents the interaction between the controllers modeled in Simulink with the vehicle operating in the test environment on TruckSim.

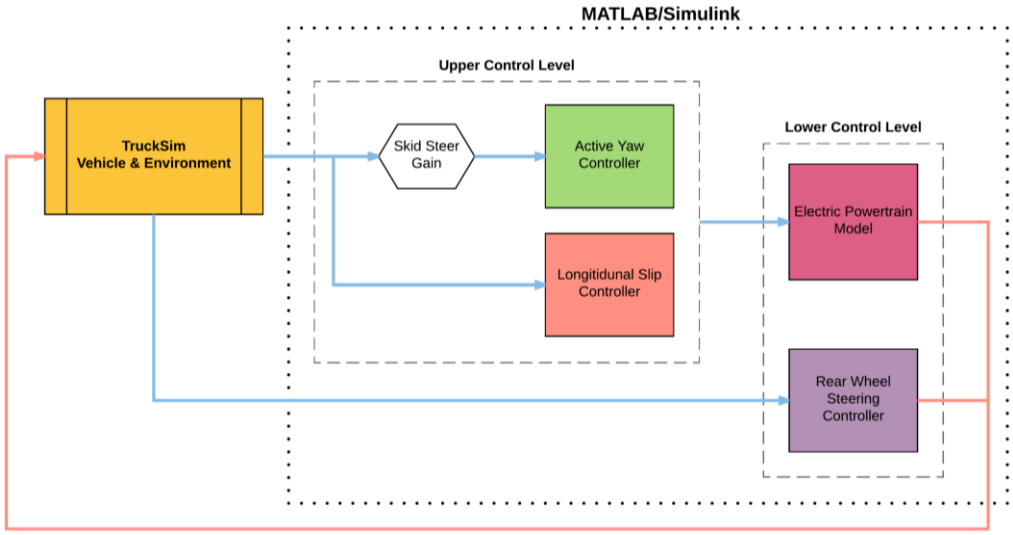

Figure 4-1 Software-in-the-Loop Interaction of TruckSim and Simulink

TruckSim provides general driver and vehicle operation data (represented by blue lines) throughout a test procedure, which is then used by each of the controllers implemented through Simulink. Processed data from the controllers (represented by red lines) are then sent back to TruckSim in the form of vehicle actuations, i.e. wheel torque and wheel steer angles. For organizational purposes, the controllers are categorized into upper and lower levels. The upper level is responsible for accepting raw vehicle data to process control actions for improving vehicle performance. This consists of the forward speed controller and unified stability controller. The lower level is responsible for translating the control actions from the upper level into vehicle actuations. This consists of the wheel torque distribution system, rear steering controller and electric motor models.

4.2 Upper Level Control Architecture

4.2.1 Forward Speed Controller

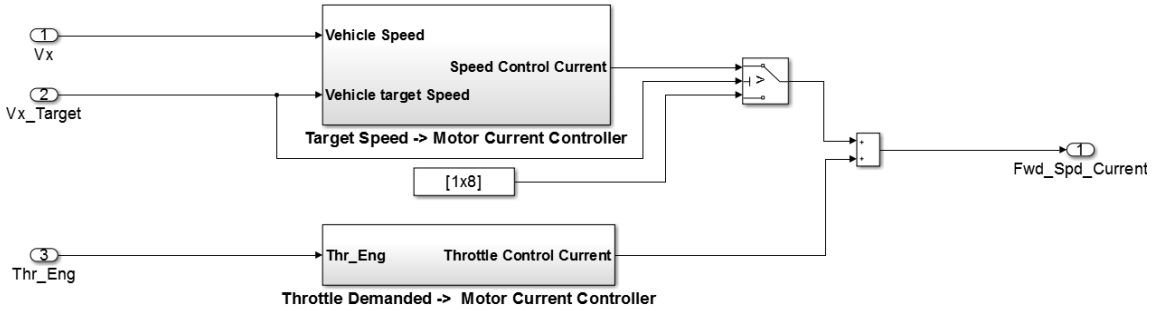

Figure 4-2 Forward Speed Controller in Simulink

Figure 4-2 presents the internal architecture of the forward speed controller. To regulate vehicle forward speed, a simple PD controller is implemented in parallel with an open-loop throttle controller. Depending on the simulation scenario, either controller will be activated through a conditional switch.

If a constant target speed is not set through the TruckSim environment, the switch disables the PD controller and enables the open-loop throttle control. From this, throttle input is read from the internal TruckSim driver model, which ranges from 0% (no throttle) to 100% (full throttle). The percentage throttle input is then multiplied by the maximum input motor current and sent equally to all eight wheels via the wheel torque distribution system.

If a constant target speed is set, the TruckSim environment will output a zero-throttle signal to the open-loop controller, thus leaving it inactive. Target speed and actual vehicle speed are read as signals from the TruckSim environment to generate an error signal for the PD controller. The PD controller was tuned using a simple maneuver in TruckSim to output an appropriate control action in the form of motor current, ranging up to the maximum input specification. Regardless of operation mode, the speed controller delivers the mean forward driving current equally to each wheel in the torque distribution system.

4.2.2 Unified Stability Control System

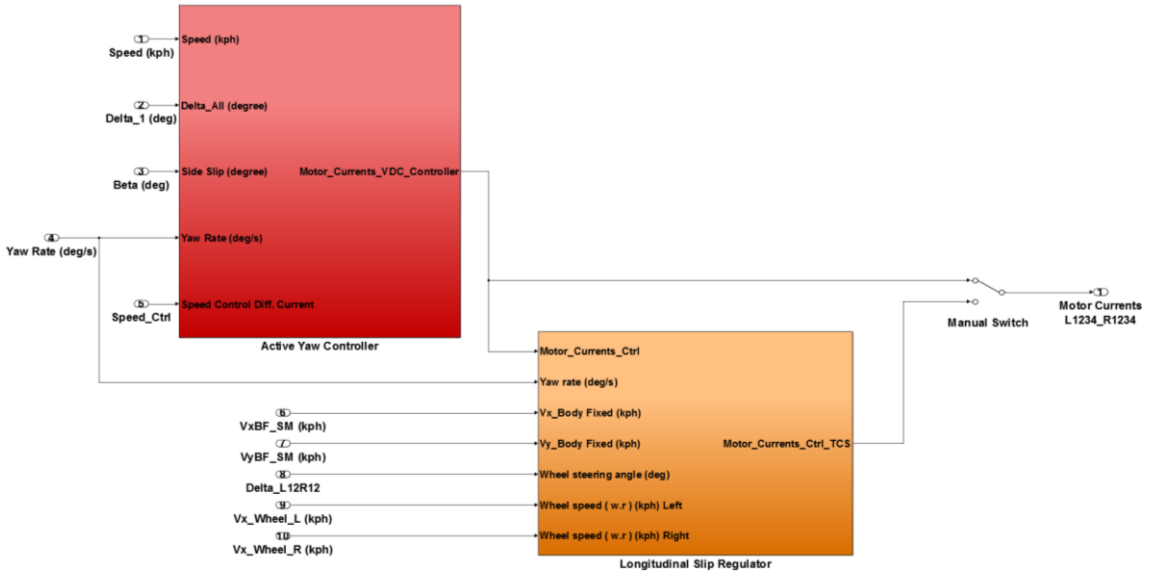

Figure 4-3 Unified Stability Control System in Simulink

Figure 4-3 presents the internal architecture of the unified stability control system, which includes the active yaw controller (in red) and longitudinal slip controller (in orange). A manual switch is present within the system to bypass the slip controller for when skid steering mode is enabled, since longitudinal slip is crucial to generate the required yaw motion. Interference of the slip controller is undesirable in skid steering mode as it would prevent power delivery to the motors.

For comprehensive operation, the unified stability controller requires that the following data be actively monitored: vehicle speed, steering angle, vehicle side slip, yaw rate, longitudinal body velocity and individual wheel angular velocities. While the wheel torque distribution system is housed within the active yaw controller block, it is still considered a component of the lower level as it translates higher-level control action into vehicle actuation, i.e. motor current.

4.2.2.1 Active Yaw Controller

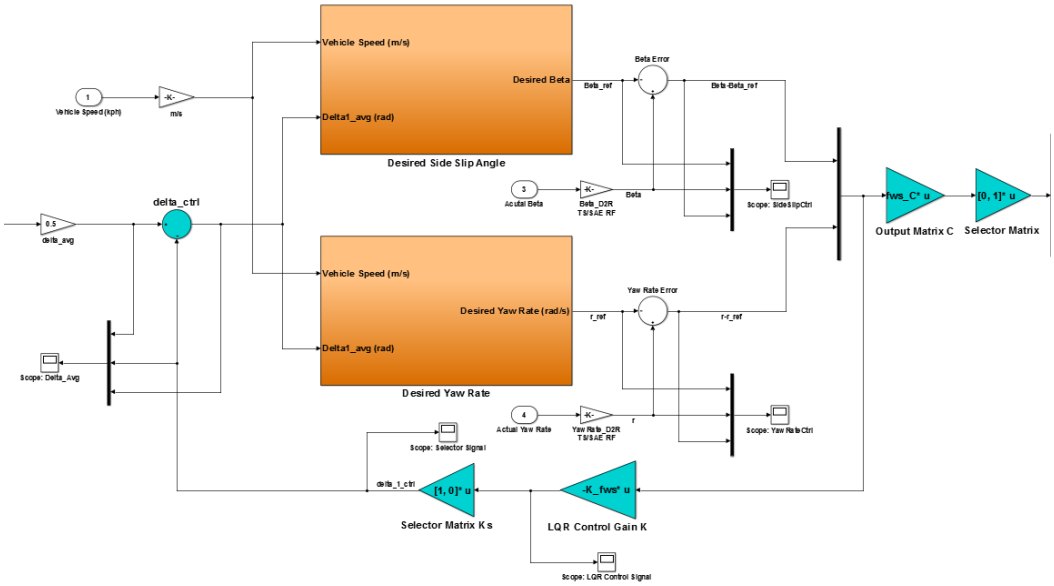

Figure 4-4 Active Yaw Controller in Simulink

Figure 4-4 above presents the internal architecture of the active yaw controller, which is modeled using the linear quadratic regulator (LQR) control method and architecture discussed in Section 3.4.

Vehicle speed and steering angle are required for determining the reference yaw rate and vehicle side slip. These values calculated using the reference two-degree-of-freedom bicycle model of the combat vehicle, as outlined in the previous chapter. The orange blocks in the diagram are functions built on the vehicle side slip gain and yaw rate gain, modeled by Equations 3-24 and 3-26, respectively. Actual yaw rate and vehicle side slip are taken from the operational vehicle within the TruckSim environment, and the difference between actual and reference values are used to calculate an error. This portion of the architecture represents the state-space matrix *A* in the standard LQR control form presented in the previous chapter, with the effective output *x* being the state error.

The LQR control gain, *K*, is a matrix that is continuously updated by an external function block which calls the **lqr** function. Within the external function block are the state-space model and tuning parameters which are built from the reference two-degree-of-freedom bicycle model. These are required by the **lqr** function to generate the control gain

matrix. The resulting control gain is continuously changed by the constantly updated tuning parameters that are based on the speed of the vehicle and road surface friction conditions. The control gain matrix is placed in negative feedback with the entire system such that the result of multiplying the error state by the control gain is subtracted from the input steering angle, which would represent u in the LQR control form. This completes the cyclic architecture of the LQR feedback control system. The resulting control output, y, is achieved by multiplying the controlled error state by the output matrix C, which then gives the required external yaw moment, M_Z, to be used by the wheel torque distribution system.

4.2.2.2 Longitudinal Slip Regulation

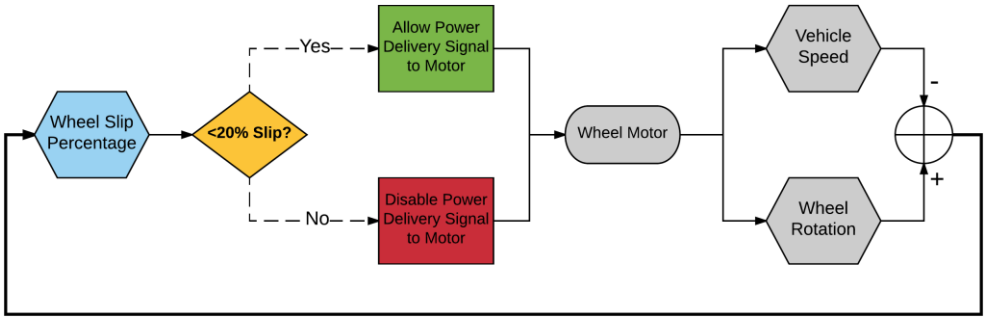

Figure 4-5 Flow Diagram of Longitudinal Slip Regulation Process

Figure 4-5 presents the logical operation for the longitudinal slip controller. The controller is a switch that regulates power delivery to individual motors based on the longitudinal slip of each wheel. The longitudinal slip percentage is continuously calculated using vehicle body speed and individual wheel angular velocities. The longitudinal slip percentage is continuously calculated using vehicle body speed and individual wheel angular velocities. If longitudinal slip for a single wheel exceeds 20%, then the power delivery signal to that wheel is disabled. The switch threshold was set to be 20% because tires maintain maximum tractive force F_X within a range of 15% to 20%. This allows other non-slipping wheels to stabilize the vehicle. Power delivery will once again be restored should the previously unstable wheels regain traction as they slow down to an acceptable level.

4.3 Lower Level Control Architecture

4.3.1 Wheel Torque Distribution

The wheel torque distribution system operates in two stages. The first is to calculate a differential motor current using external yaw moment from the upper level controllers. Next, it adds the mean driving current from the forward speed controller to distribute a respective current to each independent wheel motor. In the first stage, wheel torque is calculated for a single wheel using Equation 4-1 below;

$$T_w = \left(\frac{2M_Z}{b}\right)\left(\frac{1}{j}\right) r_{eff} \qquad \textbf{4-1}$$

Where T_W is the torque for a single wheel, N is the external yaw moment to be applied to the vehicle, b is the track width of the vehicle measured from the center of the left tire to the center of the right, r_{eff} is the effective tire rolling radius and j is the total number of axles on the vehicle. From this equation, the required differential current can be calculated from the following relation;

$$i_{motor,diff} = \frac{\left(\frac{T_w}{n_{motor}}\right) \times \omega_{wheel}}{V_{motor}} \qquad \textbf{4-2}$$

Where ω is the angular velocity of the single wheel, in radians, as taken from the TruckSim environment data, n_{motor} is the provided gear reduction of the in-wheel hub motor and V_{motor} is the operating voltage of the motor. The motor currents are distributed to the left and right sides as such.

$$i_{left} = i_{motor,mean} + i_{motor,diff} \qquad \textbf{4-3}$$

$$i_{right} = i_{motor,mean} - i_{motor,diff} \qquad \textbf{4-4}$$

This maintains compatibility with the SAE tire coordinate system upon which the active yaw controller was developed, where clockwise yaw motion is reference positive.

4.3.2 Electric Powertrain

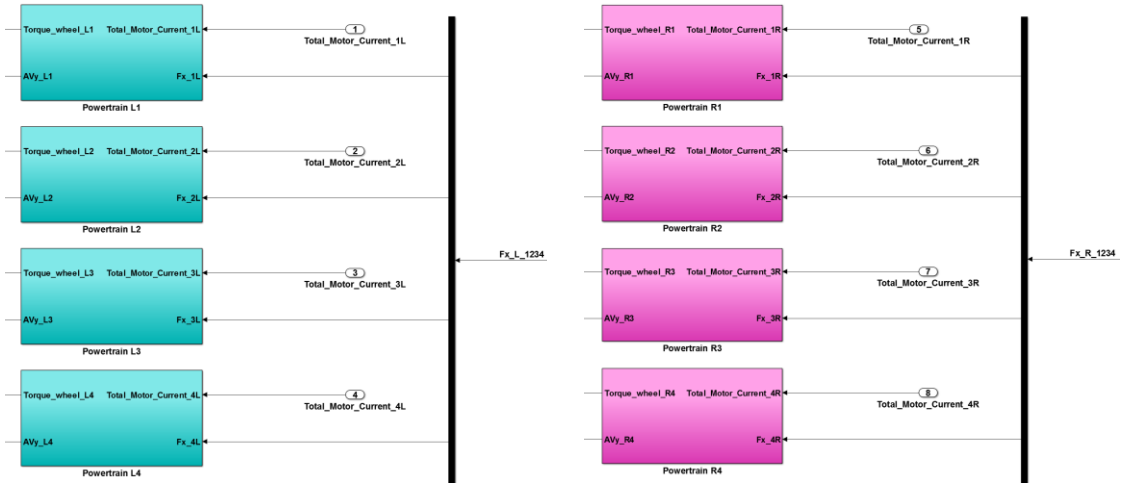

(a) **(b)**

Figure 4-6 Left Side Electric Motors (a) and Right Side Electric Motors (b)

Figure 4-6 presents the complete powertrain layout consisting of eight independent wheel motors, as modeled in Simulink. The function and derivation of the motor model is discussed in Section 3.2.2.1. During all operating tests, the vehicle is assumed to be operating under ideal power delivery conditions, meaning that the battery used to power the motors is at full capacity and gradual discharge has no effect on performance. Modeling of a full battery system and effects of discharging on vehicle operation performance are not within the scope of this work.

The implementation of eight independent motors eliminates the need for a mechanical differential, as torque vectoring can be achieved through electronic control and applied using every wheel, as done in this work. Consequently, this configuration allows for much easier implementation of skid steering due to the greatly reduced mechanical complexity. Electronic control of independent motors allows for flexibility in programming characteristic torque distribution as it provides a platform for various control systems to be applied. To implement different control systems for a new torque distribution or driving mode using a conventional powertrain would require an extensive mechanical overhaul, which is eliminated by this design.

4.3.3 Supplementary Rear Steering Control Methods

For testing purposes, each system is implemented in separate vehicle models due to the conflicting nature of each rear steering control method. Each vehicle is equipped with the same control system components as previously discussed, differing only in rear steering method. While the rear steering controller is considered a part of the lower level control architecture, its operation is independent of other controllers and is in direct feedback communication with the TruckSim environment through Simulink. Lookup tables for the first and second axle steering configurations determine the wheel angles which are sent to Simulink via software-in-the-loop. The rear steering controllers then send back the corresponding rear wheel steer angles.

4.3.3.1 Passive (Fixed Ratio) Rear Steering

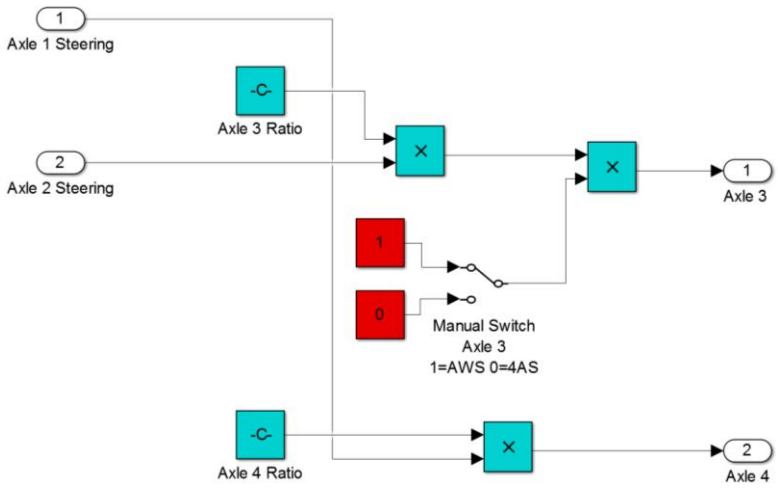

Figure 4-7 Passive (Fixed Ratio) Feedforward Rear Steering Controller in Simulink

Figure 4-7 presents the internal architecture of the passive rear steering system. Through this system, steering angles from the front two axles are translated directly into corresponding rear steering angles using fixed ratios. These fixed ratios were determined using modified Ackermann steering geometries, as outlined in Section 3.5.1. The first axle is related with the fourth, and the second axle with the third. A manual switch is present to turn off steering in the third axle for testing purposes.

4.3.3.2 Active (Zero Side-Slip) Rear Steering

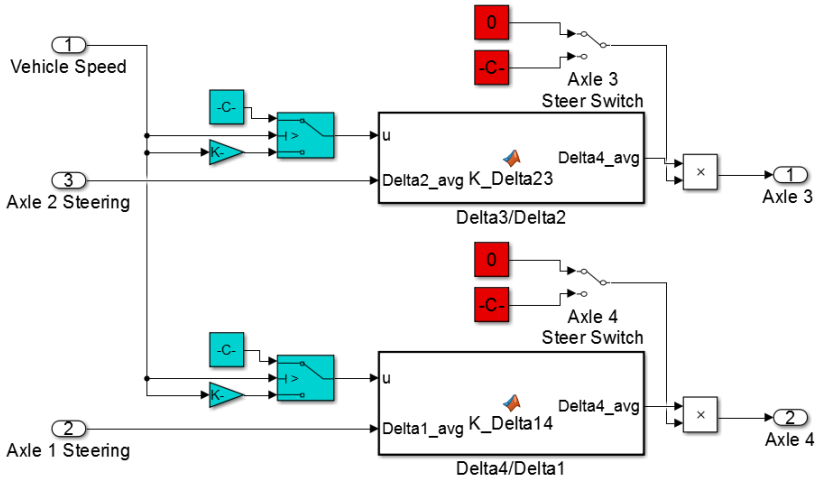

Figure 4-8 Active (Zero Side-Slip) Feedforward Rear Steering Controller in Simulink

Figure 4-8 presents the internal architecture of the active rear steering system. In this system, speed is used to determine the ratios between front and rear axles. The first axle is related to the fourth axle and the second axle is related to the third axle like the passive system. Custom-programmed blocks are used to manually implement the speed-dependent variable ratio for each rear axle, which is defined by Equation 3-53.

At lower speeds, the active system will steer the rear wheels in the opposite orientation to the front to reduce turning radius for tighter cornering. At higher speeds, the active system will steer the rear wheels in the same orientation as the front to favor vehicle stability. Like with the passive system, left and right wheel steering angles are obtained from the TruckSim environment and sent back accordingly for rear steering. A manual switch is also present for testing purposes to disable both third and fourth axle steering capabilities, as this model is also used for front-wheel steered mode with the unified stability controller.

4.4 Skid Steering Mode

Due to the flexibility of the powertrain and control structure, very few changes were needed within the vehicle model to implement skid steering. In skid steering mode, all mechanical forms of steering are disabled and all axles are locked straight as yaw motion is generated through differential torque. Longitudinal slip control is also disabled to prevent the motors from being turned off in skid steering mode, as wheel slip is a necessity in this mode.

4.4.1 Autonomous Drive Control Unit

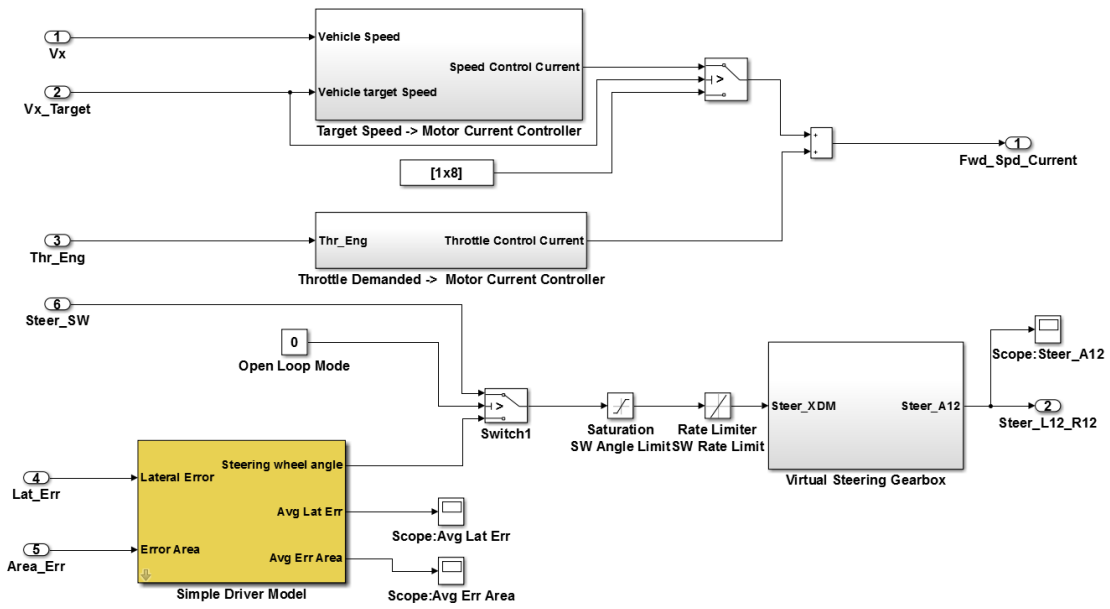

Figure 4-9 Autonomous Drive Control Unit in Simulink

Figure 4-9 presents the internal architecture of the autonomous drive control unit used specifically for skid steer mode. This control unit consists of three key components – the previously discussed forward speed controller, an external driver model and a virtual steering gearbox. This control unit serves to override both the virtual "human" driver and the mechanical steering system found within the TruckSim environment by performing the functions of throttle input and maneuvering externally.

4.4.1.1 External Driver Model

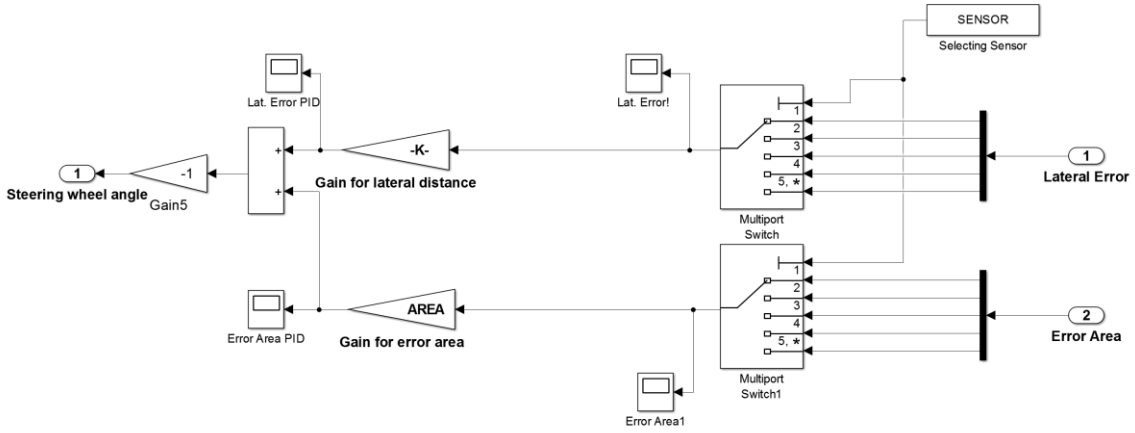

Figure 4-10 Proportional-Integral (PI) External Driver Model in Simulink

Figure 4-10 presents the internal architecture of the external driver model used in the autonomous drive control unit. The driver model is a proportional-integral (PI) controller which relies on lateral distance error and area error data. The external driver model serves to simulate the high-level integrated navigation functions of GPS-LIDAR or GPS-camera units used in [57].

This data is obtained from the TruckSim environment in which sensors are enabled within the vehicle and test procedure. Five sensors are available within TruckSim to be programmed to corresponding preview points when placed in front of or behind the vehicle. Using tuned proportional and integral gains that correspond to lateral distance and area error, respectively, the external driver model generates a steering wheel angle which is used by the virtual steering gearbox to generate an artificial ground wheel angle.

4.4.1.2 Virtual Steering Gearbox

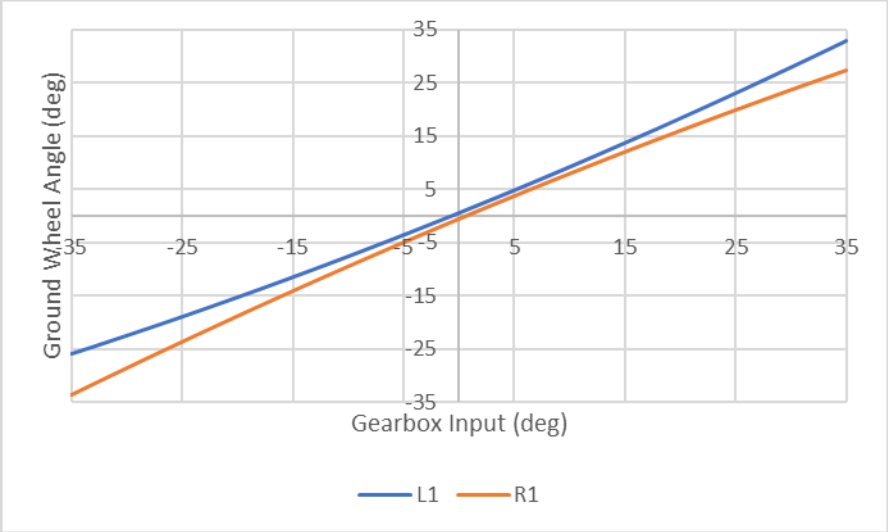

Figure 4-11 Wheel Steer Angle Data for First Axle

The purpose of this component is to override the mechanical steering actuators by using a steering wheel angle – generated either by a human driver or in this scenario, the path-following external driver model – to create an artificial ground wheel angle while the physical axles are locked. The ground wheel angle is then sent to a torque distribution system – of which two are available in this work for comparison purpose – to ultimately translate into a differential torque output through the electric powertrain. This effectively establishes skid steering mode as a drive-by-wire system.

To create an artificial ground wheel angle, the virtual steering wheel angle provided by the driver model is multiplied by the steering gearbox reduction – which in this case is the same as the mechanical system in the reference conventional combat vehicle used in this work. The reduced steering wheel angle is then forwarded to four lookup tables that represent the relationship between ground wheel angle and steering gearbox input for each of the four front wheels. The resulting ground wheel angles are averaged between left and right wheels for each axle, then sent to the torque distribution system. The relationship for each wheel was previously determined by [6] using a standard Ackermann steering geometry for the reference combat vehicle, and extracted from TruckSim. Figure 4-11 is an example of a wheel steer angle lookup table.

4.4.2 Feedforward Differential Torque Distribution System

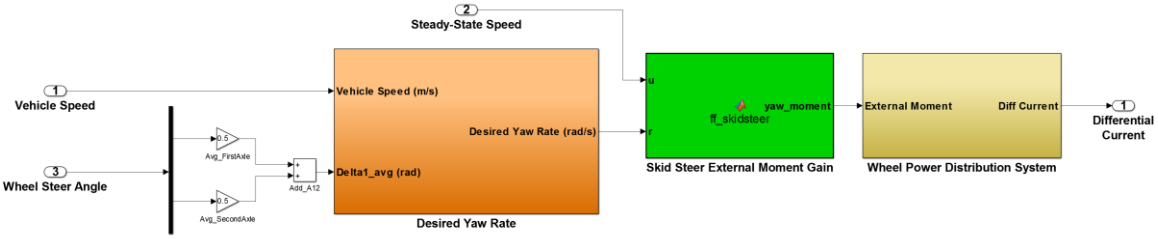

Figure 4-12 Feedforward Differential Torque Distribution System in Simulink

Figure 4-12 presents the basic layout of the feedforward torque distribution method implemented in Simulink. This system is an extremely simplified method intended to mimic a fixed mechanical double differential system used in existing conventional skid steered vehicles. For testing purposes, this system is used in a separate simulation model as a reference vehicle when compared to a vehicle using the optimal torque distribution system. All other components including the autonomous drive control unit and electric powertrain remain unchanged. The system directly translates vehicle speed and ground wheel angle provided by the autonomous drive control unit into a differential current to be delivered to the left and right side wheel motors.

Using vehicle speed and ground wheel angle, a yaw rate is determined using the yaw rate gain developed from the two-degree-of-freedom bicycle model outlined in the Section 3.3.1. No feedback control is present; hence the actual yaw rate of the vehicle is not monitored by the control system. Yaw rate and vehicle speed are then provided to a custom function which generates external yaw moment. Programmed within the custom function is the external moment gain developed from a separate bicycle model outlined in Section 0. As with the other control systems, the wheel torque distribution system is used to translate external yaw moment into individual wheel motor currents.

4.4.3 Optimal Differential Torque Distribution System

The optimal torque distribution system harnesses the active yaw controller – found in the upper level architecture of the general control system – by activating a pre-compensation gain similar to what is used in fly-by-wire aircraft control systems. Its placement within the general control architecture is outlined in Figure 4-1 at the beginning of the chapter. The pre-compensation gain is a constant, tunable multiplier that amplifies the ground wheel angle input received from the autonomous drive control unit, before being provided to the active yaw controller. This effectively amplifies the differential current signal sent to all wheels, while simultaneously reducing the steering input effort required by the driver or drive control unit.

In this work, the pre-compensation gain is manually tuned with respect to the vehicle and employed driver model over a standard simple test maneuver in the TruckSim environment. The PI simple driver model with gains tuned for the feedforward system is also used for this optimal system to eliminate the driver as a source of variance in testing, when comparing vehicle performance. The pre-compensation gain was tuned in a similar fashion to proportional controller tuning, in which a critical value was obtained where continuous oscillation was observed in the steering input signal. From the critical gain value, further adjustments were made until both no oscillations were observed and a reasonable range of steering wheel angle input for the maneuver was achieved. The steering wheel angle input from this vehicle was validated against that of a conventionally-driven combat vehicle using the internal TruckSim virtual driver model performing the same test maneuver used for tuning.

4.5 Chapter Summary

This chapter discussed the overall architecture of the control system and its individual components. The upper and lower levels and their respective roles are elaborated upon, as well as the implementation of skid steering using the existing layout.

The upper level control architecture consists of the forward speed controller and unified stability control system. The forward speed controller generates driving motor current which is sent to all wheels. The controller was design to accept a variable throttle command as a percentage of the maximum operating current of the motor. Alternatively, a PI speed controller can be used to maintain a provided constant target speed. The unified stability control system contains the active yaw controller and the longitudinal slip regulator, which work in parallel to improve vehicle stability and handling. The active yaw controller monitors vehicle side slip and yaw rate to generate an external yaw moment. The longitudinal slip regulator monitors wheel slip and regulates power delivery to individual wheels to prevent excessive slip.

The lower level control architecture consists of the wheel distribution algorithm, rear steering controller and the electric powertrain. The wheel distribution algorithm translates the external yaw moment from the active yaw controller into differential motor current to be delivered to the electric motors on opposing sides of the vehicle. The rear steering controller is a feedforward control system which translates wheel steer angles from the front axles to the rear axles. Active and passive rear steering is implemented in separate vehicles, otherwise using the same upper and lower level control architectures.

Finally, skid steering harnesses the existing lower level control architecture in two separate vehicle simulation models, for comparison. The reference vehicle used for skid steering uses a feedforward control system, and is compared to another which harnesses the active yaw controller through a pre-compensation scaling factor to amplify generated external yaw moment per degree of driver input at the steering wheel. Both vehicles use the same autonomous drive control unit which contains the forward speed controller and a PI driver model for path following using sensors within the TruckSim environment.

CHAPTER 5
LOW-SPEED OPERATION TESTING

5.1 Chapter Introduction

This chapter summarizes the results of all tests conducted on the electric combat vehicle in low-speed operation mode. All tests in this chapter evaluate autonomous skid steering control methods against the reference conventional vehicle on speeds of 40 km/h and below. Despite focusing on autonomous control, conclusions for these tests will also be drawn from a manned driving perspective. Table 5-1 below outlines the terminologies used to refer to the vehicle configurations throughout the chapter to simplify reading.

Table 5-1 Abbreviations for Test Vehicles for Low-Speed Operation

TERMINOLOGY	VEHICLE CONFIGURATION
Reference	Internal Combustion Engine w/ Conventional Steering (Axles 1&2)
FF	Skid Steering via Direct Feedforward Torque Control
AYC	Skid Steering via LQR Active Yaw Controller

Table 5-2 below outlines the entire gauntlet of tests performed in this chapter, including respective operating speeds, road conditions and vehicles used in the test. Respective chapter sections for each test are also provided in the table.

Table 5-2 Summary of Tests and Conditions for Low-Speed Operation

LOW-SPEED OPERATION TEST PLAN		
Test Procedure	**Vehicles Used**	**Conditions**
5.3 Sine Wave Path – Ideal Friction	FF AYC	20 km/h, 40 km/h Flat, μ=0.85
5.4 Sine Wave Path – Low Friction	FF AYC	20 km/h, 40 km/h Flat, μ=0.35
5.5 Sine Wave Path – Off-Road	AYC Reference	30 km/h Off-Road (ISO 8608 - E), μ=0.4

5.2 Sine Wave Path (for External Driver Model use with Skid Steering)

This test procedure is a readily-available maneuver within the TruckSim test environment which is intended for tuning a simple PI driver model on various vehicles. The procedure comes equipped with configurable sensors which are built into the TruckSim test environment. The sensors can be adjusted using vehicle preview distance to determine lateral error and error area for the PI driver model. The sine wave path features a lateral amplitude of 15.4 m and longitudinal period of 160 m, as shown below in Figure 5-1(a).

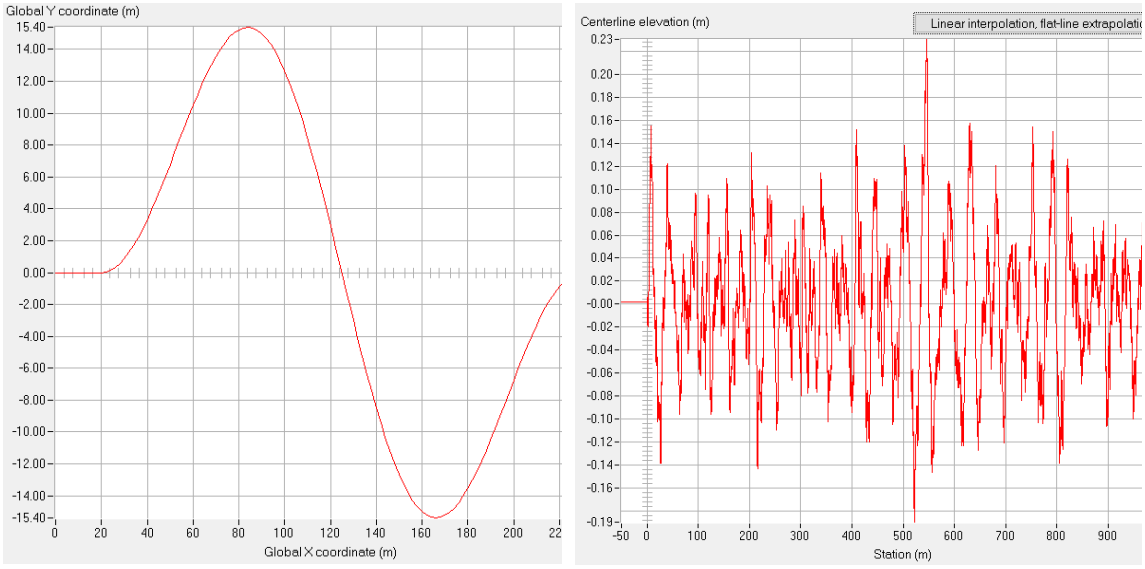

(a) **(b)**

Figure 5-1 Top View of Path (a) and ISO 8608 Class E Roughness Profile (b)

The sine wave path maneuver is primarily used for skid steering tests to evaluate maneuverability and stability at 20 km/h and 40 km/h over normal surface friction (coefficient of 0.85) and reduced friction (coefficient of 0.35). Skid steering mode is then compared to conventional steering over off-road and reduced friction conditions. To simulate off-road conditions, a road roughness profile is generated using MATLAB code designed around ISO 8608 standards and modeling methods as presented in [82] [83] [84]. For this work, a class E road was generated using the custom MATLAB code and validated through published literature. The final generated roughness profile, shown in Figure 5-1(b) above, was imported into the TruckSim environment for testing.

5.3 Skid Steering on Ideal Surface (μ=0.85)

Initial testing for the combat vehicle operating in skid steer mode is performed using the sine wave path maneuver with ideal conditions, that is, a flat surface and a nominal surface friction of 0.85. Testing is performed between a vehicle with feedforward torque distribution system (termed "FF" in Table 5-1) and a vehicle with modified active yaw control system (termed "AYC" in Table 5-1) at 20 and 40 km/h.

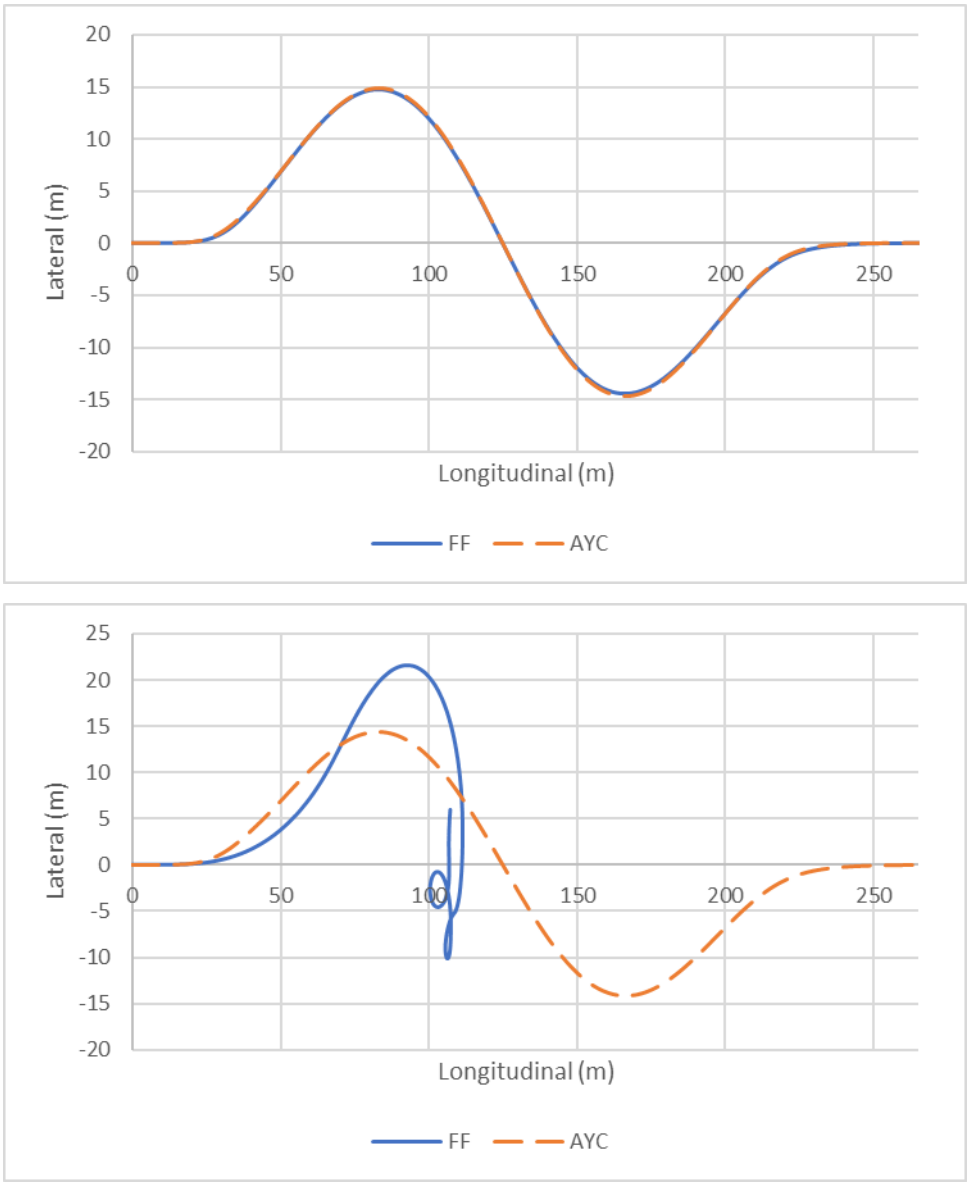

Figure 5-2 Vehicles Paths at 20 km/h (a) and 40 km/h (b) on Ideal Surface

Figure 5-2(a) shows the paths of both skid steering vehicles at 20 km/h, while Figure 5-2(b) shows the paths at 40 km/h. Both FF and AYC skid steered vehicles successfully complete the maneuver at 20 km/h, with negligible difference. At 40 km/h, the FF vehicle is unable to maintain the path and spins out, while the AYC vehicle successfully maintains its path.

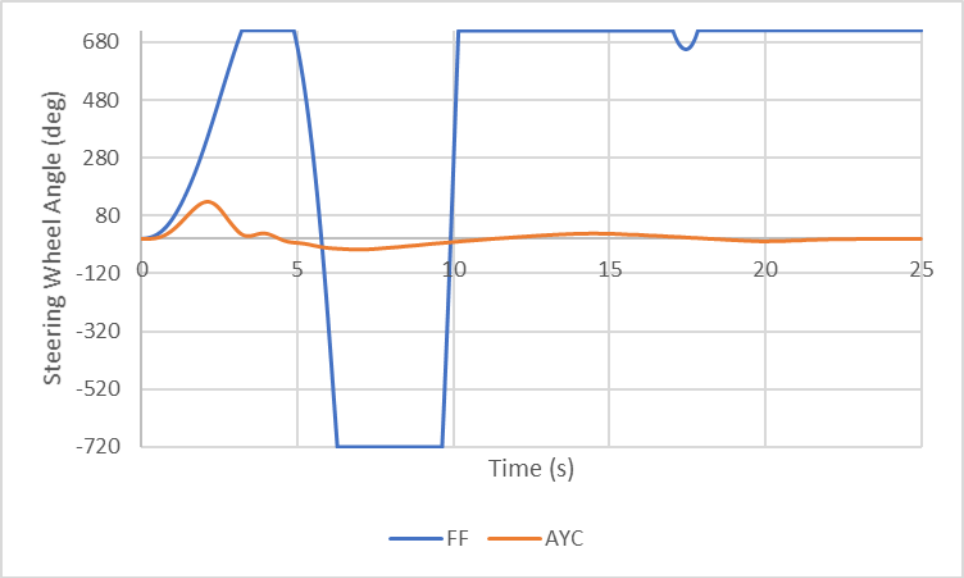

Figure 5-3 Driver Model Steering at 40 km/h on Ideal Surface

Figure 5-3 above shows the steering wheel angle generated by the external driver model used for both vehicles at 40 km/h. On the FF vehicle, the external driver model consistently locks up the steering wheel at the operational maximum of 720 degrees, attempting to correct vehicle motion. Meanwhile, the AYC vehicle does not exceed 150 degrees. This lock-up saturates the torque distribution controller as exhibited in Figure 5-4(a), below. Due to the pre-compensation factor of the active yaw controller, the AYC vehicle can maintain a stable torque distribution due to reduced output from the external driver model as shown in Figure 5-4(b), below, since the driver model does not lock the wheel. For brevity, the wheel torque distribution trends of the vehicles at 20 km/h are not displayed, as they are generally stable and do not saturate. From this, 40 km/h is the recommended maximum speed at which the AYC skid steered vehicle can operate over an ideal surface, to be just below critical stability for the driver model.

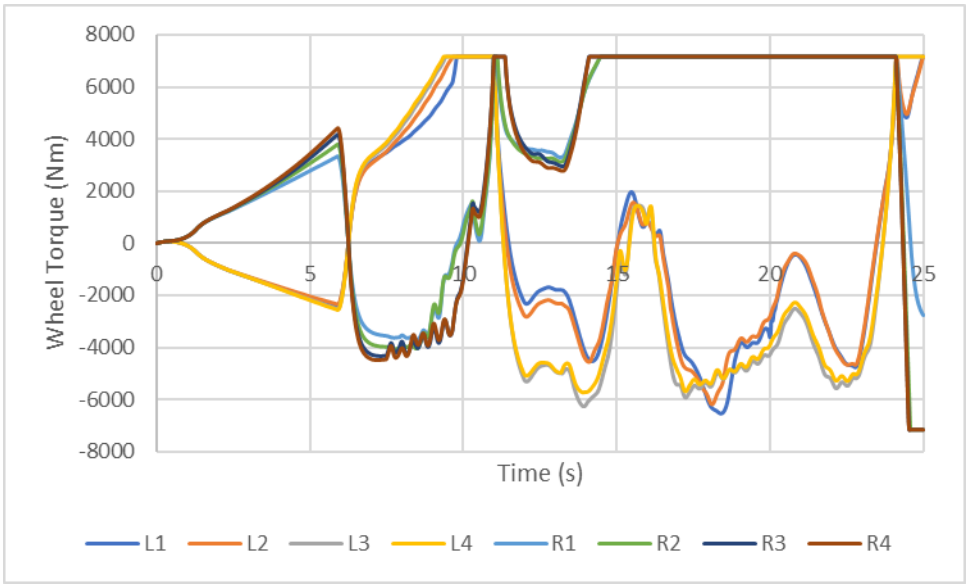

(a)

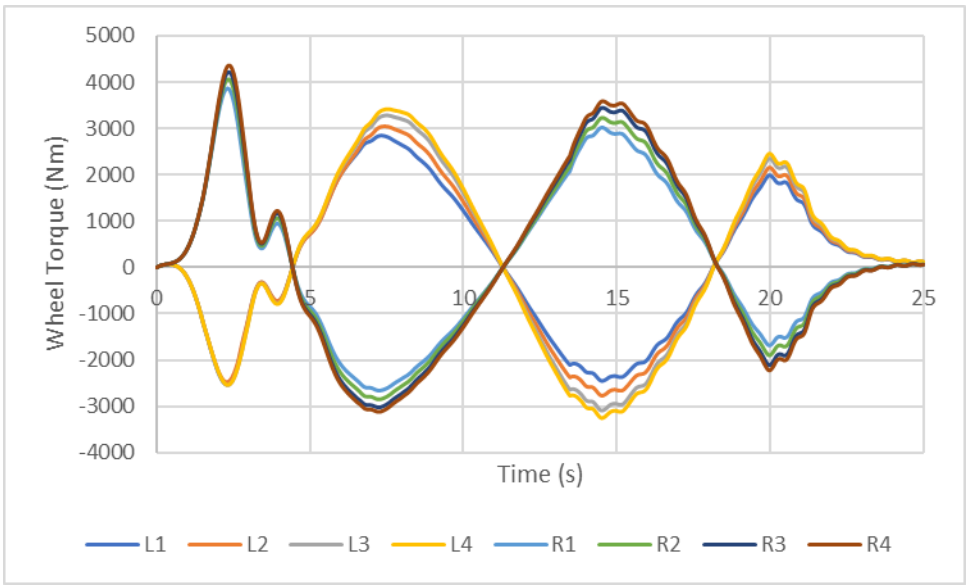

(b)

Figure 5-4 Wheel Torque Output at 40 km/h for (a) FF and (b) AYC vehicles

The following data presented in Figure 5-5 below are the performance measures of the two skid steered vehicles. Yaw rate, lateral acceleration and vehicle side slip are presented for the 40 km/h test. Performance measures at 20 km/h are omitted since both vehicles nearly identical, with the FF vehicle exhibiting small oscillations. This indicated that in the FF vehicle, the driver model operation is close to critical stability at 20 km/h.

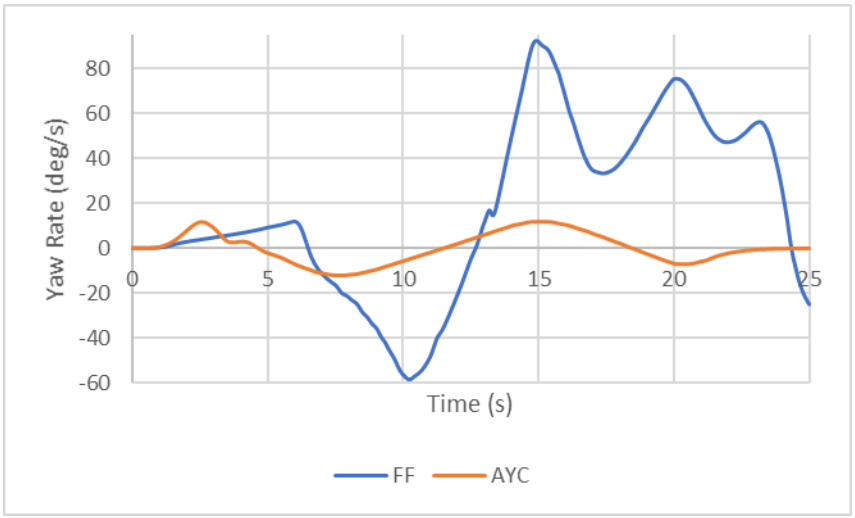

(a)

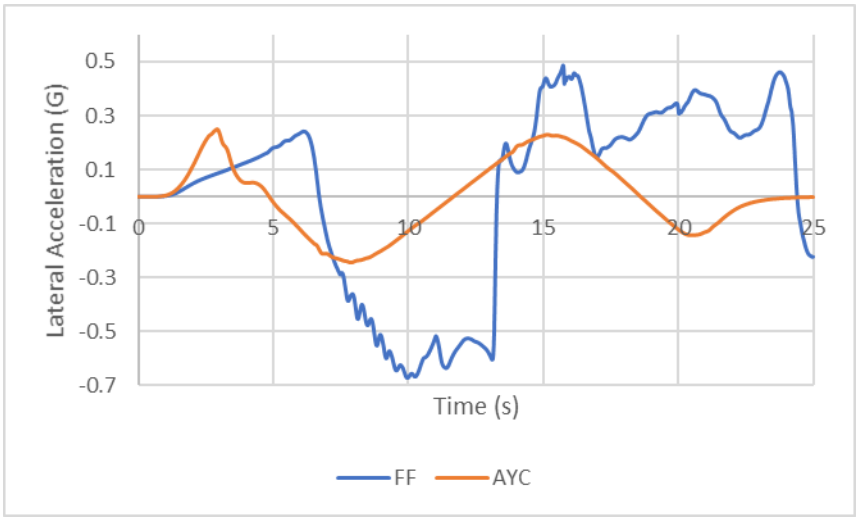

(b)

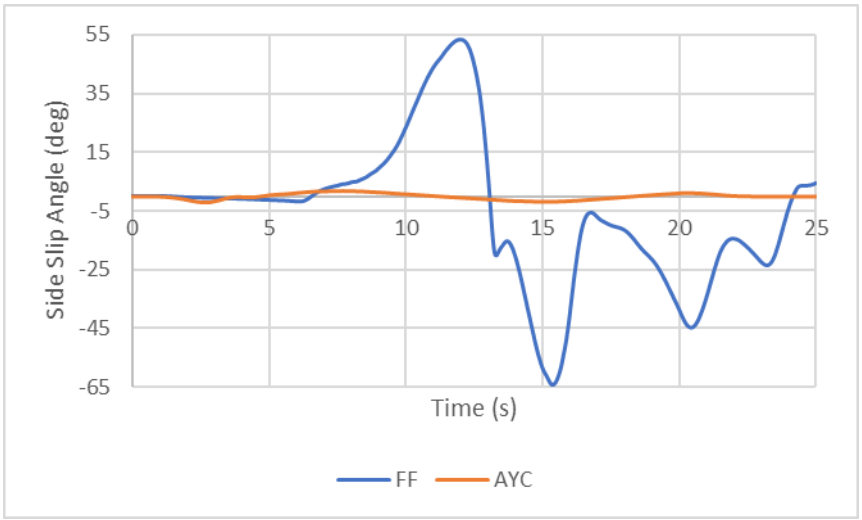

(c)

Figure 5-5 Yaw Rate (a), Lateral Acceleration (b) and Vehicle Side Slip (c) at 40 km/h on Ideal Surface

Figure 5-5(a) shows the yaw rate of the FF and AYC skid steered vehicles. As the AYC vehicle shows a stable operating yaw rate, the critical point at which the FF vehicle fails is at the initial turn-in of the sine wave path, around the 2-second mark. The FF vehicle at 40 km/h was unable to generate the required yaw to perform the initial turn-in, as shown by the yellow vehicle below in Figure 5-6(a). This forces the external driver model to consequently generate a sharp increase in steering wheel angle, making the vehicle spin out, as shown in Figure 5-6(b). This was further illustrated by the high lateral acceleration in Figure 5-5(b), above and the extreme vehicle side slip angle in Figure 5-5(c), above. The trend in both lateral acceleration and vehicle side slip was unable to match the stable case at the point of the initial turn-in of the maneuver, forcing the driver model to overcorrect, as witnessed after the 5-second mark of the test.

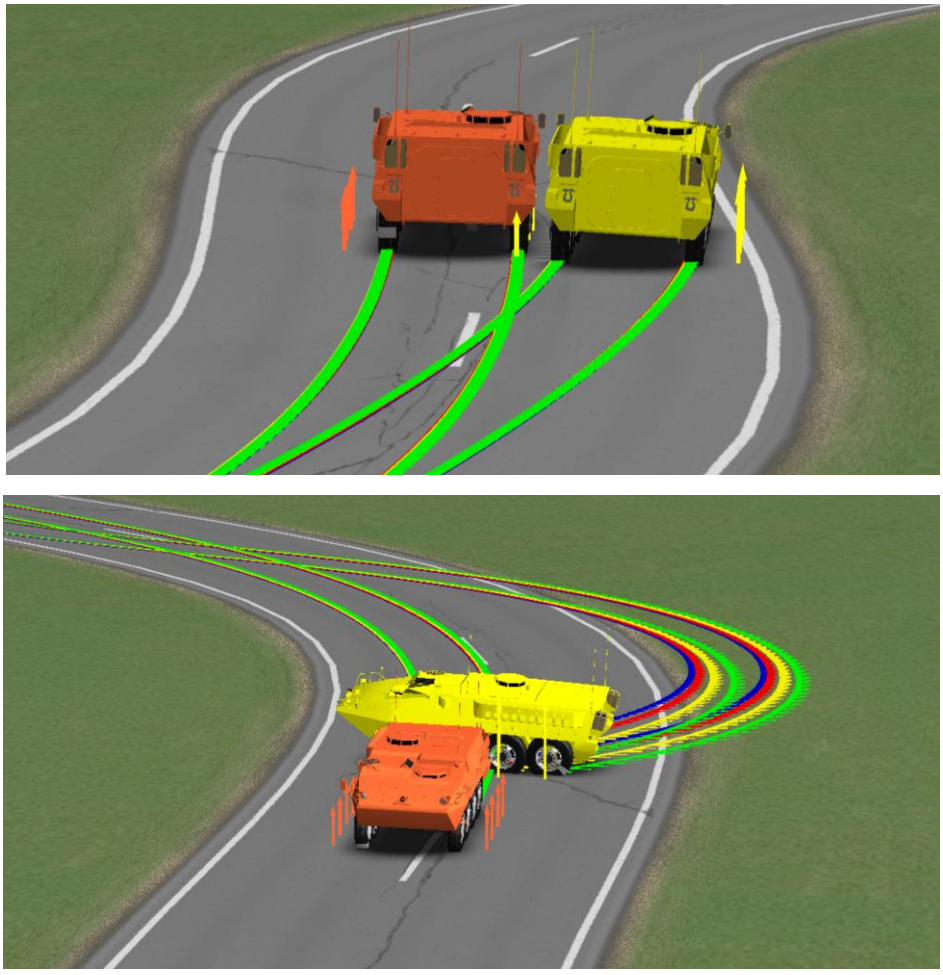

(a)

(b)

Figure 5-6 Entering First Turn-In (a) and Spin-Out After First Turn-In (b)

5.4 Skid Steering on Low-Friction Surface (μ=0.35)

Proceeding the normal surface test, both skid steer control systems are evaluated for performance on a reduced friction scenario of the same maneuver. Evaluation is performed once again at both 20 km/h and 40 km/h, with the road surface friction reduced to a coefficient of 0.35.

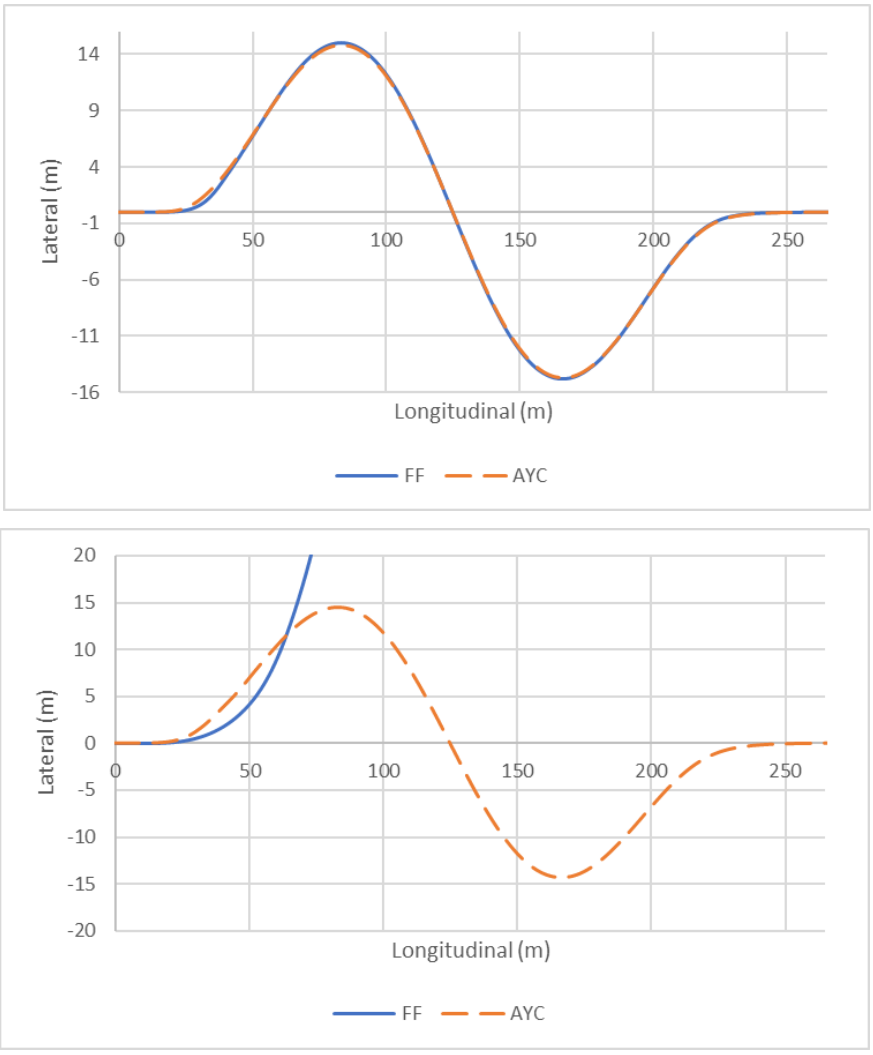

(a)

(b)

Figure 5-7 Vehicles Paths at 20 km/h (a) and 40 km/h (b) on Low-Friction Surface

Vehicle paths are shown above in Figure 5-7 for both 20 km/h and 40 km/h tests on the low friction surface. At 20 km/h in Figure 5-7(a), both vehicles have nearly identical paths. However, at 40 km/h in Figure 5-7(b), the reference vehicle loses control and is unable to complete the maneuver. Figure 5-8 shows the FF vehicle (in yellow) losing control and spinning out at the first turn-in of the sine wave path.

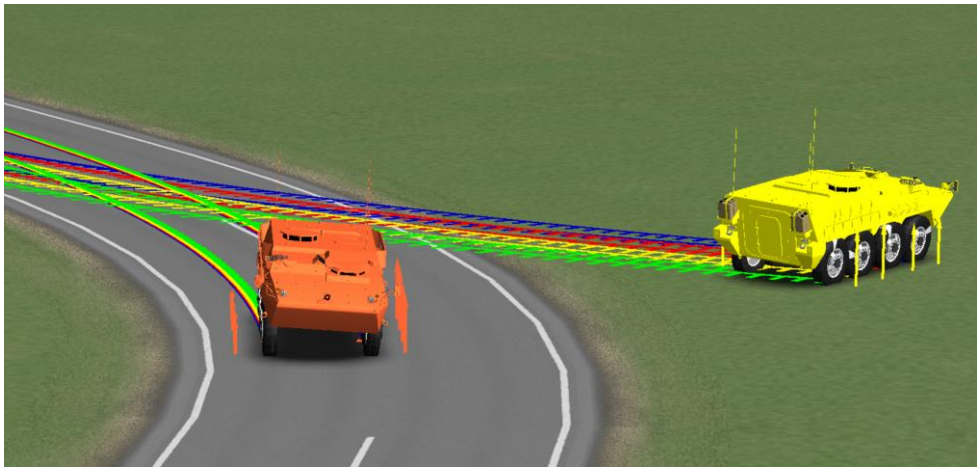

Figure 5-8 FF Skid Steered Vehicle Spin-Out at First Turn-In

Like in the previous test, the FF vehicle could not generate the required differential torque, causing the driver model to overcorrect and saturate the feedforward controller. Due to reduced surface friction, the FF vehicle is unable to attempt the second turn-in and enters spin-out much sooner than with normal road friction. The overcorrection of the driver model at 40 km/h is shown in Figure 5-9, with the steep change and consistent steering wheel lock-up at 720 degrees. Conversely, the AYC vehicle which does not exceed 125 degrees.

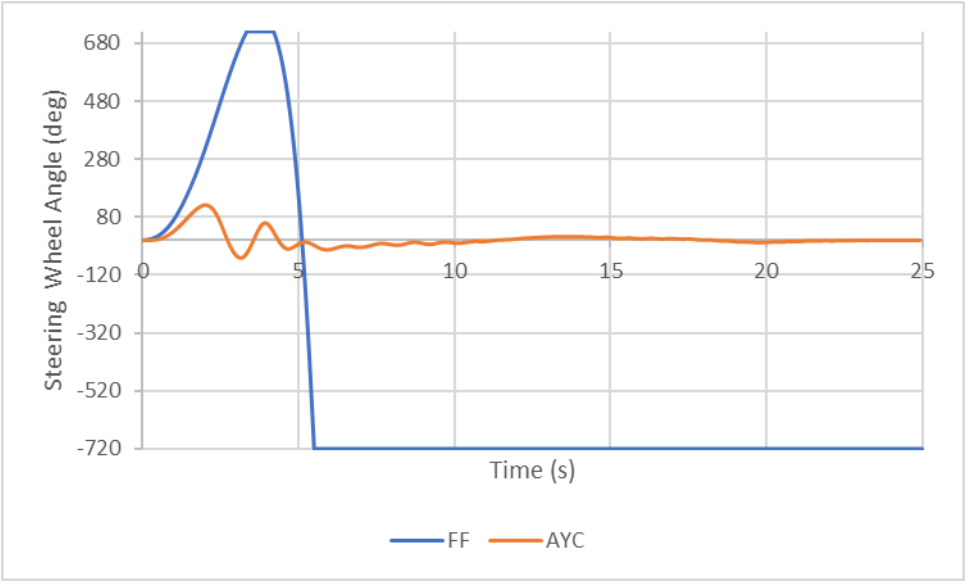

Figure 5-9 Driver Model Steering at 40 km/h on Low-Friction Surface

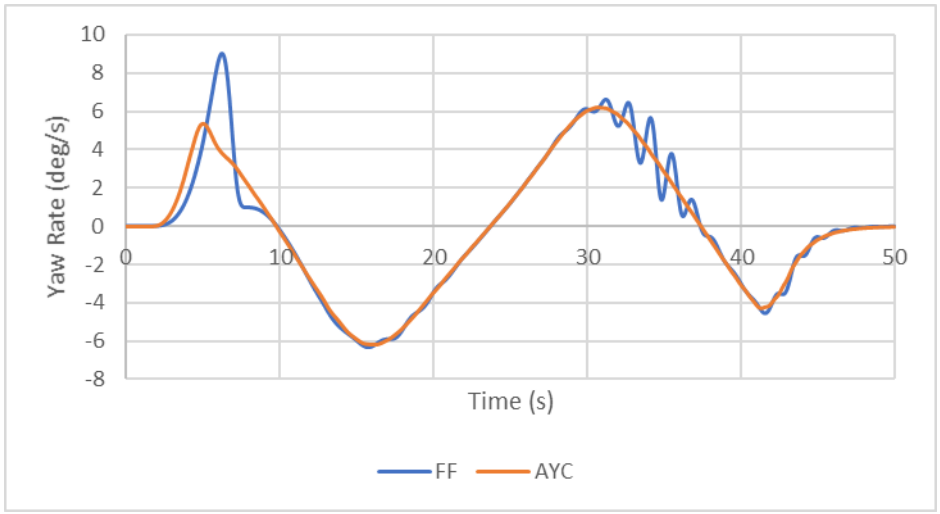

(a)

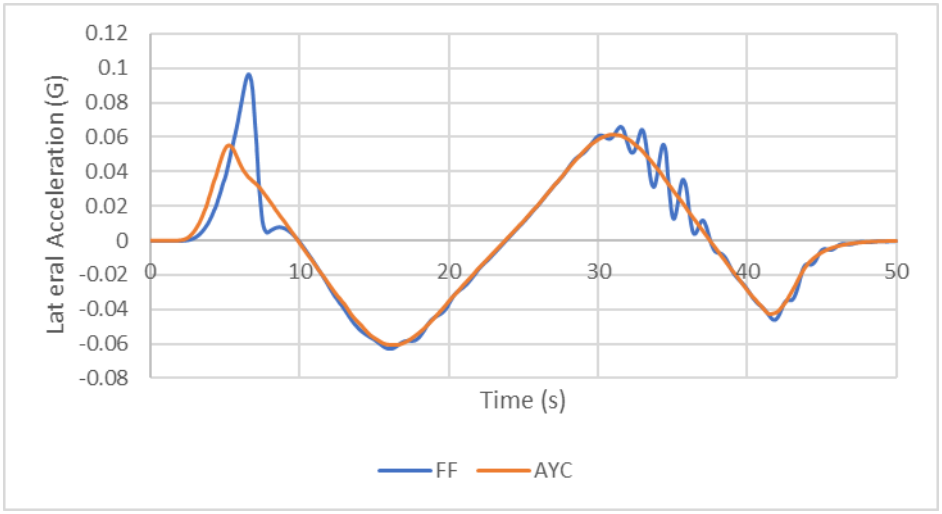

(b)

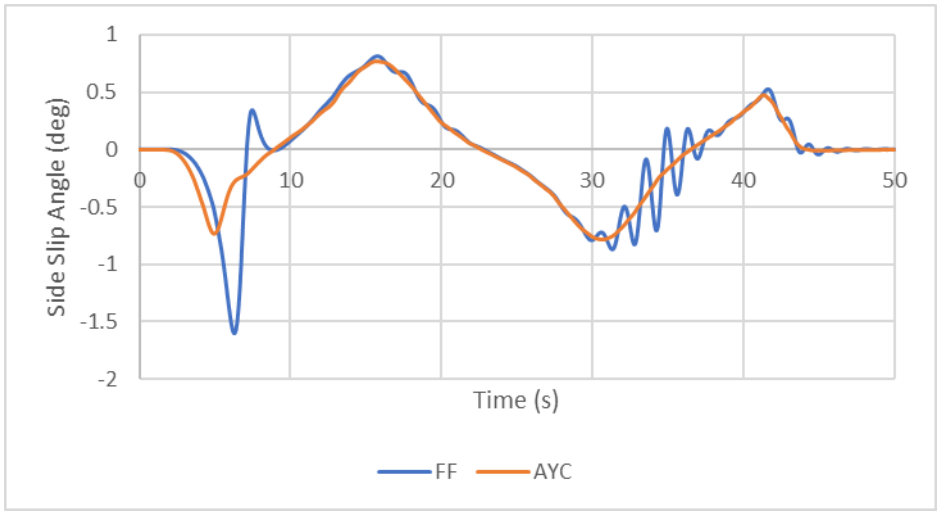

(c)

Figure 5-10 Yaw Rate (a), Lateral Acceleration (b) and Vehicle Side Slip (c) at 20 km/h on Low-Friction Surface

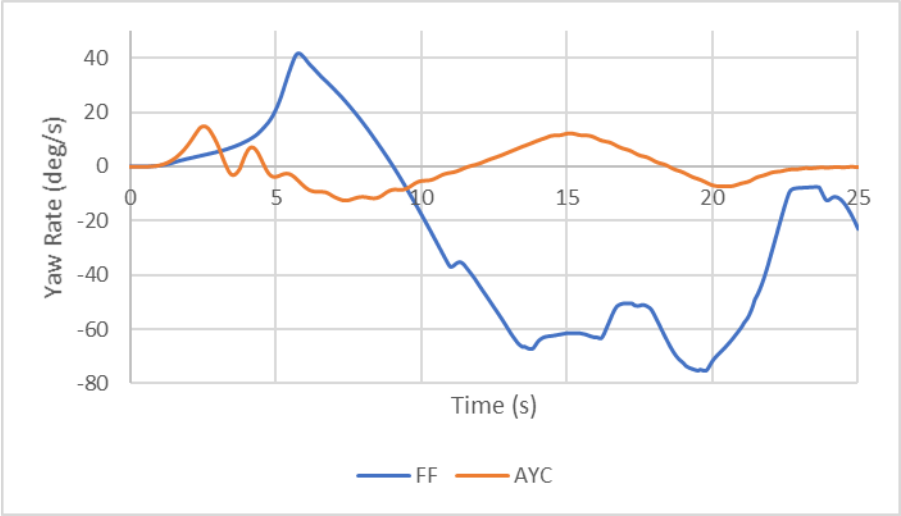

(a)

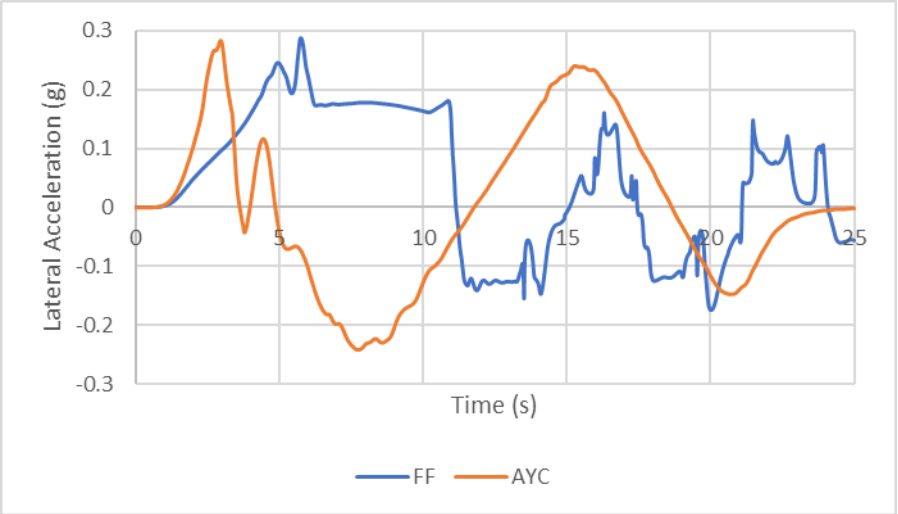

(b)

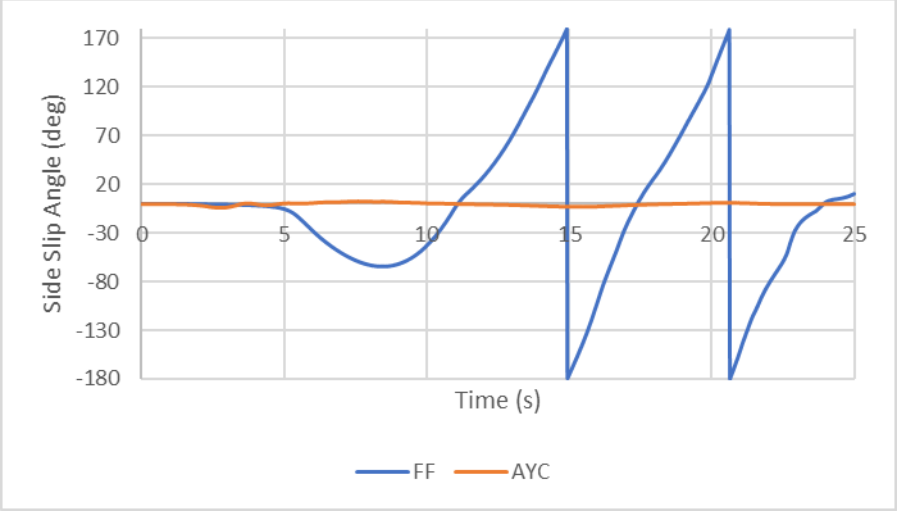

(c)

Figure 5-11 Yaw Rate (a), Lateral Acceleration (b) and Vehicle Side Slip (c) at 40 km/h on Low-Friction Surface

Figure 5-10 shows the performance measures taken for the 20 km/h test, and Figure 5-11 shows those for 40 km/h. The performance measures at 20 km/h were not omitted for this test to emphasize the critical stability operation of the driver model which is more evident on lower surface friction.

Figure 5-10(a) shows the FF vehicle at 20 km/h overcorrecting at the first turn-in, generating a large amount of yaw with some delay compared to the AYC vehicle. This leads to some instability and oscillation, which indicates the vehicle attempting to recover. The spikes in lateral acceleration and vehicle side slip, shown in Figure 5-10(b) and Figure 5-10(c), respectively, indicate fishtailing of the reference vehicle at the first turn-in. The oscillations in all measures after the 30-second mark (the third turn-in of the maneuver) indicate a similar type of instability, therefore excessive driver correction. This further establishes that the feedforward method of torque distribution forces the driver model to operate close to critical stability, and is therefore not suitable for speeds beyond 20 km/h.

Figure 5-11 shows the performance measures taken at 40 km/h. As indicated by the yaw rate, lateral acceleration, and most notably the side slip angle, the FF vehicle is unable to maintain control. In Figure 5-11(c), the side slip angle of the FF vehicle reaches 180 degrees, indicating full loss of control. The AYC vehicle is still able to successfully complete the maneuver due consistent monitoring of vehicle state by the active yaw controller. Due to the sharp initial turn-in of the maneuver, oscillation from driver model correction is exhibited, but quickly damped, as shown in all presented measures. Beyond this portion of the maneuver, the AYC vehicle can maintain stability with little to no oscillation at 40 km/h, compared to the FF vehicle at 20 km/h. This shows that the driver model can operate stably at maximum recommended speed under low friction conditions with the active yaw control method.

5.5 Driving Mode Comparison on Off-Road Conditions

For the final phase of evaluating the skid steer driving mode, the same path maneuver is used once more, with the addition of an ISO 8608 standard class E road surface roughness to simulate moderate to harsh off-road conditions. These test conditions are intended to represent typical combat vehicle operating conditions; hence evaluation is performed with a conventionally combat vehicle (termed the "Reference" in Table 5-1) against the AYC skid steered vehicle using the active yaw controller. The FF skid steered vehicle is omitted in this testing due to its failure to maintain stability at reduced road friction on a flat surface. Only the skid steered vehicle employs the external driver model to harness the steer-by-wire control architecture. Testing of both vehicles was initially conducted at 40 km/h, however the skid steered vehicle failed the maneuver after the third turn-in of the path, while the conventional vehicle was still able to traverse successfully. Testing speed was thus reduced to 30 km/h to evaluate the skid steered vehicle over off-road conditions without the failure of either test subject.

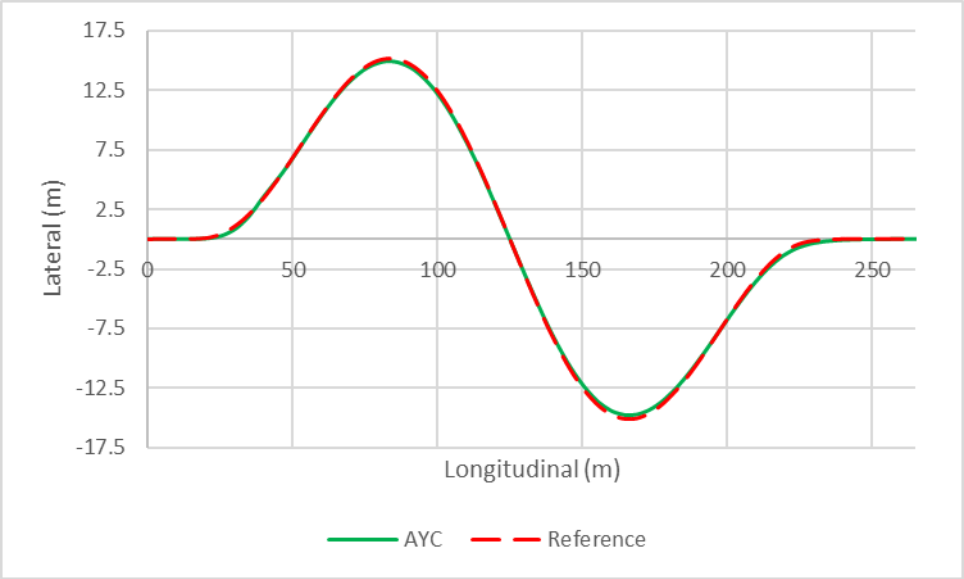

Figure 5-12 Vehicles Paths on Off-Road Surface

Figure 5-12 above shows the path of both the skid steered and reference vehicles. Both vehicles performed the maneuver with marginal difference in path following ability, despite the different driver models used in each vehicle. Where the difference in operation performance is shown is through the steering input effort, as shown below in Figure 5-13.

Using the steer-by-wire control architecture, the skid steered vehicle requires much less steering input effort compared to the reference vehicle. The variations exhibited in the steering during the transient portions of the maneuver are attributed to the uneven road surface, which has a greater impact on the conventional vehicle due to mechanical linkages providing road feedback. The steer-by-wire implementation in the skid steered vehicle reduces the mechanical feedback experienced at the steering wheel, assuming the vehicle was manned.

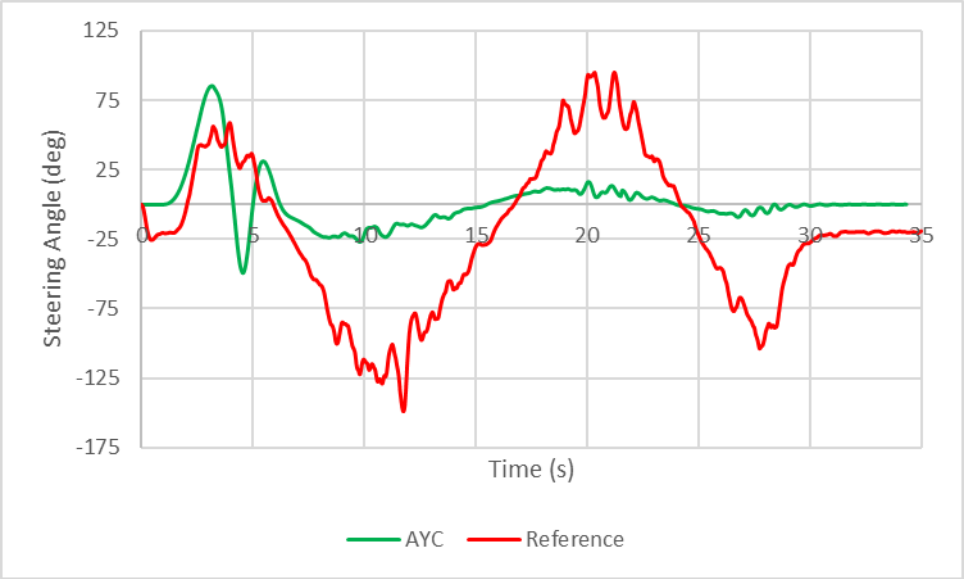

Figure 5-13 Steering Input Comparison on Off-Road Surface

The following data presented in Figure 5-14 below are the performance measures of the skid steered versus conventionally vehicles on the off-road maneuver. Yaw rate (Figure 5-14(a)) and lateral acceleration (Figure 5-14(b)) are largely similar for both vehicles, with high-frequency small oscillations being attributed to the vibrations caused by traversing over the uneven road surface. Vehicle side slip, shown in Figure 5-14(c) for both vehicles are similar in magnitude, however opposite in orientation, with the skid steered vehicle showing greater variations during transient parts of the maneuver. The difference in vehicle side slip between the two vehicles is primarily due to the two front steerable axles on the conventional vehicle, whereas all axles are locked in straight orientation on the skid steered vehicle and rely on torque differential to yaw.

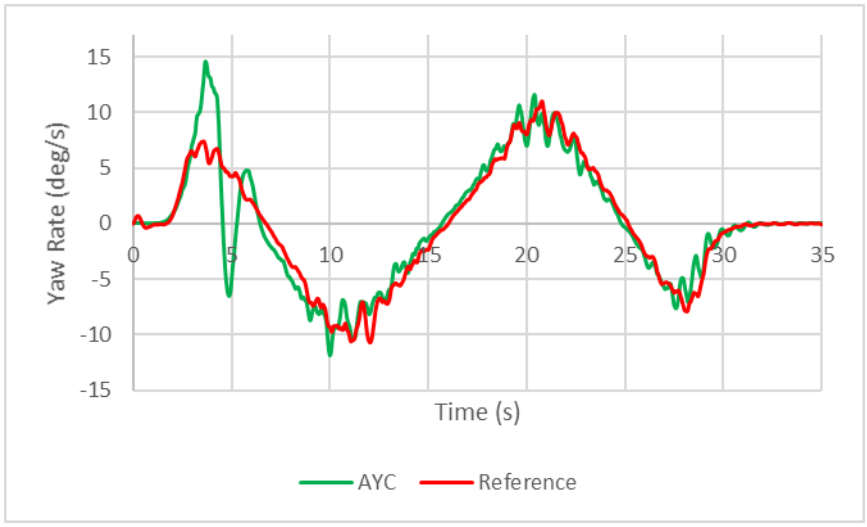

(a)

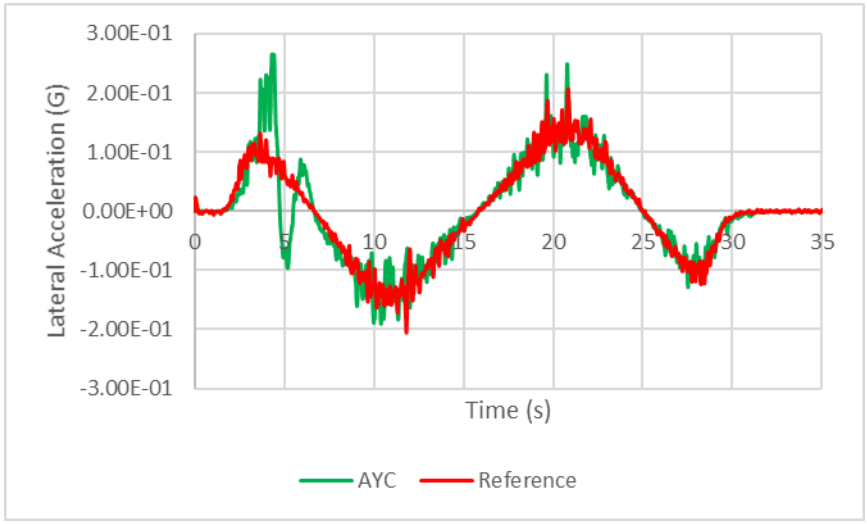

(b)

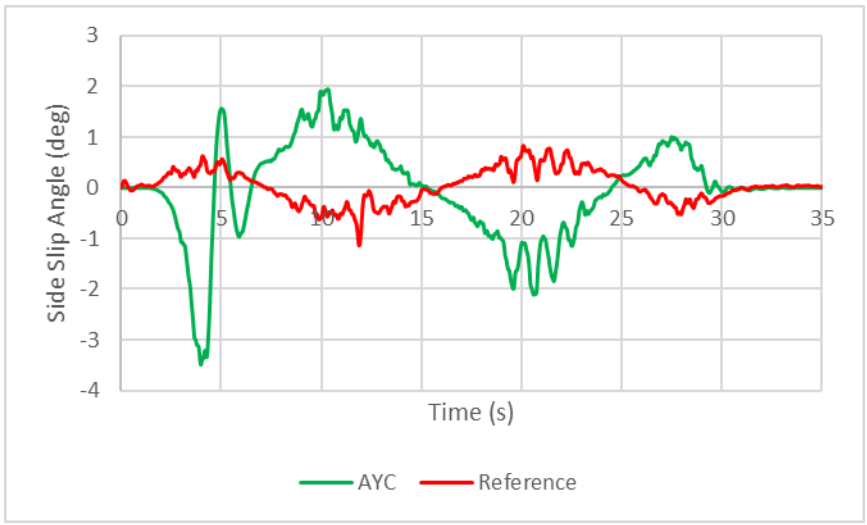

(c)

Figure 5-14 Yaw Rate (a), Lateral Acceleration (b) and Vehicle Side Slip (c) at 40 km/h on Off-Road Surface

5.6 Low-Speed Testing Conclusions

Based on the tests completed for low-speed operation, the following conclusions were established in regards to the implementation and use of skid steering on a future electric drive combat vehicle;

- Direct feedforward translation of steering wheel input to wheel torque differential through steer-by-wire control is insufficient to skid steer safely beyond 20 km/h, especially on low surface friction conditions,
- Active yaw control through yaw rate and side slip monitoring stabilizes the vehicle in skid steer maneuvers over various conditions from ideal to low-friction and off-road,
- The pre-compensation gain as part of the LQR controller of the active yaw control system – when tuned appropriately – reduces steering input effort required to generate desired yawing motion, thereby increasing the ease of control and range of controllability available for directly manned, remote or autonomous driving,
- Regardless of driver type (manned or autonomous) using active yaw control, the future electric drive combat vehicle can safely up to a recommended 40 km/h given fair road surface roughness; 30 km/h for worst-case off-road conditions as simulated in these tests,
- Under typical combat mission operating conditions, i.e. rough road surface with low traction capability, skid steering with active yaw control can perform on par with a conventionally steered vehicle up to 30 km/h, beyond which point the unpredictability of the tire behaviour becomes the limiting factor of the skid steered vehicle, however,
- With directly manned operation, the design of the steer-by-wire system with the electric powertrain, skid steering becomes much easier to use due to pre-amplified steering input and reduced road feedback due to mechanical decoupling of the steering wheel and steering actuators.

5.7 Chapter Summary

This chapter summarized the results of all tests conducted on the electric combat vehicle in low-speed operation mode. Testing was completed over a single path with three different surface conditions – ideal friction at $\mu = 0.85$, reduced friction at $\mu = 0.35$ and off-road which combined reduced friction and an ISO 8608 class E roughness profile. For ideal and reduced surface friction conditions, evaluation was performed between skid steering vehicles using the direct feedforward torque control system and the active yaw controller using a pre-compensation scaling factor. For the off-road conditions, evaluation was performed between the skid steered vehicle using the active yaw controller and the reference conventional combat vehicle.

It was found that the use of an active yaw controller modified for skid steering proved to be more stable than a direct feedforward system which translates steering input to left-right torque distribution. Over ideal conditions using the direct feedforward system, the vehicle could skid steer safely up to 20 km/h. The active yaw controller enabled skid steering up to 40 km/h on both ideal and reduced friction surfaces. With the steer-by-wire architecture used by the active yaw control method, skid steering can be recommended for use with either autonomous or manned operation due to the significantly reduced steering effort. Autonomous operation would benefit from skid steering due to the simplified powertrain application, as fewer actuators are controlled compared to conventional steering. However, regardless of control method, stable skid steering was not possible over 40 km/h flat surfaces or 30 km/h on off-road conditions due to the limits of the pneumatic tires.

CHAPTER 6
HIGH-SPEED OPERATION TESTING

6.1 Chapter Introduction

This chapter summarizes the results of all tests conducted on the electric combat vehicle in high-speed operation mode. All tests outlined in this chapter evaluate the electric combat vehicle in all possible driving configurations against reference conventional vehicle, within the range of 40 km/h to 80 km/h. For this chapter tests are organized in a process of elimination, where only successful vehicle configurations are used in proceeding tests to narrow down a conclusion for an ideal configuration. Conclusions on vehicle performance are drawn from both manned and autonomous driving perspectives. Table 6-1 below outlines the terminologies used to refer to the various driving configurations throughout the chapter to simplify reading. Terminologies ending in "-R" indicate rear-wheel drive.

Table 6-1 Abbreviations for Test Vehicles for High-Speed Operation

TERMINOLOGY	VEHICLE CONFIGURATION
Reference	Internal Combustion Engine w/ Conventional Steering (Axles 1&2)
USC, USC-R	Electric Powertrain w/ Unified Stability Control System, Conventional Steering (Axles 1&2)
A-4AS, A-4AS-R	USC + Active (Speed-Dependent) 4^{th} Axle Steering
A-AWS, A-AWS-R	USC + Active (Speed-Dependent) All-Wheel Steering
P-4AS, P-4AS-R	USC + Passive 4^{th} Axle Steering
P-AWS, P-AWS-R	USC + Passive All-Wheel Steering

Table 6-2 below outlines the entire gauntlet of tests performed in this work, including respective operating speeds, road conditions and vehicles used in the test. Respective chapter sections for each test are also provided in the table.

Table 6-2 Summary of Tests and Conditions for High-Speed Operations

HIGH SPEED OPERATION		
Test Procedure	**Vehicles Used**	**Conditions**
6.1 - Phase 1 Modified J-Turn *(* rear wheel drive also tested)*	Reference, USC* A-4AS*, A-AWS* P-4AS*, P-AWS*	40 km/h Dry Asphalt (μ=0.8) Ice-Covered (μ=0.2)
6.2 - Phase 2 100-ft Circle Skid Pad *(* rear wheel drive also tested)*	Reference, USC* A-4AS*, A-AWS* P-4AS*, P-AWS*	Acceleration (0-120 km/h, 6 km/h/s) Dry Asphalt (μ=0.8)
6.3 - Phase 3 FMVSS 126 ESC Test	Reference, USC A-4AS, A-AWS P-4AS, P-AWS	60 km/h, 80 km/h Dry Asphalt (μ=0.8) Ice-Covered (μ=0.2)
6.4 - Phase 4 NATO Double Lane Change (03-160W)	Reference, USC A-4AS, A-AWS P-4AS, P-AWS	60 km/h, 80 km/h (dry only) Dry Asphalt (μ=0.8) Ice-Covered (μ=0.2)

6.2 Phase 1 - Modified J-Turn Maneuver

(a) **(b)**

Figure 6-1 Vehicles Performing J-Turn (a) and Input Steering Time History (b)

The J-turn maneuver used in this work serves as the first phase of testing for the high-speed operation category. For this test, a steering wheel angle time history is taken from the reference combat vehicle performing a 75-ft J-turn maneuver at 40 km/h. As such, this test serves to evaluate the response of the vehicle in a simulated tight cornering maneuver, hence there is no target path. Performance is evaluated through the vehicle's maneuverability and stability given the fixed steering input. The maneuver itself consists of a gradual increase to a peak steering wheel angle of 367.2 degrees, followed by a recovery portion which would straighten the vehicle, as shown in Figure 6-1(b). The speed of 40 km/h is chosen as it is the transition speed from the low-speed to high-speed testing category, and would serve as the recommended speed at which a vehicle of this size could handle in a tight cornering maneuver. Rear-wheel drive operation is tested here with greater focus on vehicle stability. All vehicle configurations are tested over dry asphalt (friction coefficient of 0.8), and ice (friction coefficient of 0.2). Test results are organized by vehicle configuration.

6.2.1 Front Wheel Steering (Reference vs. USC)

Performance of the electric drive vehicle equipped with the unified stability control system (termed "USC" in Table 6-1) is first compared with the reference vehicle. Figure 6-2 below shows the paths of both vehicles on dry asphalt (Figure 6-2(a)) and on ice (Figure 6-2(b)). Under ideal conditions, the USC vehicle exhibits better maneuverability through a slightly tighter turn-in and earlier recovery maneuver. In the extreme low friction case both vehicles tend to understeer, with the USC vehicle still exhibiting similar behaviour as on an ideal surface.

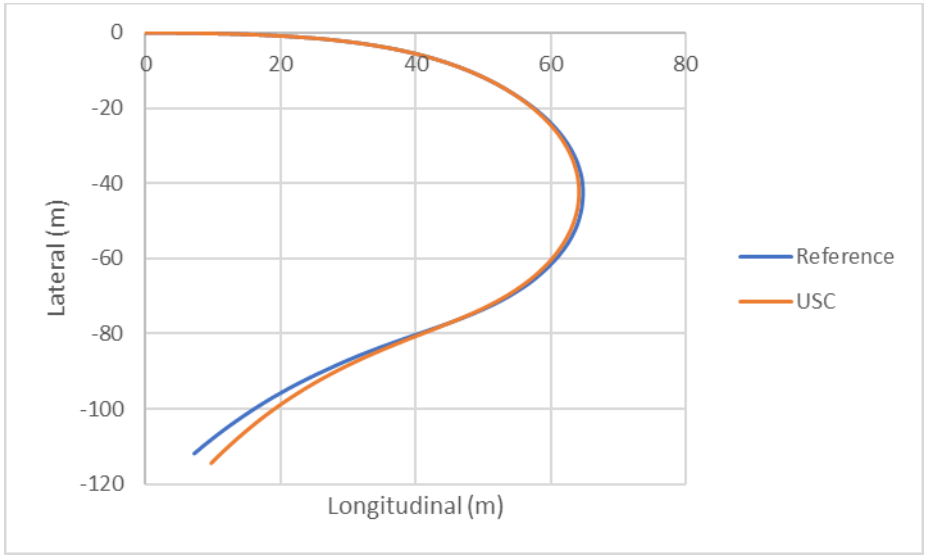

(a)

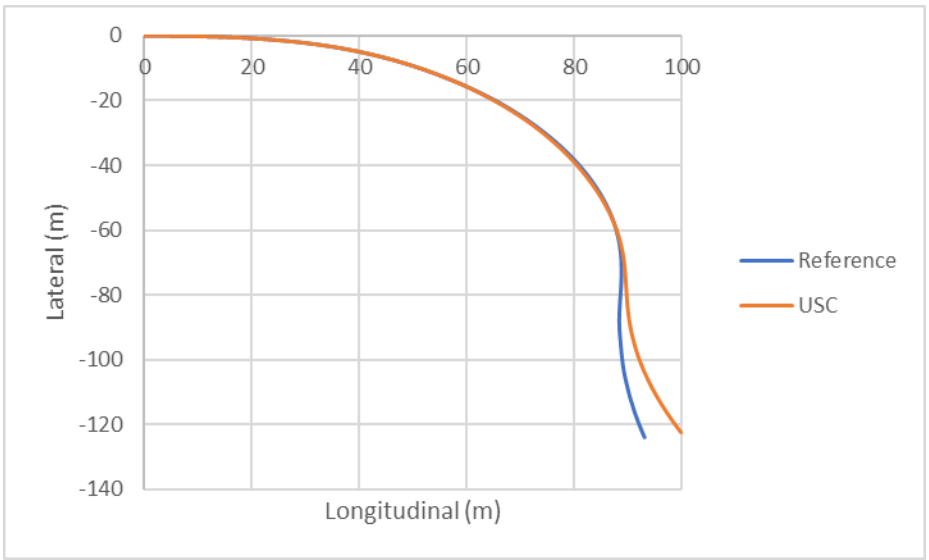

(b)

Figure 6-2 J-Turn Paths on Dry Asphalt (a) and Ice (b) for Reference vs. USC Vehicles

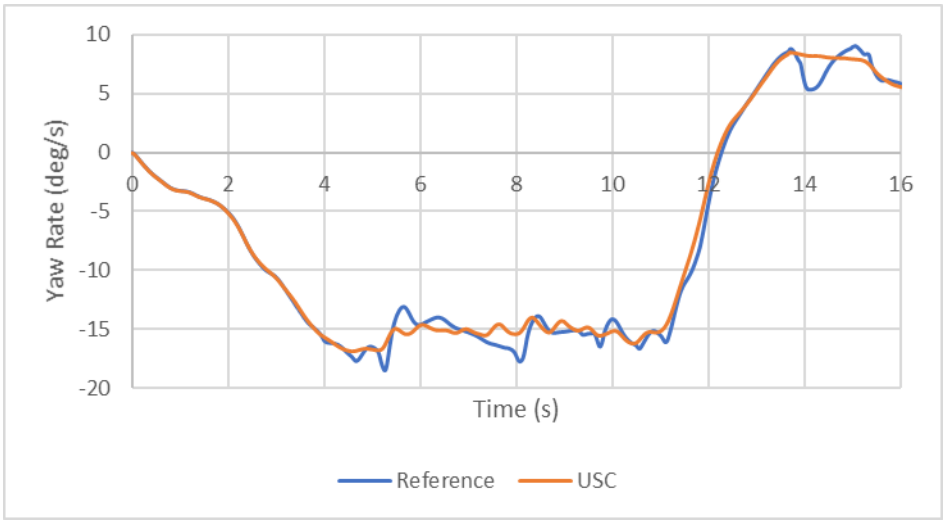

(a)

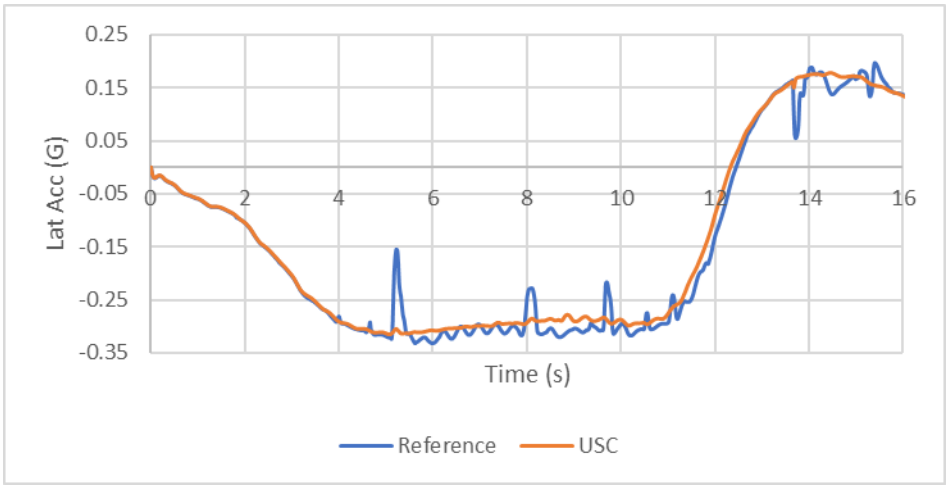

(b)

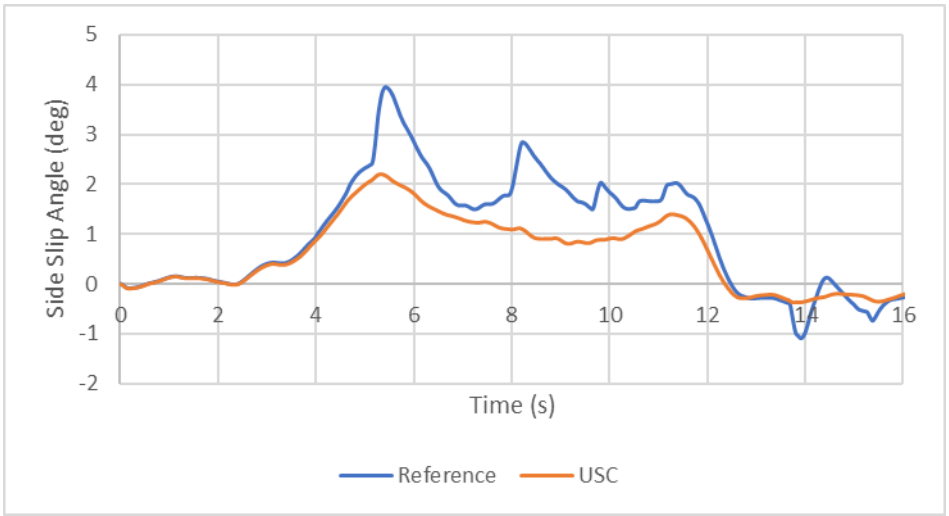

(c)

Figure 6-3 Yaw Rate (a), Lateral Acceleration (b) and Vehicle Side Slip (c) for Reference vs. USC Vehicles on Dry Asphalt

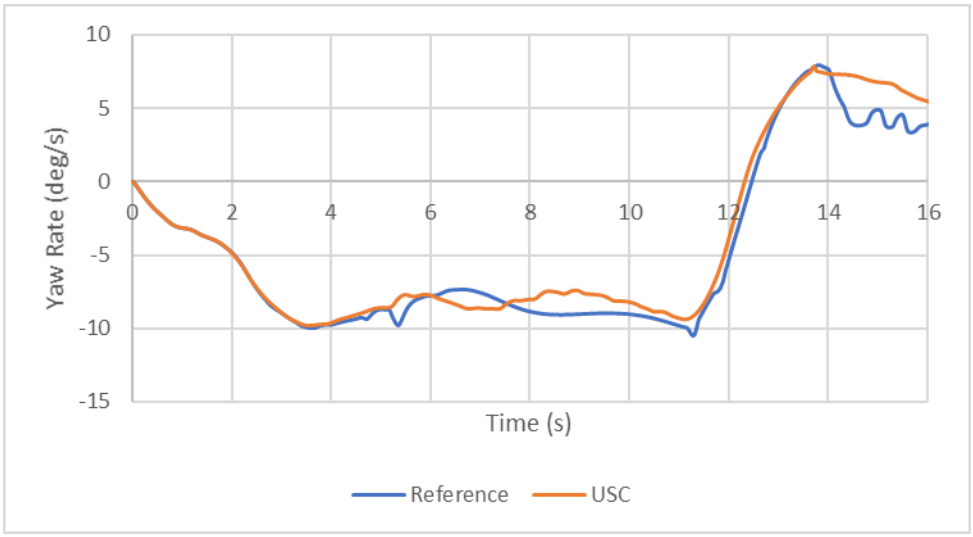

(a)

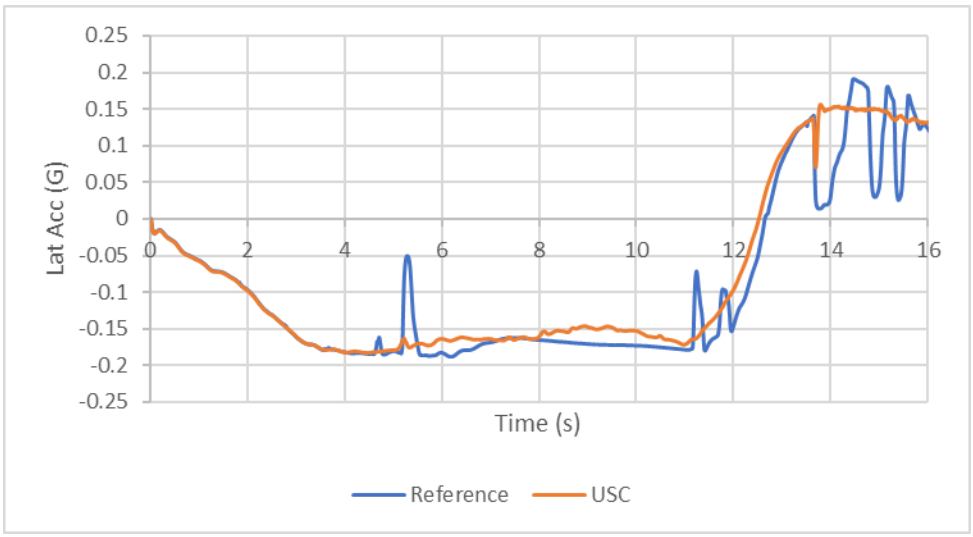

(b)

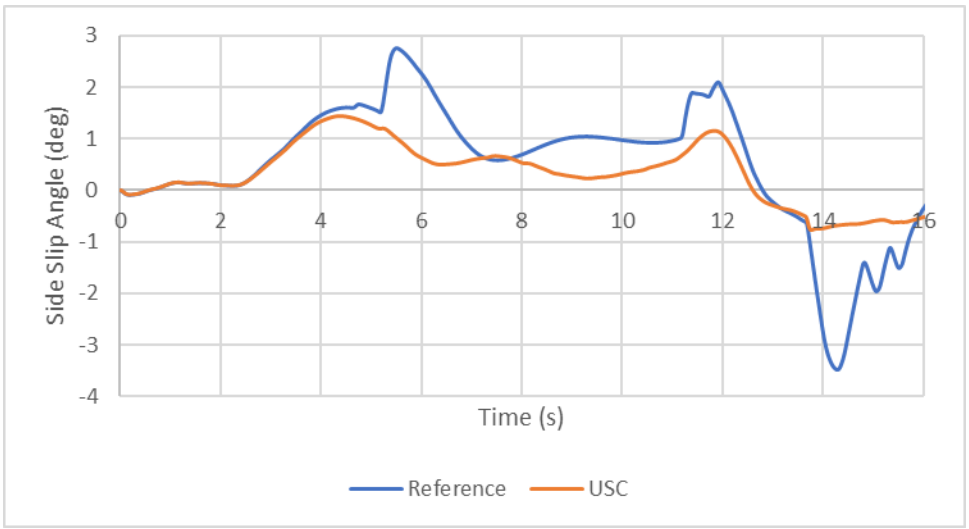

(c)

Figure 6-4 Yaw Rate (a), Lateral Acceleration (b) and Vehicle Side Slip (c) for Reference vs. USC Vehicles on Ice

Yaw rates, lateral acceleration and vehicle side slip are presented for both vehicles on dry asphalt and ice conditions, in Figure 6-3 and Figure 6-4, respectively. In both conditions, the USC vehicle equipped with the unified stability control system has shown to damp anomalous variations in yaw rate and lateral acceleration, thus providing the vehicle with greater stability compared to the reference vehicle. Overall, vehicle side slip of the USC vehicle is greatly reduced in both dry asphalt and ice conditions, which lends to improving both stability and maneuverability.

6.2.2 Supplementary Rear Steering (A-4AS, A-AWS, P-4AS, P-AWS)

Four additional rear steering configurations were tested which work in parallel with the unified stability control system: active fourth-axle steering (A-4AS), active all-wheel steering (A-AWS), passive fourth-axle steering (P-4AS) and passive all-wheel steering (P-4AS). At 40 km/h, the active control form steers the rear axle wheels in the opposite orientation of the front to reduce turning radius. The front-steered USC vehicle is used as the baseline. Figure 6-5(a) below shows the paths of the different vehicle configurations over dry asphalt, and Figure 6-5(b) over ice conditions.

Given the ideal surface, the A-4AS vehicle appears to marginally reduce the turning radius more than the A-AWS vehicle. However, the opposite is true with the passive (P) configurations, in which P-AWS reduces turning radius further than P-4AS. The passive configurations also reduce the turning radius much further compared to the active configurations. When friction is greatly reduced, both active rear steering configurations reduce the understeering exhibited by the baseline USC vehicle. Both passive configurations again further reduce the turning radius of the initial turn-in, but are unable to recover at the end.

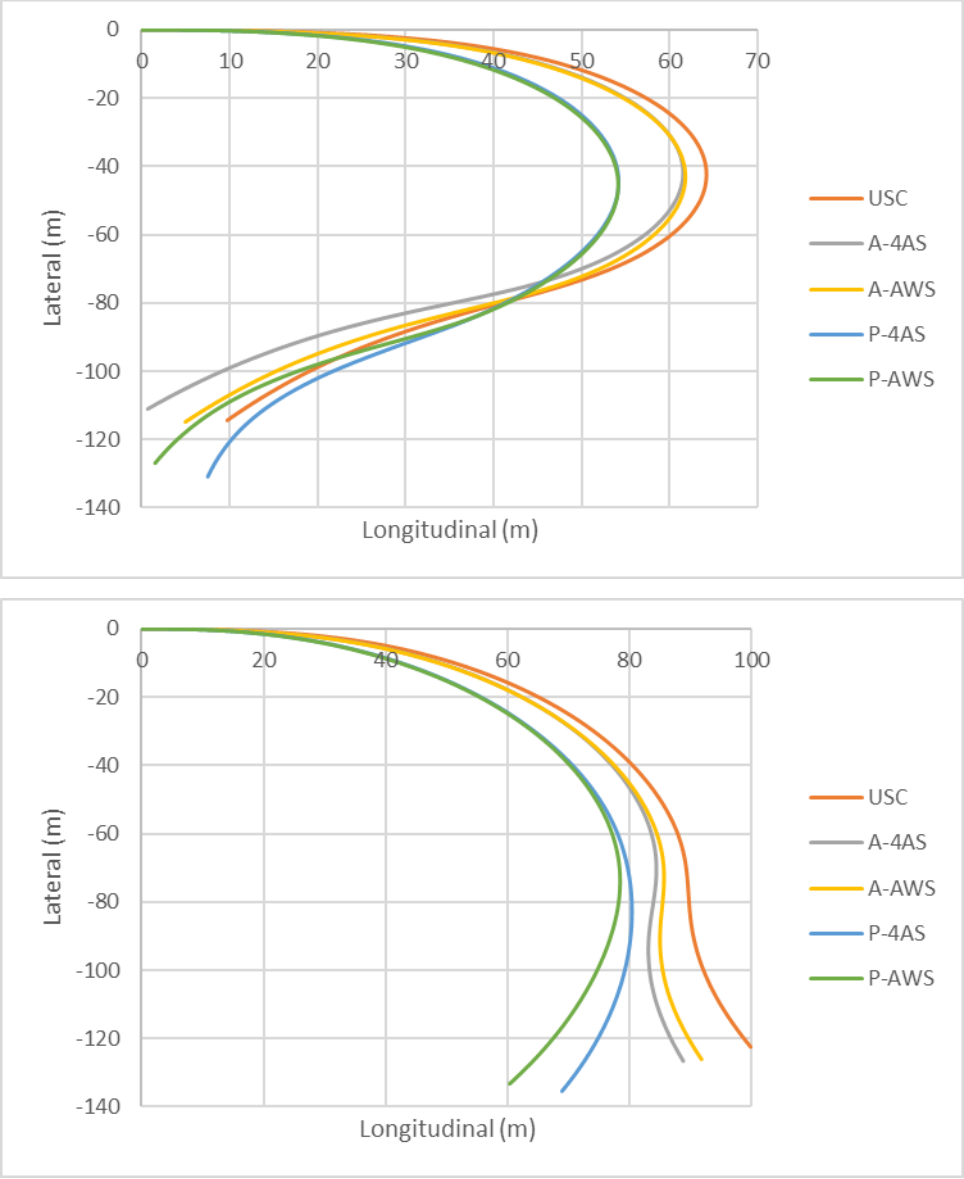

Figure 6-5 J-Turn Paths on Dry Asphalt (a) and Ice (b) for Rear Steering Configurations

Yaw rates, lateral acceleration and vehicle side slip are presented for both dry asphalt and ice conditions, in Figure 6-6 and Figure 6-7 below, respectively.

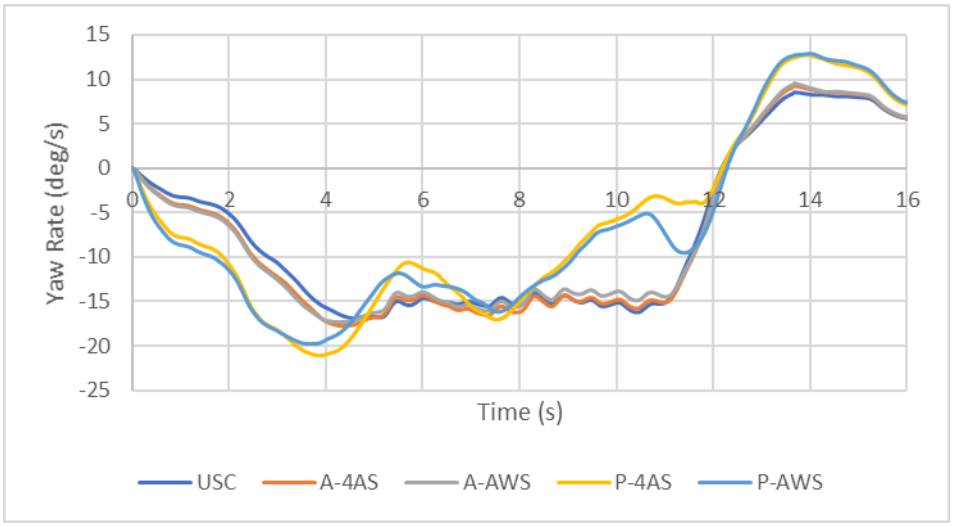

(a)

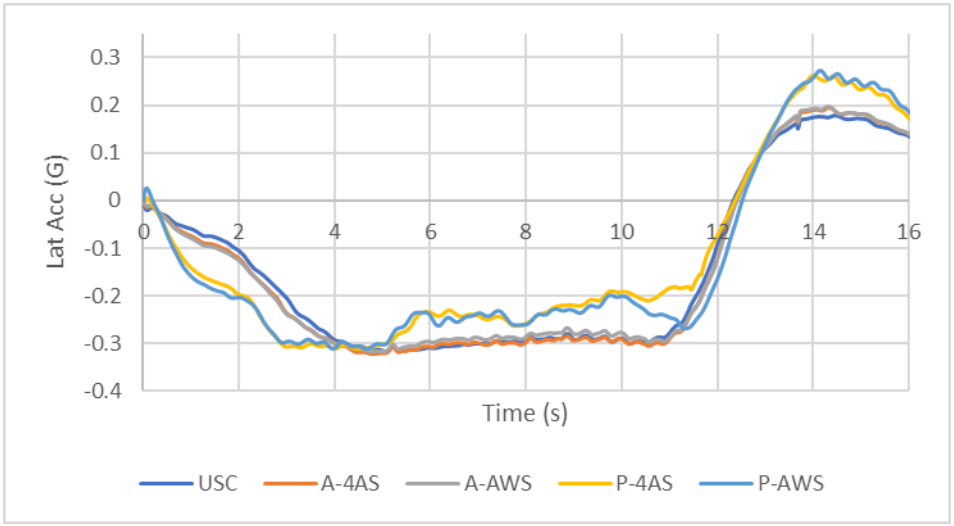

(b)

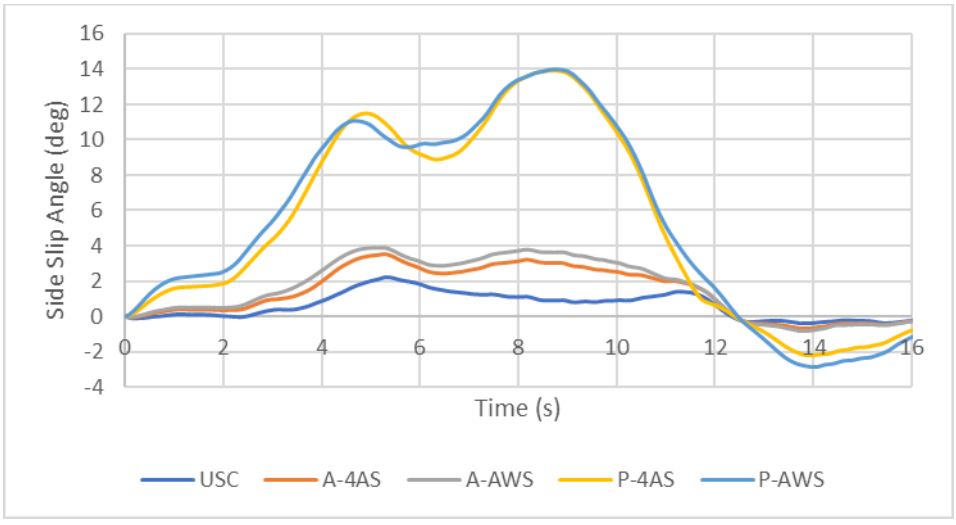

(c)

Figure 6-6 Yaw Rate (a), Lateral Acceleration (b) and Vehicle Side Slip (c) for Rear Steering Configurations on Dry Asphalt

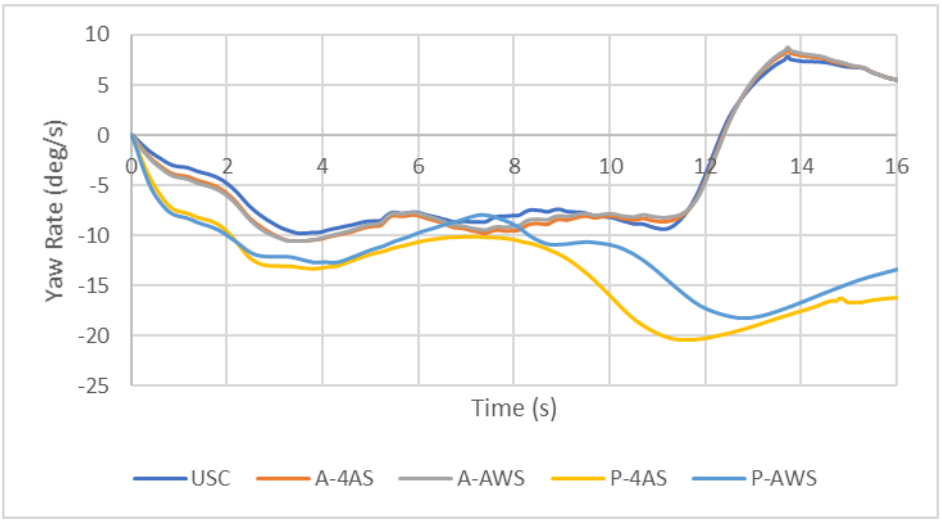

(a)

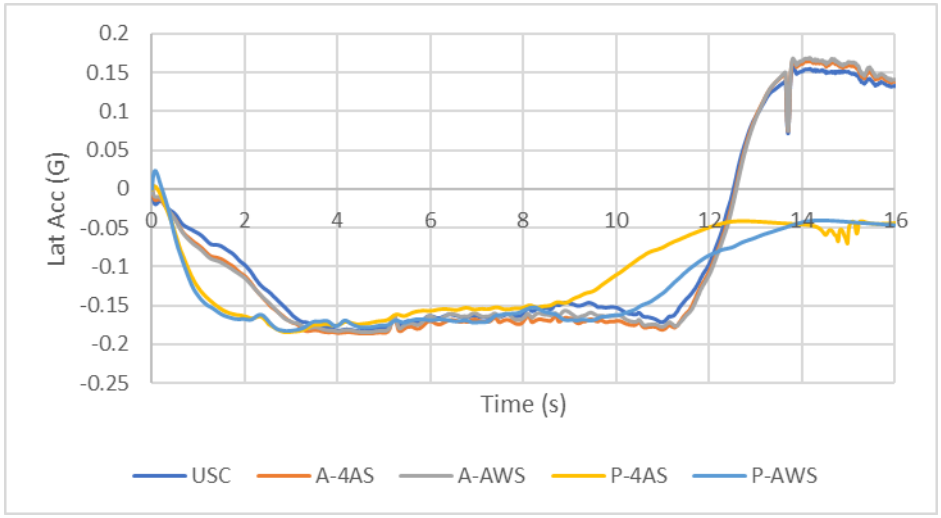

(b)

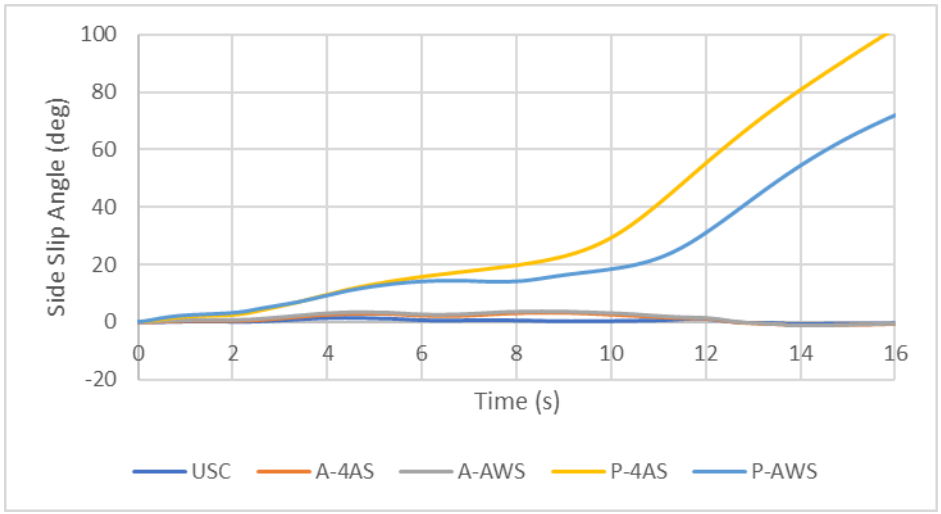

(c)

Figure 6-7 Yaw Rate (a), Lateral Acceleration (b) and Vehicle Side Slip (c) for Rear Steering Configurations on Ice

For both road surface conditions used in testing, there is a marginal increase in yaw rate and lateral acceleration for both active rear steering configurations, compared to the USC baseline vehicle. Despite having larger vehicle side slip compared to the USC vehicle, both active rear steering configurations still operate within stable limits on both dry and icy surfaces. Between the two active configurations, the fourth axle steering generates slightly less side slip, and slightly more yaw rate and lateral acceleration, which explains its tighter cornering compared to active all-wheel steering.

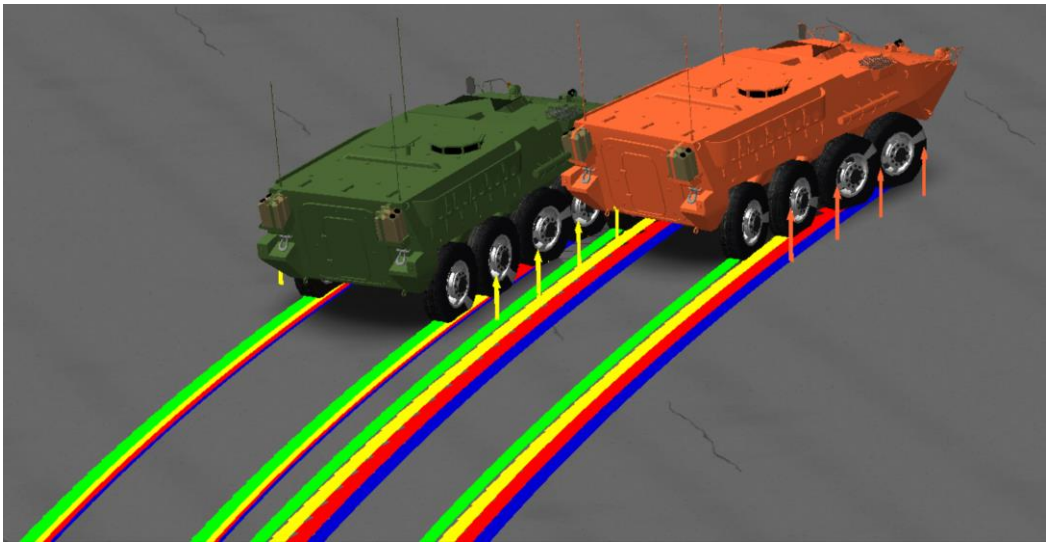

Figure 6-8 Onset of Lateral Sliding with P-AWS Vehicle (Orange)

The passive rear steering configurations, in both dry and icy conditions, have shown to be largely unstable in this maneuver. Behaviour of both yaw rate and lateral acceleration are anomalous, most notably at extremely low friction. Extremely large side slip is induced, and continuously exceeds stable limits Figure 6-7(c), where data has been scaled to show the data range of the more stable vehicles. On the dry surface, the magnitude of side slip indicates fishtailing of both passive rear steering configurations. On the icy surface, the steep rise in vehicle side slip indicates lateral sliding as shown in Figure 6-8, which further explains why neither passive configuration could complete the recovery portion of the cornering maneuver.

6.2.3 Rear-Wheel Drive ("-R" Vehicles)

The implementation of rear-wheel drive is explored with this test maneuver using all configurations of the electric drive combat vehicle. This is done to explore the feasibility of rear-wheel drive as a means of both conserving power by limiting the amount of driving motors and to improve maneuverability and handling. Like the all-wheel drive version of the combat vehicle, the rear-wheel drive vehicle is evaluated on the same testing conditions used for this maneuver. The all-wheel drive, front-steered USC vehicle with unified stability control is used as the reference vehicle for performance evaluation. Figure 6-9below shows the vehicle paths on the dry asphalt and ice conditions.

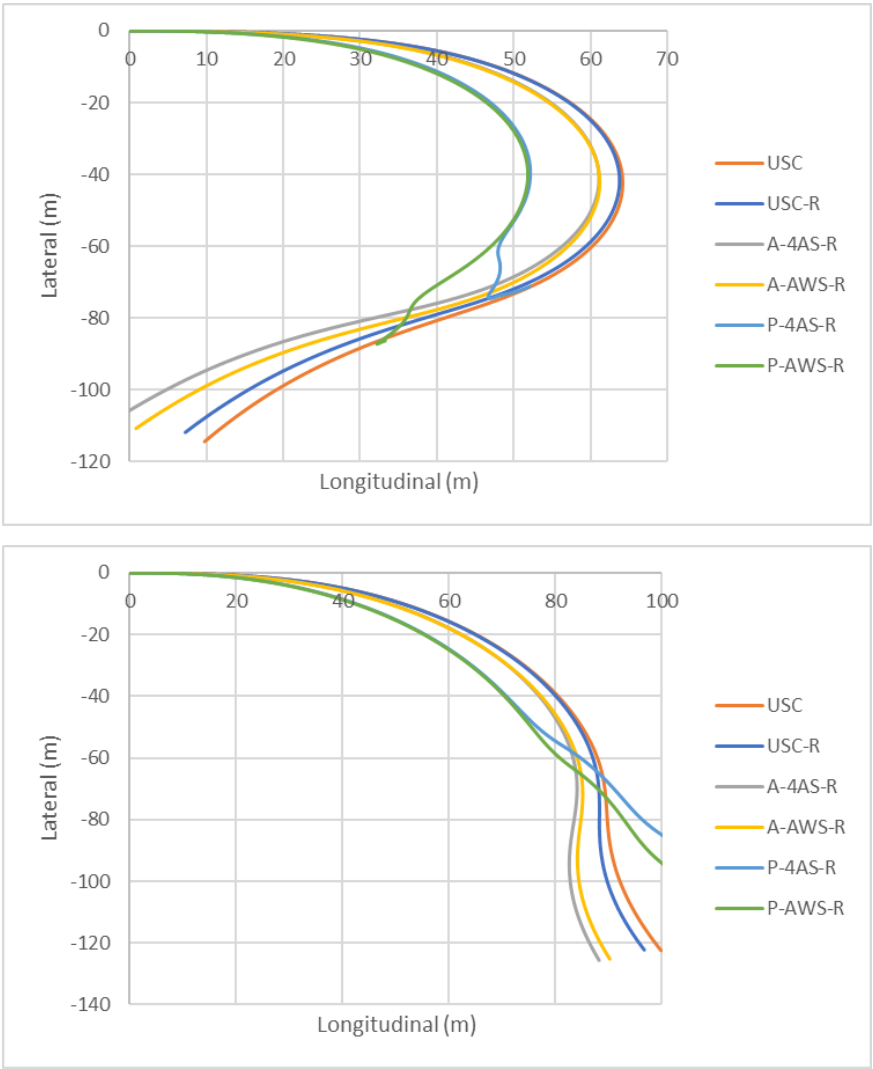

Figure 6-9 J-Turn Paths on Dry Asphalt (a) and Ice (b) for Rear-Wheel Drive Vehicles

Through evaluation of the vehicle paths in Figure 6-9, the USC-R vehicle provides a small improvement in cornering ability over its all-wheel drive counterpart in both surface conditions. With the A-4AS-R and A-AWS-R vehicles, there is no advantage in cornering ability over their all-wheel drive counterparts. Rear-wheel drive proves to be detrimental in the P-4AS-R and P-AWS-R vehicles, as loss of control is exhibited even on the ideal road surface condition. Figure 6-10 shows the P-AWS-R vehicle in orange in spin-out as shown on the path in Figure 6-9(a). With all tractive power at the rear, combined with the large front-to-rear axle steering ratios of the passive configuration, the rear end of the vehicle will increase the tendency to oversteer and make corrective maneuvers difficult.

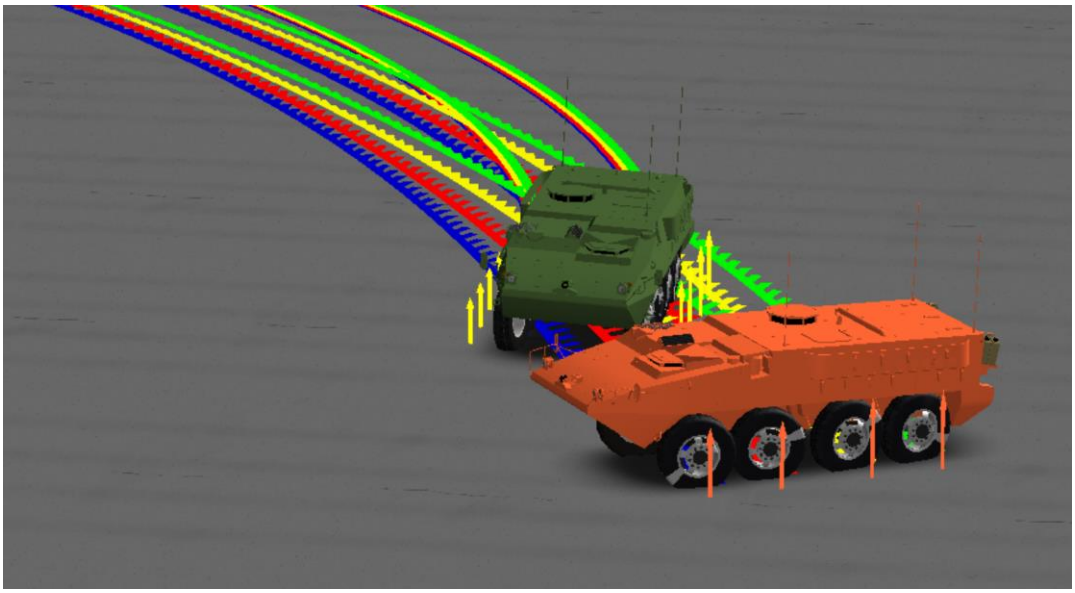

Figure 6-10 Spin-out of RWD Passive Rear Steering Vehicle (Orange)

Performance measures for the rear-wheel drive vehicle are presented below in Figure 6-11 for dry road conditions, and Figure 6-12 for icy road conditions to further support the observed behaviour. Measures for the all-wheel drive USC vehicle are omitted due to negligible difference with the USC-R vehicle.

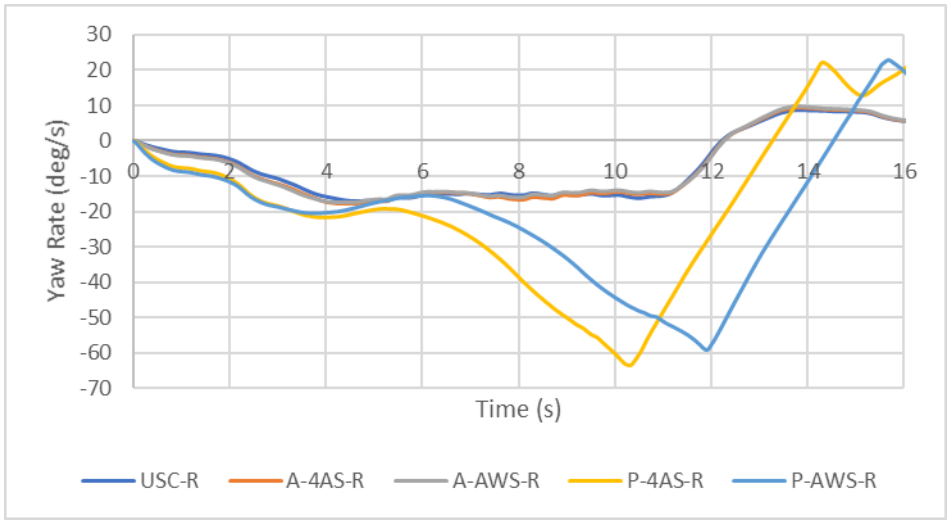

(a)

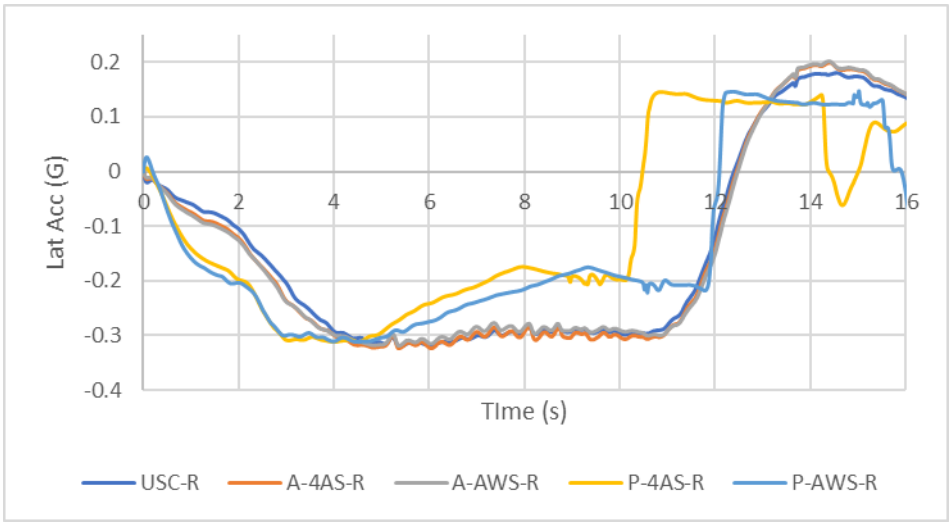

(b)

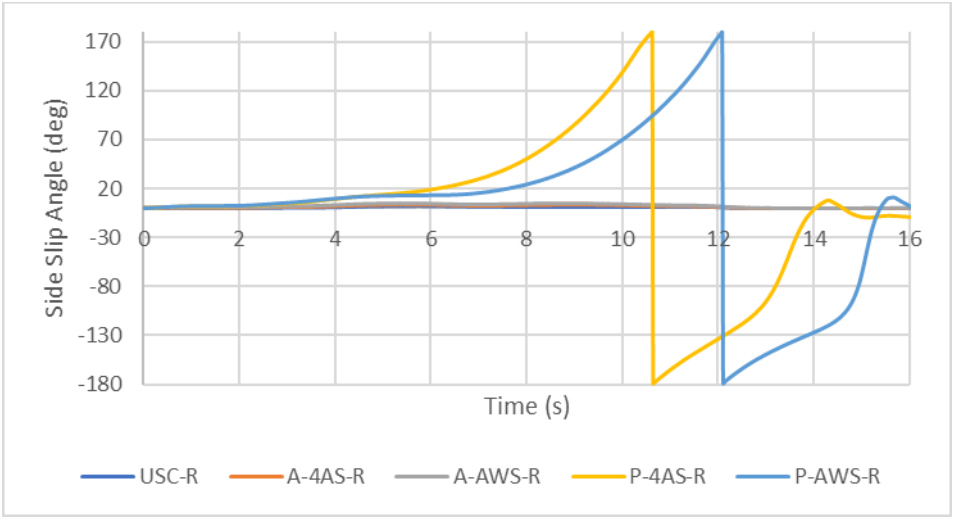

(c)

Figure 6-11 Yaw Rate (a), Lateral Acceleration (b) and Vehicle Side Slip (c) for Rear-Wheel Drive Vehicles on Dry Asphalt

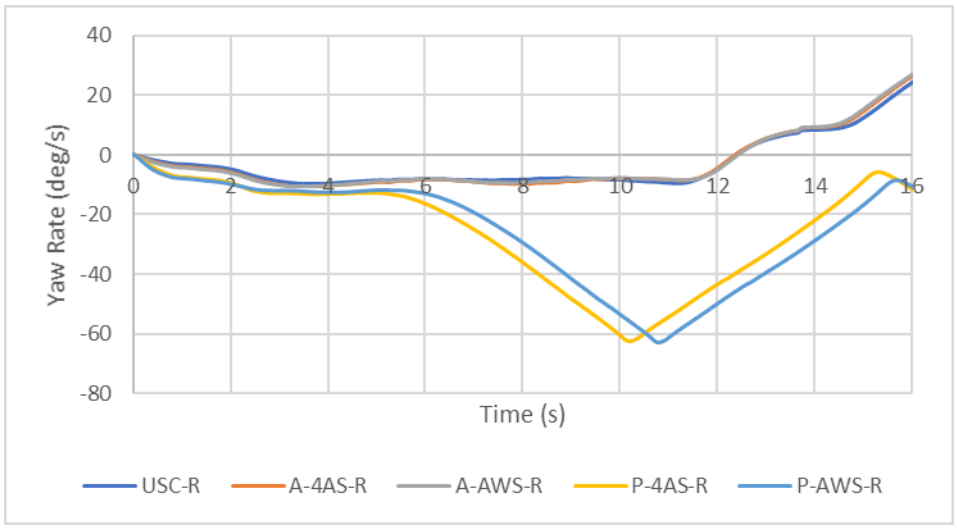

(a)

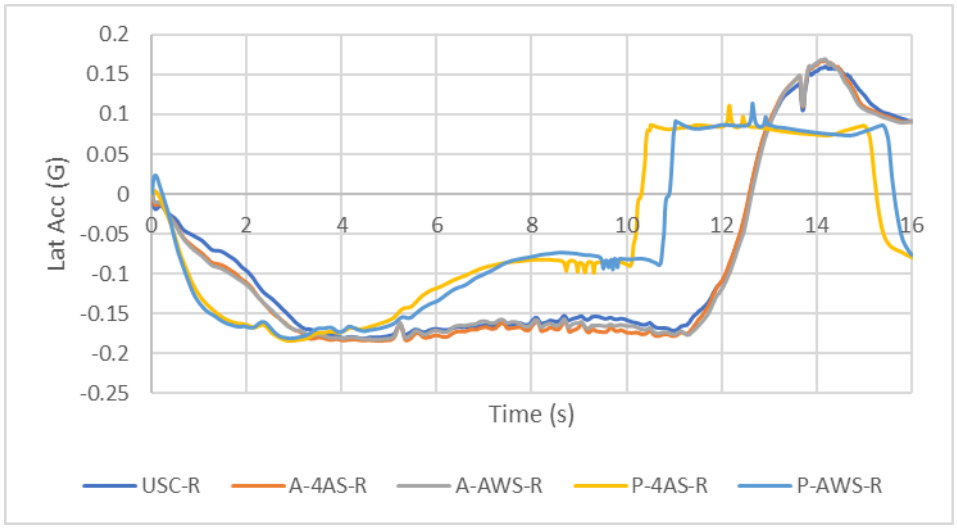

(b)

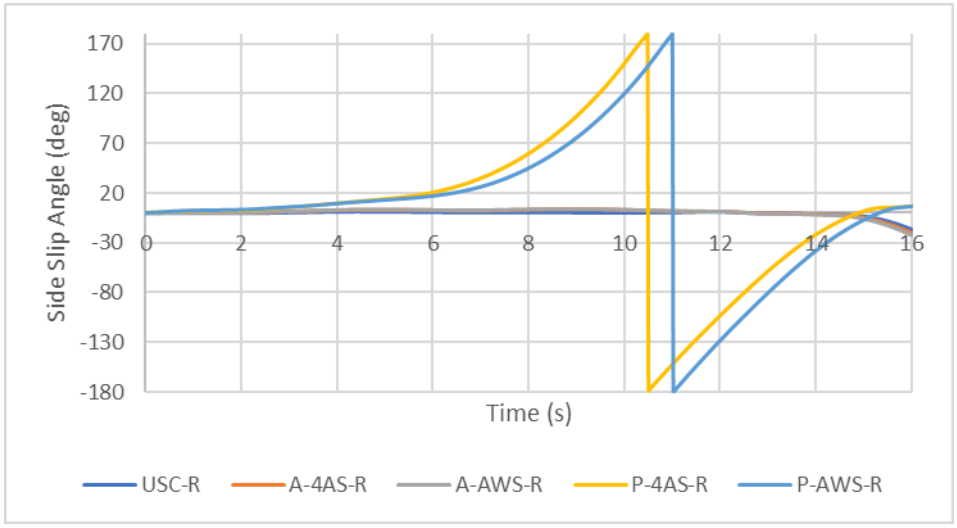

(c)

Figure 6-12 Yaw Rate (a), Lateral Acceleration (b) and Vehicle Side Slip (c) for Rear-Wheel Drive Vehicles on Ice

Through initial observation of the vehicle paths, rear-wheel drive has negligible impact on vehicle performance in terms of yaw rate, lateral acceleration, and vehicle side slip for the ideal road surface condition. However, this can only be said for the A-4AS-R and A-AWS-R configurations and the USC vehicle. For these configurations, yaw rate is within a reasonable range of 10 deg/s, lateral acceleration within 0.3 G or less, and side slip angle no greater than 5 degrees for both normal and low friction surfaces. Where notable performance impact was observed is over the extreme low friction surface. Beyond the 12-second mark of the maneuver, the steering rate is notably sharper than the from the beginning of the maneuver. Yaw rate, lateral acceleration, and vehicle side slip all indicate that a sharp change in steering input on the rear-wheel drive vehicle can induce fishtailing or complete spin-out.

As illustrated by all presented results, the P-4AS-R and P-AWS-R configurations are highly prone to losing control regardless of surface friction. This is shown by the extreme side slip angles, yaw rates and lateral acceleration on both dry asphalt (ideal conditions) in Figure 6-11, and on ice (worst-case conditions) in Figure 6-12, all indicating vehicle spin-out. For these vehicles, yaw rate peaks at 60 deg/s, while lateral acceleration shows anomalous behaviour despite being within considerably stable values. Side slip angles for normal and low friction conditions peak at 180 degrees, further demonstrating the full spin-out behaviour. Therefore, this combination cannot be recommended for use on any condition of road. From this initial test, rear-wheel drive accompanied by the proper steering configuration showed potential as a power-saving mechanism, under ideal road surface conditions only.

6.3 Phase 2 - 100-ft Radius Circle Skid Pad

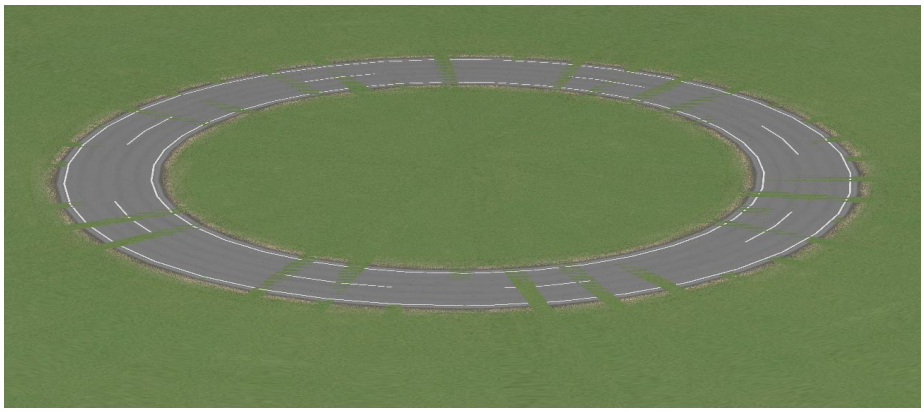

Figure 6-13 100-ft Radius Circle Skid Pad in TruckSim

This test serves as the second phase of evaluation for the high-speed testing category, on which the various vehicle configurations are run on a circle of 100-ft radius (30 m), as shown above in Figure 6-13. A constant acceleration of 6 km/h/s is applied up to a constant target speed of 120 km/h with the intention of observing the performance limits of the unified stability control system. The purpose of this test is to determine the speed at which the vehicle can no longer track the centreline of the circle, thus showing the handling and controllability limits of the vehicle configurations being tested. Rear-wheel drive operation is also tested here. Test results are organized by vehicle configuration, like the first phase.

6.3.1 All-Wheel Drive

Test results for all-wheel drive configurations of the combat vehicle are presented first. Among the all-wheel drive configurations, front-wheel steering will be evaluated first, followed by rear-wheel steering. Figure 6-14(a) below shows the paths of the reference combat vehicle with that of the USC vehicle, while Figure 6-14(b) shows respective vehicle speed behaviour.

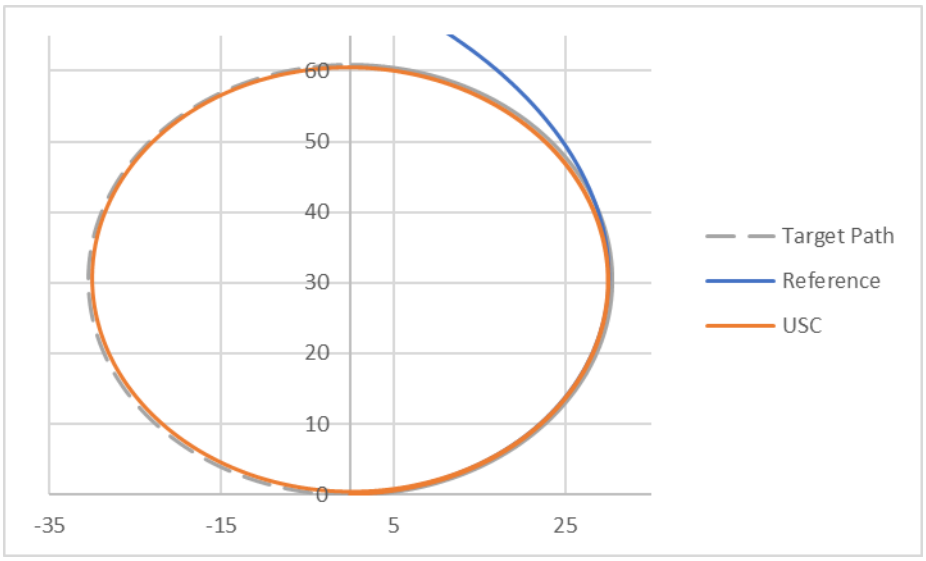

(a)

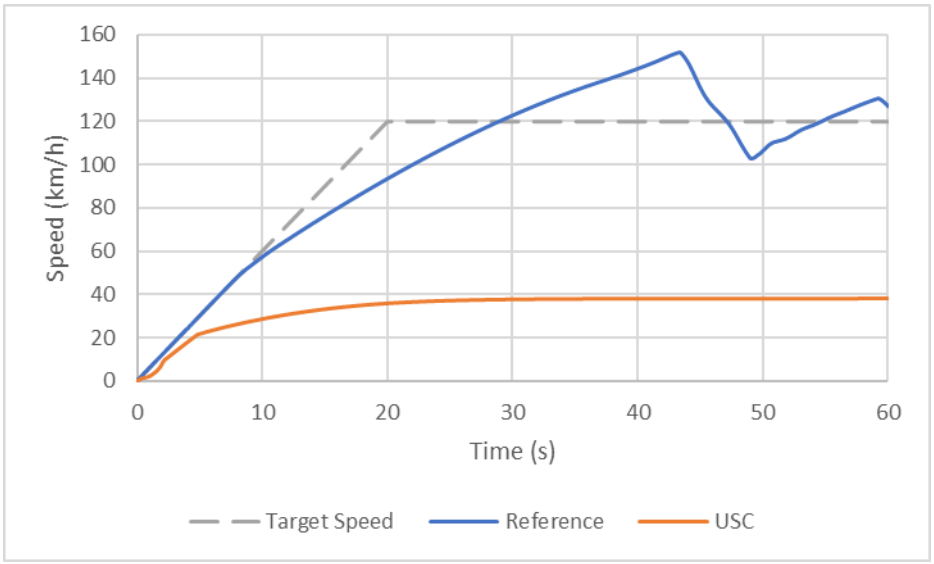

(b)

Figure 6-14 Vehicle Path (a) and Forward Speed (b) of Reference vs. USC Vehicle

The USC vehicle can continuously maintain its course on the circle, while the reference vehicle begins to leave the path entirely. Upon inspection of the vehicle speed trends, the USC vehicle reaches a maximum operating speed of 40 km/h, while the reference vehicle steadily reaches approximately 50 km/h before losing control and leaving the path. This is due to the longitudinal slip regulation intervening when active yaw control is no longer capable of stabilizing the USC vehicle independently during acceleration. This is further illustrated by vehicle performance measures in Figure 6-15 below.

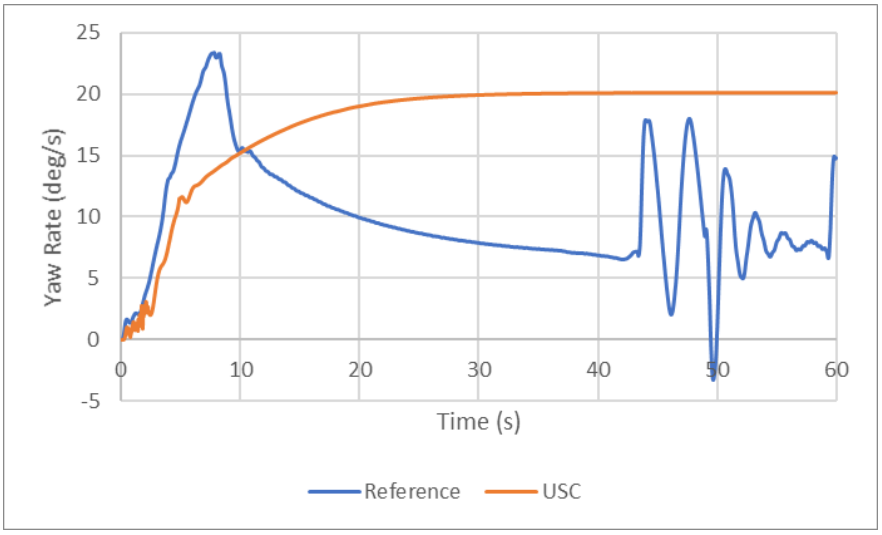

(a)

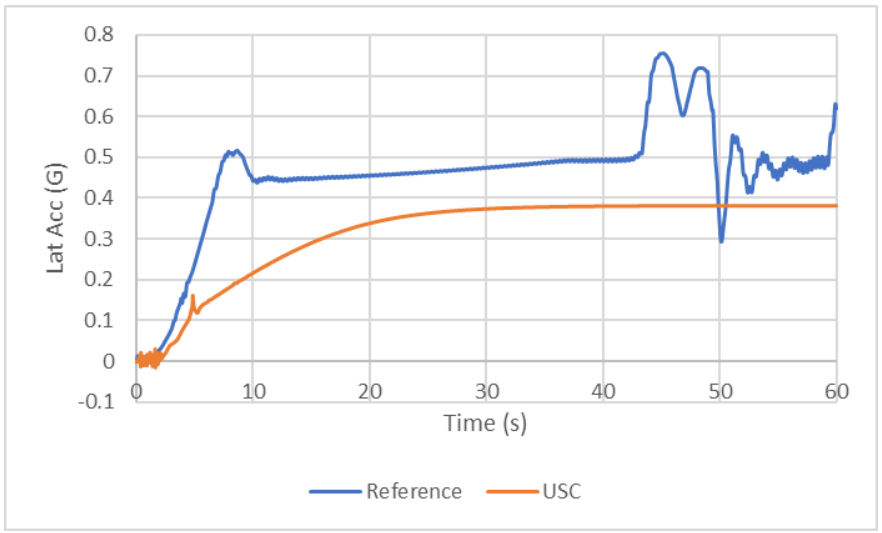

(b)

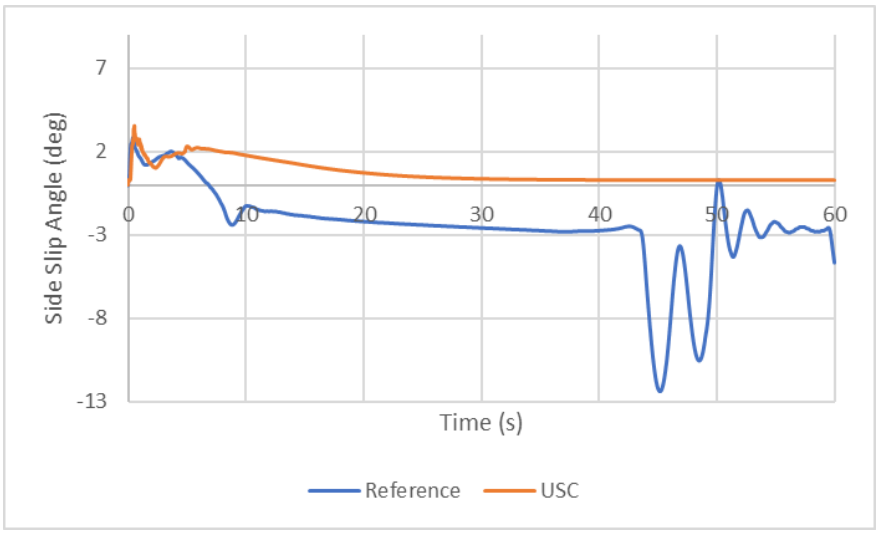

(c)

Figure 6-15 Yaw Rate (a), Lateral Acceleration (b) and Vehicle Side Slip (c) for Reference vs. USC Vehicle

As shown in Figure 6-15(a), the sudden drop in yaw rate coincides with the point in time which the speed of the reference vehicle begins to change its acceleration behaviour. Corresponding lateral acceleration and vehicle side slip also peak then drop. Where lateral acceleration and vehicle side slip begins to gradually rise once more from the 10-second mark onward, yaw rate drops, coinciding with the inability of the reference vehicle to maintain its course on the skid pad.

Conversely, the USC vehicle exhibits a gradual increase in both yaw rate and lateral acceleration up to steady state values of 20 deg/s and 0.36 G, respectively. The vehicle side slip is minimized to near zero at steady state. This is again due to longitudinal slip regulation preventing the motors from spinning the wheels when slip exceeds the 20% threshold. Demonstration of the longitudinal slip control using wheel torques is shown in Figure 6-16 below, where high-frequency on-off switching occurs at the wheels with highest slip to stabilize the vehicle. The individual wheel torques do not exceed a maximum wheel torque of 7200 Nm, while the steady state wheel torque is approximately 5200 Nm.

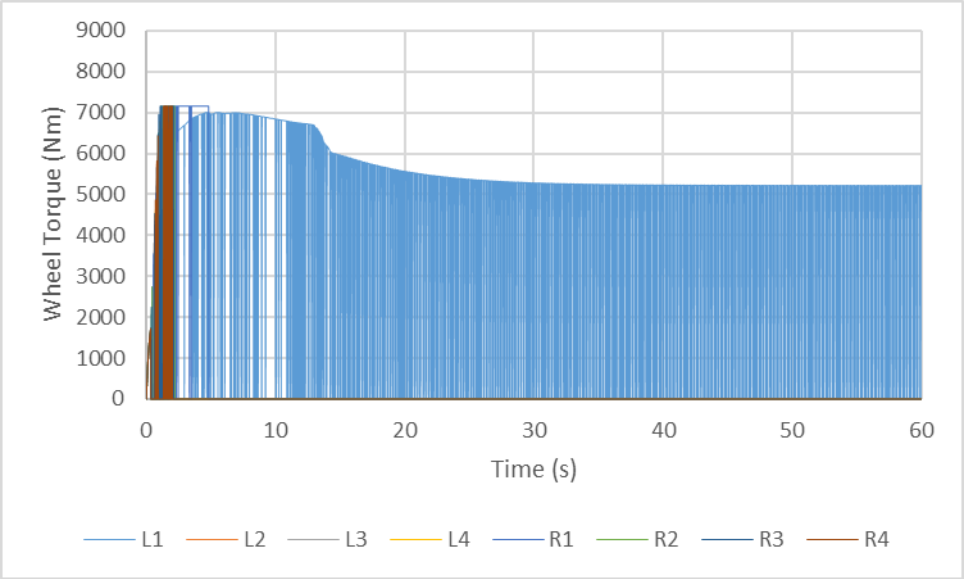

Figure 6-16 Wheel Torque Output from USC Vehicle

Rear steering configurations were then investigated with all-wheel drive. Figure 6-17(a) below shows the path and Figure 6-17(b) shows the speed of the vehicles equipped with respective rear steering configurations. Front-wheel steering with unified stability control is used as the reference vehicle in this set of results.

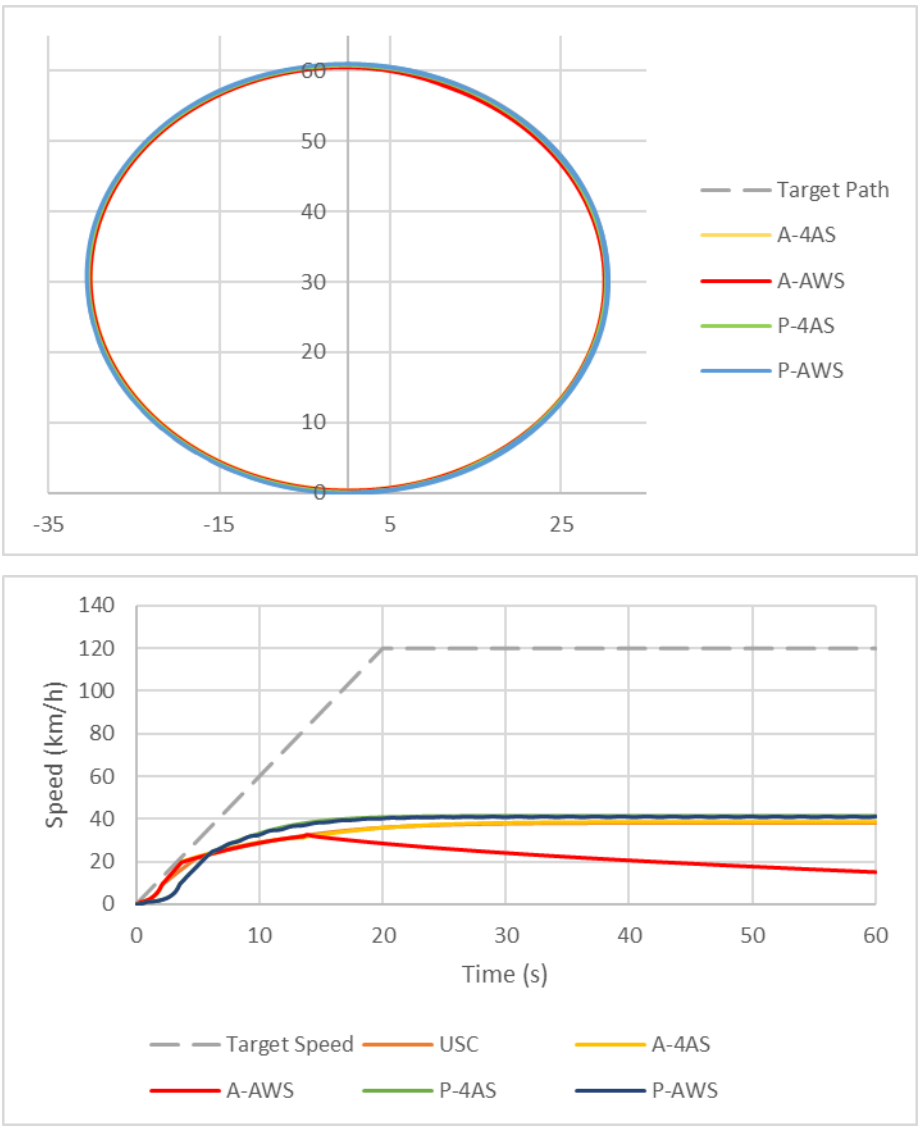

Figure 6-17 Vehicle Path (a) and Forward Speed (b) of Rear Steering Configurations

In terms of vehicle paths, none of the rear-steering configurations tested have shown any notable advantage over another as they all maintain the course. When observing patterns in longitudinal vehicle speed, the A-4AS configuration develops its speed similarly to the USC vehicle. The A-AWS configuration reaches a maximum speed of approximately 30 km/h before progressively dropping for the remainder of the test. Both passive rear steering configurations show an initial 3-second delay before increasing speed, reaching a steady 40 km/h. The P-AWS configuration shows minor oscillation in its acceleration pattern. This indicates that for passive rear-steering configurations, intervention of slip regulation happens much sooner than with other configurations.

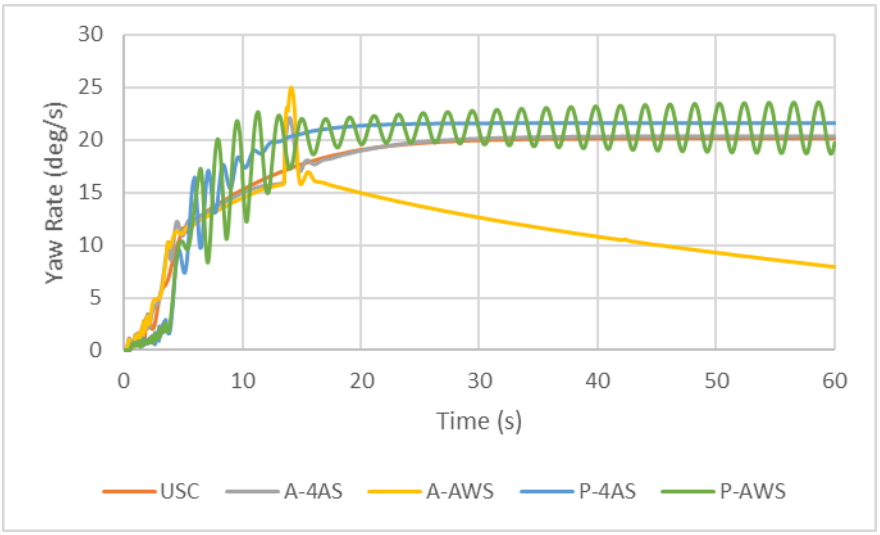

(a)

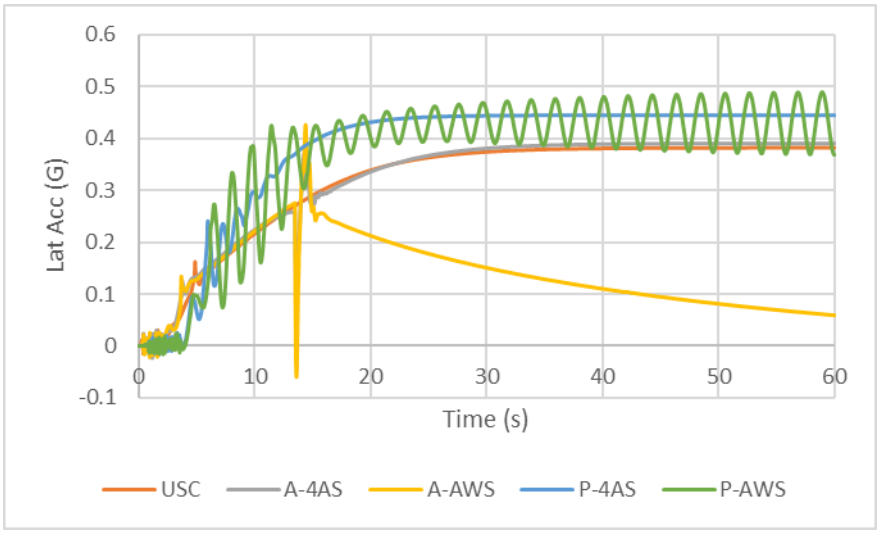

(b)

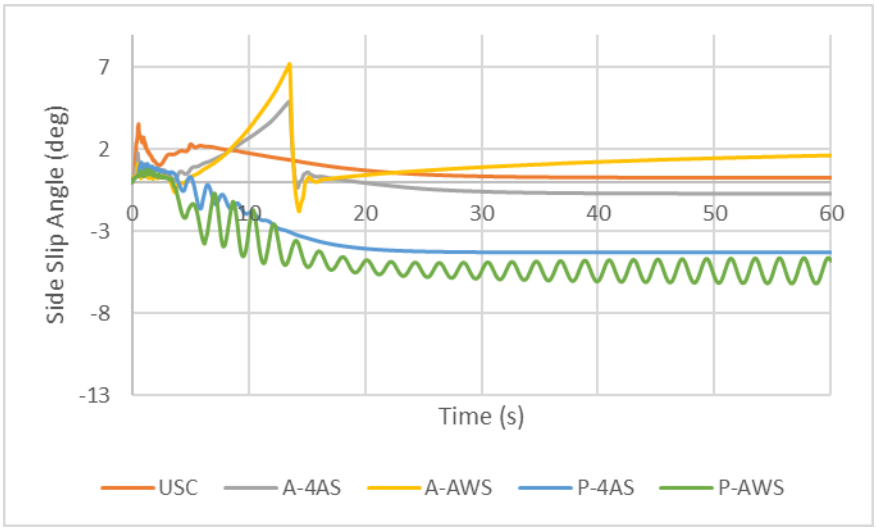

(c)

Figure 6-18 Yaw Rate (a), Lateral Acceleration (b) and Vehicle Side Slip (c) for Rear Steering Configurations

Figure 6-18 above presents the yaw rate, lateral acceleration, and vehicle side slip obtained from testing each rear steering configuration, with the USC vehicle as a baseline for comparison.

For all performance measures, both passive rear-wheel steering configurations exhibit some degree of oscillation in the transient portion of the maneuver before slip regulation intervenes to stabilize the vehicle. For the P-AWS configuration, oscillations continue and slightly increase in amplitude even at steady-state operating speed, indicating that the unified stability control system is operating just within critical stability. In physical operation, this would mean lateral instability during the maneuver, making handling difficult for both human and autonomous control.

The active rear steering configurations show an abnormal spike in all three performance measures close to the 15-second mark. In this case, the vehicle is forced into steady-state speed by slip regulation, effectively creating sudden deceleration. Due to the active rear steering controller using forward speed to control the steering angles of the third and fourth axles, the spike indicates a sudden change in the behaviour of the rear wheels as the vehicle is forced to stop accelerating. This in turn causes the vehicle to momentarily fishtail, then recover, as shown in the vehicle tire path in Figure 6-19 below. It is only the A-AWS configuration that slows down after the fishtailing phenomenon and gradually loses its ability to yaw and maintain course due to intervention of the slip regulator.

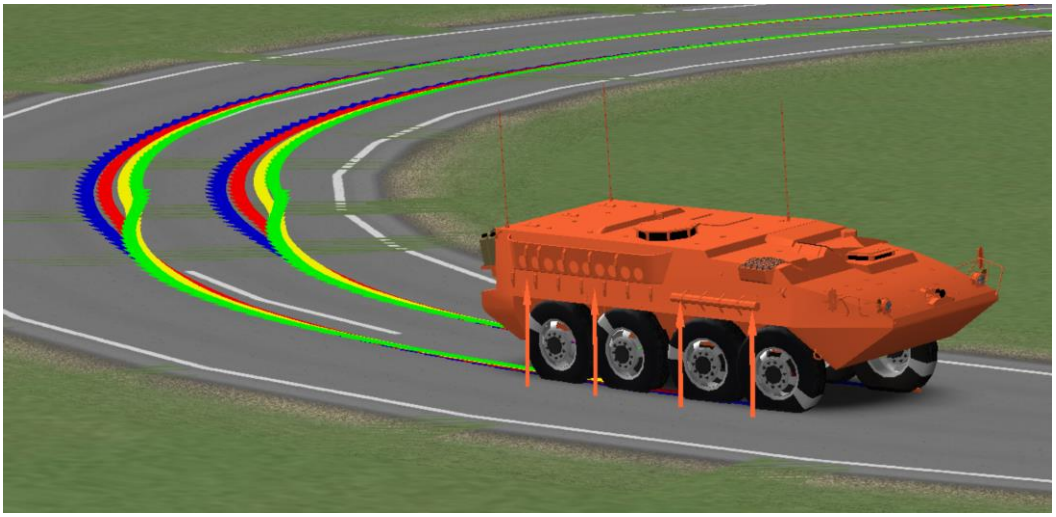

Figure 6-19 Fishtailing Induced by Slip Regulator on A-AWS Configuration

6.3.2 Rear-Wheel Drive

Proceeding all-wheel drive tests, all steering configurations were tested with rear-wheel drive. Figure 6-20(a) below shows the path of the vehicle with each steering configuration tested with rear-wheel drive operation, while Figure 6-20(b) shows vehicle speeds. None of the vehicle configurations with rear wheel drive could complete the full circle course within the allotted time, nor do any exceed a top speed of 10 km/h before slip regulation intervenes and slows the vehicle down. Of all the configurations, the A-AWS configuration has the shortest time in which slip regulation is active, accelerating once more at 45 seconds before slowing down.

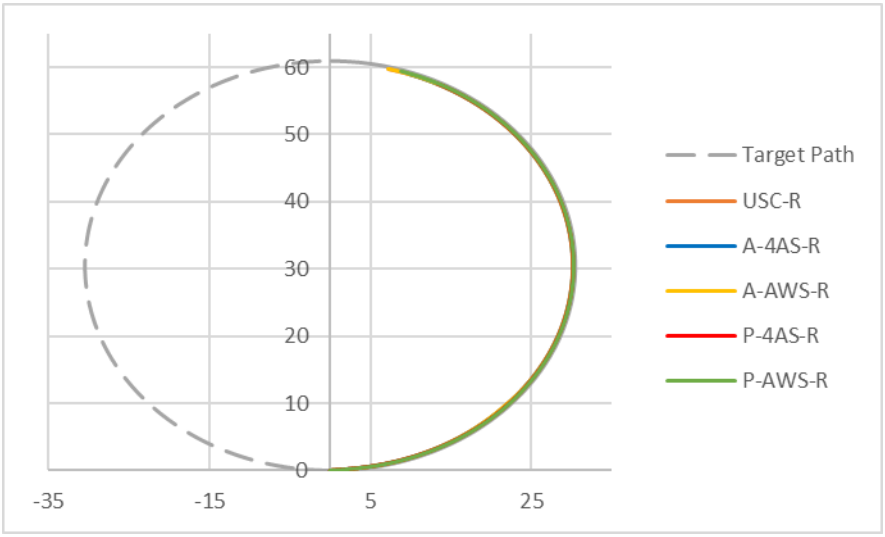

(a)

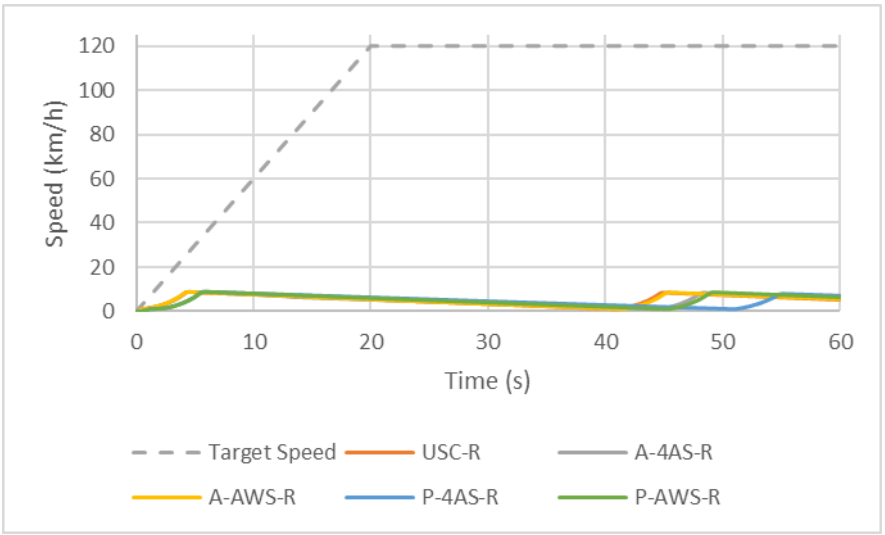

(b)

Figure 6-20 Vehicle Path (a) and Forward Speed (b) of Rear-Wheel Drive Vehicles

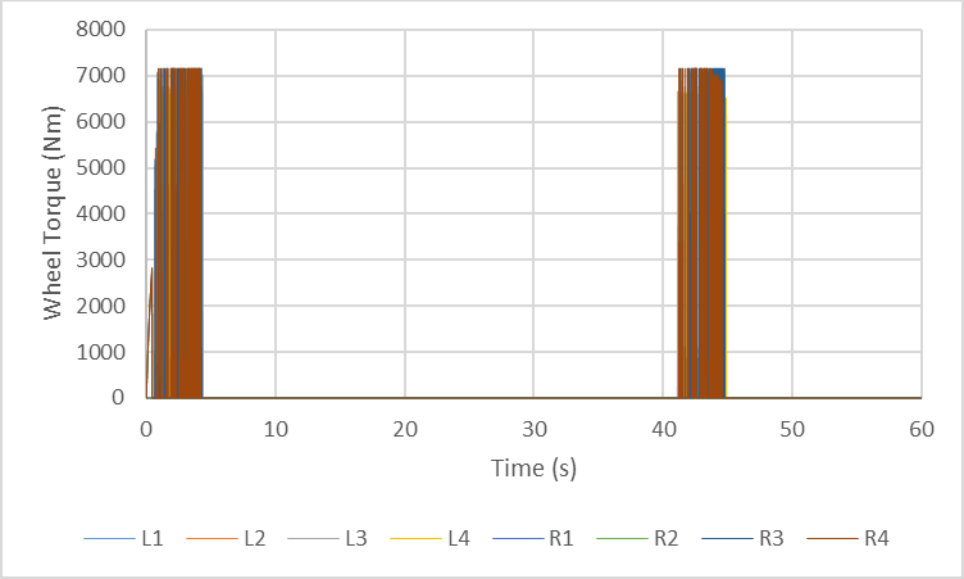

Figure 6-21 Wheel Torque Output from USC-R Vehicle

Figure 6-21 above shows individual wheel torque output from the in-hub drive motors for the USC-R vehicle as an example. The four rear wheels output approximately 7200 Nm during acceleration much like the all-wheel drive vehicle, with high-frequency on-off switching.

Due to excessive wheel slip in the rear however, the slip regulation controller completely turns off the driving motors. This leaves the vehicle to free-wheel until it is slow enough that longitudinal slip is below the 20% threshold and allowing acceleration once more. Due to this torque output pattern, none of the vehicles could accelerate beyond 10 km/h, and must slow down close to 1 km/h before being able to accelerate again. This can be attributed to front-to-rear weight transfer, which results in load too excessive for the rear driven wheels to maintain traction. This is in combination with the lack of assistance from the front wheels.

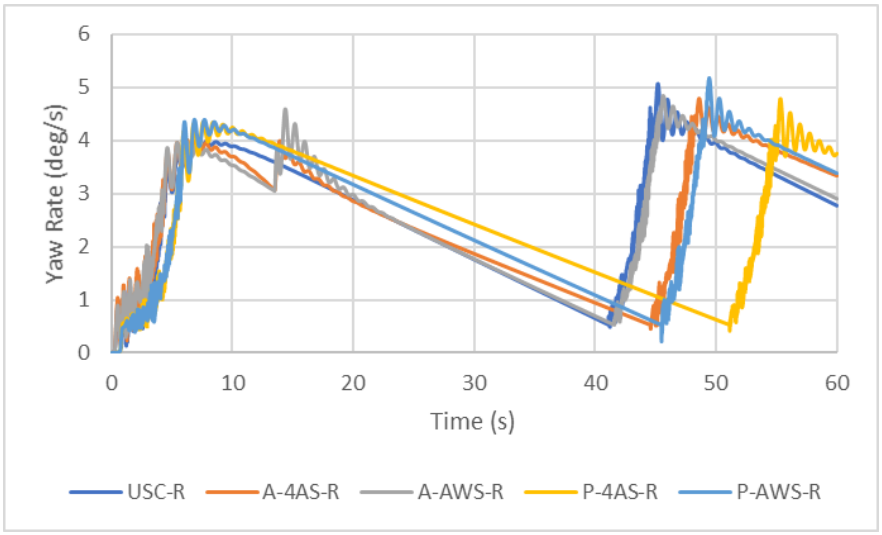

(a)

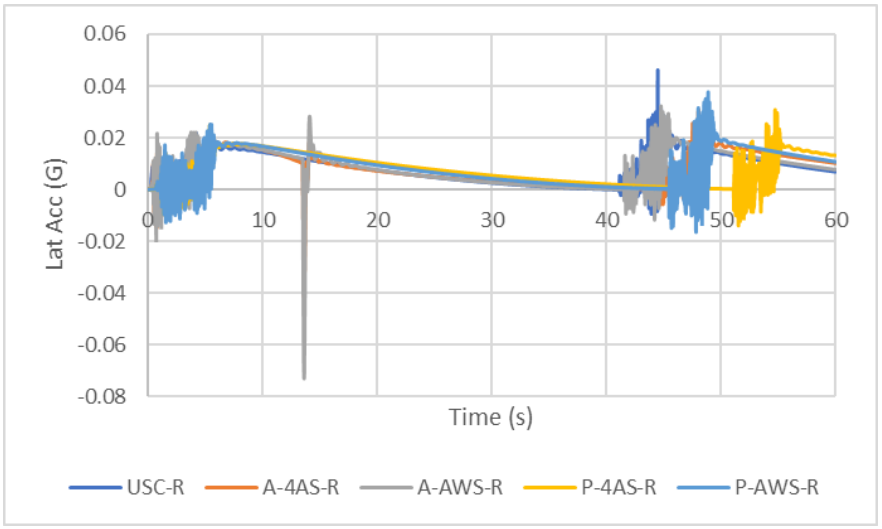

(b)

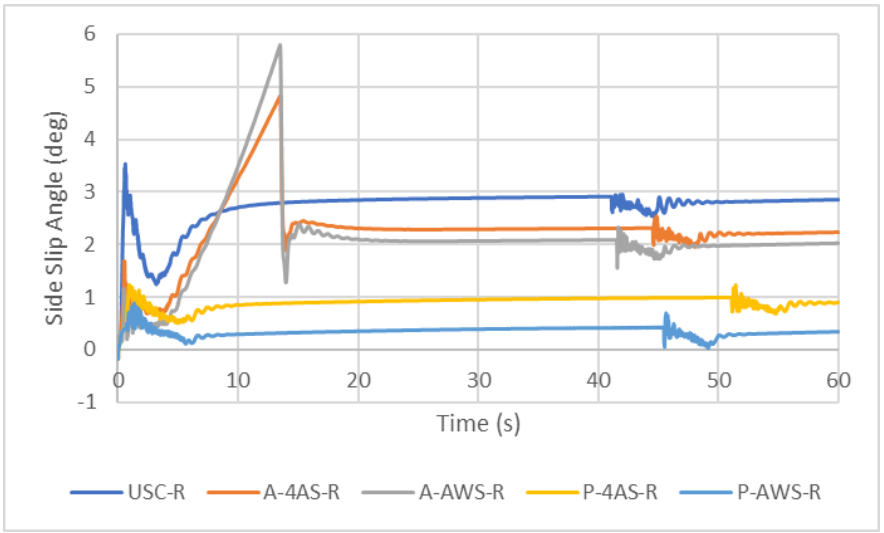

(c)

Figure 6-22 Yaw Rate (a), Lateral Acceleration (b) and Vehicle Side Slip (c) for Rear-Wheel Drive Vehicles

Figure 6-22 above presents the yaw rate, lateral acceleration and side slip of each rear-wheel drive vehicle configuration used in this testing. The all-wheel drive USC vehicle has once again been omitted in these measures due to negligible different with the USC-R vehicle. As with the all-wheel drive counterpart, in rear-wheel drive the active rear steering configurations also exhibit the same spike in all three measures, particularly during the deceleration phase when slip regulation intervenes. This spike indicates a similar fishtail phenomenon as demonstrated in Figure 6-19, earlier. Like the all-wheel drive counterpart, the fishtailing phenomenon is due to the sudden change in rear steering angle during deceleration due to the dependence on speed. This is also due to the relationship between speed and front-to-rear steering ratio being non-linear, as shown in (an earlier chapter).

While all configurations exhibit oscillations for all measures during acceleration due to low operating speed, the passive rear steering configurations perform better at reducing vehicle side slip. Particularly in this scenario, the P-AWS configuration reduces vehicle side slip closest to zero. This is in clear contrast to the results shown with all-wheel drive, which sees higher operation speeds that render the passive configurations unstable and favor the active configuration. In both all-wheel drive and rear-wheel drive tests, the passive configurations do not show the spiking phenomenon, as they are not dependent on speed to vary the steering geometry.

6.4 Phase 3 - FMVSS 126 Electronic Stability Control (ESC) Test

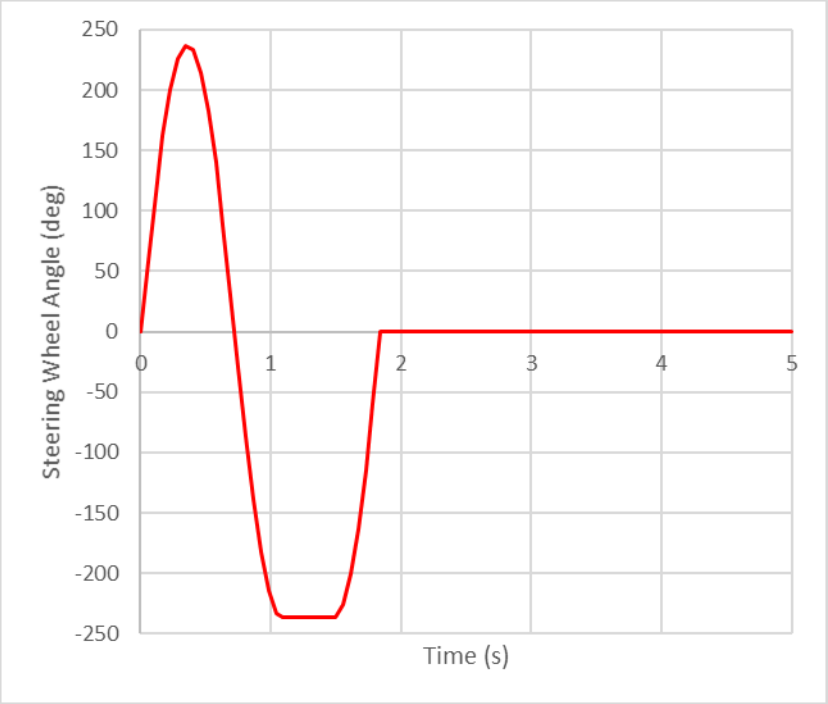

Figure 6-23 Steering Curve for FMVSS 126 EST Test [7]

The electronic stability control (ESC) test, established by the Federal Motor Vehicle Safety Standard (FMVSS) 126 serves as the third phase of testing and evaluation for the high-speed operation. It is an open-loop steering maneuver like the first phase, however a standard steering curve is used as opposed to one recorded from a reference vehicle. Like the first phase of testing there is no target path to follow. This test is for evaluating vehicle stability as it reacts to the given steering input, as shown above in Figure 6-23. The maneuver consists of a sine wave steering curve with an amplitude of 236.8 degrees and a frequency of 0.7 Hz, and a small dwell at -236.8 degrees. This test is performed over a flat surface with normal and reduced surface friction levels, both at 60 km/h and 80 km/h. At these speeds, the active rear steering controller will turn the rear wheels in the same direction as the front. Rear-wheel drive is omitted from this test phase and onward due to its lack of power delivery and lateral stability determined in previous test phases. Test results are organized by speed and road surface friction, as the number of usable vehicle configurations has been reduced.

6.4.1 60 km/h on Dry Asphalt (μ=0.8)

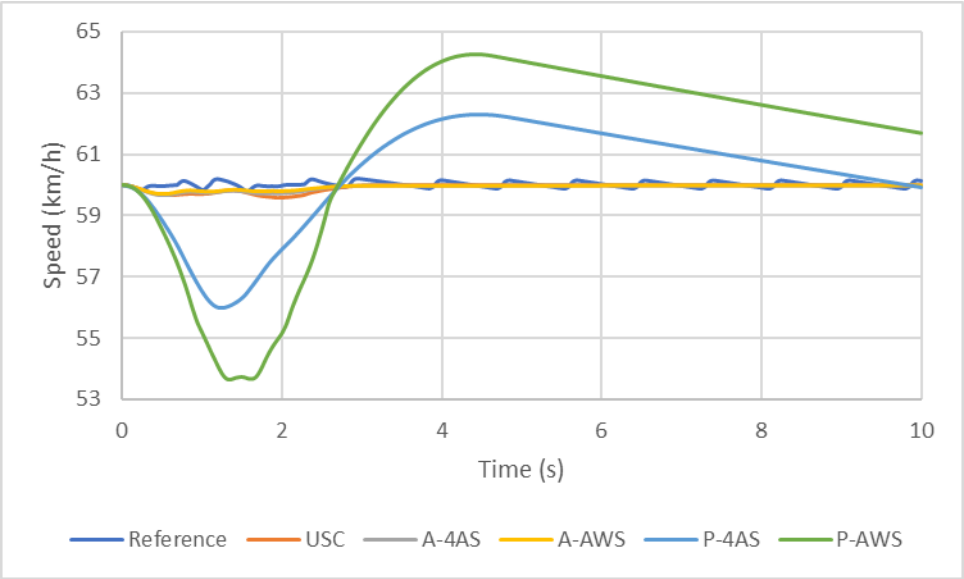

Figure 6-24 Vehicle Speeds on 60 km/h Dry Asphalt Test

Figure 6-24 above shows the pattern in longitudinal speed of each vehicle used in this test. The front-wheel steered vehicle with unified stability control could stay close to the 60 km/h target without oscillation throughout the entire test compared to the uncontrolled conventional vehicle. The addition of active rear steering further improves ability to maintain speed, indicating that the vehicle is better able to retain lateral stability given sharp, sudden changes in steering input. Using passive rear steering configurations, the large fluctuation in vehicle speed suggested lateral instability or difficulty in handling the vehicle. The P-AWS configuration showed the worst control, with a difference in operating speed of up to approximately 6 km/h from the target.

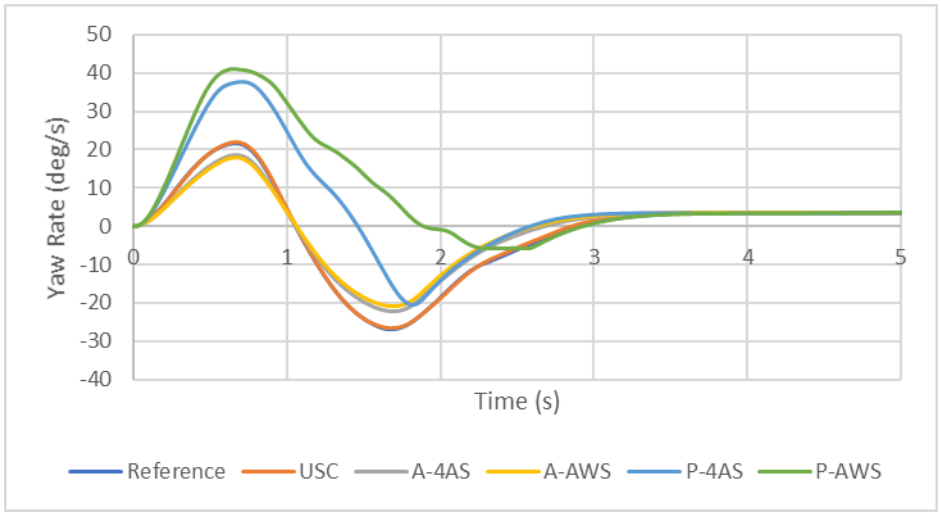

(a)

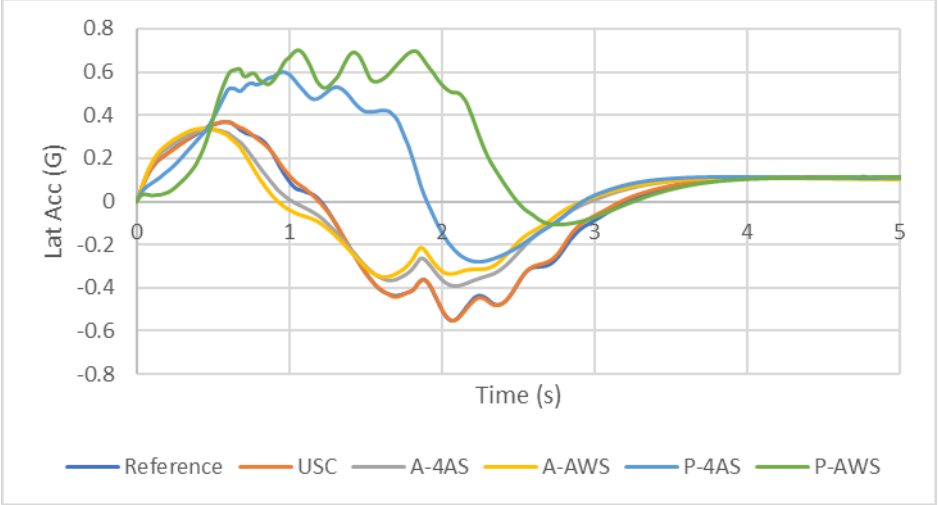

(b)

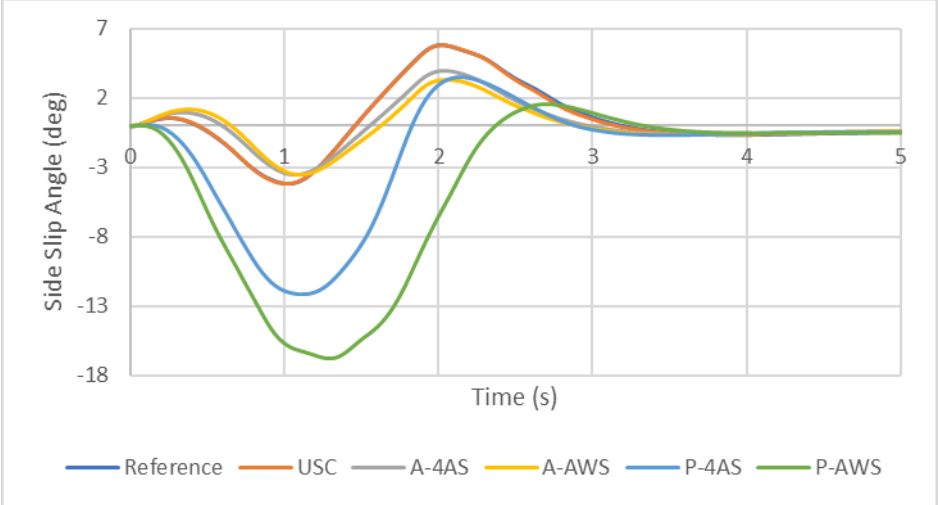

(c)

Figure 6-25 Yaw Rate (a), Lateral Acceleration (b) and Vehicle Side Slip (c) on 60 km/h Dry Asphalt Test

Figure 6-25 above shows the yaw rates, lateral acceleration, and side slip of all the vehicle configurations tested on this maneuver. On these conditions, both reference and USC vehicles show no notable difference in performance. It is with the rear steering configurations where performance changes.

Using the active rear steering configurations – which at the given speeds steer the rear wheels in direct accordance with the front – all measures of performance are reduced significantly. Yaw rate and side slip slightly reduced compared to the front-wheel steered vehicles, while lateral acceleration is both reduced with anomalous behavior greatly damped. The A-AWS configuration at this speed serves to best stabilize the vehicle compared to A-4AS in response to the sharp steering input of the maneuver, keeping lateral acceleration within 0.3 to 0.4 G and side slip closer to 3 degrees.

With either of the passive rear steering configurations – in which the rear wheels are turned directly opposite to the front – the initial yaw rate of the vehicle is double that of the front-wheel steered counterparts. During the transition portion after the 1-second mark in which the steering wheel is turned opposite, yaw rate is notably lower, indicating that with passive configurations the vehicle is unable to recover after a heavy yaw motion. This is further supported by the lateral acceleration and side slip, both of which are higher than typical stable conditions. This is most notable for the P-AWS configuration. The large side slip and lateral acceleration indicate fishtailing which would be induced by the rear wheels being steered opposite to the front.

6.4.2 60 km/h on Ice-Covered Surface (μ=0.2)

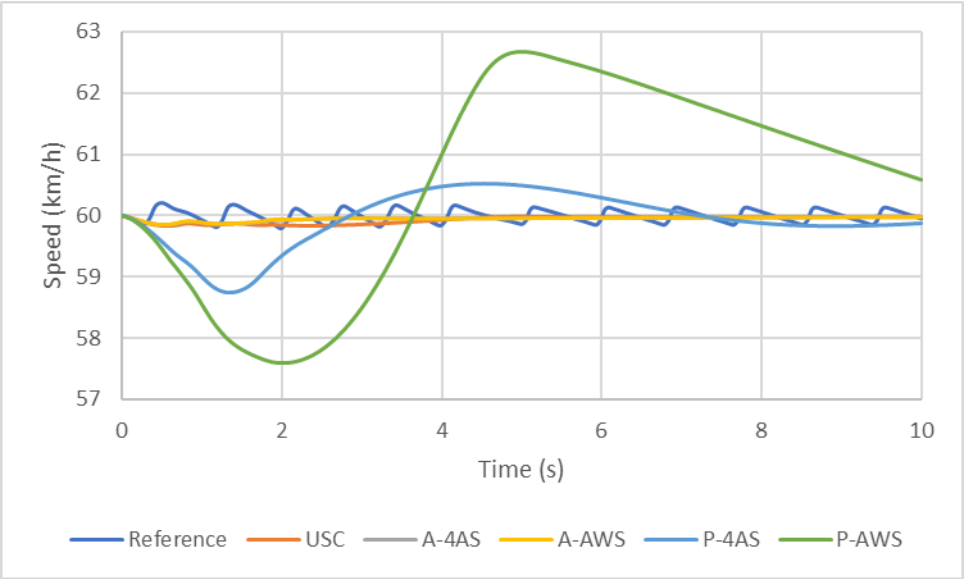

Figure 6-26 Vehicle Speeds on 60 km/h Ice Test

Figure 6-26 above shows the pattern in longitudinal speed of each vehicle used in this test. Again, the vertical axis of the plot was limited to better visualize the results of the more stable vehicles. The range of oscillation in vehicle speed for the reference vehicle is slightly larger on this reduced surface friction condition compared to the previous dry surface test, which is to be expected as this indicates more difficulty in controlling the vehicle over such road. Compared to the dry surface test, all configurations which include the unified stability control system have shown a smaller operating margin. The most notable reduction in speed variation compared to the previous test is with the P-AWS configuration, with a variation of ±2.5 km/h, as opposed to the previous ±6 km/h. This is due to the greater intervention of the unified stability control system over low-friction conditions, as witnessed in the first phase of testing. Despite smaller operating margins, the trends in vehicle speed fluctuation were similar to those observed on the previous dry surface test.

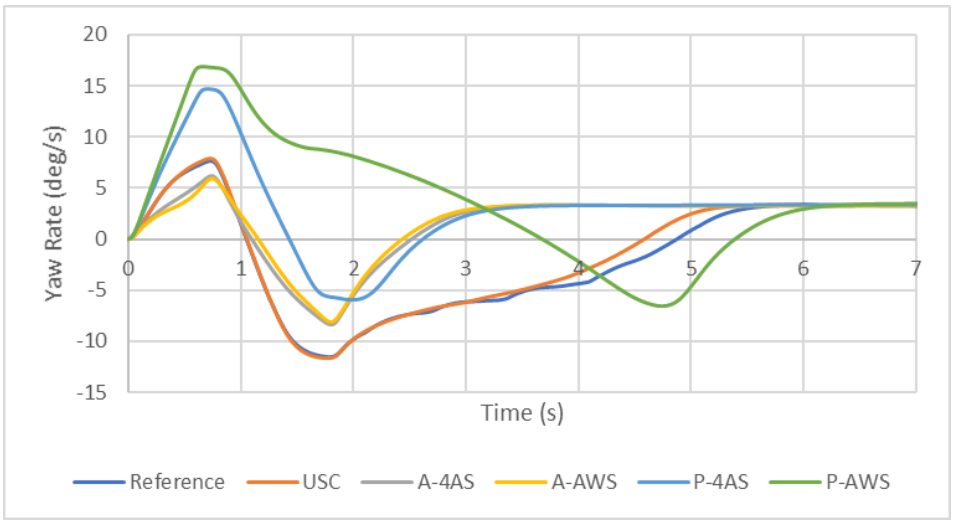

(a)

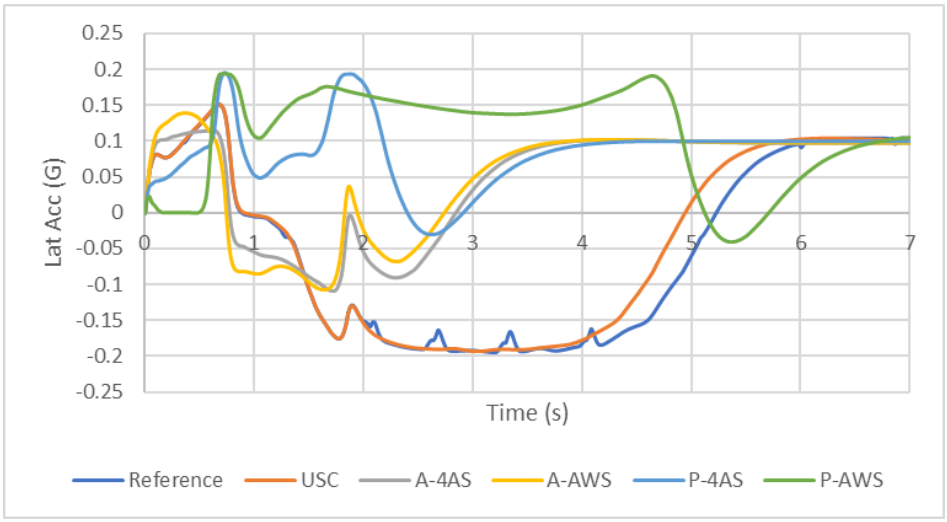

(b)

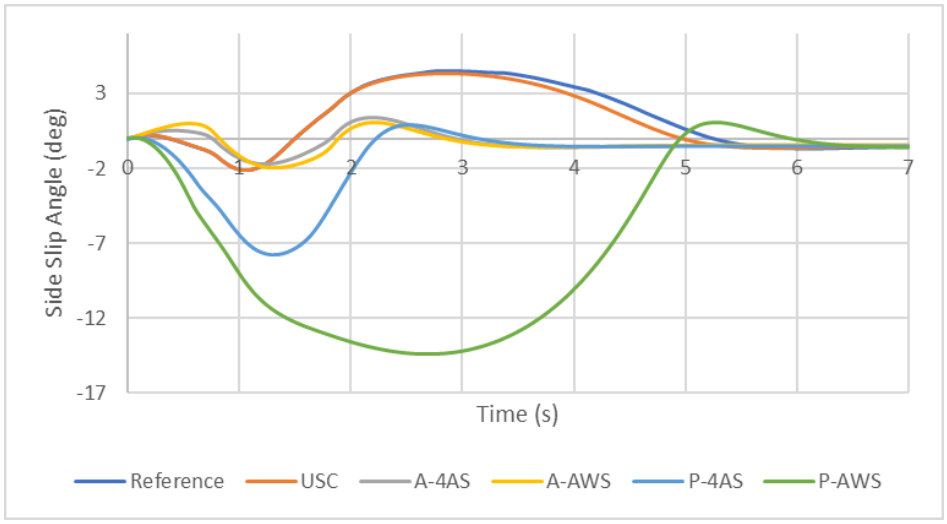

(c)

Figure 6-27 Yaw Rate (a), Lateral Acceleration (b) and Vehicle Side Slip (c) on 60 km/h Ice Test

Coinciding with the smaller range in speed variation, the yaw rates, lateral acceleration, and side slip also show smaller variations as shown above in Figure 6-27. This is again due to the greater intervention of the unified stability controller over the low-friction condition, which is evident when comparing the reference vehicle to the USC vehicle. With the unified stability control system, yaw rate and vehicle side slip are notably damped after the 2-second mark, after which the steering wheel is returned to zero degrees. Around the same time range, anomalous spikes in lateral acceleration are also eliminated with the use of the unified stability controller. This shows that the controlled vehicle is much easier to handle and recover after sharp changes in steering.

With active rear steering, vehicle handling and stability is further improved when working in parallel with the unified stability controller. Yaw rate, lateral acceleration and vehicle side slip are greatly reduced, most notably after the 2-second mark when steering is returned to zero. As with the previous test, the A-AWS configuration performs better than the A-4AS configuration.

Using the passive rear steering configurations, yaw rates, lateral acceleration and side slip are greatly increased and show unusual behavior. The P-AWS configuration exhibited the largest of each measure, showing that on such conditions this configuration is not ideal for ease of handling or maneuverability. The vehicle side slip shows that given low-friction conditions, the response of the vehicle body to driver input is greatly delayed compared to all other configurations.

6.4.3 80 km/h on Dry Asphalt (μ=0.8)

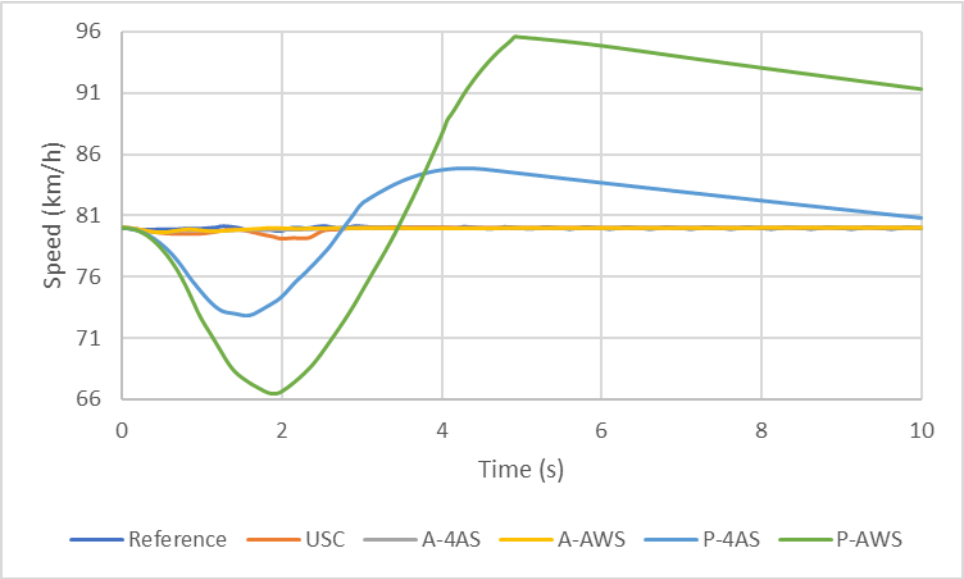

Figure 6-28 Vehicle Speeds on 80 km/h Dry Asphalt Test

Figure 6-28 above shows the pattern in longitudinal speed of each vehicle used in this test. With the target at 80 km/h, variations in speed are slightly greater than compared to the 60 km/h target speed. The reference vehicle once again oscillates around 80 km/h target, while the USC vehicle falls below the target during the transient portion of the test and maintains a constant 80 km/h after recovering with no oscillation. Variations in speed when supplementing the vehicle with active rear steering are further reduced, especially with the A-AWS configuration, indicating improved stability. With the passive rear steering configurations, the vehicle was difficult to handle and did not respond well to the given steering input. The difference between the lowest and highest speed recorded was up to 30 km/h for the P-AWS configuration. Conversely, the difference between the lowest and highest speed recorded for the P-4AS configuration was only 15 km/h.

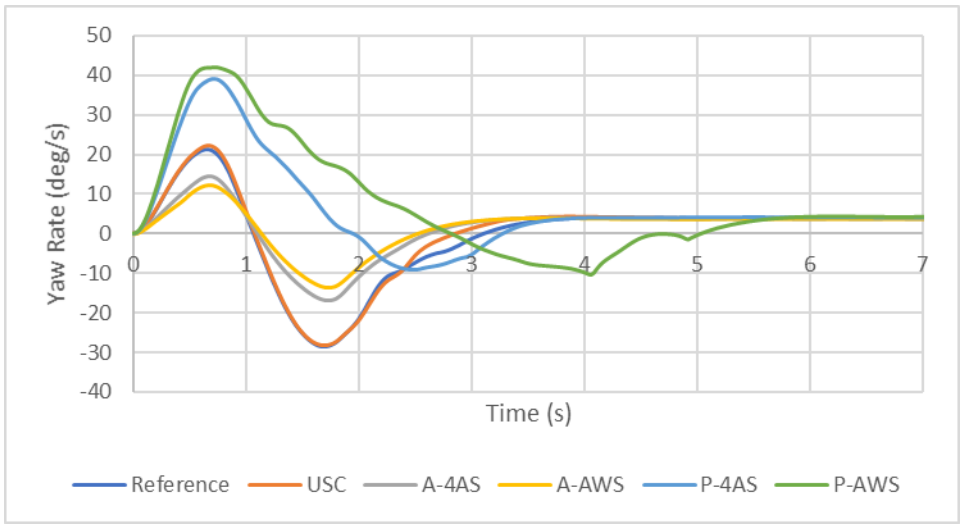

(a)

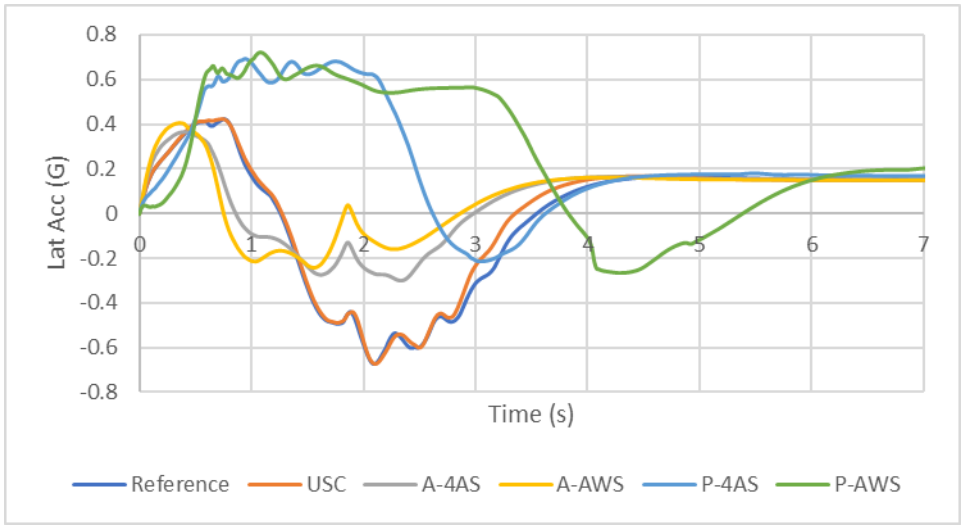

(b)

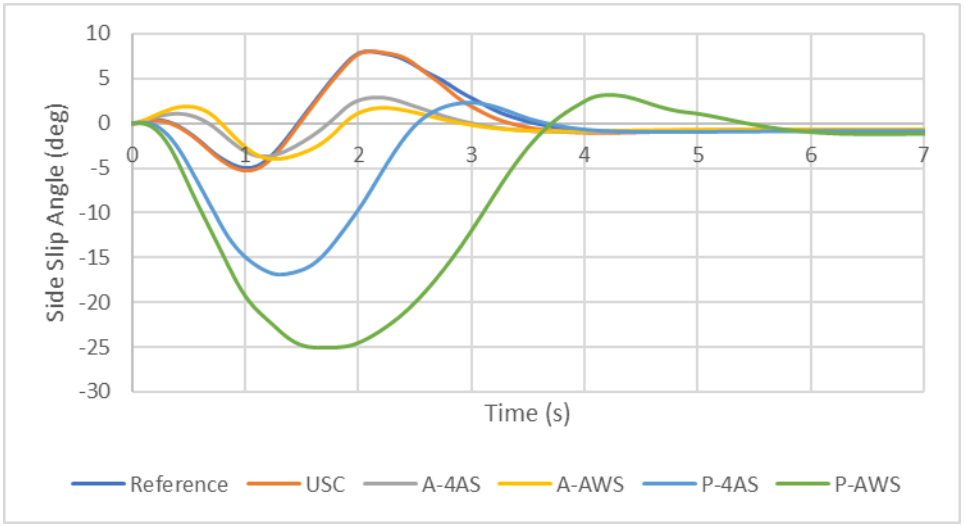

(c)

Figure 6-29 Yaw Rate (a), Lateral Acceleration (b) and Vehicle Side Slip (c) on 80 km/h Dry Asphalt Test

Figure 6-29 above presents the yaw rates, lateral acceleration and side slip of each vehicle used in this test. At 80 km/h, the yaw rates for each configuration are like those found at 60 km/h, given the same surface. The yaw rate of the USC vehicle is more damped compared to the reference vehicle after the recovery portion of the steering maneuver. The damping effect is more pronounced at 80 km/h compared to 60 km/h. This shows that with more extreme operating conditions, the controller is providing more intervention to allow the vehicle to respond faster to the recovery steer and making the vehicle easier to handle. This increased damping trend is also reflected in the lateral acceleration and side slip of both controlled and uncontrolled front-steered vehicles.

When using active rear steering configurations, all three measures are greatly reduced as similarly observed in the 60 km/h test. Despite the higher operating speed, the vehicle is kept within a stable operating range of vehicle side slip, well within driver controllability. As with the preceding 60 km/h tests, the active all-wheel steering configuration performs best in improving vehicle stability and ease of handling.

The passive rear steering configurations amplify the overall instability of the vehicle at higher speeds. This is particularly noticeable with the P-AWS configuration. While yaw rate and lateral acceleration are similar at 60 km/h, peak vehicle side slip is increased to 25 degrees from 15 degrees. Thus, with either passive rear steering configuration, risk of fishtailing and spin out is greater at higher speeds even on ideal surfaces, making this vehicle configuration much more difficult to handle if driven aggressively.

6.4.4 80 km/h on Ice-Covered Surface (μ=0.2)

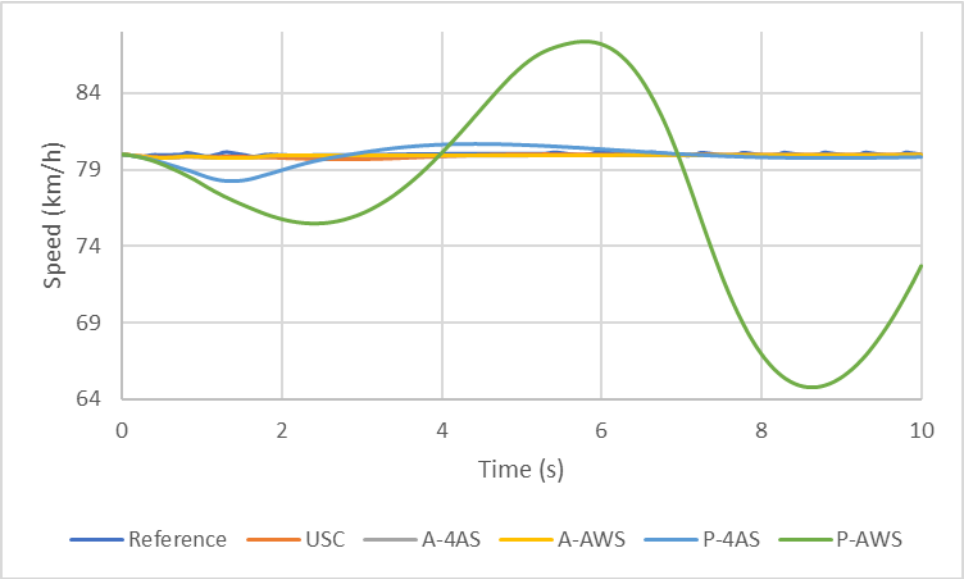

Figure 6-30 Vehicle Speeds on 80 km/h Ice Test

Figure 6-30 above shows the pattern in longitudinal speed of each vehicle used in this test. Like with the 60 km/h low friction test, the variation gap in speed is much smaller. This is most notable with the passive all-wheel steering configuration in which the difference between the lowest and highest recorded speed was approximately 22 km/h as opposed to the 30 km/h gap in the previous test. The reduction in difference is due to greater interference of the unified stability controller as the road surface friction is reduced. Unlike the passive fourth-axle steering configuration, the trend in vehicle speed for the passive all-wheel steering is much different and more unpredictable in this scenario compared to previous tests in which a similar trend was observed between the two. Recorded vehicle speed trends for the USC, A-4AS and A-AWS configurations were stable with little variation in response to the maneuver. The reference vehicle showed abnormal oscillation past the point in which steering is returned to zero.

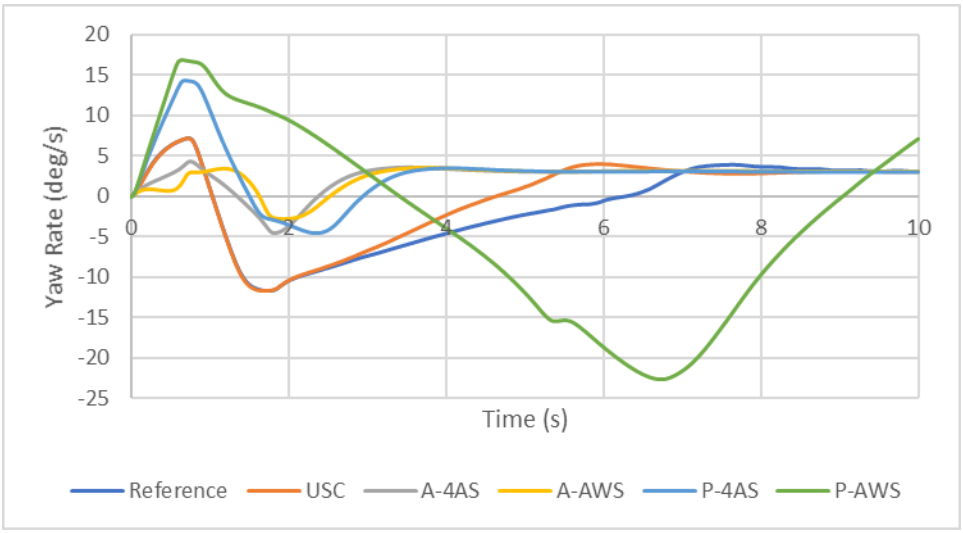

(a)

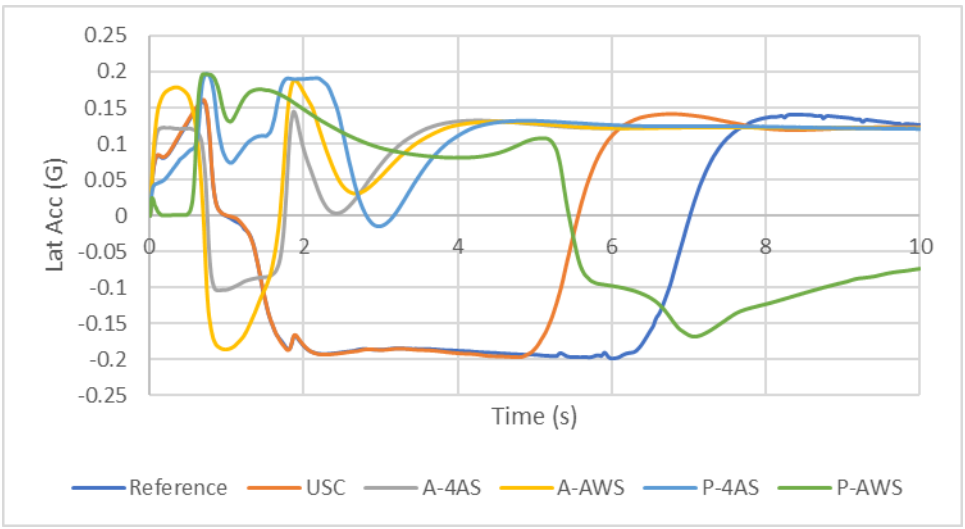

(b)

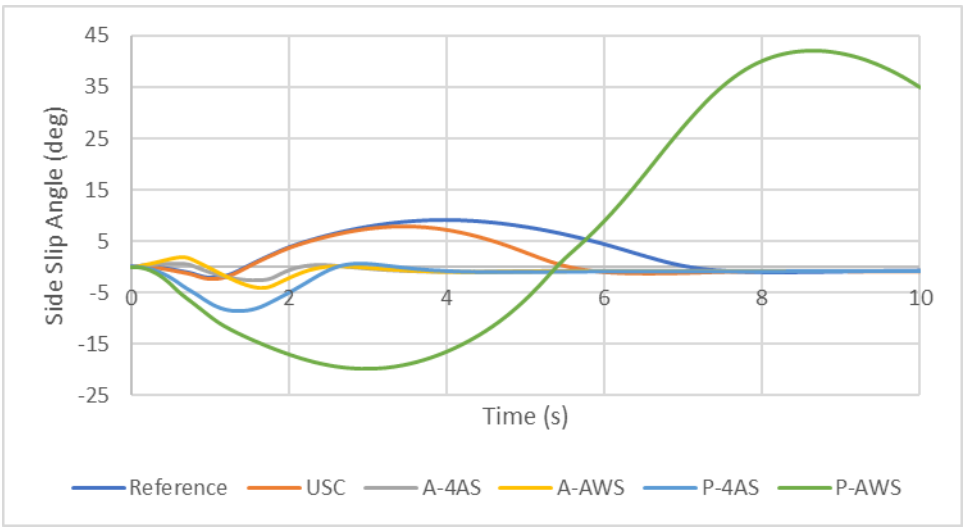

(c)

Figure 6-31 Yaw Rate (a), Lateral Acceleration (b) and Vehicle Side Slip (c) on 80 km/h Ice Test

Figure 6-31 above presents the yaw rates, lateral acceleration and side slip for the vehicle configurations used in this test. At 80 km/h and extremely low friction, the intervention of the unified stability control system is most evident when compared to the previous tests. When observing the USC vehicle against the reference vehicle, all three measures indicate a faster and more stable response to steering input is achieved. This is shown by the yaw rate, lateral acceleration and side slip reaching zero as much as one second sooner than with the reference vehicle.

Implementing active rear steering configurations in this test have shown to further reduce yaw rate, lateral acceleration, and side slip significantly. Active rear steering also delivers the benefit of significantly faster vehicle motion response to input. This is again observed when all three measures go to zero after the steering wheel is fixed to center after the 2-second mark. The A-AWS configuration once again performed best, reducing the delay in response by as much as three seconds. Overall, this leads to significantly improved maneuverability over extreme conditions compared to relying only on the unified stability controller on a front-wheel steered vehicle.

With the P-4AS configuration, the yaw rate, lateral acceleration, and side slip indicate only slightly worse performance compared to either of the active rear steering configurations on this test. This phenomenon was also observed in the previous 60 km/h test over low friction. The least stable configuration is the P-AWS, in which no measures directly correspond to vehicle motion relatable to the steering input. The extremely high side slip exhibited by this configuration suggests lateral sliding or rear fishtailing of the body.

6.5 Phase 4 - NATO Double Lane Change (AVTP 03-160W)

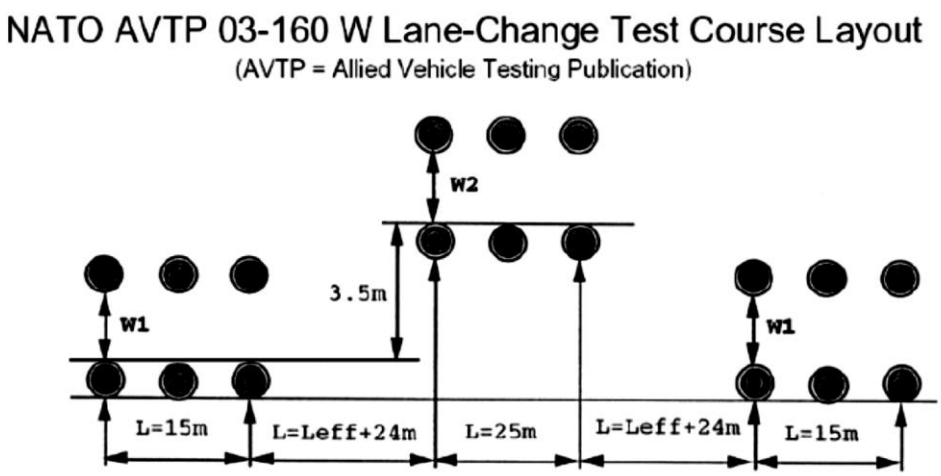

Figure 6-32 Standard Layout of Double Lane Change Test (Source: GDLS-C)

The fourth phase of the high-speed operation tests is a double lane change maneuver standardized for evaluation of NATO allied combat vehicles. The purpose of this test is to evaluate both handling capability and lateral stability in a transient maneuver. Figure 6-32 shows the path layout and cone layout used for the double lane change maneuver in this work. Cone spacing and path dimensions are dependent upon the physical dimensions of the vehicle being tested, as dictated by the testing standard. Thus, the double lane change maneuver has been customized specifically for the vehicle in this work. Regardless of size, the vehicle must not touch any of the cones during the test. In this work, the vehicle is tested with all configurations except rear-wheel drive at speeds of 60 km/h and 80 km/h. Ultra low friction (ice conditions) are also tested at 60 km/h. For this final phase of testing, results are sorted out by speed and road surface friction.

6.5.1 60 km/h on Dry Asphalt (μ=0.8)

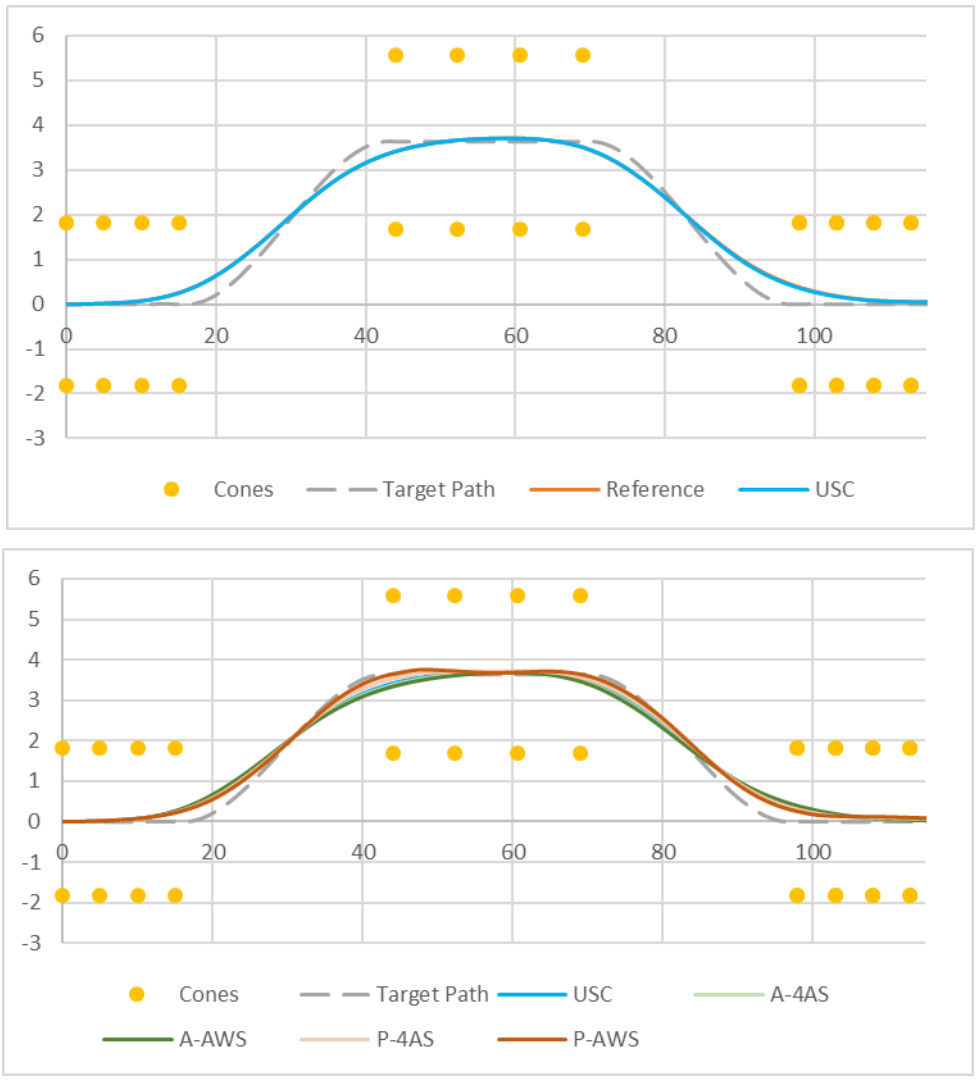

Figure 6-33 Vehicle Paths on 60 km/h Dry Asphalt Double Lane Change

Figure 6-33(a) presents the paths of the reference and USC vehicles. In comparing both front-wheel steered vehicles, it was observed that the unified stability control system provided no effect on path following ability. Figure 6-33(b) shows the paths of all rear-steering configurations used against the USC vehicle as a baseline. When equipped with passive rear steering, the vehicle can follow the target path much closer, more notably with P-AWS. The observed behaviour is contrary to the active rear steering configurations, which move farther away from the target path compared to the front-wheel steered vehicle. In this test, none of the vehicles hit the cones, hence all pass the maneuver successfully.

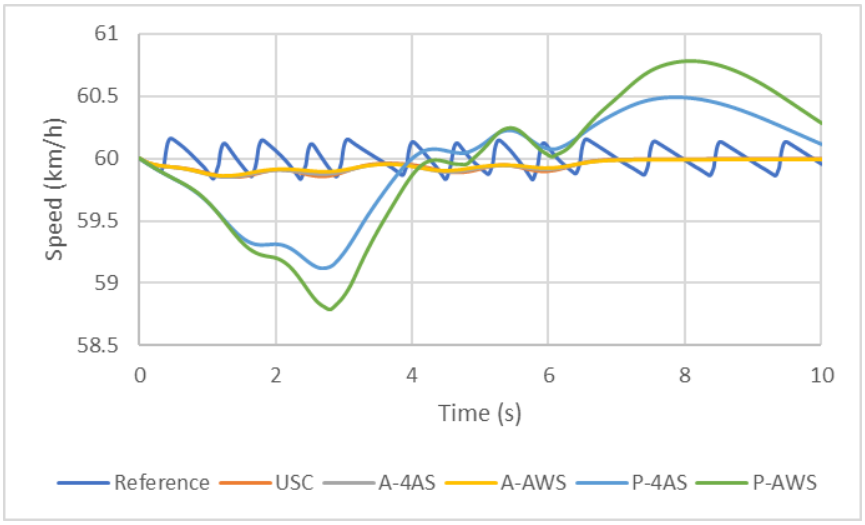

(a)

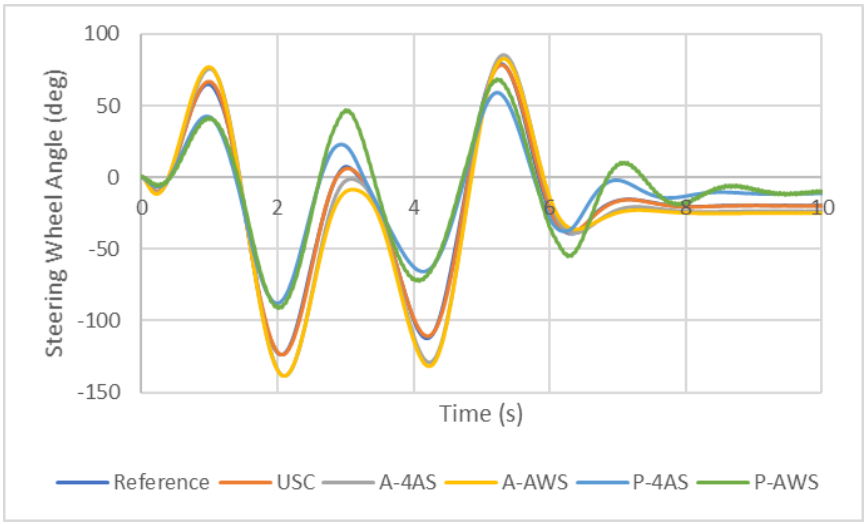

(b)

Figure 6-34 Vehicle Speeds (a) and Steering Input Effort (b) on 60 km/h Dry Asphalt Double Lane Change

Figure 6-34 above presents the speed and steering wheel input effort for each vehicle in this test. In comparing both the reference and USC vehicles, the USC vehicle has no advantage on steering input effort. However, the USC vehicle maintains a steady pattern in speed contrary to the oscillation of the reference vehicle. While with the passive rear steering configurations, the steering input effort is reduced but large variations in speed are observed. With the P-AWS configuration, small continuous oscillations are observed, indicating undesirable mechanical feedback from the road. Both active rear steering configurations slightly increase the steering input effort, but implementation of either allows the vehicle to maintain constant speed in a more stable manner compared to the passive configurations.

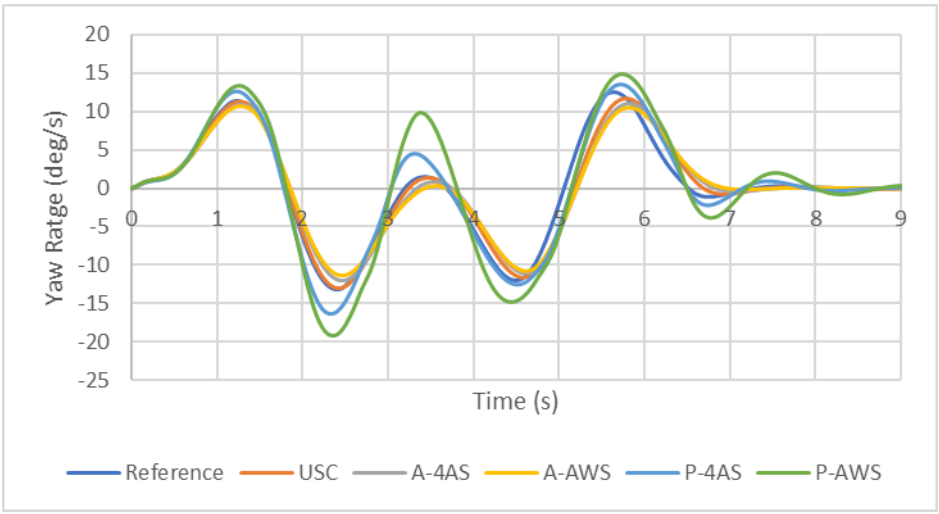

(a)

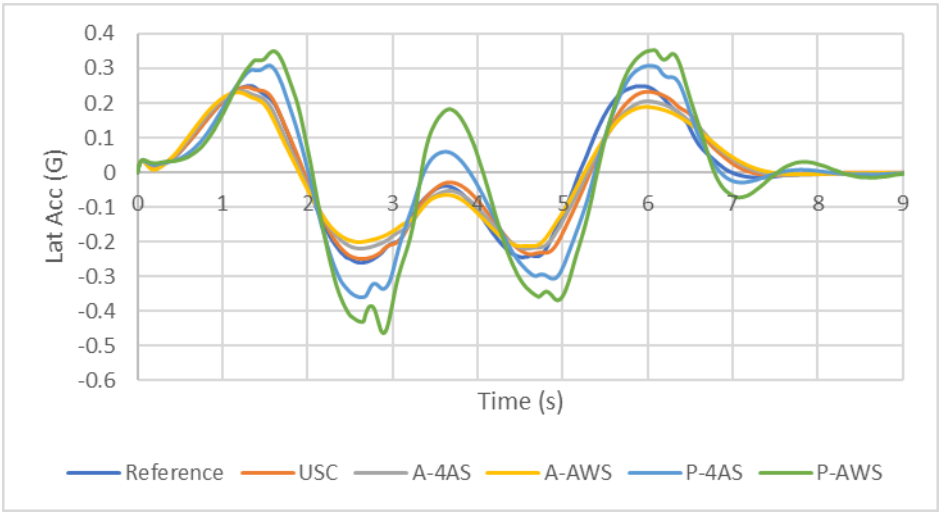

(b)

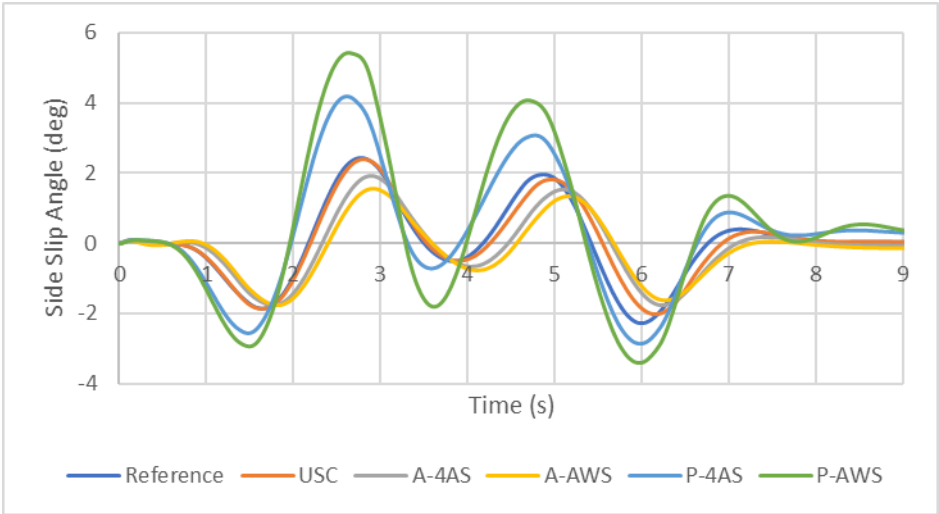

(c)

Figure 6-35 Yaw Rate (a), Lateral Acceleration (b) and Vehicle Side Slip (c) on 60 km/h Dry Asphalt Double Lane Change

Figure 6-35 above presents the yaw rate, lateral acceleration and side slip observed from the vehicles in this test. The front-wheel steered vehicle equipped with the unified stability controller works to slightly reduce the yaw rate, lateral acceleration, and side slip despite having little to no effect on speed, steering effort or path following ability. Use of the controller thereby slightly improves stability compared to the conventional uncontrolled reference vehicle.

When the active rear steering configurations are enabled alongside unified stability control, all measures are considerably reduced further, despite requiring slightly more steering effort. At the given speed, both the active rear steering control directing the rear wheels in the same orientation as the front, and the unified stability controller through active yaw control favor improved stability and safety of the vehicle over tighter maneuverability. While steering effort is slightly increased, sprung body motion is overall reduced given similar maneuverability, allowing the vehicle to be easier to handle.

Observations using the passive rear steering configurations are contrary to those of the active configurations, wherein tighter maneuverability is favored over vehicle stability. Steering effort is reduced and the vehicle attempts to follow closer to the target path. However, a larger variation in speed with higher yaw rate, lateral acceleration and side slip indicate the vehicle less table and difficult to handle. The higher measures – most notably with the P-AWS configuration – indicate greater amount of rolling and fishtailing through the maneuver which defeat the reduced steering input effort.

6.5.2 60 km/h on Ice-Covered Surface (μ=0.2)

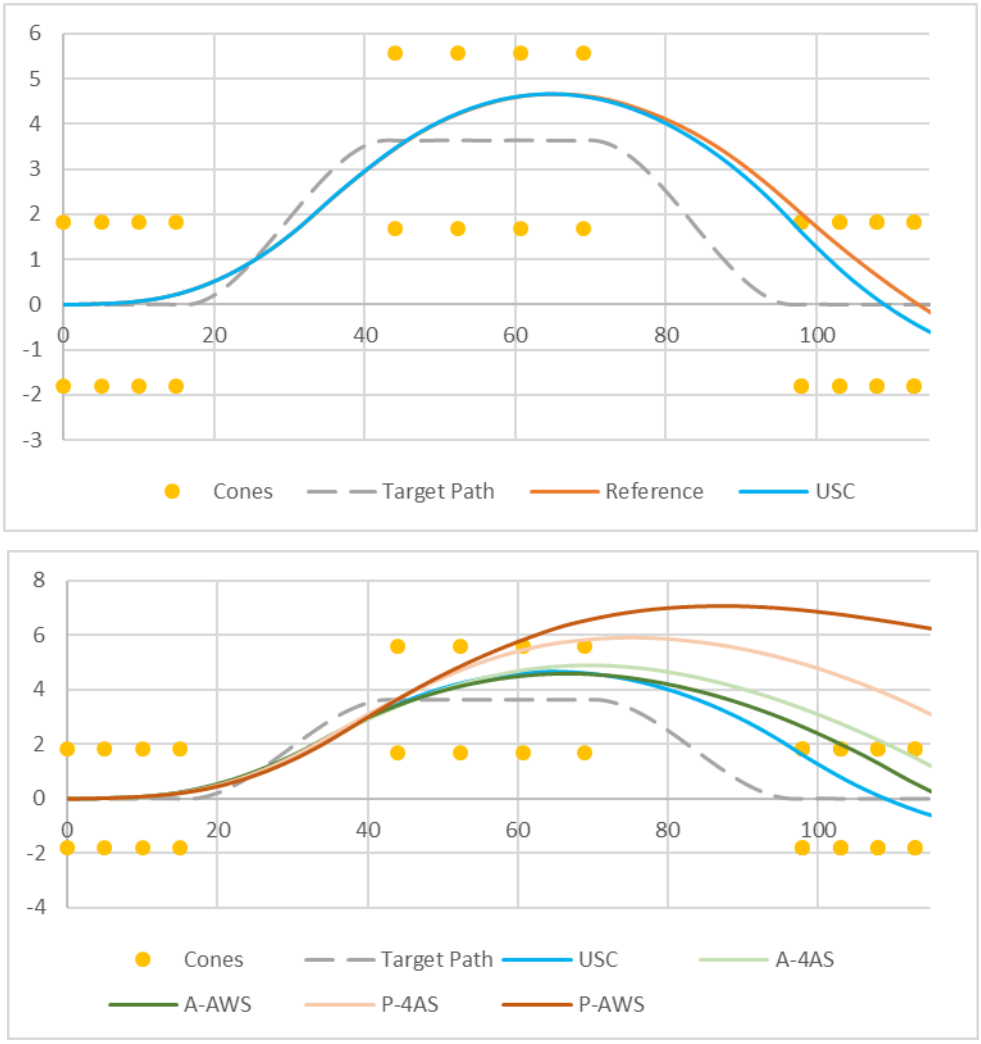

Figure 6-36 Vehicle Paths on 60 km/h Ice Double Lane Change

Figure 6-36(a) presents the paths of the reference and USC vehicles. While neither front-wheel steered configuration passes the maneuver successfully, the USC vehicle can turn tighter and straighten after entering the third set of cones. Figure 6-36(b) shows the paths of all rear steering configurations used against the USC vehicle as a baseline. Contrary to previous testing on ideal friction conditions, all rear-steering configurations make the vehicle less able to enter the third set of cones, with all passive configurations completely exiting the test area within the second set of cones. As observed in past tests with low-friction conditions, rear steering configurations diminish the path following ability of the vehicle.

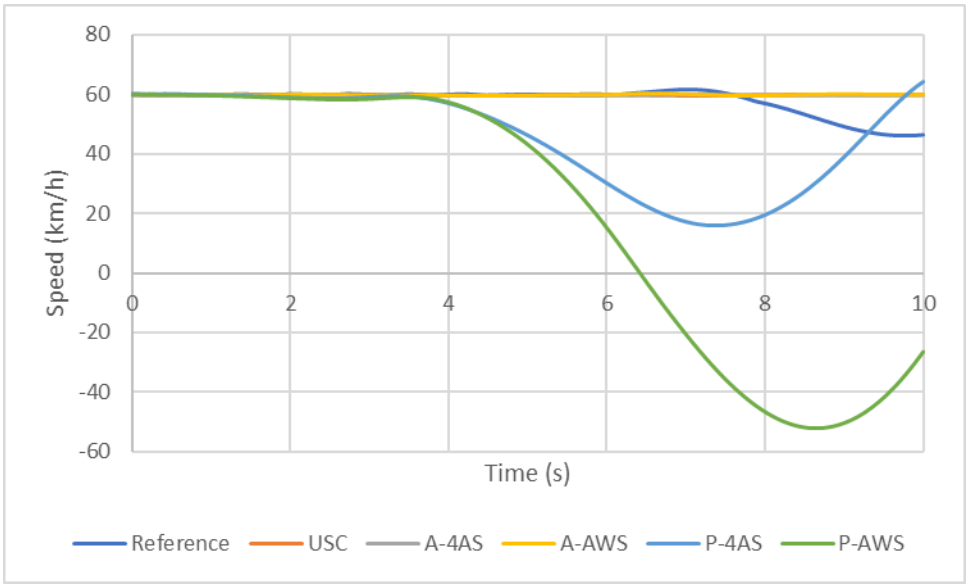

(a)

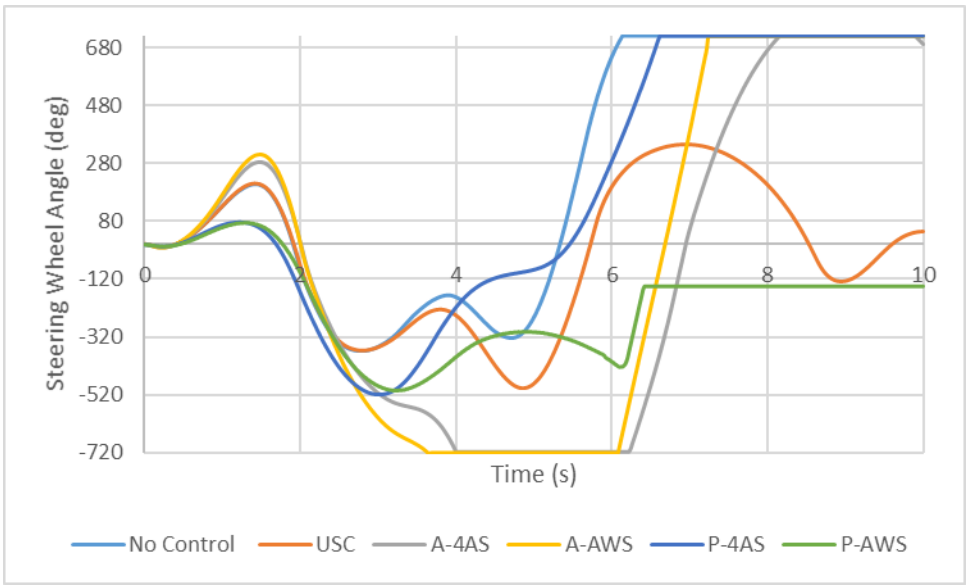

(b)

Figure 6-37 Vehicle Speeds (a) and Steering Input Effort (b) on 60 km/h Ice Double Lane Change

Figure 6-37 above presents the speed and steering wheel input effort for each vehicle in this test. Both active rear steering configurations can maintain a constant 60 km/h as well as the USC vehicle. The passive rear steering configurations exhibit large fluctuation in speed which correspond to the point in the maneuver where the respective vehicles are unable to stay within the testing area. As observed with the previous test, all rear steering configurations increase the steering effort required. Over low-friction surfaces, these configurations induce lock-up at 720 degrees. The USC vehicle required the least steering effort to complete the maneuver.

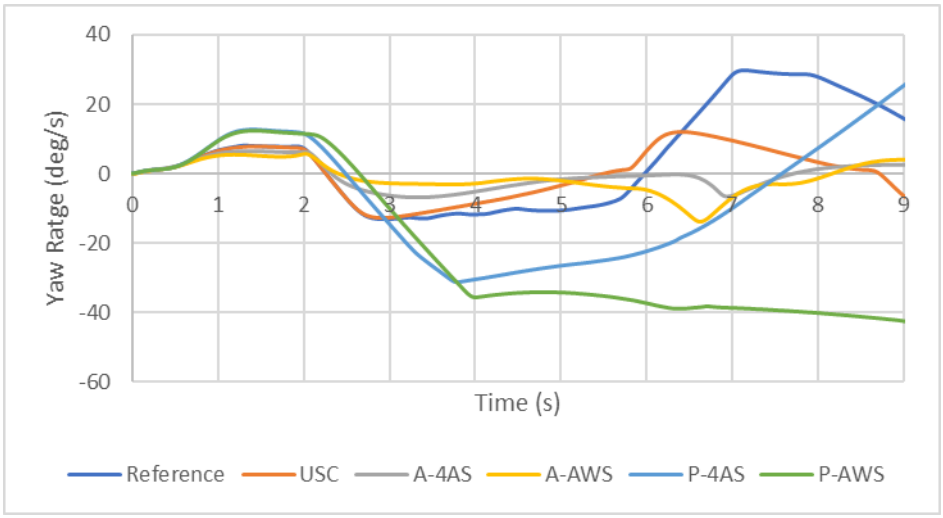

(a)

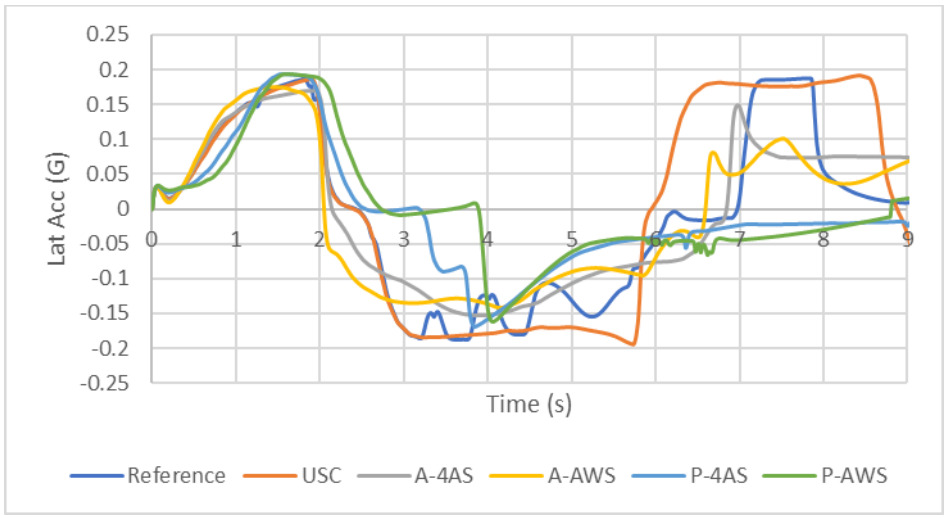

(b)

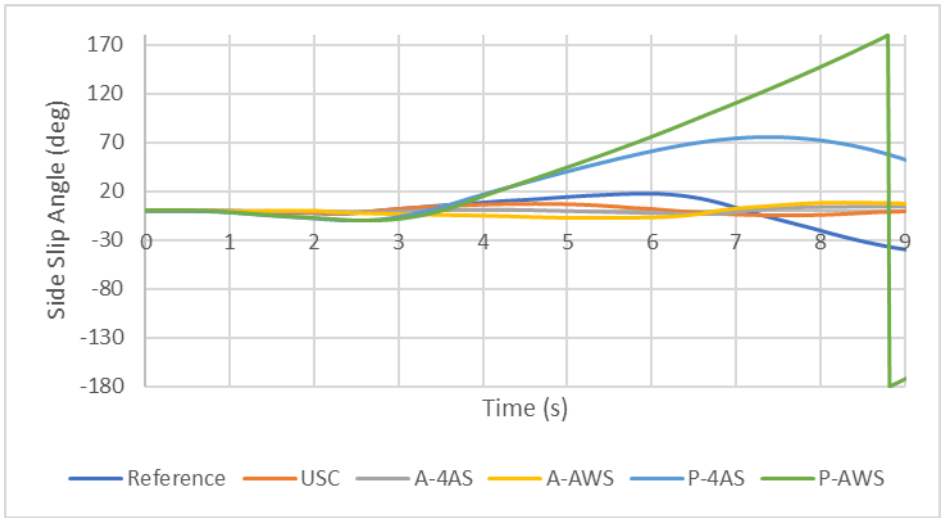

(c)

Figure 6-38 Yaw Rate (a), Lateral Acceleration (b) and Vehicle Side Slip (c) on 60 km/h Ice Double Lane Change

Figure 6-38 above presents the yaw rate, lateral acceleration and side slip observed from the vehicles in this test. Between both front-wheel steered vehicles, the USC vehicle exhibits lower yaw rate, a more stable trend in lateral acceleration with no anomalous spiking, and a greatly minimized trend in vehicle side slip compared to the reference vehicle. The ability of the USC vehicle to straighten out over the low-friction surface condition is illustrated by the vehicle side slip and yaw rate returning to zero near the end of the maneuver. At the same point the corresponding values for the reference vehicle do not reach zero, indicating lateral sliding through the third set of cones.

When equipped with the active rear steering configurations, both yaw rate and lateral acceleration are reduced, however the A-4AS configuration has shown to be more stable in this test case. The side slip of the A-4AS configuration is the lowest of all, and its trend in lateral acceleration exhibits less variations while similar in magnitude with the A-AWS configuration. However, in referring to vehicle paths in Figure 6-36, the A-4AS configuration has shown to be slightly less capable of maintaining the target path compared to the A-AWS configuration, despite not locking the steering wheel at the end of the maneuver.

Passive rear steering has shown to be an unstable option over the low friction surface on this maneuver, particularly the P-AWS configuration. All measured parameters for the P-4AS configuration indicate the vehicle in lateral sliding when exiting of the second set of cones in the maneuver. For the P-AWS configuration, all recorded parameters – particularly the spike in side slip – show that this vehicle completely loses control and leaves the boundaries of the test area after exiting the second set of cones.

6.5.3 80 km/h on Dry Asphalt (μ=0.8)

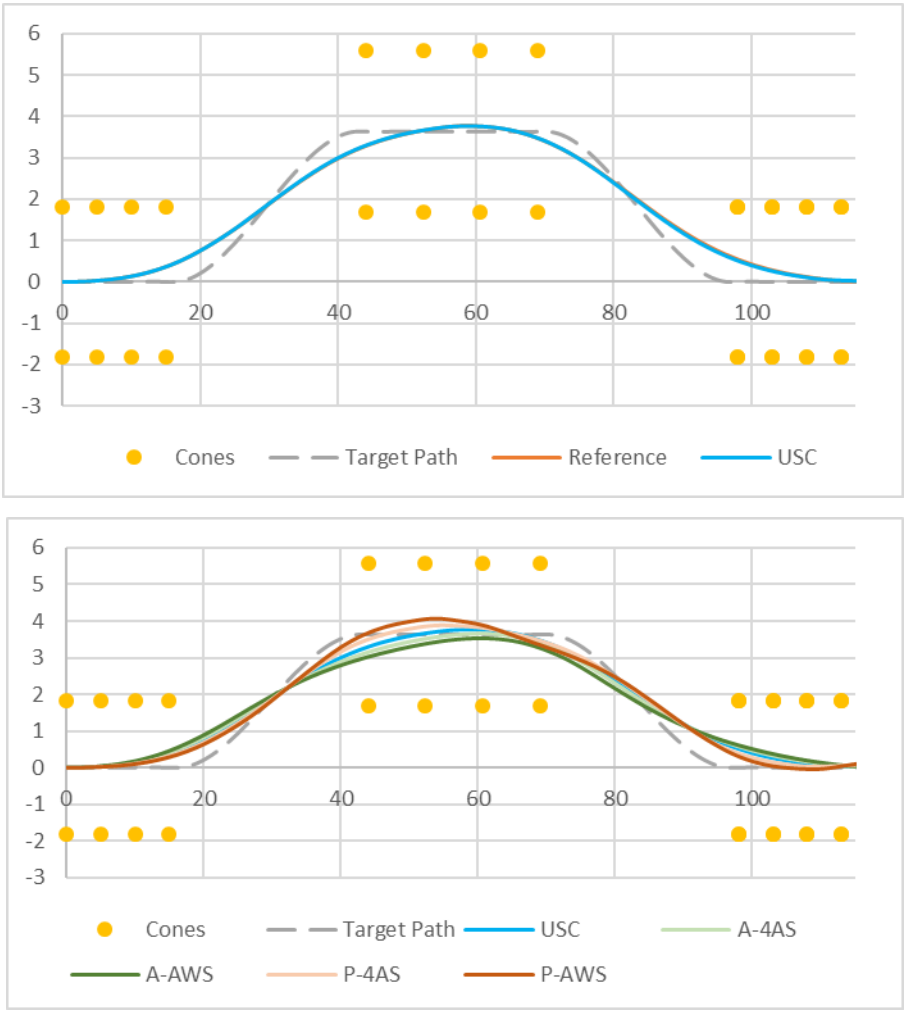

Figure 6-39 Vehicle Paths on 80 km/h Dry Asphalt Double Lane Change

Figure 6-39(a) presents the paths of the reference and USC vehicles. Both vehicles complete the double lane change maneuver with no notable difference in trajectory. Figure 6-39(b) shows the paths of all rear-steering configurations used against the USC vehicle as a baseline. The active rear steering configurations are less capable of following the target path at both the exit and entry points of each set of cones. The passive rear steering configurations force the vehicle to follow the target path much closer. However, this is at the cost of stability as shown by the path of the P-AWS vehicle entering the second set of cones. Of all the rear steering configurations, only the P-4AS vehicle passes, with the rest crashing into various numbers of cones throughout the maneuver.

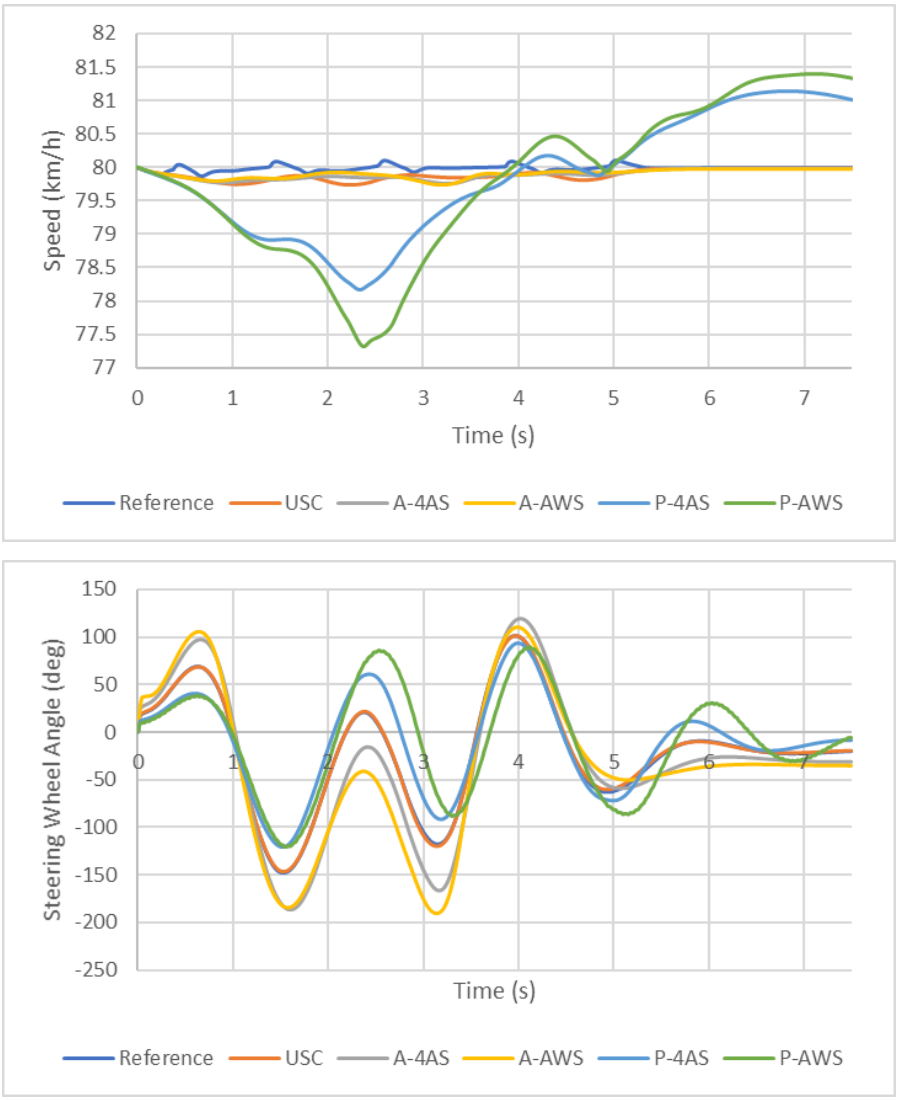

(a)

(b)

Figure 6-40 Vehicle Speeds (a) and Steering Input Effort (b) on 80 km/h Dry Asphalt Double Lane Change

Figure 6-40 above presents the speed and steering wheel input effort for each vehicle in this test. As observed with previous tests, no difference is observed in steering effort between the reference and USC vehicles, however the USC vehicle exhibits better speed management. In general, the USC vehicle as well as the active rear-steered vehicles show the most stable trends in speed variation, but a notable increase in overall steering effort observed in the active rear-steered vehicles. While steering effort is reduced with the passive rear-steered configurations, there is large variation in speed throughout the test procedure. For the P-AWS configuration, small oscillations are observed in the steering curve which indicate undesirable mechanical feedback.

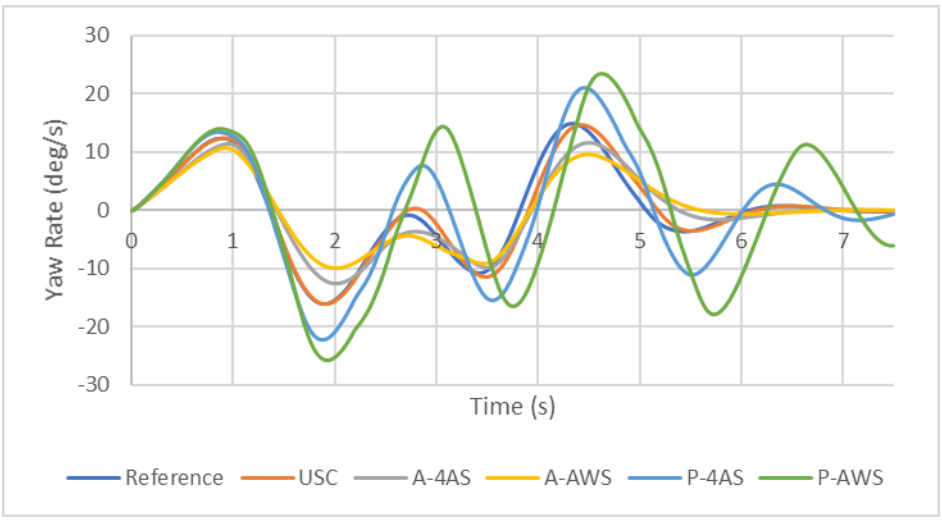

(a)

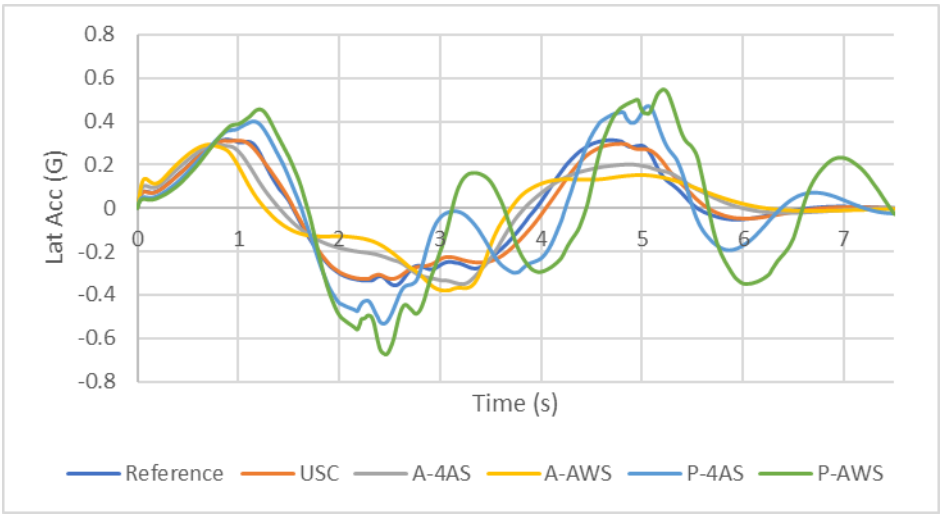

(b)

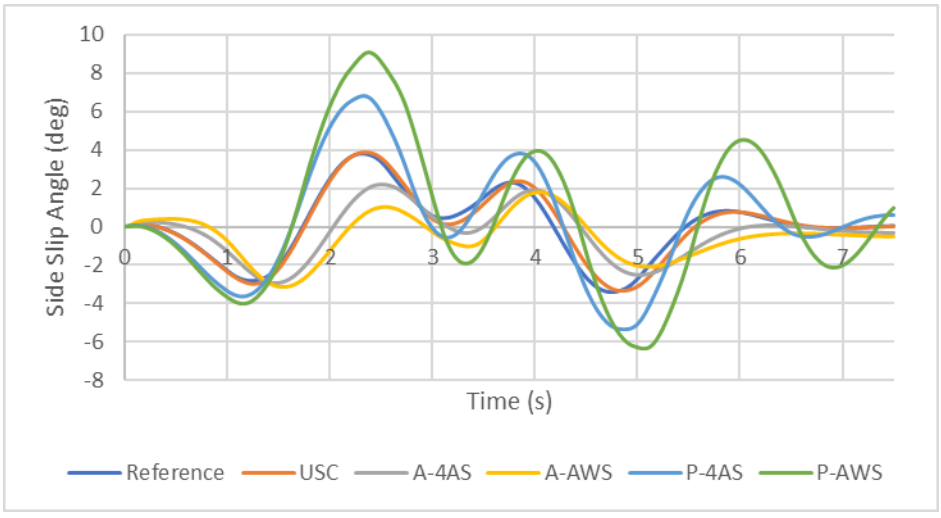

(c)

Figure 6-41 Yaw Rate (a), Lateral Acceleration (b) and Vehicle Side Slip (c) on 80 km/h Dry Asphalt Double Lane Change

Figure 6-41 above presents the yaw rate, lateral acceleration and side slip observed from the vehicles in this test. In operating at the given speed over ideal road surface conditions, the performance difference between both reference and USC vehicles is negligible in terms of the measured parameters. Both vehicles operate within stable, acceptable ranges of yaw rate, lateral acceleration and vehicle side slip and only very minor smoothing of the lateral acceleration trend is observed.

With active rear steering, it is once again observed that overall vehicle stability is favoured over precision maneuverability. Despite being less able to track the target path accurately, yaw rate and lateral acceleration are appreciably reduced, while vehicle side slip is greatly reduced. This indicates a significant reduction in undesired sprung mass motion, thus greater overall vehicle stability and controllability despite increased steering effort. The most stable configuration for travelling over ideal road surface conditions is the A-AWS configuration, as similarly observed in the 60 km/h test.

Contrary to active rear steering, passive rear steering increases yaw rate, lateral acceleration and vehicle side slip beyond stable levels in exchange for tighter path following. Lateral acceleration and side slip together show that in order to achieve tighter path following, the vehicle will exhibit more fishtailing, therefore worse lateral stability and excess sprung mass motion. This leads to overall increased difficulty in controlling the vehicle despite reduced steering effort as general vehicle motion becomes less predictable.

6.6 High-Speed Testing Conclusions

Based on observations from all tests completed within the high-speed category of vehicle operation, the following conclusions can be deduced.

For front-steered configurations;

- The unified stability control system performs best under low friction conditions in maintaining vehicle stability; lesser intervention is observed under ideal road surface conditions regardless of speed,
- Use of the unified stability control system also aids in stabilizing vehicle motion by providing smooth lateral torque distribution, thereby eliminating anomalies in lateral acceleration and vehicle side slip to improve controllability and predictability.

With respect to passive (fixed ratio) rear steering;

- The fixed ratios between front and rear axles promote greater precision maneuverability than active rear steering at comparable low speeds, but sacrifices greater amounts of stability as speed increases and therefore cannot be recommended,
- Passive all-wheel steering is the least stable configuration as observed in all tests performed, inducing a great amount of fishtailing as operating speed increases, thus reducing controllability and predictability of vehicle motion,
- Despite the presence of active yaw control, passive rear steering cannot be recommended at higher speeds due to saturation of tire operating characteristics and unpredictable body motion.

With respect to active (variable ratio) rear steering;

- The variable speed-dependent ratios favour different conditions at both low and high speeds – steering the rear wheels opposite to the front at low speeds allows for greater precision in maneuvering, while steering the rear wheels in the same orientation as the front allows for greater stability at the cost of precision,

- Under low speed operation and/or low surface friction conditions, the active fourth-axle steering configuration was observed to be more stable with negligible difference in precision of maneuvering compared to all-wheel steering; when exceeding 40 km/h, the active all-wheel steering promotes greater stability,
- Despite the active yaw controller using a front-steered vehicle as a reference control model, the implementation of speed-dependent active rear steering complements it by further increasing vehicle stability, indicating that the method used for active yaw control is in fact robust.

In terms of general vehicle operation, the following recommendations are presented;

- Basic turning using any of the proposed rear steering configurations should not be performed above 30 km/h or with acceleration/deceleration due to triggering sudden intervention of the slip regulator when equipped with the active rear steering controller,
- A pre-compensation factor that operates in the same manner as in skid steering can be used to alleviate the issue of higher required steering input during active rear steering. While this was not enabled in the active yaw controller during high-speed testing to provide a fair comparison, it will amplify the steering input and consequently, the torque distribution to reduce driver input effort,
- Implementation of active road surface condition monitoring methods is highly recommended to tune the unified stability control system in real-time and to switch between either active rear steering configurations
- Rear-wheel drive was not to a feasible power-saving method due to the tendency to oversteer in basic cornering, lack of power delivery during acceleration, and the tendency to trigger the slip regulator;
- The overall recommended configuration is thus all-wheel drive, with active fourth-axle steering enabled below 50 km/h or on low-friction conditions and active all-wheel steering when traveling above 50 km/h; autonomous driving is not recommended at higher speeds with this configuration to simplify control actions to fewer actuators in AI-driven operation.

6.7 Chapter Summary

This chapter summarized the results of all tests conducted on the electric combat vehicle in high-speed operation mode. A conventionally-driven combat vehicle is compared against the proposed electric combat vehicle in all available steering configurations. Rear-wheel drive was also investigated for feasibility as a means of conserving power through use of less electric motors. A set of four test procedures were conducted to evaluate vehicle performance – a modified J-Turn maneuver, a 100-ft radius circle skid pad acceleration test, the FMVSS 126 ESC test and the NATO 03-160W double lane change maneuver. These tests are organized in the manner of a process of elimination, to narrow down the most successful configuration on all maneuvers.

It was concluded that with speeds under 50 km/h, active fourth-axle steering was the most stable configuration while being able to maneuver as precisely the all-wheel steered counterpart. Above 50 km/h, active all-wheel steering was recommended to further improve the stability of the vehicle at high speeds. The unified stability control system was found to be most effective under low surface friction conditions. Active rear steering also improved stability further over low-friction surfaces, at the cost of increased driver input effort and greater likelihood of locking the steering wheel. This can be solved through the addition of a pre-compensation factor in the active yaw controller. Between both active rear steering configurations, fourth-axle steering proved to be the more stable option on low-friction surfaces, compared to all-wheel steering. The recommended configuration is to be all-wheel drive, as rear-wheel drive did not provide the required stability or torque output under certain conditions to be feasible as a method of conserving power. Finally, high-operation was deemed best suited for manned operation by trained drivers. The complexity of the powertrain in high-speed operation mode would require a more complex autonomous control system tasked with communicating to a larger number of actuators on the vehicle control network.

CHAPTER 7
CONCLUSIONS AND FUTURE WORK

7.1 General Conclusions

The rise of modern electric vehicle technology and autonomous driving control has brought forth new benefits in the mobility and safety of civilian passenger vehicles and show great potential in military applications – particularly in multi-wheeled combat vehicles. An electric powertrain provides the potential for reduced operating costs due to increased mechanical robustness, as well as a more effective and responsive platform for vehicle dynamics and stability control systems. Implementation of autonomous driving in military applications can further reduce risk of accidents such as rollover or spinout because of delayed human response, since autonomous control algorithms boast significantly faster decision and reaction time. In front-line operations, autonomous driving can reduce loss of life by eliminating the need for human presence and control error in highly-volatile environments.

To take advantage of the benefits provided by these technological advancements, this work proposed a comprehensive multi-wheel drivetrain control system for a fully electric 8x8 combat vehicle. The proposed control system consists of an autonomous navigation control unit, a unified stability control system for active yaw control (torque vectoring) and slip control, and an electric powertrain consisting of independently-actuated wheels. Each wheel in the vehicle contains its own in-hub electric driving motor and linear actuator for steering, allowing for mechanical decoupling and a high degree of configuration flexibility. Thanks to this control system, skid steering can be implemented at lower operating speeds for autonomous driving mode, or torque vectoring and rear-wheel steering at higher speeds with manned control.

The design process of the control system began with a survey of control techniques and vehicle applications for skid steering, torque vectoring, rear-wheel steering, and autonomous driving. Upon completing the survey and considering system requirements and available resources, the foundation of the control system was decided. Autonomous driving control was modeled using a gain-scheduled PID path-following algorithm using

path preview sensors. A single controller was developed using linear quadratic regulation (LQR) to achieve skid steering at lower speeds and active yaw control through torque vectoring at higher speeds. A feedforward rear steering controller was implemented to decouple steering control from torque vectoring control and maintain compatibility with skid steering mode. The rear steering controller used the feedforward zero side-slip control method, and operated in both fourth-axle and all-wheel steering mode. A separate feedforward controller to mimic the fixed contra-steering behaviour of existing combat vehicles was used as a baseline for testing. For autonomous skid steering mode, two control methods were made for comparison purposes – one using the LQR controller and another feedforward method synthesized from a single-track vehicle model, to mimic the fixed double-differential mechanisms found in combustion-engine powered vehicles.

To develop the LQR controller for skid steering and torque vectoring, a two-degree-of-freedom bicycle model of the 8x8 combat vehicle was used to derive steady-state yaw rate and vehicle side slip response, as well as to create a state-space model for control gain synthesis. Cost function weighting was based on maximum vehicle yaw rate, side slip angle, and external yaw moment – all of which allow the cost function to be re-tuned as a function of vehicle forward speed. The feedforward skid steering control method was created using a separate bicycle model with all tires fixed and differential lateral force distribution about the centre of gravity. The resulting external yaw moment response was derived and used as both a tuning parameter for the LQR controller and as a standalone controller translating steering input into yaw moment. Skid steering mode with the LQR controller was enabled by means of a pre-amplification scaling factor, which resulted in greater output per unit input. The feedforward zero side-slip rear steering controller was developed using an all-wheel steered bicycle model in which a speed-dependent steady-state response was derived by equating the vehicle side slip to zero. This controller was applied to the individual rear axles for allowing fourth-axle and all-wheel steering configurations. The fixed-ratio rear-steering controller was developed using two modified Ackermann steering geometries for fourth-axle and all-wheel steering, for which constant contra-steering gains relating the front and rear axles were determined. Finally, longitudinal slip control was handled using an on-off switch to cut motor power in the event of exceeding a 15% slip threshold, which is monitored consistently by vehicle sensors. The

autonomous driver model, torque vectoring controller, and longitudinal slip controller were organized into an “upper” control architecture to translate input command into a control signal. The “lower” control architecture, which consisted of the rear steering controller, electric motor model and motor current distribution system, translated the control signal into vehicle actuation.

Vehicle testing was separated into two distinct operating categories: low-speed autonomous driving mode using skid steering, and high-speed manned driving mode for torque vectoring and rear-wheel steering. In the low-speed testing category, all tests occurred on a sine-wave path with varying road conditions. The feedforward and LQR skid steering control methods were compared over ideal and low friction surfaces, and finally the LQR control method was compared against a conventional combat vehicle over off-road conditions. It was found that the feedforward method required large steering input to generate a desired yaw motion and saturated the motors on low-friction conditions. The feedforward control method was unable to achieve stable skid steering for the multi-wheeled combat vehicle above 20 km/h. The LQR control method for skid steering using a pre-compensation scaling factor could achieve steady maneuvering on both ideal and low-friction surfaces up to 40 km/h, without saturating the electric motors. Over off-road conditions, the LQR skid steering control method allowed the vehicle to perform on par with a conventional vehicle up to 30 km/h, with the advantage of reduced control input effort, regardless of driver type.

The high-speed testing category consisted of four tests intended to observe the performance and limitations of the LQR torque vectoring controller and rear steering configurations. Rear-wheel drive was also evaluated as a potential means of conserving power. The four tests included a modified J-turn maneuver, 100-ft radius skid pad, FMVSS 126 ESC test and the NATO double lane change maneuver. It was found that the electric combat vehicle equipped with torque vectoring control performed better over low-friction conditions than the equivalent front-steered combat vehicle. When considering rear-wheel steering, both fixed and zero side-slip control methods improved cornering precision at lower speeds. Fourth-axle steering was found to provide similar cornering performance with better stability than all-wheel steering when operating at low speed. However, as

speed increased, the fixed rear steering control method promoted oversteer and loss of control, while the zero side-slip method maintained vehicle stability, even under reduced friction conditions. At higher speeds with the zero side-slip control method, all-wheel steering provided better stability than fourth-axle steering. Rear-wheel drive was not found to be a feasible means of power conservation as the torque distribution system doubled the torque output of the rear wheels to compensate for the lack of tractive power at the front. This saturated the motors, promoted oversteer under normal conditions, and increased tire wear on the rear wheels due to excessive slip during acceleration.

Based on the results of both low and high-speed operation tests, the final recommended final configuration of the future electric combat vehicle is concluded. All-wheel drive is recommended for general vehicle stability as power is evenly distributed among all eight wheels with reduced risk of saturation. The zero side-slip rear steering control method is preferred. The fourth-axle configuration is recommended below 50 km/h when the rear wheels are steered opposite to the front, while all-wheel steering is recommended for speeds above 50 km/h when the rear wheels are steered in the same orientation as the front. Skid steering is recommended in autonomous driving mode up to 40 km/h as it is simpler to control with a less complex actuator network, and reduced input effort.

7.2 Future Work

Aspects of the multi-wheel drivetrain control system can be further be developed for future work. For the torque vectoring and skid steering controller, active surface friction and vehicle side slip estimation algorithms are recommended for a full vehicle implementation. Autonomous drive control can further be expanded upon to include environment localization and mapping. Integrating an obstacle detection and avoidance algorithm may also require more robust vehicle dynamics controllers. A more intelligent autonomous driver controller can be implemented to encompass navigation, obstacle avoidance, and powertrain configuration switching using this control system to maximize mobility over variable road conditions for potential high-speed autonomous operation, which is not covered in this thesis.

A scaled-down prototype vehicle is currently being produced which will allow for further testing of the control system. The prototype vehicle consists of the exact powertrain layout proposed in this thesis, and will allow further performance testing of various configurations. Further testing is recommended for skid steering due to the functional limitations of the TruckSim-Simulink co-simulation system. The scaled prototype will also be used as a platform for developing a sensor implementation and control algorithms for autonomous driving, inspired by the works reviewed in this thesis. The control system should be implemented in a driver-hardware-in-the-loop simulation system to test controller and vehicle performance in a full-scale application and investigate the effect of human control at high-speed operation.

PUBLICATIONS

Odrigo, A., El-Gindy, M., Nedělková, Z., Petterson, P., Lindroth, P., Öijer, F., "Design and Development of a Road Profile Generator", *International Journal of Vehicle Systems Modelling and Testing (IJVSMT), Vol. 11, No. 3,* 2016

Odrigo, A., El-Gindy, M., "Application of Optimal Control for Skid Steering in Future Electric Combat Vehicle", *International Journal of Automation and Control (IJAAC),* 2017 (Submitted)

*Parts of the publications listed above have been completed by the author of this thesis and are contained in this work. The author conducted all writing, design, and development. Listed co-authors have provided technical support as required and have been part of the review process of these publications.

REFERENCES

[1] T. Markel and A. Simpson, "Cost-Benefit Analysis of Plug-In Hybrid," *World Electric Vehicle Journal,* vol. 1, 2006.

[2] L. De Novellis, A. Sorniotti, P. Gruber, L. Shead, I. Ivanov and K. Hoepping, "Torque Vectoring for Electric Vehicles with Individually Controller Motors: State-of-the-Art and Future Developments," in *EVS26 International Battery, Hybrid and Fuel Cell Electric Vehicle Symposium*, Los Angeles, 2012.

[3] C. Urmson and W. Whittaker, "Self-Driving Cars and the Urban Challenge," *IEEE Intelligent Systems,* vol. 23, no. 2, pp. 66-68, 2008.

[4] S. Fish, "Power Simulation for All-Electric Combat Vehicles," University of Texas at Austin, Austin, 1995.

[5] N. Jonson, "Hybrid-electric combat vehicle completes 1,000-mile test," Aerosapce Daily, 2003.

[6] H. Ragheb, *Torque Control Strategy for Off-Road Vehicle Mobility,* PhD Thesis, Oshawa: University of Ontario Institute of Technology, 2014.

[7] P. D'Urso, *Development of H∞ Control Strategy for a Multi-Wheeled Combat Vehicle,* MASc Thesis, Oshawa: University of Ontario Institute of Technology, 2016.

[8] J. Wong, Theory of Ground Vehicles, 4th ed., Wiley, 2008.

[9] H. B. Pacejka, Tyre and Vehicle Dynamics, Butterworth-Heinemann, 2006.

[10] N. Nise, Control Systems Engineering, 6th ed., Wiley, 2011.

[11] A. Bryson, Applied Optimal Control: Optimization, Estimation and Control, CRC Press, 1975.

[12] K. Zhou and J. Doyle, Essentials of Robust Control, Prentice Hall, 1997.

[13] P. Antsaklis and K. Passino, An Introduction to Intelligent and Autonomous Control, Kluwer Academic Publishers, 1993.

[14] B. Maclaurin, "Comparing the steering performances of skid- and Ackermann-steered vehicles," Institution of Mechanical Engineers, 2008.

[15] Artec GmbH, "BOXER Command Post Vehicle," [Online]. Available: http://www.artec-boxer.com/fileadmin/documents/BOXER_CP.pdf. [Accessed 2017].

[16] L. Mangialardi and A. Gentile, "Behavior of a Non-Conventional Transmission and Skid-Steering Vehicle," in *19th International FISITA Congress: Energy Mobility*, Melbourne, 1982.

[17] L. Mangialardi and A. Gentile, "Dynamic Steering Multiaxle Vehicles: Influence on Axle Numbers," in *20th Internation FISITA: The Automotive Future*, Vienna, 1984.

[18] J.-C. Fauroux and P. Vaslin, "Modeling, Experimenting and Improving Skid Steering on a 6x6 All-Terrain Mobile Platform," *Journal of Field Robotics*, vol. 27, no. 2, pp. 107-126, 2010.

[19] Y. Zhang, j. Hu and X. Li, "Steady-state characteristics of skid steering for wheeled vehicles," *Journal of Automobile Engineering*, vol. 228, no. 9, pp. 1095-1104, 2014.

[20] R. Colyer and J. Economou, "Soft modelling and fuzzy logic control of wheeled skid-steer vehicles with steering prioritisation," *International Journal of Approximate Reasoning*, vol. 22, pp. 31-52, 1999.

[21] J. Economou and R. Colyer, "Modelling of Skid Steering and Fuzzy Logic Vehicle Ground Interaction," in *American Control Conference*, 2000.

[22] J. Economou, R. Colyer, A. Tsourdos and B. White, "Fuzzy Logic Approaches for Wheeled Skid-Steer Vehicles," in *IEEE 56th Vehicular Technology Conference*, 2002.

[23] Z. Song, Y. Zweiri, L. Seneviratne and K. Althoefer, "Non-linear Observer for Slip Estimation of Skid-steering Vehicles," in *IEEE International Conference of Robotics and Automation*, Orlando, 2006.

[24] E. Lucet, C. Grand, D. Salle and P. Bidaud, "Dynamic yaw and velocity control of the 6WD skid-steering mobile robot RobuROC6 using sliding mode technique," in *IEEE/RSJ International Conference on Intelligent Robots and Systems*, St. Louis, 2009.

[25] E. Lucet, C. Grand and P. Bidaud, "Sliding-Mode Velocity and Yaw Control of a 4WD Skid-Steering Mobile Robot," in *Brain, Body and Machine: Proceedings of an International Symposium on the Occasion of the 25th Anniversary of McGill University Centre for Intelligent Machines*, Berlin, Springer, 2010, pp. 247-258.

[26] C. Jin, L. Xiong, Z. Yu and Y. Feng, "Path Following Control for Skid Steering Vehicles with Vehicle Speed Adaption," Society of Automotive Engineers, 2014.

[27] J. Kang, W. Kim, J. Lee and K. Yi, "Skid steering-based control of a robotic vehicle with six in-wheel drives," *Journal of Automobile Engineers*, vol. 224, no. D11, pp. 1369-1391, 2010.

[28] V. Nazari and M. Naraghi, "Sliding Mode Fuzzy Control of a Skid Steer Mobile Robot for Path Following," in *10th International Conference on Control, Automation, Robotics and Vision*, Hanoi, 2008.

[29] J. Aslam, S.-Y. Qin and M. Alvi, "Fuzzy sliding mode control algorithm for a four-wheel skid steer vehicle," *Journal of Mechanical Science and Technology*, vol. 28, no. 8, pp. 3301-3310, 2014.

[30] T. Miura, Y. Ushiroda, K. Sawase, N. Takahashi and K. Hayashikawa, "Development of Integrated Vehicle Dynamics Control System 'S-AWC'," *Mitsubishi Motors Technical Review*, vol. 20, pp. 21-25, 2008.

[31] M. Hancock, R. Williams, T. Gordon and M. Best, "A comparison of braking and differential control of road vehicle yaw-sideslip dynamics," *Journal of Automobile Engineering*, vol. 219, pp. 309-327, 2005.

[32] H. Kim, S. Lee and J. Hedrick, "Active Yaw Control for Handling Performance Improvement by using Traction Force," *International Journal of Automotive Technology*, vol. 16, no. 3, pp. 457-464, 2015.

[33] S. Chocholek, "The development of a differential for the improvement of traction control," *Proceedings of the Institution of Mechanical Engineering*, vol. C368/88, pp. 75-82, 1988.

[34] J. Kisney, "The advantages of an electronically controlled limited slip differential," Society of Automotive Engineers, 2004.

[35] E. Esmailzadeh, A. Goodarzi and G. Vossoughi, "Optimal yaw moment control law for improved vehicle handling," University of Victoria, 2003.

[36] F. Cheli, S. Melzi, E. Sabbioni and M. Vignati, "Torque Vectoring Control of a Four Indepedent Wheel Drive Electric Vehicle," in *2013 ASME International Design Engineering Technical Conferences and Computers and Information in Engineering Conference*, Portland, 2013.

[37] O. Mokhiamar and M. Abe, "Simultaneous Optimal Distribution of Lateral and Longitudinal Tire Forces for the Model Following Control," *Journal of Dynamic Systems, Measurment and Control*, vol. 126, pp. 753-763, 2004.

[38] W. Cho, J. Yoon, J. Kim, J. Hur and K. Yi, "An investigation into unified chassis control scheme for optimised vehicle stability and manoeuverability," *Vehicle System Dynamics*, vol. 46, pp. 87-105, 2008.

[39] W. Kim, K. Yi and J. Lee, "An optimal traction, braking and steering coordination strategy for stability and manoeuverability of a six-wheel drive and six-wheel steer vehicle," *Institution of Mechanical Engineers*, vol. 226, no. 1, pp. 3-22, 2011.

[40] M. Jalili-Kharaajoo and F. Besharati, "Sliding Mode Traction Control of an Electric Vehicle," in *IEEE Conference on Emerging Technologies and Factory Automation*, 2003.

[41] Q. Liu, G. Kaiser, S. Boonto, H. Werner, F. Holzmann, B. Chretien and M. Korte, "Two-Degree-of-Freedom LPV Control for a Through-the-Road Hybrid Electric Vehicle via Torque Vectoring," in *50th IEEE Conference on Decision and Control and European Control Conference*, Orlando, 2011.

[42] C. Poussot-Vassal, O. Sename, S. Fergani, M. Doumiati and L. Dugard, "Global Chassis Control Using Coordinated Control of Braking/Steering Actuators," in *Robust Control and Linear Parameter Varying Approaches: Application to Vehicle Dynamics*, 2013, pp. 237-266.

[43] A. Ulsoy, H. Peng and M. Cakmacki, Automotive Control Systems, Cambridge University Press, 2012.

[44] M. Blundell and D. Harty, The Multibody Systems Approach to Vehicle Dynamics, Elsevier, 2015.

[45] G. Nalecz and A. Bindemann, "Handling properties of four wheel steering vehicles," Society of Automotive Engineers, 1989.

[46] FNSS, "PARS 8x8 Wheeled Armored Combat Vehicle," [Online]. Available: http://www.fnss.com.tr/content/docs/fnss-pars8x8-en.pdf. [Accessed 2017].

[47] "Piranha V Armoured Wheeled Vehicles, United Kingdom," [Online]. Available: http://www.army-technology.com/projects/piranhav/. [Accessed 2017].

[48] S. Sano, Y. Furukawa, T. Nihei and M. Abe, "Handling Characteristics Of Steer Angle Dependent Four Wheel Steering System," Society of Automotive Engineers, 1988.

[49] Y. Furukawa, N. Yuhara, S. Sano, H. Takeda and Y. Matsushita, "A review of four-wheel steering studies from the viewpoint of vehicle dynamics and control," *Vehicle System Dynamics*, vol. 18, pp. 151-186, 1989.

[50] T. Eguchi, Y. Sakita, K. Kawagoe and S. Kaneko, "Development of “Super Hicas”, a New Rear Wheel Steering System with Phasereversal Control," Society of Automotive Engineers, 1989.

[51] T. Takiguchi, N. Yasuda, S. Furutani and H. Kanazawa, "Improvement of Vehicle Dynamics by Vehicle-Speed-Sensing Four-Wheel Steering System," Society of Automotive Engineers, 1986.

[52] T. Hiraoka, O. Nishihara and H. Kumamoto, "ACTIVE FOUR-WHEEL STEERING SYSTEM FOR ZERO SIDESLIP ANGLE AND LATERAL ACCELERATION CONTROL," 2003.

[53] G.-D. Yin, N. Chen, J.-X. Wang and J.-S. Chen, "ROBUST CONTROL FOR 4WS VEHICLES CONSIDERING A VARYING TIRE-ROAD FRICTION COEFFICIENT," *International Journal of Automotive Technology*, vol. 11, no. 1, pp. 33-40, 2010.

[54] M. Kreutz, M. Horn and J. Zehetner, "Improving vehicle dynamics by active rear wheel steering systems," *Vehicle System Dynamics*, vol. 47, no. 12, pp. 1551-1564, 2009.

[55] K. Bayar and Y. Unlusoy, "Steering strategies for multi-axle vehicles," *International Journal of Heavy Vehicle Systems*, vol. 15, pp. 208-236, 2008.

[56] H. Wang, B. Wang, B. Liu, X. Meng and G. Yang, "Pedestrian recognition and tracking using 3D LiDAR for autonomous," *Robotics and Autonomous Systems*, vol. 88, pp. 71-78, 2016.

[57] S. Sukkarieh, E. Nebot and H. Durrant-Whyte, "A High Integrity IMU/GPS Navigation Loop for Autonomous Land Vehicle Applications," *IEEE TRANSACTIONS ON ROBOTICS AND AUTOMATION*, vol. 15, no. 3, pp. 572-578, 1999.

[58] E. Bicho, P. Mallet and G. Schoner, "Target Representation on an Autonomous Vehicle with Low-Level Sensors," *The International Journal of Robotics Research*, vol. 19, no. 5, pp. 424-447, 2000.

[59] J. Kim, F. Zhang and M. Egerstedt, "Curve Tracking Control for Autonomous Vehicles with Rigidly Mounted Range Sensors," *Journal of Intelligent Robot Systems*, vol. 56, pp. 177-197, 2009.

[60] S. Jung, J. Kim and S. Kim, "Simultaneous localization and mapping of a wheel-based autonomous vehicle with ultrasonic sensors," in *14th International Symposiumon Artificial Life and Robotics*, Oita, 2009.

[61] Z. Xu, W. Yang, K. You, W. Li and Y. Kim, "Vehicle autonomous localization in local area of coal mine tunnel based on vision sensors and ultrasonic sensors," PLoS ONE, 2017.

[62] C. Chatzikomis and K. Spentzas, "Apath-following driver modelwith longitudinal and lateral control of vehicle's motion," Springer, 2009.

[63] L. Menhour, D. Lechner and A. Charara, "Two degrees of freedom PID multi-controllers to design a mathematical driver model: experimental validation and robustness tests," *Vehicle System Dynamics*, vol. 49, no. 4, pp. 595-624, 2011.

[64] N. Ding, Y. Zhang, F. Gao and G. Xu, "A Gain-Scheduled PID Controller for Automatic Path Following of a Tractor Semi-Trailer," Society of Automotive Engineers, 2013.

[65] G. Tan, M. Liu, C. Lin and W. Shu, "Design and Simulation of Fuzzy PID Driver Model," Institute of Electrical and Electronics Engineers, 2015.

[66] R. Bulirsch, M. Vogel, O. von Stryk, C. Chucholowski and T.-M. Wolter, "An Optimal Control Approach To Real-Time Vehicle Guidance," in *Mathematics — Key Technology for the Future*, Springer, 2003, pp. 84-102.

[67] A. Ungoren and H. Peng, "An Adaptive Lateral Preview Driver Model," *Vehicle System Dynamics,* vol. 43, no. 4, pp. 245-259, 2005.

[68] J. Edelmann, M. Plochl, W. Reinalter and W. Tieber, "A passenger car driver model for higher lateral accelerations," *Vehicle System Dynamics,* vol. 45, no. 12, pp. 1117-1129, 2007.

[69] "Inverted Pendulum: State-Space Methods for Controller Design," University of Michigan, [Online]. Available: goo.gl/rwRq7B. [Accessed 2017].

[70] "Aircraft Pitch: State-Space Methods for Controller Design," University of Michigan, [Online]. Available: goo.gl/GxKaa2. [Accessed 2017].

[71] S. B. D. Alves, *Helicopter Flight Modeling and Robust Autonomous Control with Uncertain Dynamics,* Covilhã: Universidade da Beira Interior, 2012.

[72] M. Biao, L. Yahui, G. Yefeng, Y. Yiyong, J. Xuewu and B. Ying, "Estimation of vehicle sideslip angle based on steering torque," *The International Journal of Advanced Manufacturing Technology,* 2016.

[73] X. Li, C.-Y. Chan and Y. Wang, "A Reliable Fusion Methodology for Simultaneous Estimation of Vehicle Sideslip and Yaw Angles," *IEEE Transactions on Vehicular Technology,* vol. 65, no. 6, pp. 4440-4458, 2016.

[74] S. Chung and H. Lee, "Vehicle sideslip estimation and compensation for banked road," *International Journal of Automotive Technology,* vol. 17, no. 1, pp. 63-69, 2016.

[75] D. Bevly, J. Ryu and J. Gerdes, "Integrating INS Sensors With GPS Measurements for Continuous Estimation of Vehicle Sideslip, Roll, and Tire Cornering Stiffness," *IEEE Transactions on Intelligent Transport Systems,* vol. 7, no. 4, pp. 483-493, 2006.

[76] J.-H. Yoon, S. Li and C. Anh, "Estimation of vehicle sideslip angle and tire-road friction coefficient based on magnetometer with GPS," *International Journal of Automotive Technology,* vol. 17, no. 3, pp. 427-435, 2016.

[77] J.-O. Hahn, R. Rajamani and L. Alexander, "GPS-based real-time identification of tire-road friction coefficient," *IEEE Transactions on Control Systems Technology,* vol. 10, pp. 331-343, 2002.

[78] J. Wang, L. Alexander and R. Rajamani, "Friction estimation of highway vehicles using longitudinal measurements," *Journal of dynamic systems, measurement, and control,* vol. 126, pp. 265-275, 2004.

[79] R. Rajamani, G. Phanomcheng, D. Piyabongkarn and J. Lew, "Algorithms for real-time estimation of individual wheel tire-road friction coefficients," *IEEE/ASME Transactions on Mechatronics,* vol. 17, pp. 1183-1195, 2012.

[80] K. Singh and S. Taheri, "Estimation of tire-road friction coefficient and its application in chassis control systems," *Systems Science & Control Engineering,* vol. 3, pp. 39-61, 2015.

[81] L. Chrif and Z. Kadda, "Aircraft Control System Using LQG and LQR Controller with Optimal Estimation-Kalman Filter Design," *Procedia Engineering,* vol. 80, pp. 245-257, 2014.

[82] A. Odrigo, M. El-Gindy, P. Petterson, Z. Nedelkova, P. Lindroth and F. Oijer, "Design and development of a road profile generator," *International Journal of Vehicle Systems Modelling and Testing,* vol. 11, no. 3, pp. 217-233, 2016.

[83] M. Agostinacchio, D. Ciampa and S. Olita, "The vibrations induced by surface irregularities in road pavements - a Matlab approach," *European Transport Research Review,* vol. 6, no. 3, pp. 267-275, 2013.

[84] K. Bogsjo, K. Podgorski and I. Rychlik, "Models for road surface roughness," *Vehicle System Dynamics,* vol. 50, no. 5, pp. 725-747, 2012.